TECHNISCHE
UNIVERSITÄT
DARMSTADT

Mussel-inspired microgels with improved mechanical and adhesive properties

vom Fachbereich Physik
der Technischen Universität Darmstadt

zur Erlangung des akademischen Grades
Doctor rerum naturalium
(Dr. rer. nat.)

genehmigte Dissertation
von M. Sc. Sandra Forg

Erstgutachterin: Prof. Dr. Regine von Klitzing
Zweitgutachter: Prof. Dr. Matthias Karg

Darmstadt 2023

Forg, Sandra: Mussel-inspired microgels with improved mechanical and adhesive properties
Darmstadt, Technische Universität Darmstadt
Jahr der Veröffentlichung der Dissertation auf TUprints: 2024
URN: urn:nbn:de:tuda-tuprints-264920
Tag der mündlichen Prüfung: 20.12.2023

Promotionsausschuss:

Referentin:	Prof. Dr. Regine von Klitzing
Koreferent:	Prof. Dr. Matthias Karg
Prüfer:	Prof. Dr. Michael Vogel
Prüfer:	Prof. Dr. Jens Braun
Tag der Disputation:	20.12.2023

"Some things I cannot change, but ’til I try I’ll never know."

"I think I’ll try defying gravity"
[’cause]
"Everyone deserves the chance to fly"

- Stephen Schwartz, *Wicked*

Erklärungen laut Promotionsordnung

§8 Abs. 1 lit. c PromO
Ich versichere hiermit, dass die elektronische Version meiner Dissertation mit der schriftlichen Version übereinstimmt.

§8 Abs. 1 lit. d PromO
Ich versichere hiermit, dass zu einem vorherigen Zeitpunkt noch keine Promotion versucht wurde. In diesem Fall sind nähere Angaben über Zeitpunkt, Hochschule, Dissertationsthema und Ergebnis dieses Versuchs mitzuteilen.

§9 Abs. 1 PromO
Ich versichere hiermit, dass die vorliegende Dissertation selbstständig und nur unter Verwendung der angegebenen Quellen verfasst wurde.

§9 Abs. 2 PromO
Die Arbeit hat bisher noch nicht zu Prüfungszwecken gedient.

Darmstadt, den 10.11.2023 _____

(Sandra Forg)

Wissenschaftlicher Werdegang

10/2018 - heute	Wissenschaftliche Mitarbeiterin im Rahmen einer Promotion am Institut für Physik Kondensierter Materie an der Technischen Universität Darmstadt in der AG von Prof. Dr. Regine von Klitzing
07/2017 - 09/2018	Studentische Hilfskraft an der Technischen Universität Darmstadt mit Schwerpunkt "Physik weicher und kondensierter Materie" in der AG von Prof. Dr. Regine von Klitzing Themen: Synthese von PNIPAM Mikrogelen, Magnetische Mikrogele, Charakterisierung mithilfe von Rasterkraftmikroskopie (AFM), Dynamischer Lichstreuung (DLS) und Zetasizer
09/2016 - 09/2018	Studium der Physik (M. Sc.) an der Technischen Universität Darmstadt mit Schwerpunkt "Physik weicher und kondensierter Materie" Forschungspraktikum in der AG von Prof. Dr. Barbara Drossel mit dem Thema: "A molecular dynamics study of water and octanol confined in a silica nanopore" Masterarbeit in der Gruppe von Prof. Dr. Regine von Klitzing mit dem Thema: "The stabilization of Pickering emulsions with the use of polystyrene latex particles for hydroformylation of long chain olefins""
10/2012 - 08/2016	Studium der Physik (B. Sc.) an der Technischen Universität Darmstadt Bachelorarbeit in der AG von Prof. Dr. Michael Vogel mit dem Thema: "1H-NMR-Diffusometrie an PMMA-Mikrogelen im statischen Feldgradienten"

Wissenschaftliche Veröffentlichungen

Parts of this thesis are taken from the following publications of the author:

- "Mixtures of Alcohols and Water Confined in Mesoporous Silica- a Combined Solid-State NMR and Molecular Dynamic Simulation Study" B. Kumari, M. Brodrecht, H. Breitzke, M. Werner, B. Grünberg, H.-H. Limbach, S. Forg, E. P. Sanjon, B. Drossel, T. Gutmann, and G. Buntkowsky, *J. Phys. Chem. C*, **2018**, 122, 34, 19540-19550.
- "Copolymerization Kinetics of Dopamine Methacrylamide during PNIPAM Microgel Synthesis for Increased Adhesive Properties" S. Forg, A. Karbacher, Z. Ye, X. Guo, and R. von Klitzing, *Langmuir*, **2022**, 38, 17, 5275-5285.
- "Influence of Dopamine Methacrylamide on swelling behaviour and nanomechanical properties of PNIPAM microgels" S. Forg, X. Guo, and R. von Klitzing, *submitted*.
- "Mussel-inspired P(NIPAM-co-dopamine methacrylamide) microgels with increased adhesive properties" S. Forg, C. Schneider, B. Füßer, F. Berner, R. Berger and R. von Klitzing, *in preparation*.
- "Gram-scale synthesis of homogeneous Fe3N nanoparticles for magnetic fluid hyperthermia by advanced thermal decomposition process" Y. Ablets, L. Kubíčková, A. Chanda, I. Orue, D. Koch, S. Najma, S. Forg, E. Adabifiroozjaei, L. Molina-Luna, T. Kmječ, J. Á. García, F. Plazaola, R. von Klitzing, W. Donner, H. Srikanth, O. Gutfleisch, I. Dirba, *in preparation*.

Abstract

This thesis aims to develop microgels with improved adhesive and mechanical properties by drawing inspiration from the remarkable under-water adhesion of mussels. The synthesised microgels are based on poly(*N*-isopropylacrylamide) (PNIPAM), known for its temperature-responsive behaviour. Dopamine methacrylamide (DMA) can be used as a co-monomer to mimic the mussel's properties. Due to its catechol group, it is capable of cross-linking microgel structures. However, its scavenging ability demands a precise synthesis control.

In the first part of this thesis, the microgel synthesis is analysed and controlled through kinetic studies. Time-samples, taken during the synthesis, are evaluated by using mass spectrometry (MS) to determine the individual monomer consumption rates. The incorporation of DMA is quantified using UV-vis and nuclear magnetic resonance (NMR) spectroscopy. An optimised synthesis protocol is developed: A DMA injection after 15 min ensures the full NIPAM and cross-linker *N*,*N*'-methylene-bis-acrylamide (BIS) consumption, while an overall synthesis reaction time of 60 min guarantees the DMA incorporation. The synthesis is reproducible and independent of UV light. DMA exhibits second-order reaction kinetics.
In the second part, the temperature-dependent swelling behaviour of P(NIPAM-co-DMA) microgels with varying DMA incorporations is analysed: DMA lowers the volume phase transition temperature (VPTT) due to its higher hydrophobicity when compared to NIPAM and sharpens the transition itself. Force spectroscopy measurements on single adsorbed microgel particles reveal that the incorporation of DMA stiffens PNIPAM microgels over their entire cross-section. The swelling behaviour and mechanical properties are linearly correlated as predicted by the affine network model for both types of microgels. Nonetheless, when a large amount of DMA is incorporated, catechol interactions within the network inhibit the shrinking of the microgel, while maintaining its high mechanical stiffness.
In the final part of this thesis, the adhesive properties of the microgels are characterised by colloidal probe atomic force microscopy (AFM) on monolayers of microgels prepared by the Langmuir-Blodgett technique. P(NIPAM-co-DMA) microgels exhibit superior adhesion when compared to pure PNIPAM microgels. Adhesive forces reach their maximum at 10 mol% DMA content. However, higher DMA amounts lead to reduced adhesive but increased mechanical properties - this highlights the delicate bal-

ance between the material's cohesive and adhesive properties. When further increasing the packing densities of microgel particles, the adhesion of P(NIPAM-co-DMA) microgels decreases, possibly due to catechol interactions within the densely compressed microgels.

Kurzzusammenfassung

Ziel dieser Arbeit ist die Entwicklung von Mikrogelen mit verbesserten adhäsiven und mechanischen Eigenschaften, inspiriert von der bemerkenswerten Unterwasserhaftung von Muscheln. Die synthetisierten Mikrogele basieren auf dem Polymer Poly(*N*-isopropylacrylamid) (PNIPAM), das für sein temperatursensitives Verhalten bekannt ist. Dopaminmethacrylamid (DMA) kann als Comonomer verwendet werden, um die Eigenschaften von Muscheln zu imitieren. Aufgrund seiner Catecholgruppe ist es in der Lage, Mikrogelstrukturen zu vernetzen. Da DMA auch als Radikalfänger wirkt, ist eine genaue Kontrolle der Synthese erforderlich.

Im ersten Teil dieser Arbeit wird die Mikrogelsynthese mithilfe von kinetischen Untersuchungen analysiert und kontrolliert. Durch die Auswertung von Zeitproben, die während der Synthese entnommen werden, können die Verbrauchsraten der einzelnen Monomere mittels Massenspektrometrie (MS) bestimmt werden. Der Einbau von DMA wird mittels UV-Vis-Spektroskopie und Kernspinresonanzspektroskopie (NMR) quantifiziert. Ein optimiertes Syntheseprotokoll wird entwickelt, bei dem DMA nach 15 min zur Reaktion hinzugefügt wird, um die vollständige Umsetzung von NIPAM und dem Vernetzer *N*,*N*'-Methylenbisacrylamid (BIS) sicherzustellen. Eine Gesamtreaktionszeit von 60 min garantiert die Einbindung von DMA. Die Synthese ist reproduzierbar und unabhängig von UV-Licht. DMA zeigt eine Kinetik zweiter Ordnung.
Im zweiten Teil wird das temperatursensitive Quellverhalten von P(NIPAM-co-DMA)-Mikrogelen mit unterschiedlichem DMA-Gehalt analysiert: DMA senkt die Volumenphasenübergangstemperatur (VPTT) aufgrund seiner höheren Hydrophobizität im Vergleich zu NIPAM und beschleunigt den Übergang. Kraftspektroskopische Messungen an einzelnen adsorbierten Mikrogelpartikeln zeigen, dass PNIPAM-Mikrogele durch die Einbindung von DMA über ihren gesamten Querschnitt hin versteift werden. Das Quellverhalten und die mechanischen Eigenschaften werden mithilfe des affinen Netzwerkmodells für beide Arten von Mikrogelen linear korreliert. Für hohe DMA-Konzentrationen behindern Catechol-Wechselwirkungen im Netzwerk jedoch das Schrumpfen des Mikrogels, während seine hohe mechanische Steifigkeit erhalten bleibt.
Im letzten Teil dieser Arbeit werden die adhäsiven Eigenschaften der Mikrogele mithilfe der kolloidalen Sonden-Rasterkraftmikroskopie an Mikrogel-Monoschichten

untersucht, die mit Hilfe der Langmuir-Blodgett-Technik hergestellt werden. P(NIPAM-co-DMA)-Mikrogele weisen im Vergleich zu reinen PNIPAM Mikrogelen eine erhöhte Adhäsion auf. Die Adhäsionskräfte erreichen ihr Maximum bei einem DMA Gehalt von 10 mol %. Höhere DMA-Gehalte führen zu einer geringeren Adhäsion, aber besseren mechanischen Eigenschaften – was das empfindliche Gleichgewicht zwischen den kohäsiven und adhäsiven Eigenschaften des Materials aufzeigt. Bei weiterer Erhöhung der Packungsdichte der Mikrogelpartikel, nimmt die Adhäsion jedoch ab. Dies könnte auf Catechol-Wechselwirkungen innerhalb der stark komprimierten Mikrogele zurückzuführen sein.

Contents

List of abbreviations

ACF	Auto-correlation function
AFM	Atomic force microscopy
AAPH	2,2′-azobis-2-methyl-propanimidamide dihydrochloride
BIS	*N,N′*-methylene-bisacrylamide
CD_3OD	Methanol-d_4
DLS	Dynamic light scattering
DC	Direct voltage
DMSO-d_6	Dimethyl sulfoxide-d_6
DMA	Dopamine methacrylamide
DMT	Derjaguin-Muller-Toporov
DOPA	L-3,4-Dihydroxyphenyalanine
dp	densely paking
EDL	Electric double layer
EDLS	Electrophoretic dynamic light scattering
ESI	Electrospray ionization
FT	Fourier transformation
FID	Free-induction decay
HPLC	High-performance liquid chromatograph
invOLS	Inverse optical lever sensitivity
JKR	Johnson-Kendall-Roberts
LCST	Lower critical solution temperature
lp	low packing
mfp	Mussel foot protein
mp	medium packing
MS	Mass spectrometry

NIPAM	*N*-isopropylacrylamide
NND	Nearest neighbour distance
NMR	Nuclear magnetic resonance
PDI	Polydispersity index
PNIPAM	Poly(*N*-isopropylacrylamide)
P(NIPAM-co-DMA)	Poly(*N*-isopropylacrylamide-co-dopamine methacrylamide)
RF	Radio-frequency
SEM	Scanning electron microscopy
SFA	Surface force apparatus
SLS	Static light scattering
THQ	Toluhydroquinone
TOF	Time-of-flight
UV	Ultraviolet
vis	Visible
VPT	Volume phase transition
VPTT	Volume phase transition temperature
VPT CT	Volume phase transition completion temperature

List of symbols

A	Contact area
A	Adsorbed light
a	Contact radius
α	Swelling ratio
$\vec{B}_0$	Magnetic field
β	Affine network factor

c	Monomer consumption
c	Concentration
$c_{\mathrm{DMA,injected}}$	injected DMA concentration
$c_{\mathrm{DMA,incorporated}}$	incorporated DMA concentration
Γ	Decay rate
D	Diffusion coefficient
δ	Indentation depth
δ	Chemical shift
$\vec{E}$	Electric field
E	Energy
E	Elastic modulus
E_{loc}	Local elastic modulus
E_{glob}	Global elastic modulus
E_{P}	Elastic modulus probe
E_{S}	Elastic modulus sample
ϵ	Strain
ϵ	Molar absorption / extinction coefficient
ϵ_0	Permittivity of vacuum
ϵ_{r}	Relative permittivity
F	Force
F	Helmholtz energy
F_{adh}	Adhesion force
f_{res}	Resonance frequency
ζ	Zeta potential
G	Gibbs energy
g^1	First order correlation function
g^2	Second order correlation function

η	Viscosity
h	Tip height relative to sample
$h_{\mathrm{amb,AFM}}$	Height measured by AFM Imaging in ambient conditions
θ	Scattering angle
I	Quantum number
I	Light intensity
$\vec{I}$	Spin
k	Spring constant
k	Reaction rate coefficient
k_{B}	Boltzmann constant
κ^{-1}	Inverse Debye screening length
λ	Wavelength
m	Mass
M	Molar mass
M_{w}	Molecular weight
μ_{e}	Electrophoretic mobility
$\vec{\mu}$	Magnetic moment
n	Solvent refractive index
n	Amount of substance
ν	Poisson ratio
ξ	Mesh size
Π	Osmotic pressure
Π	Surface pressure
Q	Degree of swelling
$\vec{q}$	Scattering vector
R_{G}	Radius of gyration
R_{H}	Hydrodynamic radius

R_P	Probe radius
S	Entropy
σ	Stress
T	Temperature
T	Transmittance of light
t	Time
t_{reac}	Reaction time
t_{DMA}	DMA injection time
τ	Correlation time
v	Velocity
$w_{amb,AFM}$	Width measured by AFM Imaging in ambient conditions
Φ	Polymer volume fraction
ω_0	Nuclear Larmor frequency
z	Charge
z_c	Deflection of cantilever
z_p	Height of cantilever

List of physical constants

Archimedes constant	$\pi = 3.14159265359...$
Boltzmann constant	$k_B = 1.38065 \cdot 10^{-23}\,\mathrm{J\,K^{-1}}$
Elementary charge	$e = 1.602176634 \cdot 10^{-19}\,\mathrm{C}$
Permittivity of vacuum	$\epsilon_0 = 8.8541878128 \cdot 10^{-12}\,\mathrm{F\,m^{-1}}$
Planck constant	$h = 6.62607015 \cdot 10^{-34}\,\mathrm{J\,s}$
Velocity of light in vacuum	$c = 299792458\,\mathrm{m\,s^{-1}}$

Non-essential and empirical parameters are not included

1 Introduction

Water covers 71 % of the earth's expanse. 96.5 % of this water is kept in the ocean [1], whose dark depths hide a lot of yet unknown. Throughout history, mankind has drawn inspiration from nature for new developments in science and technology.
Marine organisms like mussels gained substantial attention in the scientific community during the last decades due to their unique under-water adhesive capabilities and remarkable mechanical properties. These properties are mainly attributed to the mussel foot proteins (mfps) secreted by the mussel byssus, which contain large amounts of the catechol-based L-3,4-dihydroxyphenylalanine (DOPA) [2]. Catechols can adhere to various surfaces through multiple interaction mechanisms, including hydrogen bonding and metal coordination. They also possess the ability to cross-link structures [3–6], which primarily contributes to the robustness of the mussel byssus.
Mussel-inspired properties are therefore highly interesting in biomedicine [7–9], demanding robust adhesive materials. However, the extraction of mfps from the mussel byssus provides substantial costs [10–12] and not to forget, the extraction causes harm to the animals. The catechol-based dopamine methacrylamide (DMA) can serve as a synthetic replacement to mimic the mussel's properties and has been successfully used as co-monomer [4, 13–15] and cross-linker [4, 6, 16] for polymers, to improve the adhesiveness of materials [16–19] or to produce self-healing materials [13]. When using DMA, it is crucial to consider the radical scavenging capability of catechols, which can impact gel growth [20].

Besides from the use of mussel-inspired materials, hydrogels have gained considerable attraction in science [21–23] as for example tissue adhesives [24–26], in drug delivery [23, 27, 28] or as self-healing materials [13, 29, 30]. Hydrogels are defined as polymer networks that can swell by absorbing large amounts of water [31], similar to human body tissues. They feature a micro-network, characterised by the mesh size, which influences the diffusion and transport of oxygen, nutrients and drugs.

Hydrogels can be manufactured with good biocompatibility and a large variety of properties. Nonetheless, they are often limited by their low stiffness, which can restrict their use for applications demanding mechanical robustness [22]. To overcome this limitation, stiffness can be introduced and adjusted by chemically cross-linking the polymer network. In the biomedical context, hydrogels need to replicate the stiffness of the tissue they mimic [21]. While the cartilage, for example, has a Young's modulus of around 700 kPa, muscles only possess moduli around $10 - 15$ kPa [21].
Hydrogels undergo reversible changes in their physical or chemical properties in response to specific external stimuli such as temperature [32–34], pH [33, 35–37], ionic strength [33, 37], light [38, 39] or magnetic fields [40]. Smaller hydrogels, e.g. microgels, exhibit quicker response to external triggers [41, 42] and are easier adaptable to the size of defects [23, 43, 44], thereby facilitating their filling. The preparation of surface coatings is furthermore easier when prepared from microgels than from macrogels [45, 46].
Among microgels, poly(*N*-isopropylacrylamide) (PNIPAM) microgels have been widely employed. PNIPAM microgels can be easily synthesised with a narrow size distribution [47] by free radical precipitation polymerisation [48]. The microgels undergo a volume phase transition (VPT) when heated above the lower critical solution temperature (LCST) of the linear PNIPAM polymer, which is around 32°C [49] in water. To cross-link the microgel structure, *N*,*N*'-methylene-bis-acrylamide (BIS) is typically used. BIS exhibits a faster reaction kinetic compared to NIPAM and thus, accumulates in the microgel's core leading to a core-shell structure [50, 51]. The versatility of PNIPAM extends further as it can be easily co-polymerised [52–55] with monomers holding specific properties like charge or hydrophobicity. This enables the design of polymer architectures tailored to defined needs. Introducing hydrophobic or hydrophilic co-monomers allows the VPTT to be tuned to lower or higher temperatures. Tuning the sharpness of the transition additionally affects the release rate of e.g. drugs incorporated in the microgel network, making it possible to accelerate or decelerate drug delivery [56].

The combination of these two outstanding systems - the catechol-based chemistry of mussels with microgels - enables the possibility to create systems that fuse stimuli-responsiveness, mechanical durability, self-healing properties [13, 29, 30] and high surface adhesion [57–59]. The main goal of this thesis is therefore the development of mussel-inspired microgels based on PNIPAM, aiming to enhance

the mechanical and adhesive properties of the microgels. We use the co-monomer dopamine methacrylamide (DMA) to mimic the properties of mussels. This approach requires a balance between the material's cohesion and adhesion, with the microgel's swelling behaviour having the potential to weaken both characteristics [60].
To enable the precise synthesis control for further research, especially paying attention to the scavenging effect of DMA [20], in-depth investigations of the co-polymerisation of PNIPAM with DMA are provided in **chapter 4**. Reaction kinetics of the components are determined by analysing time-samples taken throughout the microgel synthesis by mass spectrometry (MS). To date, the kinetics of DMA co-polymerisation is rather unknown. Particularly, the examination of different synthesis parameters is of high importance to further control the synthesis process and characterise the co-polymerisation. The reproducibility and UV influence of the synthesis is tested. The incorporated amount of DMA is investigated with a combination of UV-vis and nuclear magnetic resonance (NMR) spectroscopy.
In **chapter 5**, we explore the effect of an increasing DMA incorporation on the swelling behaviour and nanomechanical characteristics of P(NIPAM-co-DMA) microgels. Their correlation is investigated using the affine network model, derived from the Flory-Rehner theory. Changes in their swelling behaviour are studied in bulk solution through dynamic light scattering (DLS), revealing insights into how DMA influences the microgels' volume phase transition (VPT) behaviour, swelling ratio, and mesh size. The microgel's nanomechanical properties (at the solid surface) are studied by atomic force microscopy (AFM), more precisely by the force spectroscopy technique. A tip is indented into individual microgel particles to gain information about their laterally resolved mechanical properties (local elastic modulus E_{loc}) [61].
In **chapter 6**, the influence of DMA on the adhesive abilities of the microgels is investigated by AFM, indenting a colloidal probe into a closed microgel layer. Colloidal probes are especially suitable in the determination of adhesive forces, as they provide a well-defined contact area in contrast to the tips used in chapter 5 [62–64]. The cross-linking ability of DMA can counteract the adhesion of microgels at the surface, providing the challenge to optimise the microgel's adhesive properties while preserving the material's toughness. The global mechanical properties of the layers can be determined from the measurements, yielding a global elastic modulus E_{glob}.
This work contributes significantly to the tailoring of P(NIPAM-co-DMA) microgels, aligning their properties with the requirements needed for further applications in both bulk solution and at solid surfaces.

2 Scientific background

This chapter explains the scientific background of polymer gels, especially microgels. Microgels based on poly(*N*-isopropylacrylamide) (PNIPAM) are introduced. The synthesis of microgel particles is discussed including aspects of reaction kinetics. Principles of thermodynamics are explained to understand the swelling of microgels and provide information about their elasticity. The chapter also examines the behaviour of microgels adsorbed at interfaces. Additionally, it includes a scientific background about the remarkable under-water adhesion exhibited by mussels, offering insights into selected mussel-inspired materials. For a more comprehensive and in-depth exploration of these topics, readers are encouraged to refer to more specialised literature sources.

2.1 Microgels

Microgels are colloidal gel particles consisting of a three-dimensional polymer network, which is physically or chemically cross-linked. They highly swell when exposed to a solvent like water [31] with water contents ranging from 10 to 90 wt% [42]. However, microgel particles are also dispersed in the solvent [42] ("colloidal dispersion"). Colloidal dispersions can undergo aggregation, either flocculation or coagulation, although they often maintain colloidal stability due to the presence of surface charges. The unique combination of colloidal and polymeric properties is what makes microgels highly interesting for many applications. Microgels possess sizes of colloidal dimension (several nanometers to micrometers, $10 - 1000\,\mathrm{nm}$) [42, 65]. In contrast to macrogels, microgels reveal advantages over larger hydrogels [23, 43, 44]. They act minimally invasive because they can be introduced with needles and are highly adaptable when filling defects of various sizes. Moreover, microgels respond more rapidly

to environmental changes [41, 42] than macrogels, which follows from the relationship derived by Tanaka [66]:

$$\tau = \frac{R^2}{\pi^2 D}, \tag{2.1}$$

where τ represents the characteristic time of the gel volume change, R is the gel radius and D its diffusion coefficient. In addition, the preparation of surface coatings is easier when prepared from microgels than from macrogels [45, 46].
Environmental changes, which affect the shape and volume of the microgels and thus the microgel's properties, can be caused by external stimuli. The change in the microgel's volume upon swelling and collapsing (volume phase transition) is illustrated in fig. 2.1. Stimuli are for example temperature [32–34], pH [33, 35–37], ionic strength [33, 37], light [38, 39] or magnetic fields [40].

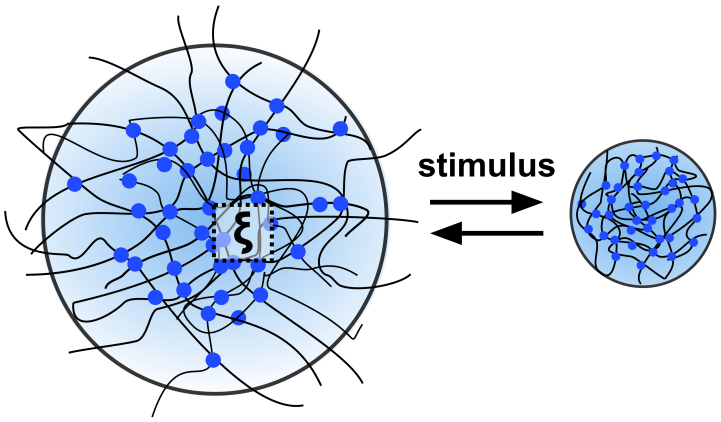

Figure 2.1: Microgels reversible swell and deswell due to the application of an external stimulus. Microgels in the swollen state possess a heterogeneous structure due to a faster consumption of the cross-linker compared to the monomer. The mesh size ξ characterises the micro-network of the microgel.

The introduction of a cross-linker supplies a stable micro-network within the microgel's structure. This micro-network is characterised by the mesh size (see fig. 2.1). Microgels prepared through the classical free radical precipitation polymerisation (batch synthesis) possess a non-uniform cross-linker distribution, originating from the different reaction kinetics of cross-linker and monomer. The cross-linker typically exhibits a faster reaction kinetics compared to the monomer and thus, accumulates in the microgel core [16, 50, 51]. This results in a heterogeneous, core-shell microgel structure [67] with a cross-linker-rich core and a loosely cross-linked shell with dan-

gling polymer ends (see fig. 2.1 left). Rudyak *et al.* [68] demonstrated that for microgels with a 1 mol% cross-linker concentration, the dangling ends account for almost the half of the total microgel mass. However, the formation of this heterogeneous microgel structure can be suppressed through a continuous feeding approach ("feeding method"), where both monomer and cross-linker are continuously feeded into the reaction mixture [69, 70]. This method leads to a more homogeneous distribution of cross-linking. In the recent years, there has been also growing scientific interest in exploring "self-cross-linked" microgels [71–73].
Nonetheless, the stiffness and swelling ability of microgels can be finely tuned by adjusting the cross-linker concentration: with an increasing cross-linker concentration, microgels become stiffer [51, 74, 75] and show a reduced swelling ability [67, 76].
Microgels can also be easily functionalised by introducing a co-monomer [52–55]. This enables the incorporation of various triggers for stimuli-responsiveness, adhesion, or the improvement of mechanical and colloidal stability. Such functionalisation offers the opportunity to design architectures tailored to desired needs.

A large amount of research focuses on poly(*N*-isopropylacrylamide) (PNIPAM) microgels, composed primarily of the monomer *N*-isopropylacrylamide (NIPAM). They can be easily synthesised with a narrow size distribution [47] through free radical precipitation polymerisation [48]. Usually *N,N'*-methylene-bis-acrylamide (BIS) is used to cross-link the microgel structure, resulting in the characteristic heterogeneous microgel structure.
PNIPAM microgels undergo a volume phase transition (VPT) when heating beyond the lower critical solution temperature (LCST) of the linear polymer at 32°C in water [49]. Below the volume phase transition temperature (VPTT), PNIPAM is soluble in water. The amide groups of PNIPAM form hydrogen bonds with the surrounding water molecules. When heating above the VPTT, these hydrogen bonds break and a phase separation occurs. Inter- and intramolecular hydrogen bonds among PNIPAM side chains form, leading to the formation of a polymer-rich and a polymer-poor phase in the system [49]. The VPT consequently induces a collapse of PNIPAM microgel particles when the temperature exceeds the VPTT, as depicted in fig. 2.1. The phase diagram of PNIPAM shown in fig. 2.2 [49] illustrates the two-phase and one-phase regime of the polymer (PNIPAM) and solvent (water) mixing. The VPTT is defined as minimum of the binodal curve.
The collapse of heterogeneously cross-linked PNIPAM microgel particles was pro-

posed to happen in three different stages [77]: The initial core collapse ($25 - 35°C$) is followed by a partial collapse of the shell ($35 - 38°C$). As temperatures increase even further to $38 - 50°C$, the core experiences an additional collapse. It leads to the formation of a hard particle surrounded by a partially collapsed and non-rigid shell.

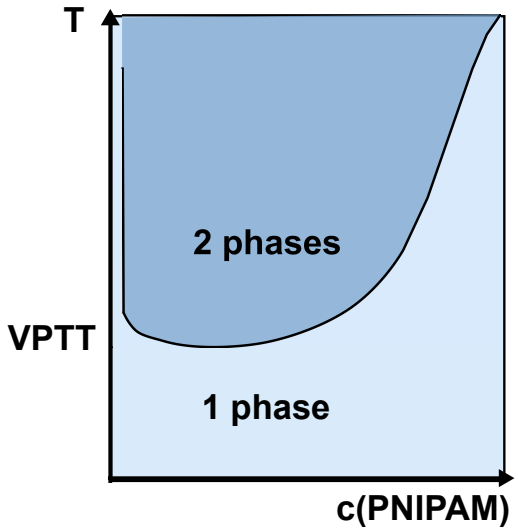

Figure 2.2: Phase diagram of PNIPAM in water, adapted from [49]. Below the volume phase transition temperature (VPTT), PNIPAM and water are mixed. The microgels are swollen. Above the VPTT, PNIPAM and water demix, resulting in the collapse of the microgel particles.

2.1.1 Microgel synthesis

The most widely used technique for preparing microgels is free radical precipitation polymerisation. The polymerisation kinetics in free radical precipitation polymerisation [78] and the particle formation mechanism [42, 68, 79–81] should be discussed in this section.

Polymerisation kinetics in free radical precipitation polymerisation

Free radical precipitation polymerisation involves several kinetic aspects, as illustrated in the reaction scheme in table 2.1: (1) Initiation, (2) propagation, (3) termination and (4) chain transfer.

Table 2.1: Kinetic scheme of free radical precipitation polymerisation adapted from [78].

(1) Initiation	Decomposition initiator	$I \xrightarrow{k_D} 2I\cdot$
	Formation active species	$M+I\cdot \xrightarrow{k_I} I\text{-}M\cdot$
(2) Propagation		$P_n\cdot+M \xrightarrow{k_P} P_{n+1}\cdot$
(3) Termination	Recombination	$P_n\cdot+P_m\cdot \xrightarrow{k_T} P_{n+m}$
	Disproportionation	$P_n\cdot+P_m\cdot \xrightarrow{k_T} P_n+P_m$
(4) Chain transfer		$P_n\cdot+P_m \xrightarrow{k_{CT}} P_n+P_m\cdot$

I: initiator, M: monomer, P_i: polymer with i repeating units, $\cdot$ denoting radical, k different reaction rate constants.

(1) During initiation, the radical initiator (I) thermally decomposes, subsequently reacts with a monomer (M) and then generates an active species. The amount of radicals increases during this phase.
(2) Chains grow and form polymers P_i with i repeating units during the propagation phase through the addition of monomers to the initiated species. The amount of free radicals stays constant during this phase, since initiation and termination of radicals are in equilibrium, considering the initiator's half-life time. Monomers are rapidly consumed.
(3) The termination of chains results from recombination or disproportionation processes. Recombination describes the circumstance when two growing radicals meet and form a bond, generating an inactive species. In contrast, disproportionation describes when a hydrogen atom is transferred from one radical to another, leading to the saturation of one polymer chain. Termination events slow down the monomer consumption rate and can be induced by introducing stoppers into the reaction system.
(4) Chain transfer describes the transfer of an active centre to another molecule.

All of these reactions occur with a different reaction rate constant k. The overall rate of polymerisation R_P can finally be described by [78]:

$$R_P = -\frac{d[M]}{dt} \propto [M][I]^{\frac{1}{2}}, \tag{2.2}$$

where [M] is the monomer concentration and [I] the initiator concentration. This implies that the polymerisation rate increases with increasing temperature (faster decomposition of initiator) and with an increasing initiator concentration. Reaction kinetics are important factors when controlling the microgel synthesis and therefore when tuning the properties of the final microgel particle.

Formation of microgel particles by free radical precipitation polymerisation

Microgel particles form through homogeneous nucleation during free radical precipitation polymerisation. As explained in the previous section, the polymerisation starts with the initiation (1) phase, followed by the (2) propagation phase. Initially, it is crucial for all reactants to remain soluble in the chosen solvent. However, when the growing chains reach a critical size, they precipitate due to the insolubility of the polymer in the solvent under the reaction conditions. Typically, the reaction temperature falls within the range of $50 - 80°C$, where temperature-responsive polymers collapse. If these conditions are not met, macrogels will form as polymers may continue to interconnect, forming a three-dimensional gel-like network. In contrast, when precipitation occurs, particle nuclei ("precursor particles") form, initially lacking colloidal stability. According to Rudyak *et al.* [68], who simulated the particle growth of 1 mol% BIS cross-linked microgels, this process lasts up to monomer conversions of $0.11 - 0.12$ (equivalent to $2 - 3$ min in the synthesis). Due to their instability, precursor particles tend to aggregate into larger entities known as "primary particles" or grow by reacting with further monomers or oligomers. The charges originating from the initiator tend to accumulate at the outer part of the microgel particle, electrostatically stabilising the primary particle. This process takes up to $9 - 13$ min during the synthesis [68]. Once particle stabilisation is achieved, the number of particles remains constant until the end of the reaction [81]. Primary particles grow further by aggregation of additional precursor particles until the final particle size is reached. This process begins after approximately 40% of monomer conversion [68]. The introduction of a cross-linker like BIS during the polymerisation of PNIPAM microgel particles prevents them from dissolving in water at low temperatures. BIS was shown to decrease the particle number density, while increasing the particle volume [81]. The formation of microgel particles is illustrated in fig. 2.3.
This procedure can yield highly monodisperse particles. The particle growth was found to follow pseudo-first order kinetics [81], as the initiator concentration stays

mainly constant throughout the synthesis when considering its half-life time. Therefore, the reaction kinetics are mainly determined by the concentration of unreacted monomer and the initiator concentration.

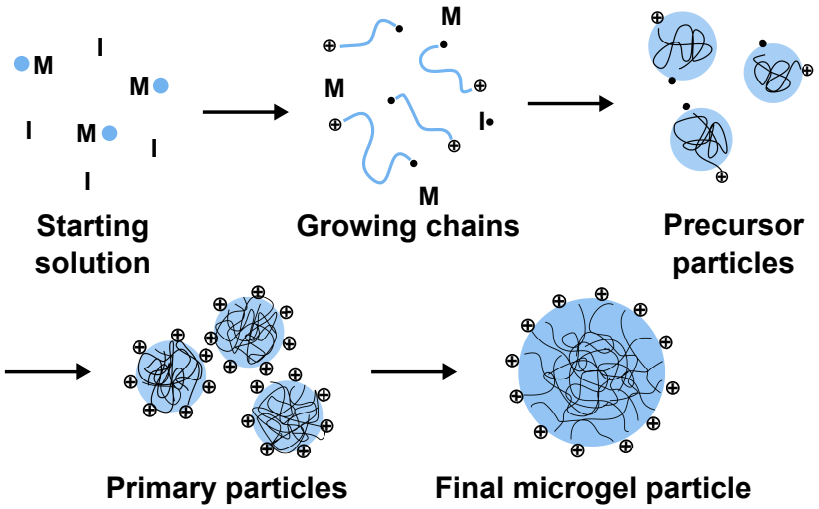

Figure 2.3: Formation of microgel particles by free radical precipitation polymerisation. After starting the reaction, chains start to grow until they form unstable precursor particles. These aggregate to stable primary particle. At the end of the reaction, the final particle size is reached. The figure is adapted from [42].

2.1.2 Swelling thermodynamics

The VPT exhibited by microgels is characterised by an abrupt change in their swelling in response to an external stimulus. This section provides a more detailed theoretical framework [82] needed to understand the swelling behaviour of microgels.

The change of swelling is characterised by a change in the Gibbs energy ΔG. For neutral PNIPAM microgels, it can be expressed by:

$$\Delta G = \Delta G_{\text{mix}} + \Delta G_{\text{el}}. \tag{2.3}$$

ΔG_{mix} describes the contribution to the Gibbs energy arising from the mixing of polymer chains with solvent molecules (Flory-Huggins theory). In contrast, ΔG_{el} describes the contribution resulting from the deformation of the elastic microgel network, recovering after the deformation (Flory-Rehner theory). For charged microgels, an additional ionic contribution is added to the term, although it is not required for this thesis.

In thermodynamic equilibrium, contributions to the osmotic pressure in the microgel become zero:

$$\Pi = \Pi_{\text{mix}} + \Pi_{\text{el}} = 0. \tag{2.4}$$

Swelling (positive osmotic pressure) or deswelling (negative osmotic pressure) occurs, when the microgel is out of equilibrium.

Flory-Huggins theory

Microgel particles can be regarded as a binary mixture of polymer chains and the solvent. Solvents can be categorised as either "good" solvents, resulting in a homogeneous mixture of both, or "bad" solvents, resulting in a heterogeneous mixture. For PNIPAM microgels, water is a good solvent below the VPTT, but becomes a bad solvent upon heating. The mixing can be described using the lattice model by Flory [83] and Huggins [84]: In this model, the lattice can be described by the addition of n_{P} polymers with a length of x segments to n_{S} solvent molecules, giving a total number of lattice sites by $n_0 = n_{\text{S}} + x n_{\text{P}}$.
The mixing process is primarily influenced by the internal mixing energy U_{mix} and the mixing entropy S_{mix}. While entropy always promotes mixing, the internal energy can either promote or inhibit it. The total free energy can be described by the Helmholtz energy F_{mix}, which equals the Gibbs energy ΔG_{mix}, as pressure, volume and temperature are assumed to be constant:

$$\begin{aligned} \Delta G_{\text{mix}} \approx \Delta F_{\text{mix}} &= \Delta U_{\text{mix}} - T\Delta S_{\text{mix}} \\ &= k_{\text{B}}T[n_{\text{S}} \ln \Phi_{\text{S}} + n_{\text{P}} \ln \Phi_{\text{P}} + \chi_{\text{S,P}} n_{\text{S}} \ln \Phi_{\text{P}}]. \end{aligned} \tag{2.5}$$

$\Phi_{\text{S}} = n_{\text{S}}/n_0$ and $\Phi_{\text{P}} = x n_{\text{P}}/n_0$ are the volume fractions of the solvent and polymer. $\chi_{\text{S,P}} = \frac{\Delta E}{k_{\text{B}}T}$ denotes the Flory-Huggins interaction parameter, describing the interaction between solvent and polymer. The replacement of a polymer-polymer or a solvent-solvent contact by a polymer-solvent contact requires a change of energy ΔE. It's important to note that the model only considers nearest neighbour interactions, sometimes failing to describe the swelling behaviour of microgels. Therefore, other models have been developed to provide more accurate results [85], such as a series expansion of $\chi_{\text{S,P}}$ [86] or a Hill-like model [87, 88], although their detailed discussion is beyond the scope of this chapter.

The process of mixing additionally leads to a change in osmotic pressure:

$$\begin{aligned}\Pi_{\text{mix}} &= -\frac{1}{\nu_{\text{S}}}\left(\frac{\partial \Delta G_{\text{mix}}}{\partial n_{\text{S}}}\right)_{T,p,n_{\text{P}}} \\ &= -\frac{N_{\text{A}} k_{\text{B}} T}{\nu_{\text{S}}}\left[\Phi_{\text{P}} + \ln(1-\Phi_{\text{P}}) + \chi_{\text{S,P}}\Phi_{\text{P}}^2\right].\end{aligned} \tag{2.6}$$

N_{A} is the Avogadro's constant and ν_{S} the molar volume of the solvent molecule.

Flory-Rehner theory

The presence of cross-links imparts a permanent structure to the microgel network, allowing the microgels to recover after a deformation process, such as during swelling - the microgel network is elastic. The change in the elastic free energy ΔG_{el} turns out to be mainly of entropic nature. The entropy change can be calculated by using the affine approximation [89], where the relative deformation of each polymer chain is equal to the deformation of the whole polymer network. By using this assumption, Flory and Rehner [90, 91] calculated ΔG_{el} by:

$$\begin{aligned}\Delta G_{\text{el}} &= -T\Delta S_{\text{el}} \\ &= \frac{3k_{\text{B}}TN_{\text{c}}}{2}[\lambda^2 - 1 - \ln\lambda].\end{aligned} \tag{2.7}$$

N_{c} is the number of polymer chains and λ defines the volume change due to swelling. In the case of homogeneous and isotropic swelling it follows:

$$\lambda = \left(\frac{V}{V_0}\right)^{\frac{1}{3}} = \left(\frac{\Phi_{\text{P,0}}}{\Phi_{\text{P}}}\right)^{\frac{1}{3}} = \left(\frac{R_{\text{H}}}{R_{\text{H,0}}}\right). \tag{2.8}$$

$\Phi_{\text{P,0}}$ is the polymer volume fraction for a particle volume V_0 and a hydrodynamic radius $R_{\text{H,0}}$. The notation 0 always refers to the reference state (mostly collapsed state). Based on λ a swelling ratio α can be derived:

$$\alpha = \left(\frac{V}{V_0}\right) = \left(\frac{R_{\text{H}}}{R_{\text{H,0}}}\right)^3. \tag{2.9}$$

Again, the change in the Gibbs free energy ΔG_{el} results in a change of osmotic pressure:

$$\begin{aligned}\Pi_{\text{el}} &= -\frac{1}{\nu_s}\left(\frac{\partial \Delta G_{\text{el}}}{\partial n_{\text{S}}}\right)_{T,p,n_{\text{P}}} \\ &= \frac{k_{\text{B}}TN_{\text{c}}}{V_0}\left[\frac{\Phi_{\text{P}}}{2\Phi_{\text{P,0}}} - \left(\frac{\Phi_{\text{P}}}{2\Phi_{\text{P,0}}}\right)^{\frac{1}{3}}\right].\end{aligned} \tag{2.10}$$

The affine network factor β is then defined as:

$$\begin{aligned}\beta &= -\left[\frac{\Phi_P}{2\Phi_{P,0}} - \left(\frac{\Phi_P}{2\Phi_{P,0}}\right)^{\frac{1}{3}}\right] \\ &= -\left[\frac{1}{2}\left(\frac{R_{H,0}}{R_H}\right)^3 - \left(\frac{R_{H,0}}{R_H}\right)\right].\end{aligned} \tag{2.11}$$

2.1.3 Microgels adsorbed at interfaces

Microgels deform when adsorbing at interfaces due to their softness. This deformation not only alters their shape, but also impacts their physical properties, including their swelling ability, volume phase transition and stiffness. Understanding the behaviour of microgels when adsorbed at interfaces in comparison to their behaviour in bulk solution is crucial for developing "smart" stimuli-responsive microgel systems, such as surface coatings, and should be regarded in this section.

Deformation in shape and change in swelling ability

In general, microgels tend to stretch radially after adsorbing at the interface, while expanding laterally due to their soft nature. The interfacial adsorption of microgels results from an interplay between two factors: The adhesive energy favours large contact areas to minimise energy. In contrast, the elasticity of the microgel network works against the deformation [92, 93]. Therefore, the cross-linking degree highly influences the microgel's shape at interfaces as it defines the conformational flexibility of the microgel network.
Microgels with a lower cross-linking density possess a lower network elasticity, consequently being more flexible and deforming more easily at the surface. In the case of heterogeneously cross-linked microgel particles, the highly cross-linked core possesses a hemispherical shape, which deforms less. Conversely, the surrounding loosely cross-linked shell flattens extensively at the surface [92, 94–96], often referred to as "fried egg" structure. Increasing the degree of cross-linking results in stiffer microgel particles and increases the elasticity. As a consequence, the "fried egg" structure vanishes. The microgels adopt a more pronounced hemispherical shape and protrude more from

the surface [51, 74, 92, 97, 98]. So for higher cross-linker concentrations, microgels approach a behaviour resembling that of hard spheres at the surface, which do not deform at all. Differences in deformation of microgels adsorbed at interfaces based on their cross-linking degrees are illustrated in fig. 2.4.
In this context, Mourran *et al.* [92] could show that co-polymer microgels based on PNIPAM with a minimal amount of cross-linker (0.05 mol% of cross-linker BIS) deform even in a "pancake" like structure when adsorbed at the surface. The spreading of those microgels at the surface is high. They observed the scission of polymer strands on the outer shell of these microgels. However, a slight increase in the cross-linker amount to 0.5 mol% leads to the typical "fried egg" structure. Microgels with $1 - 3$ mol% of cross-linker exhibit a hemispherical shape, where the diameter of the sphere is similar to the hydrodynamic diameter of the microgels in bulk solution.
It should be noted that homogeneously cross-linked microgels, prepared by the feeding method, exhibit distinct surface deformations due to their uniform cross-linking density [98]. Witte *et al.*, for example, demonstrated that microgels with a homogeneous cross-linking density of 10 mol% cross-linker are softer than their counterparts prepared via the conventional free radical precipitation polymerisation with the same cross-linker amount.

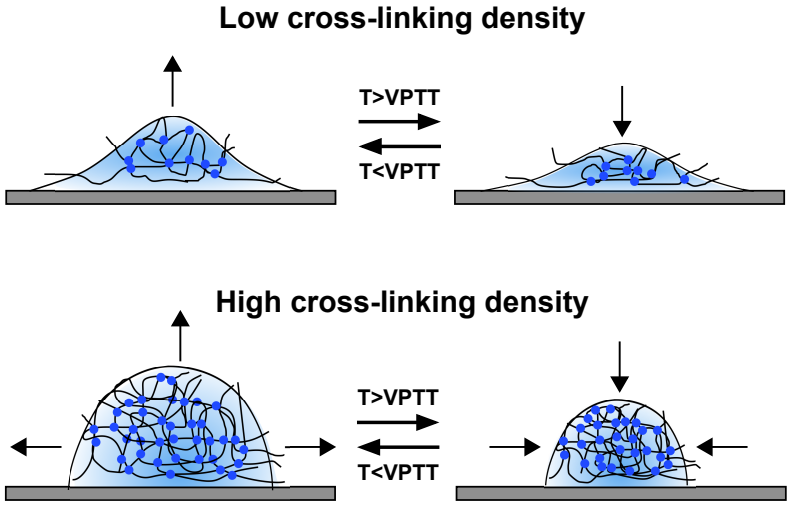

Figure 2.4: Deformation of microgel particles upon adsorption at the interface for different cross-linking degrees and depending on the temperature.

Additionally to changes in their shape, the swelling ability of microgels alters notably upon adsorption at interfaces. It has been observed that adsorbed microgel particles exhibit a reduced swelling ability compared to their counterparts in bulk solution, with

the reduction reaching one order of magnitude [99, 100]. This phenomenon is primarily attributed to the interaction of polymer chains with the substrate, resulting in a partial collapse of them [100]. The decrease in swelling ability increases with increasing cross-linker content within the microgel structure [51].

Temperature-dependent behaviour

The temperature-responsiveness of microgels plays a crucial role in their interfacial behaviour. Heating induces changes in the shape of microgels adsorbed at interfaces [51, 54, 97]: microgel particles tend to decrease their width, while increasing their height. The change in shape varies depending on the cross-linking amount. Microgels with $2-5$ mol% cross-linker primarily collapse laterally, becoming flatter due to their low cross-linker content. In contrast, those with a higher cross-linker content of 10 mol% exhibit both, radial and lateral collapse, retaining their shape due to the increased elasticity of the network [51]. The highly cross-linked core provides structural stability after the adsorption [98]. The behaviour is illustrated in fig. 2.4.
Notably, this behaviour is different for homogeneously cross-linked microgels. These microgels exhibit a larger collapse than heterogeneously cross-linked microgels with the same cross-linker amount of 10 mol% [98], as they lack the structural stability of a highly cross-linked core.
Another parameter to consider is the VPTT. It was shown that the VPTT of microgels adsorbed at surfaces tends to be higher than in bulk solution. This has been explained by the suppression of internal fluctuations, normally facilitating the VPT [51, 101]. The temperature-induced swelling and deswelling of adsorbed microgel particles was shown to be reversible [51, 101, 102], although some reported a hysteretic behaviour [51, 102].
A study by Burmistrova *et al.* [51] investigated P(NIPAM-co-acrylic acid) (P(NIPAM-co-AAc) microgels with different cross-linking degrees adsorbed at silicon wafers. They observed a hysteresis for microgels with 2 mol% cross-linker during the first swelling/deswelling cycle, which decreases with repeating cycles and with increasing cross-linker content. The underlying mechanism is attributed to the formation of hydrogen bonds: when hydrogen bonds between water molecules and polymer chains break, intra- and inter-polymer chain hydrogen bonds form [103]. These act as additional cross-linker, suppressing the swelling of the microgels to their initial size and resulting in the observed hysteresis of the VPTT. Higher cross-linked microgels do not

exhibit this effect because their cross-linking density is already too high to enable the formation of these additional intra- and inter-polymer hydrogen bonds.

Mechanical behaviour of adsorbed microgels

In the present thesis, the change in mechanical behaviour upon adsorption at the interface was investigated by atomic force microscopy (AFM), particularly through force spectroscopy measurements. Indenting an AFM probe into adsorbed microgel particles allows the determination of an elastic modulus E, which expresses their stiffness. The elastic modulus E is known to increase with an increasing cross-linker concentration within the microgel network [51, 74, 75]. As depicted in fig. 2.5, the augmentation in E is attributed to an increasing polymer and cross-linking density, effectively probed by the AFM cantilever. Elastic moduli E obtained from measurements conducted in the centre of microgel particles were found to vary from 17 to 600 kPa [51, 74, 97, 98, 104–106] for PNIPAM microgels cross-linked by BIS. For microgels containing around $1 - 2$ mol% cross-linker BIS, values between $17 - 100$ kPa [51, 74, 104] were determined. Higher cross-linked PNIPAM microgels with around 10 mol% cross-linker possess E moduli between $312 - 600$ kPa [51, 74, 98, 106].

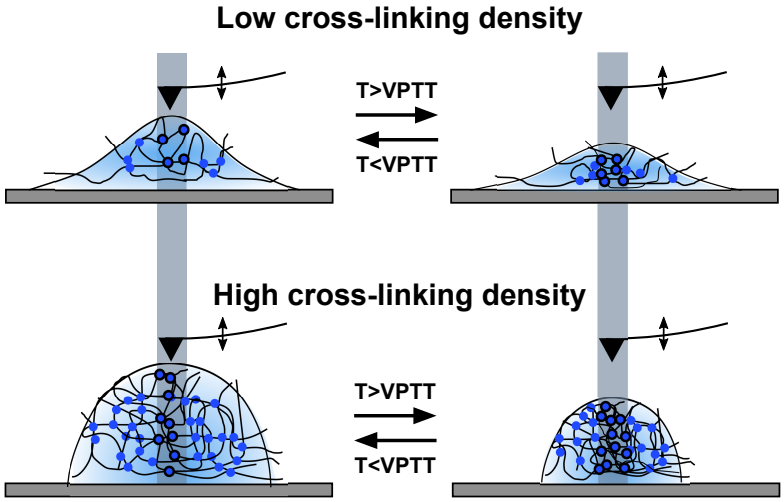

Figure 2.5: Mechanical behaviour of microgel particles upon adsorption at the interface for different cross-linking degrees and depending on the temperature. To determine their elastic modulus E, an AFM probe is indented into the particles and compresses the polymer including its cross-links (illustrated by grey area).

The stiffness of the microgels also increases significantly with rising temperature [51, 75, 97, 107, 108]. When microgels are heated above their VPTT, the adsorbed microgel particles shrink [51], as explained before, leading to a denser polymer network (see fig. 2.5). It has been demonstrated that the E modulus increases by a factor of 5 (for low cross-linked PNIPAM) to 110 (for high cross-linked PNIPAM) when the temperature exceeds the VPTT [51, 75, 107, 109–111].
It's important to note that because of the heterogeneity of the microgel particles, possessing a highly cross-linked core and a loosely cross-linked outer shell, the E modulus decreases from the centre of the microgel particles to the outer periphery [51, 70, 98, 112]. In contrast, homogeneously cross-linked microgel particles show a constant E modulus distribution over the whole cross-section [70, 98, 112] due to the absence of the core-shell structure.

2.2 Mussel adhesion

Marine organisms such as mussels gained popularity in science owing to their extraordinary under-water adhesive properties and exceptional mechanical, as well as self-healing capabilities. This section gives brief insights into the underlying mechanism of mussel adhesion and cohesion [3, 5, 113, 114] and presents illustrative examples of materials, especially hydrogels inspired by mussels.

The unique properties exhibited by mussels can be primarily attributed to six proteins that they secrete to form the mussel byssus. Those proteins are called mussel foot proteins (mfps) and contain large amounts of the catechol-based L-3,4-dihydroxyphenylalanine (DOPA), in addition to other components like tyrosine, phenylalanine or lysine. However, DOPA was identified as the key element of the adhesive properties of mussels [2]. Importantly, the mussel byssus exhibits not only remarkable adhesive, but also cohesive properties, providing the byssus with the necessary mechanical stability and self-healing capabilities needed in rough sea water conditions.

Therefore, the DOPA content in the mfps varies in dependence on their location in the mussel byssus and their function, as depicted in fig. 2.6. Mfp-1 acts as a protective skin of the mussel byssus and comprises approximately $10 - 15\,\mathrm{mol\%}$ of DOPA [115].

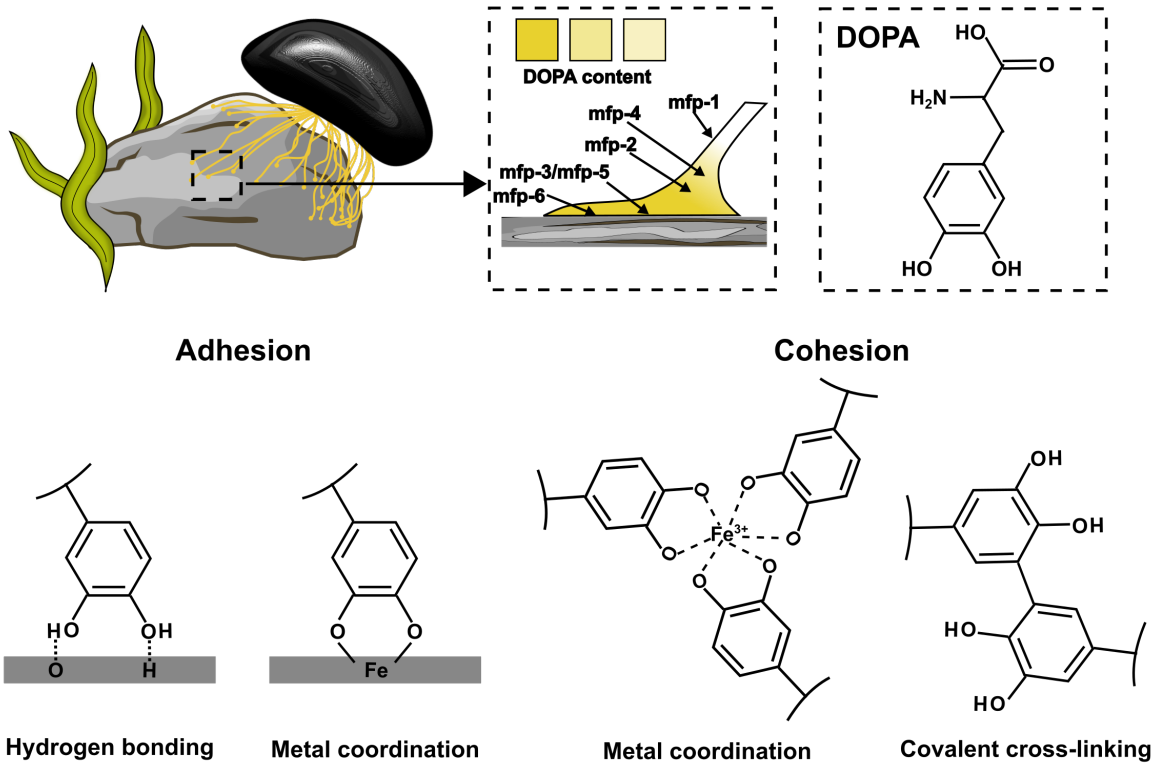

Figure 2.6: Overview of mussel composition: Depending on their location in the mussel byssus, mussel foot proteins (mfps) possess different DOPA contents, which is the key element of the mussel's properties. Different interaction mechanisms of the catechol group of DOPA enable the adhesive, as well as cohesive properties of mussels. Exemplary, hydrogen bonding and metal coordination with surfaces for adhesion, as well as metal coordination and covalent cross-linking for cohesion are illustrated.

Mfp-3 and mfp-5 were predominantly found in the lowest part of the mussel byssus, called plaque, which directly adheres to different surfaces. They are the principal adhesive mfps [115–117]. Thus, it's obvious that these proteins contain the highest amounts of DOPA ($10 - 30$ mol%) [118–120]. Mfp-6 is located in the same area within the byssus, but it only contains 3 mol% of DOPA [120]. Though, mfp-6 is acidic and contains high levels of thiol groups. To comprehensively understand this distinctive composition of mfp-6 and the various interaction mechanisms enabled by the catechol group of DOPA, responsible for the adhesive as well as the cohesive properties of mussels, it's essential to understand catechol chemistry.

Catechols like DOPA exhibit pH-dependent oxidation behaviour [121]. At acidic pH's, catechols predominantly exist in their reduced state. It was demonstrated that reduced catechols possess high adhesion strength to surfaces [3, 5, 113, 114]. Conversely, at basic pH's, they easily oxidise to quinones in the presence of oxygen. These oxidised catechols are electrophilic and highly reactive [5]. Their reactivity allows the further interaction through covalent cross-linking, thereby contributing to the cohesive characteristics of mussels [3, 5, 113, 114].
For the adhesion of mussels to surfaces, four main catechol-surface interactions [3] have been identified: Hydrogen bonding, π-π stacking, metal coordination and covalent bonding with amine groups of the surface [3, 113, 114]. The two relevant interactions in this work are hydrogen bonding and metal coordination as illustrated fig. 2.6. Metal coordination describes the interaction of the catechol group of DOPA bonding with surface metals. These catechol-metal complexes form by donating a non-bonding electron pair to the metal. However, it is worth noticing that various interaction mechanisms exist, but they fall beyond the scope of this work. For further details, refer to [3, 5, 113, 114].
The cohesive properties of the mussel byssus are arising from either covalent cross-linking of oxidised catechols or from metal coordination [5], which is illustrated in fig. 2.6 as well. The catechols of DOPA can reversibly cross-link via metal coordination [5], conferring self-healing properties to the mussel byssus. Here, catechols and metal ions form either mono, bis or tris complexes. The tris complex of DOPA with Fe^{3+} ions, found in significant quantities within the mussel byssus, is depicted in fig. 2.6. The type of catechol-metal complex is highly depending on the pH: mono-complexes dominate under acidic conditions, while tris-complexes dominate under basic pH conditions. At intermediate pH values, bis-complexes are formed [122].

The unique properties of the mussel byssus are a balance of both - adhesion and cohesion. This is highlighted on the example of mfp-6. The composition of mfp-6, being acidic and rich in thiol groups, serves multiple purposes: Since oxidation can suppress the adhesive properties of DOPA, mfp-6 creates an acidic environment around mfp-3 and mfp-5 to ensure that DOPA remains in its reduced state. This guarantees the adhesive properties of those mfps located in the mussel plaque. Furthermore, thiols can serve as reductants to reverse the oxidation of catechols [5, 123], further enhancing the adhesive properties of mfp-3 and mfp-5.
This underscores the uniqueness of mussels as organisms, utilising the versatility of

catechol mechanisms to create out-standing properties. This can be used to develop mussel-inspired materials for various applications.

2.2.1 Mussel-inspired materials

Mussel-inspired materials, especially hydrogels, have acquired significant attention in scientific research due to the unique properties of both systems, as discussed in the previous sections. Hydrogels with self-healing ability [13, 29, 124], great adhesive properties [124, 125], high toughness [125, 126] and stimuli-responsiveness [13, 29] have been developed based on these findings. These hydrogels find applications in various fields, including biomedicine for use as tissue adhesives or drug delivery systems [8, 124, 127, 128], bioelectronics [125], and as adhesive coatings [57, 58].

For instance, Wang *et al.* [30] synthesised negatively charged poly(acrylic acid) (PAAc) polymers containing 30 mol% catechol moieties. These polymers demonstrate pH dependent, irreversible switchable behaviour when combined with the weak metal chelator Zn^{2+}. It's noteworthy that Zn^{2+} is rarely used in mussel-inspired materials due to its low cross-linking ability. However, the inclusion of zinc offers additional advantage, as it promotes wound healing [129], which is highly beneficial for biomedical applications.
The switching of the polymer from a coacervate to a self-healing hydrogel is explained as followed: At low pH values, positively charged zinc ions interact with the negatively charged PAAc chains by electrostatic interactions, leading to the formation of reversible cross-links. This coacervate exhibits exceptional dry and wet adhesive properties when compared to conventional glues. Interestingly, in the dry state, the coacervate even surpasses the adhesive strength of comparable Fe^{3+} adhesives (strong metal chelator) and mussel adhesives. Irreversible oxidation of the DOPA groups occurs with an increase in pH, involving the ionisation of hydroxyl groups. This process enables the metal chelation between Zn^{2+} and the catechol group, resulting in cross-links. Nonetheless, this transition from the coacervate to the hydrogel leads to a significant decrease in the material's adhesive properties. The formed hydrogel exhibits rapid self-healing capabilities. Wang *et al.* [30] harnessed the principles of catechol chemistry at varying pH values to develop a promising material.

A common strategy in the design of mussel-inspired polymers or hydrogels involves the initial synthesis of the monomer dopamine methacrylamide (DMA) [4, 13, 17, 17, 19, 114, 130]. In the second step, polymers or hydrogels are synthesised via radical co-polymerisation with DMA.
This approach was applied in a study by Xue *et al.* [4] to synthesise microgel particles based on various acrylamide-based monomers, including NIPAM, by free radical precipitation polymerisation. The microgels were co-polymerised with unprotected DMA, serving as a cross-linker. Remarkably, this synthesis does not require the addition of any supplementary cross-linking agent or stabiliser. The researchers demonstrated that, owing to the scavenging ability of unprotected DMA [20], DMA needs to be introduced at a later point of the reaction. Phenols function as radical scavengers, where ortho-structured phenols such as catechols possess the highest scavenging abilities [20]. Xue *et al.* added DMA approximately 10 min after initiating the polymerisation for NIPAM-based microgels. When DMA is introduced at the beginning of the synthesis, no microgel particles form. However, the study does not involve a systematic investigation of different injection times of DMA. Xue *et al.* identified the cross-linking mechanism of the microgel network using UV-vis spectroscopy: interchain C-O or C-C bonds are responsible for the cross-linking, wherein the catechol group of one polymer chain reacts with radicals from another polymer chain during the polymerisation. All synthesised microgel particles exhibit reversible thermo-responsive behaviour, as studied by dynamic light scattering measurements (DLS). This work enables the design of temperature-responsive microgel particles by only using the reactivity of catechol moieties.
Vatankhah-Varnoosfaderani *et al.* [13] used the same approach, synthesising DMA first, to develop P(NIPAM-co-DMA) co-polymers. These co-polymers exhibit sensitivity to different stimuli: temperature, pH and ion type and concentration. The co-polymers were reversibly cross-linked by metal coordination of the catechol groups with boron, introduced by the addition of boric acid. The cross-linking can be manipulated by changing the pH value, using the fundamental principles of catechol chemistry: Under basic conditions, cross-links are formed as catechol oxidation is promoted, favouring cohesive coupling. Conversely, under acidic pH values, hydrogen bonds of the catechol group are protected, breaking the bond. The gelation process is significantly influenced by the catechol concentration in the respective P(NIPAM-co-DMA) copolymer. While for low catechol contents of 1 mol% no gelation is observed, for higher catechol contents of 5 mol% complete gelation

occurs. The reason is the number of catechols per chain, which is crucial to build a stable gel. All P(NIPAM-co-DMA) co-polymers show thermo-responsive behaviour, and the LCST of the co-polymer solutions shows to be dependent on the DMA content, explained by the higher hydrophobicity of DMA when compared to NIPAM. The formed macroscopic gels demonstrate fast and full self-healing properties, which are much faster than those of comparable systems. It can be attributed to the random distribution of catechol moieties within the co-polymer network, as opposed to other systems where functional groups are primarily located at the end chains.
Putnam *et al.* [59] employed DMA as a co-monomer during the synthesis of a terpolymer, consisting of three different types of monomers. While methyl metacrylate was incorporated to impart stiffness to the material, poly(ethylene glycol) methyl ether methacrylate was used to incorporate flexibility. DMA plays the role as the adhesive co-monomer, and its content within the terpolymer was systematically varied. Through lap shear adhesion tests, the researchers were able to determine different optimal catechol amounts for achieving adhesion to different substrate materials: An optimal catechol content of 10 mol% is identified for adhesion to aluminium surfaces, characterised by high surface energy. In contrast, for the adhesion to teflon surfaces with low surface energy, a higher catechol content of 41 mol% is necessary. It becomes evident that the increase in catechol amount additionally increases the stiffness of the material, at the expense of its adhesive properties. This observation highlights the critical importance of balancing adhesive and cohesive properties of the polymer, which additionally depends on the target surface.
These examples serve to illustrate the unique potential of mussel-inspired polymers and hydrogels, highly interesting for future applications.

3 Experimental section

This chapter provides details on the materials and methodologies employed during this thesis. It includes the synthesis protocols of dopamine methacrylamide (DMA) and P(NIPAM-co-DMA) microgels. It further gives details about the measurement techniques employed, offering both theoretical details and experimental insights. Parts have been taken from the publications of the author.

3.1 Material

Dopamine methacrylamide (DMA) synthesis: 3,4-dihydroxyphenethylamine hydrochloride (dopamine HCl) (purity = 99 %) and sodium hydrogen carbonate (purity = 99 %) were purchased from Alfa Aesar (Haverhill, Massachusetts, USA). Sodium tetraborate (purity = 99 %) was purchased from Sigma Aldrich (St. Louis, Missouri, USA). *n*-Hexane (purity $\geq$ 99 %) and magnesium sulfate (anhydrous, purity $\geq$ 98 %) were purchased from TH Geyer (Renningen, Germany). Hydrochloric acid (HCl), isopropanol (purity $\geq$ 99.5 %), tetrahydrofuran (THF) (purity $\geq$ 99.5 %) and sodium chloride (NaCl) (purity $\geq$ 99.5 %) were purchased from Carl Roth (Karlsruhe, Germany). Ethyl acetate (purity = 99.9 %) was purchased from VWR chemicals (Radnor, Pennsylvania, USA). Sodium hydroxide (NaOH) solution ($c = 1\,\mathrm{mol/l}$) was purchased from Merck (Darmstadt, Germany).

Microgel synthesis: *N*-isopropylacrylamide (NIPAM) (purity $\geq$ 99 %) and *N,N'*-methylene-bis(acrylamide) (BIS) (purity $\geq$ 99.5 %) were purchased from Sigma Aldrich (St. Louis, Missouri, USA). 2,2'-azobis-2-methyl-propanimidamide dihydrochloride (AAPH) (purity $\geq$ 98 %) was purchased from Cayman (Ann Arbor, Michigan, USA). Toluhydroquinone (THQ) (purity $\geq$ 99 %) was purchased from Carl Roth (Karlsruhe, Germany). Ethanol (purity $\geq$ 99.8 %) was purchased from Fisher Scientific (Waltham, MA, USA).

NMR solvents: Dimethyl sulfoxide-d_6 (DMSO-d_6) (purity = 99 %) and methanol-d_4 (CD_3OD) (purity $\geq$ 99.8 %) were purchased from Sigma Aldrich (St. Louis, Missouri, USA).
AFM materials: Silicon wafers were purchased from SK Siltron (Gumi City, South Korea). AC160TS-R3 and BL-AC40TS cantilevers were purchased from Olympus Corporation (Tokyo, Japan). Tipless CSC38/No Al cantilevers were purchased from µmasch (Tallinn, Estonia). Silica microspheres with a radius of $R = 2.5\,\mu m$ were purchased from Bangs Laboratories, Inc. (Fishers, Indiana, USA).

All chemicals were used as received without further purification. Ultrapure water was obtained from a Millipore Milli-Q device (Merck, Darmstadt, Germany; resistance 18.2 MΩ cm at 25°C).

3.2 Dopamine methacrylamide (DMA) synthesis

Dopamine methacrylamide (DMA) was synthesised as described in literature [17]: Sodium tetraborate and sodium hydrogen carbonate are added to protect the catechol group of dopamine HCl. They were dissolved in ultrapure water. The solution was then degassed with N_2 and dopamine HCl was subsequently added. Methacrylate anhydride was added dropwise to the solution while maintaining the pH value above 8 to keep the catechol groups protected. The reaction proceeded over night under protection from UV light, since the reaction is UV sensitive. Afterwards, the solution was washed with ethyl acetate. The catechol groups were deprotected by lowering the pH to 2 through the addition of HCl. The product was extracted by washing the solution again with ethyl acetate and dried over magnesium sulfate. The solution volume was reduced using a rotary evaporator and the product was precipitated with hexane. It was then stored at 4°C over night to facilitate the crystallisation. The product was dissolved in ethyl acetate and precipitated in hexane again for further purification. After the purification, the product was dried in a vacuum oven overnight. A schematic representation of the synthesis is provided in fig. 3.1. For more comprehensive details, refer to [17]. DMA was stored in a N_2 atmosphere in a freezer until further use.

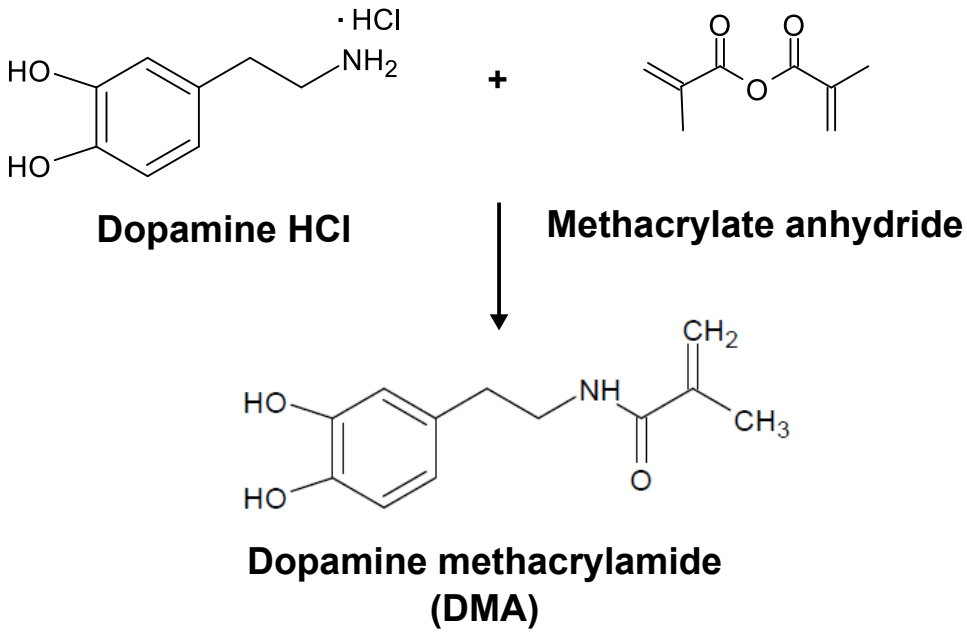

Figure 3.1: Synthesis scheme of dopamine methacrylamide (DMA).

^{1}H and ^{13}C nuclear magnetic resonance (NMR) spectroscopy confirmed the successful synthesis (see fig. A1, appendix; abbreviations corresponding to chemical groups are included with apostrophes). The catechol hydroxy protons are very sensitive to changes in temperature and concentration and can therefore slightly shift in the ^{1}H NMR spectra [131]. Details on NMR spectroscopy are given in chapter 3.7.
^{1}H NMR (300 MHz, DMSO-d$_6$, 301 K): δ = 7.93 (t, 1H, "e"), 7.46 − 7.95 (m, 3H, "e" and "b"), 6.65 − 6.58 (m, 2H, "a"), 6.44 (dd, 1H, "a"), 5.62 (s, 1H, "f"), 5.29 (m, 1H, "f"), 3.23 (m, 2H, "d"), 2.55 (t, 2H, "c"), 1.84 (t, 3H, "g"). **^{13}C NMR (75 MHz, DMSO-d$_6$):** δ = 167.4 ("h"), 145.1 ("b"), 143.6 ("b"), 140.1 ("j"), 130.4 ("k"), 119.3 ("a"), 118.9 ("f"), 116.0 ("a"), 115.5 ("a"), 41.0 ("d"), 34.7 ("c"), 18.7 ("g").

3.3 Microgel synthesis

Microgel particles were synthesised using free radical precipitation polymerisation [48] in a home-built reactor [16, 70]. More theoretical details on the reaction kinetics and microgel particle formation can be found in chapter 2.1.1. A schematic representation of the reactor and the used reactants is depicted in fig. 3.2.

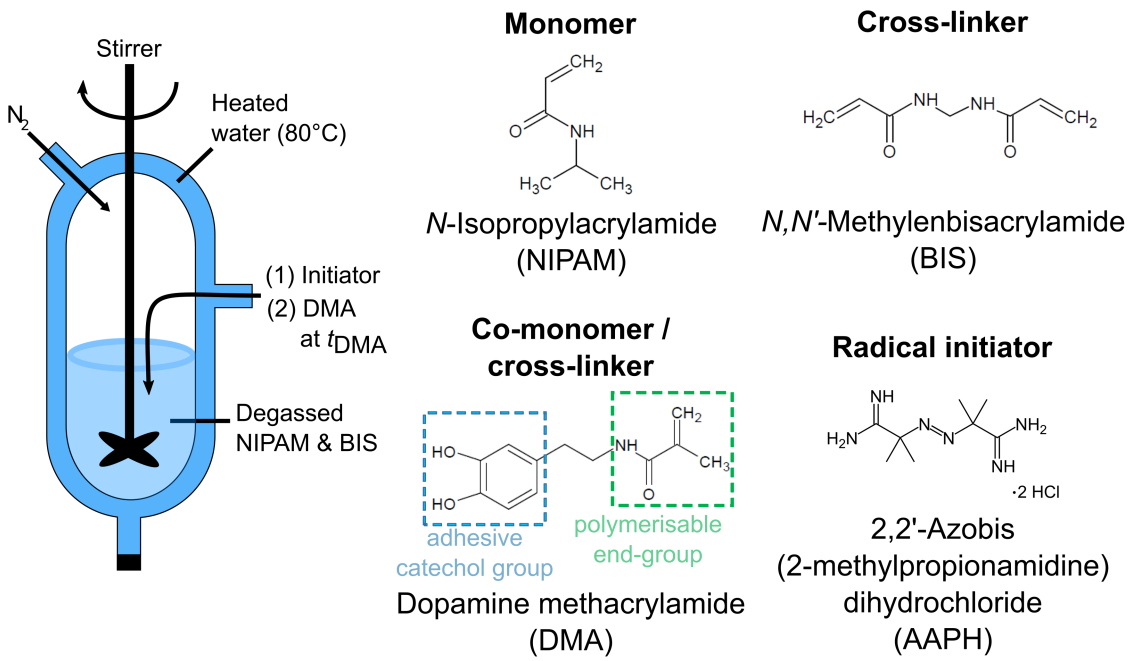

Figure 3.2: Free radical precipitation polymerisation of microgel particles including the home-built reactor on the left, and the used reactants on the right.

The **synthesis protocol** involves following steps: Initially, $n_{\mathrm{NIPAM}} = 18.6\,\mathrm{mmol}$ of the monomer *N*-isopropylacrylamide (NIPAM) and either $n_{\mathrm{BIS}} = 0.2$ or $0.4\,\mathrm{mmol}$ of the cross-linker *N,N'*-methylene-bis(acrylamide) (BIS) were dissolved in 120 ml of ultrapure water. The solution was directly poured into the reactor (Batch method [69, 70]), heated to 80°C and degassed with N_2 for 1 h while being continuously stirred. The polymerisation was initiated by the addition of 1 ml of the positively charged radical initiator 2,2'-azobis-2-methyl-propanimidamide dihydrochloride (AAPH; $c = 67\,\mathrm{mg\,ml^{-1}}$). The solution turned opaque within the first 3 min, confirming a successful polymerisation. To synthesise P(NIPAM-co-DMA) microgels, varying amounts of the co-monomer dopamine methacrylamide (DMA, dissolved in $5 - 15\,\mathrm{ml}$ pure ethanol; $n_{\mathrm{DMA}} = 1, 2.1, 3.3, 5\,\mathrm{mmol}$) were injected at the time t_{DMA}. The timing of the DMA addition is critical, as the catechol groups of DMA are known for their scavenging ability [4, 20], which can largely influence - impede or stop - the microgel formation. After the addition of DMA, a colour change from white to orange-pink occurred in the reaction mixture, indicating the formation of semiquinones or radicals [132]. Exceptions to this colour change were observed in the case of the microgels MG-$t_{15,60}$ #2 and #3, as explained in greater detail in chapter 4. For these microgels, the reactor and fume hood

were covered with aluminium foil to shield them from UV light. UV light can have a significant effect on chemical reactions involving dopamine derivatives [133]. The polymerisation was stopped at the reaction time t_{reac} by the addition of 1 ml toluhydroquinone (THQ; $c = 1.24\,\mathrm{mg\,ml^{-1}}$).
For reference, pure PNIPAM microgels were synthesised following the same procedure but without the addition of DMA. Additionally, microgels were synthesised without using the cross-linker BIS, solely relying on DMA's cross-linking properties [4].
To analyse the consumption of the reactants, time-samples were taken during the microgel synthesis, and analysed by mass spectrometry (MS) as described in sec. 3.9.
The microgels were **purified** with dialysis against ultrapure water for 10 d in a dialysis tube with a molecular weight cut-off (MWCO) of 14000 Da. They were freeze-dried afterwards for 2 d at -85°C with a pressure of 1 mbar. The freeze-dried microgels had a white to orange-pink colour, as shown in the exemplary image in fig. 3.3 (more images are available in fig. A4, appendix). The microgels were stored in a freezer until further use.

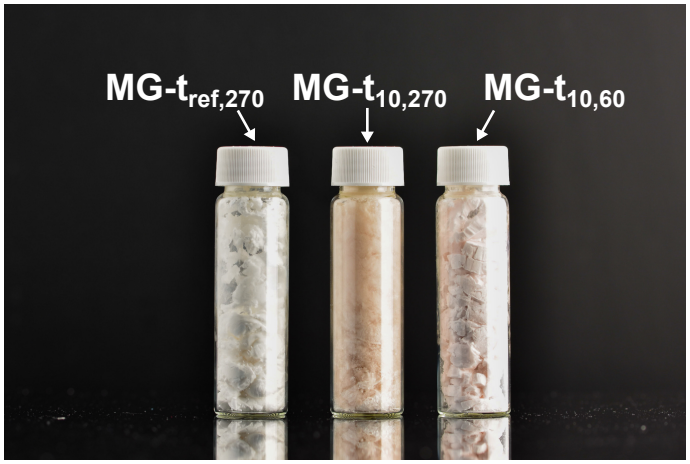

Figure 3.3: Freeze-dried reference PNIPAM microgel MG-$t_{ref,270}$ compared to P(NIPAM-co-DMA) microgels MG-$t_{10,270}$ and MG-$t_{10,60}$. These P(NIPAM-co-DMA) microgels were synthesised with different total reaction times t_{reac} ($t_{\mathrm{reac}} = 270\,\mathrm{min}$ and $t_{\mathrm{reac}} = 60\,\mathrm{min}$), but identical DMA injection times $t_{\mathrm{DMA}} = 10\,\mathrm{min}$. The reference PNIPAM microgel MG-$t_{ref,270}$ exhibits a purely white colour, while the P(NIPAM-co-DMA) microgels possess an orange to pinkish colour.

The resulting **microgel samples**, including their specific reaction parameters and final compositions, are detailed in table 3.2. In the subsequent chapters, the samples are

referred to as follows: MG-t$_{t_{\mathrm{DMA}},t_{\mathrm{reac}}}$ in chapter 4, where the letter "t" indicates the variation in the synthesis time parameters, specifically t_{DMA} and t_{reac}. Both are replaced in the sample naming with the corresponding values chosen according to table 3.2. Microgels synthesised without the additional cross-linker BIS are identified by the suffix "-noBIS". Similarly, microgel samples analysed in chapter 5 and chapter 6 are denoted as MG-c$_{\mathrm{B}\,c_{\mathrm{BIS}},\mathrm{D}\,c_{\mathrm{DMA,injected}}}$, where "c" represents compositional changes made to the microgels. c_{BIS} and $c_{\mathrm{DMA,injected}}$ are substituted in the sample nomenclature with the respective concentration values for BIS and the injected DMA, as given in table 3.2. The incorporated amount of DMA $c_{\mathrm{DMA,incorporated}}$ was calculated by nuclear magnetic resonance (NMR) spectroscopy and by UV-vis standard addition as described in sec. 3.7 and sec. 3.8. The results of these analyses are also listed in table 3.2.

Table 3.1: Overview of the synthesised microgels used in this thesis with corresponding reaction parameters and compositions.

Microgel	t_{DMA} [a] /min	t_{reac} [b] /min	c_{NIPAM} /mol%	c_{BIS} / mol%	$c_{DMA,injected}$ [c] / mol%	$c_{DMA,incorporated}$ [d] / mol%	
						UV-vis	NMR
Chapter 4:							
Reference microgel							
MG-$t_{ref,270}$	-	270	98	2	-	-	-
Influence of overall reaction time t_{reac}							
MG-$t_{10,270}$	10	270	93	2	5	2.4 ± 0.1	0.9
MG-$t_{10,60}$	10	60	93	2	5	2.7 ± 0.1	3.5
Influence of DMA injection time t_{DMA}							
MG-$t_{0,60}$	0	60	93	2	5	2.8 ± 0.2	4.1
MG-$t_{4.5,60}$	4.5	60	93	2	5	4.4 ± 0.4	0.9
MG-$t_{8,60}$	8	60	93	2	5	2.0 ± 0.0	0.9
MG-$t_{10,60}$	10	60	93	2	5	2.7 ± 0.1	3.5
MG-$t_{15,60}$ #1	15	60	93	2	5	2.2 ± 0.4	1.7
Reproducibility and influence of UV light							
MG-$t_{15,60}$ #1	15	60	93	2	5	2.2 ± 0.4	1.7
MG-$t_{15,60}$ #2 [e]	15	60	93	2	5	2.9 ± 0.0	2.5
MG-$t_{15,60}$ #3 [e]	15	60	93	2	5	2.1 ± 0.0	1.1
Influence of cross-linker BIS							
MG-$t_{0,60}$-noBIS	0	60	95	-	5	3.9 ± 0	1.8
MG-$t_{7.5,60}$-noBIS	7.5	60	95	-	5	3.4 ± 0	4.4
MG-$t_{15,60}$-noBIS	15	60	95	-	5	2.5 ± 0	2.9

Continued on next page

[a] Injection time of DMA; [b] overall reaction time of the synthesis; [c] injected DMA amount;

Table 3.1: Overview of the synthesised microgels used in this thesis with corresponding reaction parameters and compositions. (Continued)

Microgel	t_{DMA} [a] /min	t_{reac} [b] /min	c_{NIPAM} /mol%	c_{BIS} / mol%	$c_{DMA,injected}$ [c] / mol%	$c_{DMA,incorporated}$ [d] / mol%	
						UV-vis	NMR
Chapter 5 & 6:							
MG-$c_{B1,D0}$	-	60	99	1	-	-	-
MG-$c_{B2,D0}$	-	60	98	2	-	-	-
MG-$c_{B1,D5}$	15	60	94	1	5	2.2 ± 0.1	2.3
MG-$c_{B2,D5}$	15	60	93	2	5	2.9 ± 0.0	2.5
MG-$c_{B2,D10}$	15	60	88	2	10	6.7 ± 0.1	6.3
MG-$c_{B2,D15}$	15	60	83	2	15	7.8 ± 0.3	11.0
MG-$c_{B2,D20}$	15	60	78	2	20	16.5 ± 0.8	21.2

[d] incorporated DMA amount, determined separately by UV-vis and NMR spectroscopy;

[e] UV light protection applied; details on sample naming can be found in the text

3.4 Dynamic light scattering (DLS)

Theory and instrument

Dynamic light scattering (DLS) is a technique used to study the diffusion of particles in a dispersion, caused by Brownian motion, and determine their hydrodynamic radius R_H by using the elastic scattering of light. For a more detailed description, please refer to literature [134–136].

In **light scattering experiments**, a monochromatic light wave typically generated by a laser is irradiated. The light scattered by the sample is detected as an intensity $I(\vec{q})$, where $\vec{q} = \vec{q_\theta} - \vec{q_i}$ represents the scattering vector. Here, $\vec{q_i}$ denotes the direction of propagation of the incident and $\vec{q_\theta}$ of the scattered light wave. The experimental set-up is illustrated in fig. 3.4 (a). The magnitude of the scattering vector is calculated as

follows:

$$q = |\vec{q}| = 2|q_i| \sin\left(\frac{\theta}{2}\right) = \frac{4\pi n}{\lambda_i} \sin\left(\frac{\theta}{2}\right), \tag{3.1}$$

where n is the solvent refractive index and λ_i the incident laser wavelength.

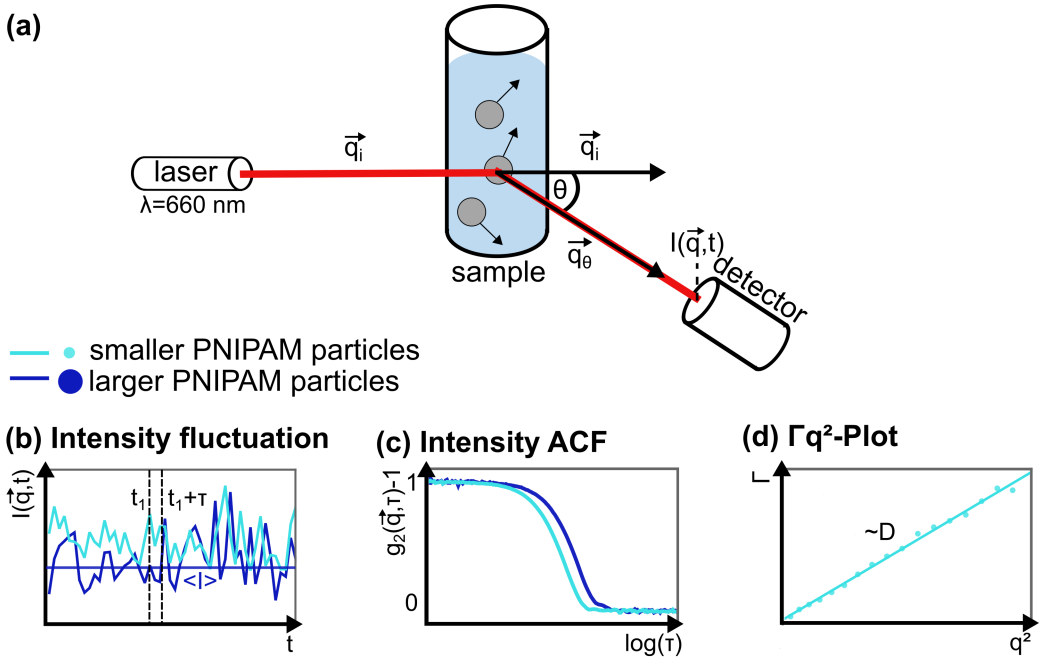

Figure 3.4: (a) Scheme of DLS set-up: A laser beam hits a sample, in which dispersed particles move due to Brownian motion. The scattered intensity $I(\vec{q}, t)$ is measured in a detector. (b) the intensity fluctuation $I(\vec{q}, t)$ of smaller and larger PNIPAM particles illustrates that smaller particles exhibit faster fluctuations. (c) the intensity auto-correlation function (ACF) $g_2(\vec{q}, \tau) - 1$ of both particles is shown, demonstrating a faster decay for smaller particles. (d) Γ is plotted against the squared scattering vector q^2 for the smaller PNIPAM microgel particles. The diffusion coefficient D can be directly obtained from the slope of the plotted data.

The scattered light includes structural and dynamical information about the particles. **Static light scattering (SLS)** measures the angular dependency of the time-averaged scattering intensity $I(\vec{q})$ to gain these structural information (molecular weight M_W, radius of gyration R_G and second virial coefficient A_2). In contrast, **dynamic light scattering (DLS)** measures the time-dependency of the scattered light at a fixed scattering angle $I(\vec{q}, t)$ to obtain the dynamic information about the scatterer, notably the hydrodynamic radius R_H. Due to the (random) Brownian motion of the sample particles

within the dispersion, the scattered intensity at a fixed scattering angle $I(\vec{q},t)$ fluctuates in time, as depicted in fig. 3.4 (b) for two exemplary PNIPAM microgel particles. Brownian motion results from the thermal collision of particles with the surrounding solvent molecules. Smaller particles move faster, therefore leading to faster intensity fluctuations $I(\vec{q},t)$ as illustrated in fig. 3.4 (b) as well.
The fluctuation of the scattered intensity $I(\vec{q},t)$ can be described through a **time-dependent correlation function**. Correlation functions describe to what extent two properties are correlated over a defined (time) interval. The time auto-correlation function (ACF) correlates the property $A(\vec{q},t_0)$ with its time-delayed property $A(\vec{q},t_0+\tau)$ at a lag time τ:

$$\langle A(\vec{q},t_0)A(\vec{q},t_0+\tau)\rangle = \lim_{T\to\infty}\frac{1}{T}\int_{t_0}^{t_0+T} dtA(t)A(t+\tau). \tag{3.2}$$

Here, t_0 represents the starting time of the measurement and T is the time interval over which the intensity is averaged. For stationary signals, the starting time becomes irrelevant, leading to:

$$\langle A(\vec{q},0)A(\vec{q},\tau)\rangle = \lim_{T\to\infty}\frac{1}{T}\int_{0}^{T} dtA(t)A(t+\tau). \tag{3.3}$$

This allows to define the normalised intensity $g_2(\vec{q},\tau)$ and the electric field $g_1(\vec{q},\tau)$ ACF's:

$$g_2(\vec{q},\tau) = \frac{\langle I(\vec{q},0)I(\vec{q},\tau)\rangle}{\langle|I(\vec{q},0)|\rangle^2}, \tag{3.4}$$

$$g_1(\vec{q},\tau) = \frac{\langle E_s(\vec{q},0)E_s(\vec{q},\tau)\rangle}{\langle|E_s(\vec{q},0)|^2\rangle}, \tag{3.5}$$

where $E_s(\vec{q},\tau)$ refers to the scattered electric field. For short lag times τ, the two signals are similar, indicating strong correlation. The ACF becomes maximal. For large lag times τ, the correlation of the two signals vanishes. In the case of homodyne scattering, the two ACF are related by the Siegert relation:

$$g_2(\vec{q},\tau) = 1+\beta|g_1(\vec{q},\tau)|^2. \tag{3.6}$$

The parameter β represents the coherence factor, depending on the laser beam set-up. For monodisperse samples, the electric field ACF can be modelled by an exponential decay and eq. 3.6 changes to:

$$g_2(\vec{q},\tau) - 1 = \beta\exp(-2\Gamma\tau) \tag{3.7}$$

with the decay rate $\Gamma = q^2 D$. D denotes the diffusion coefficient. Fig. 3.4 (c) displays $g_2(\vec{q}, \tau) - 1$, which is obtained directly from the instrument. For smaller particles, the intensity ACF exhibits a faster decay than for larger particles due to their faster fluctuations, as illustrated in fig. 3.4 (c) as well.
In order to account for polydispersity, the exponential behaviour can be approximated using a Taylor expansion known as the **Cumulant method** [137]. For monodisperse samples, the Taylor expansion of the logarithmic of $g_1(\vec{q}, \tau)$ would result in a linear relationship. Any deviations from this linearity reflect the sample's polydispersity. The Cumulant fit for $g_2(\vec{q}, \tau) - 1$ is expressed as:

$$\ln[g_2(\vec{q}, \tau) - 1] = \ln \beta - 2\Gamma\tau + 2\frac{K_2\tau^2}{2!} - 2\frac{K_3\tau^3}{3!} + ... \tag{3.8}$$

In the case of monodisperse samples, K_i becomes 0. Thus, polydispersity of the sample can be quantified by the polydispersity index $PDI = K_2/\Gamma^2$.
After determination of Γ with the Cumulant fit, a plot of Γ against q^2 can be created, as shown in fig. 3.4 (d) for the smaller PNIPAM microgel particles (similar results are obtained for larger PNIPAM microgel particles). The diffusion coefficient D can be directly obtained from the slope of this plot. By employing the Stokes-Einstein relation, the hydrodynamic radius R_H of the particles can be calculated:

$$R_\mathrm{H} = \frac{k_\mathrm{B}T}{6\pi\eta D}, \tag{3.9}$$

where η is the temperature-dependent viscosity of solvent, T the temperature and k_B the Boltzmann coefficient.

Measurement conditions

DLS measurements were performed with a multi-angle set-up from LS Instruments (LS Instruments AG, Fribourg, Switzerland) to ascertain the temperature-dependent hydrodynamic radius R_H of the microgel particles. The set-up contains a solid-state laser with a wavelength of $\lambda = 660\,\mathrm{nm}$ and a power of 100 mW, and is equipped with a temperature-controlled decaline bath. The samples were diluted to a concentration of approximately $c = 25\,\mu\mathrm{g\,ml^{-1}}$ to exclude multiple scattering events, which complicate the analysis of scattering data. Angles between 30° and 120° were measured in steps of 5° and a measurement time of $20 - 30\,\mathrm{s}$ was set. Scattering intensities $I(q, t)$ were transferred into intensity correlation functions $g_2(q, \tau) - 1$ by the LS spectrometer (as

shown in fig. 3.4). Data were fitted with a home-written Mathematica script from Marcus Witt by a Cumulant fit of third order [137].
Temperature-dependent swelling curves were conducted at temperatures between 15°C and 60°C (controlled with a thermostat). For the analysis, the temperature adjusted and measured by the device in the index-matching vat was taken, which can deviate up to 0.15°C from the set temperature. Swelling curves were fitted with a sigmoidal function, and the derivative $\mathrm{d}R_\mathrm{H}/\mathrm{d}T$ of this function was calculated. While the temperature at the minimum of the derivative function equals the volume phase transition temperature (VPTT), the temperature where $\mathrm{d}R_\mathrm{H}/\mathrm{d}T$ approaches zero describes the VPT completion temperature (VPT CT) [14, 16, 138]. The VPT CT was defined as the minimum temperature at which a maximum difference of 2.5 nm was achieved for a 5°C temperature change.
The swelling of the microgel network can be described by the Flory-Rehner theory [90, 91] (details see chapter 2.1.2). The swelling ratio α of the microgels was calculated by eq. 2.9 and the affine network factor β was derived from eq. 2.11. The hydrodynamic radius of the microgels in their swollen state R_H was set to be equivalent to $R_\mathrm{H}(20°\mathrm{C})$, while the hydrodynamic radius of the microgels in the reference, collapsed state $R_{\mathrm{H},0}$ was defined as $R_\mathrm{H}(50°\mathrm{C})$.
Mesh sizes ξ of the microgels, which describe the average distance between sequential cross-links, can be additionally calculated by [139]:

$$\xi = l \left(\frac{2M_\mathrm{c}}{M}\right)^{\frac{1}{2}} c_\mathrm{N}^{\frac{1}{2}} Q^{\frac{1}{3}}, \tag{3.10}$$

where l is the length of the C-C bond with $l = 0.154\,\mathrm{nm}$, M the average molar mass of the monomer NIPAM with $M = 113.16\,\mathrm{g\,mol^{-1}}$, c_N the characteristic ratio with $c_\mathrm{N} = 6.9$ [140] and M_c the molar mass between two cross-links with $M_\mathrm{c} = \frac{n_\mathrm{NIPAM} M_\mathrm{NIPAM}}{n_\mathrm{BIS}} + M_\mathrm{BIS}$ [141]. Q is the degree of swelling, which is in contrast to the swelling ratio α, defined as the ratio of the volume of the swollen polymer to the initial "dry" volume V_d:

$$Q = \left(\frac{V}{V_\mathrm{d}}\right). \tag{3.11}$$

The "dry" volume specifically refers to the completely dehydrated state. It was estimated with the microgel's volume in the collapsed state at 50°C, in which the microgel remains partially swollen in water.

3.5 Electrophoretic dynamic light scattering (EDLS)

Theory and instrument

Electrophoretic dynamic light scattering (EDLS) is a technique employed to study the electrophoretic mobility μ_e of charged particles, moving in an applied electric field $\vec{E}$. The electrophoretic mobility μ_e can serve for deducing the zeta potential ζ of the particles, providing insights into their surface charge characteristics. For a more comprehensive description, see [134, 142].

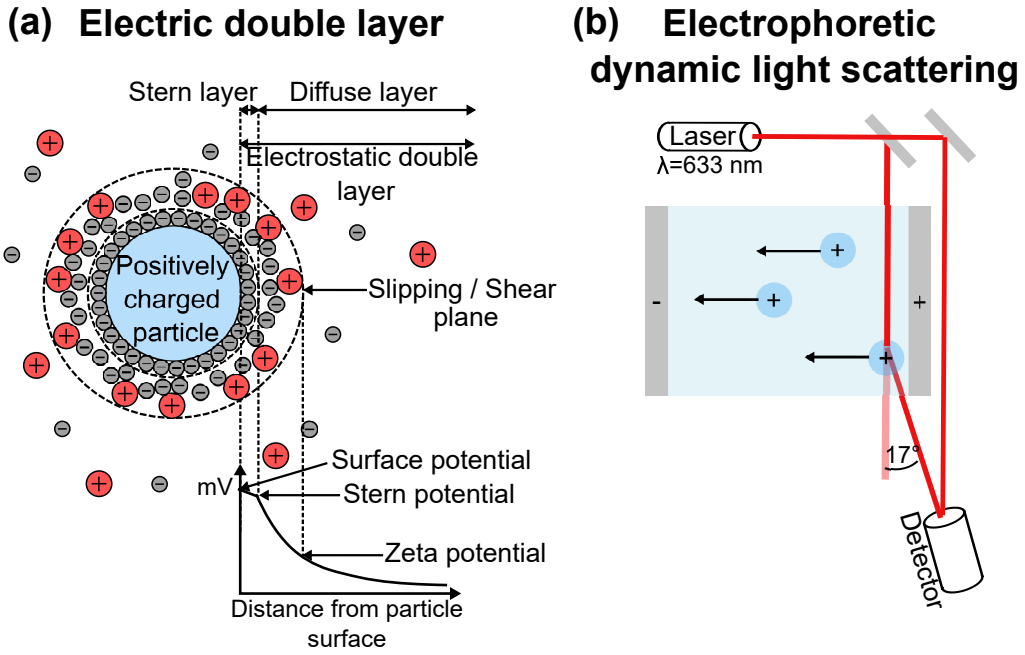

Figure 3.5: (a) Scheme of the formation of an electric double layer (EDL) at the surface of a positively charged particle: The EDL consists of the Stern layer and the diffuse layer. The zeta potential ζ is defined at the slipping or shear plane, which corresponds to the point where ions exhibit motion while others remain dispersed in the surrounding medium. The corresponding electrostatic potential is illustrated below. (b) Schematic set-up of electrophoretic dynamic light scattering (EDLS): It's employed to measure the electrophoretic mobility μ_e of the moving particles in response to an applied electric field. A laser detects the movement of the particles.

Charged particles in dispersion develop an **electric double layer (EDL)** of ions on their

surface, which consists of the Stern layer and the diffuse layer. The Stern layer is in nearest proximity to the surface and mainly consists of oppositely charged ions and molecules. In contrast, the diffuse layer consists of mobile anions and cations. The electrostatic potential within the Stern layer exhibits a linear decrease. In contrast, the electrostatic potential within the diffuse layer experiences an exponential decay, described by Debye's law [134, 143]. When the particle starts moving within the liquid environment, some ions stay bound to the particle's surface, accompanying its movement. However, ions at a certain distance are not able to follow the movement. The boundary between these differently behaving ions is referred to as slipping or shear plane, at which the zeta potential ζ is defined. As the surface potential cannot be accessed experimentally, the zeta potential ζ solely provides an idea about the surface charge of the particle. The different layers and the respective electrostatic potential are illustrated in fig. 3.5 (a).
When such a charged, dispersed particle is placed in an electric field, its electrophoretic mobility μ_e can be assessed using dynamic light scattering, leading to the method known as **electrophoretic dynamic light scattering (EDLS)**. The applied electric field induces the movement of charged particles towards an electrode of opposite charge (electrophoresis). The frequency of the original laser light differs from that of the laser light scattered by the moving particle. From the frequency shift, the particle's drift velocity $\vec{v}$ can be calculated by the laser Doppler shift. The experimental set-up of an EDLS is illustrated in fig. 3.5 (b). The electrophoretic mobility μ_e can be calculated by:

$$\mu_e = \frac{|\vec{v}|}{|\vec{E}|}, \tag{3.12}$$

The zeta potential ζ can then be derived by Henry's equation:

$$\mu_e = \frac{2\epsilon_r\epsilon_0\zeta f(\kappa R)}{3\eta}, \tag{3.13}$$

where ϵ_r signifies the relative permittivity, ϵ_0 represents the permittivity of vacuum, $f(\kappa R)$ is the Henry's function depending on the inverse Debye screening length κ^{-1} and the particle radius R, and η corresponds to the viscosity of the medium at the given experiment temperature.
Two approximations can be applied to assess the Henry's function. The Helmholtz-Smoluchowski equation [134, 144] assumes that the EDL is significantly smaller than the particle radius R, which is valid for large particles and/or high ionic strength. This

approximations results in $f(\kappa R) = 1.5$, leading to the simplified expression:

$$\mu_e = \frac{\epsilon_r \epsilon_0 \zeta}{\eta}. \tag{3.14}$$

Conversely, the Hückel approximation [134, 143] is valid when the EDL is much larger than the particle radius R ($\leq$ 100 nm), which is valid for small spherical particles and/or low ionic strength. In this case, $f(\kappa R) = 1$, yielding:

$$\mu_e = \frac{2\epsilon_r \epsilon_0 \zeta}{3\eta}. \tag{3.15}$$

It's important to note that the choice between these approximations depends on the specific characteristics of the system under investigation. For microgel particles with hydrodynamic radii R_H ranging from $200 - 500$ nm, the Helmholtz-Smoluchowski approximation is mostly used. It's worth highlighting that both the Helmholtz-Smoluchowski and Hückel equations apply only to spherical hard particles. This condition, however, does not hold for heterogeneously cross-linked microgels characterised by a soft shell with dangling ends. Therefore, in the context of this thesis, only the electrophoretic mobility μ_e was provided.

Measurement conditions

The electrophoretic mobility μ_e of the microgels was measured at 20°C and 50°C with a Zetasizer NanoZ (Malvern Panalytical, UK) to gain information about the surface charge of the microgels. Prior to the measurements, the sample cell was tested with a Malvern zeta potential transfer standard. Measurements were conducted at microgel sample concentrations of 0.5 mg ml^{-1}. Each measurement was repeated 10 times to obtain good statistics.

3.6 Atomic force microscopy (AFM)

Atomic force microscopy (AFM) is a technique developed in 1986 [145] to study the topography of samples with a high resolution even on an atomic scale. It was subsequently refined, so it became possible to determine the physical and chemical properties of materials, such as mechanical and adhesive properties, through force spectroscopy measurements. For some excellent descriptions and in-depth reviews, see [61, 146, 147].

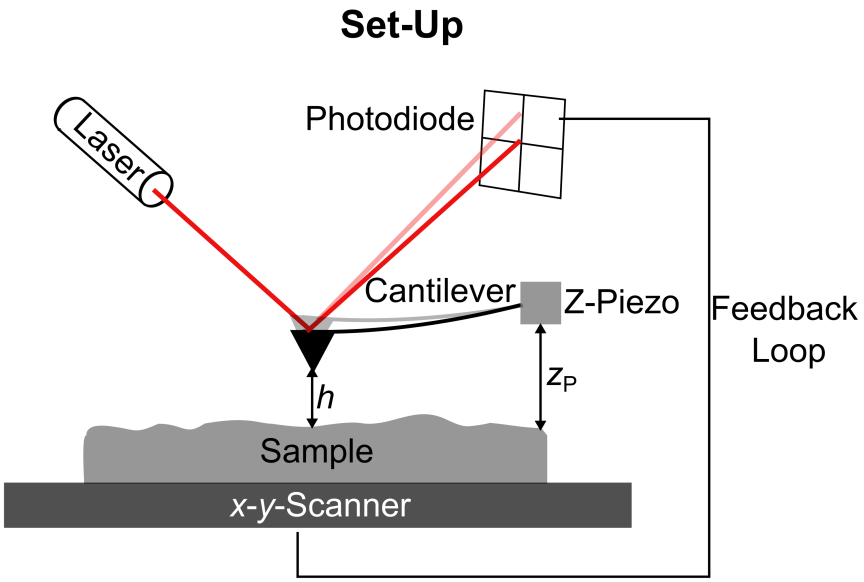

Figure 3.6: Basic set-up of an AFM: A laser beam is reflected from the reflective backside of a cantilever onto a four-segment photodiode to measure the cantilever deflection. This deflection is caused by the interaction of probe and sample. Piezo elements control the height of the cantilever (z_p) and the position of the sample ($x - y$). A feedback loop can be employed to maintain a constant probe-sample interaction, thereby regulating the tip height relative to the sample (h).

The basic principle underlying AFM is to measure the interaction forces between a probe, fixed to a flexible cantilever, and the sample. These interaction forces include magnetic, capillary and van der Waals forces for larger probe-sample separations ($10 - 100\,\text{nm}$), and repulsive forces such as Pauli repulsion and Coulomb repulsion at shorter distances ($0.01 - 1\,\text{nm}$) [146, 147]. These interaction forces induce a bending of the cantilever, either upwards for repulsive or downwards for attractive forces, which can be measured. The force can be described by Hooke's law:

$$\Delta F = -k\Delta z_c. \tag{3.16}$$

Here, k represents the spring constant of the cantilever and Δz_c the deflection of the cantilever.

The deflection of the cantilever can be measured using a laser focused on the reflective backside of the cantilever and then reflected onto a four-segment photodiode. When no forces act on the cantilever, the laser remains centrally reflected on the photodiode.

When interacting with the sample, the laser is either deflected up- or downwards, or it shifts horizontally. The former one allows to measure the height of the sample, while the latter one provides information about the lateral forces acting on the cantilever, causing it to torque. The AFM set-up also incorporates piezo elements, which control the height of the cantilever (z_p) and the lateral position of the sample ($x - y$). A feedback loop can be employed to maintain a constant probe-sample interaction by regulating the probe height relative to the sample (h). The schematic representation of an AFM set-up is depicted in fig. 3.6.

3.6.1 Imaging

Theory

AFM imaging can be proceeded in different modes, categorised into static and dynamic modes depending on the driving mechanism of the cantilever.
In the **static/contact mode**, the cantilever bends solely due to interactions between probe and sample. The probe makes actual contact with the surface, so repulsive forces become dominant. Typically, the contact mode is operated in a constant force mode implemented by a feedback loop: The feedback loop maintains the cantilever's deflection at a pre-defined setpoint value. This ensures additionally a constant relative height h between probe and sample. The contact between probe and sample results in high lateral forces, which can damage either the probe or the sample.
During **dynamic modes**, conversely, the cantilever oscillates near to its resonance frequency induced by a piezo element. The oscillation amplitude is referred to as the free amplitude of the cantilever. The oscillation is damped due to the probe-sample interaction, which results in a reduced amplitude and phase shift as depicted in fig. 3.7. During dynamic modes, the lateral forces acting on the cantilever are small, thus mitigating the risk of probe and sample damage. Dynamic modes encompass the non-contact mode and the intermittent contact mode. Additionally, phase imaging can be conducted to gain further information about the surface's properties. These dynamic modes should be examined in more detail:

- *Non-contact mode:* In the non-contact mode the cantilever oscillates above the sample, while probe and sample are not being in physical contact. Consequently, only attractive forces act on the cantilever, primarily van der Waals forces. As the

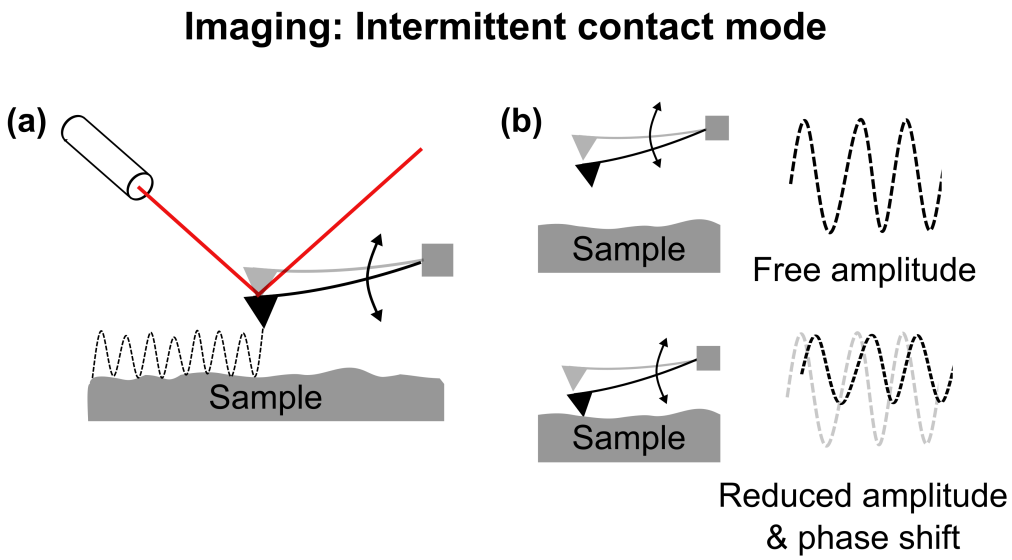

Figure 3.7: (a) Illustration of the intermittent contact mode: the cantilever oscillates due to the excitation of a piezo element, briefly making contact with the sample at the minimum of its oscillation. (b) The excited free amplitude of the oscillation is damped due to interaction forces between tip and sample when measuring. This results in a reduced amplitude and phase shift. A feedback loop keeps the amplitude of the oscillation constant.

cantilever experiences predominantly weak forces, the primary advantage of the non-contact mode is to minimise the risk of damaging the probe and the sample. However, the resolutions achieved in this mode are relatively low.

- *Intermittent contact mode:* The intermittent contact mode, also known as AC or tapping mode, overcomes the disadvantages of static/contact (damage of probe and sample due to high forces) and non-contact mode (low resolution). During the intermittent contact mode - as the name implies - the probe is shortly in contact with the sample at the minimum of its oscillation, while being in the non-contact regime at the maximum of its oscillation. The amplitude of the oscillation is chosen according to these conditions and typically falls within the range of $1 - 100\,\mathrm{nm}$ [148]. Therefore, forces acting on the cantilever, whether repulsive or attractive, are dependent upon the probe's position during the oscillation. The feedback loop keeps the amplitude of the oscillation constant by constantly regulating the cantilever's height by the z-piezo element, as illustrated in fig. 3.7.

- *Phase imaging:* Phase imaging monitors the phase shift in the cantilever's oscillation relative to the driven oscillation by the piezo (see fig. 3.7). It allows sensing regions of the sample with different material properties, such as elasticity, which are not detectable by other dynamic modes. Phase imaging can be simultaneously conducted with non-contact and intermittent contact modes.

The **choice of cantilever and probe** is important and they should be selected according to the used imaging mode and surface properties. Soft cantilevers are a good choice for contact mode imaging, as they minimise the risk of damage. Conversely, stiffer cantilevers with a high resonance frequency are preferable for intermittent contact mode imaging as they help to overcome capillary forces [149]. During imaging, tips are typically used as probes because of their sharpness. The tip's radius and geometry define the resolution of the images: Tip radii should be preferentially small to resolve the sample features. If this condition is not met, the convolution effect [150, 151] can lead to image artefacts.

Measurement conditions and sample preparation

Microgels deposited on silicon wafers were scanned in ambient conditions using an AC160TS-R3 cantilever on either a MFP-3D AFM (Asylum Research, Santa Barbara, California, USA) or a JPK Nanowizard II (JPK, Berlin, Germany) by intermittent contact mode. AC160TS-R3 cantilevers have an average spring constant of $k = 26\,\mathrm{N\,m^{-1}}$ and an average resonance frequency of $f_{\mathrm{res}} = 300\,\mathrm{kHz}$. Scan sizes were set to 10x10 µm and a scan rate of $0.5 - 1\,\mathrm{Hz}$ was used for imaging.
In **chapter 5**, cross-sections of microgel particles were analysed. The samples were allowed to equilibrate for at least 30 min at a temperature of 20°C before starting the measurement. For the analysis, 5 individual microgel particles were selected from the scans and their profiles were averaged. The height $h_{\mathrm{amb,AFM}}$ and width $w_{\mathrm{amb,AFM}}$ in ambient conditions were calculated, to determine a height-to-width ratio $h_{\mathrm{amb,AFM}}/w_{\mathrm{amb,AFM}}$.
In **chapter 6**, the nearest neighbour distance (NND) was assessed through image analysis of the corresponding AFM scans with the use of the image analysis software ImageJ (including a NND plugin [152] provided by Yuxiong Mao). ImageJ identifies circular objects in the AFM scans, corresponding to the microgel particles in this case. It extracts the $x - y$-coordinates of the particle's centroids, from which the NND was computed.

3.6.2 Force spectroscopy

Theory

AFM serves not only as a tool for imaging, but also to gain information about the mechanical and adhesive properties of samples through **force spectroscopy measurements**. In this technique, a probe approaches the sample in a perpendicular direction and indents into the sample, while its vertical position and deflection are monitored. The underlying principle is illustrated in fig. 3.8 (a).
The measurement generates a force curve as depicted in fig. 3.8 (b). When the probe is far away from the sample, there is no interaction between probe and sample, so the force acting on the cantilever is zero. As the probe approaches the sample, attractive forces between probe and sample start to act onto the probe, resulting in what is referred to as an approach curve (fig. 3.8 (b) black curve). The contact point is defined as the point at which probe and sample come into physical contact. Upon further indenting, primarily repulsive forces exerted on the probe increase. Once a defined threshold is reached, the retraction of the cantilever from the surface is triggered (trigger point), resulting in the retract curve (fig. 3.8 (b) grey curve). The threshold can be defined as a specific force exerted on the cantilever. When the cantilever retracts, it needs to overcome the attraction to the sample. The difference between the minimum force measured and the baseline is defined as F_{adh}. After overcoming this force, the force equals zero again. Multiple force curves can be conducted in a defined $x-y$-area by the force mapping tool. It provides information about the topography (topography map), gained from the tip position at which the trigger point is reached, and the adhesion force (adhesion map, lift-off map).
To quantitatively analyse force curves, the exact spring constant of the cantilever has to be determined before the measurement. Additionally, a calibration force curve on a rigid surface must be performed: Upon contact between probe and sample, the movement of the cantilever by the piezo element z_{p} is linearly correlated with the cantilever deflection z_{c} - referred to as "constant compliance". Within this region, the inverse optical lever sensitivity (invOLS) can be determined by the slope of the force curve. This invOLS value enables to convert the signals coming from the photodiode and the piezo position z_{p} into a force vs. distance curve, thereby enabling quantitative analysis of force spectroscopy data.

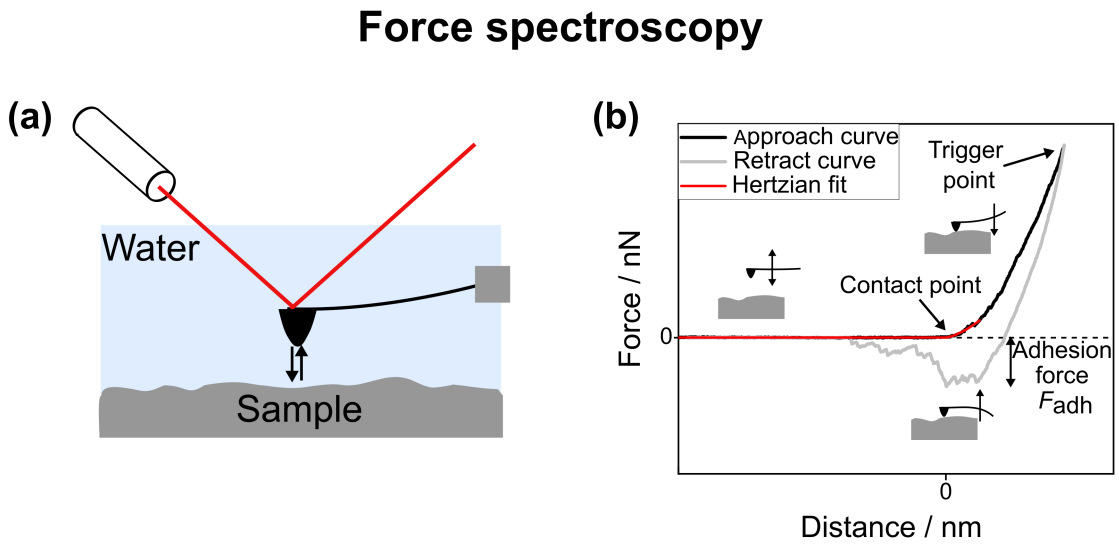

Figure 3.8: (a) Illustration of force spectroscopy measurements: the probe indents into the sample, while its deflection is monitored. The interaction between the probe and the sample during this process yields force vs distance curves, depicted in (b). The approach curve (black) provides the elastic modulus E by fitting the data with the Hertz model. An exemplary fit is highlighted in red. The retract curve (grey) can be used to ascertain the adhesion force F_{adh} of the sample. During retraction, the probe adheres to the sample which causes a negative force quantified by the adhesion force F_{adh}.

Force spectroscopy data can then be analysed to extract information about the sample's mechanical properties. Their elastic modulus E can be determined by **contact mechanics** [153, 154], signifying the sample's resistance to deformation. It is defined as:

$$E = \frac{\sigma}{\epsilon} = \frac{F/A}{\Delta L/L}. \tag{3.17}$$

Here, σ denotes the uniaxial stress and ϵ the strain upon the deformation. It can be expressed by the force applied by the probe during compression F, the area of applied force A, the original length L of the deformed body and the change in length upon compression ΔL. Equivalently N is the original breadth of the body and ΔN the change in breadth.

The Poisson ratio ν connects the normal compression of the body to the orthogonal

compression by:

$$\frac{\Delta L}{L} = -\nu \frac{\Delta N}{N}. \tag{3.18}$$

ν ranges from -1 to 0.5 for isotropic elastic materials and varies from 0.25 to 0.5 for microgels [112, 155–158]. Under- or overestimating the Poisson ratio by $\pm$ 0.15 leads to errors of 11.6% for the elastic modulus E.

The E modulus is finally determined by fitting the Hertz model [154] to the approach curve. The Hertz model is defined for the contact of two fully elastic bodies without adhesion forces. Therefore, it only holds true by fitting the approach curves. Alternative models, such as the Derjaguin-Muller-Toporov (DMT) model [159] and the Johnson-Kendall-Roberts (JKR) model [160] consider adhesive forces outside or inside the contact area.

In our case, data fitted using the Hertz model have proven to provide reasonable results. It is illustrated in fig. 3.8 (b) in red for an exemplary force curve. The effective elastic modulus E^* fitted by this model can be described as:

$$\frac{1}{E^*} = \frac{(1-\nu_S)^2}{E_S} + \frac{(1-\nu_P)^2}{E_P}, \tag{3.19}$$

where the sample is denoted with S and the probe with P. Assuming that the probe is much stiffer than the sample $E_P \gg E_S$, this simplifies to:

$$E^* = \frac{E_S}{(1-\nu_S)^2}. \tag{3.20}$$

Probes have to be chosen accordingly to this condition to extract valid values of E^*. For simplicity, E^* is denoted as E in the following. The relation between force F and E modulus then follows:

$$F = \frac{4E\sqrt[2]{R_P}}{3(1-\nu^2)}\delta^{\frac{3}{2}}. \tag{3.21}$$

R_P is the radius of indenter, while δ is the indentation depth. The relationship only holds true for spherical indenters.

The **choice of cantilever and probe** plays a crucial role during force spectroscopy measurements similarly as for AFM imaging. For the measurements, either tips ($5-50\,\text{nm}$) or colloidal probes ($1-50\,\mu\text{m}$ [153]) can be chosen: Tips provide information about the lateral structure of the sample in combination with obtaining mechanical properties such as the E modulus [61]. They can penetrate the sample sufficiently enough since high forces can be applied [75, 108], while not damaging the sample [107, 108].

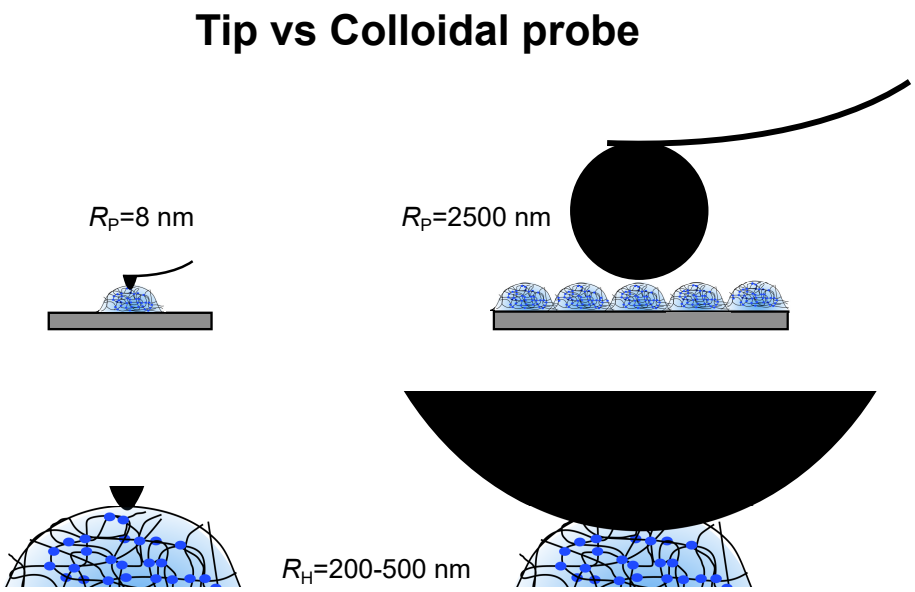

Figure 3.9: The differences in probe sizes highlighted in the scope of our measurements: While tips offer structural information in combination with determining an E modulus distribution, colloidal probes compress an entire microgel layer. Global E moduli E_{glob} for the whole layer as well as adhesion forces F_{adh} can be evaluated in this case.

Therefore, high indentation depth can be obtained. One limitation, though, is that the tip radius/shape cannot be precisely controlled during the manufacturing, leading to variations in contact geometry. This drawback is overcome by using colloidal probes [62–64]. They provide a well-defined contact area between probe and surface, thereby enabling precise measurements of adhesion forces F_{adh}. However, due to their large probe size, features of the sample cannot be localised or laterally resolved.
Fig. 3.9 depicts the differences between tip and colloidal probe, highlighted in the scope of our measurement conditions. While the tip can penetrate single adsorbed microgel particles at various positions resulting in an E modulus distribution, colloidal probes are substantially larger than microgel particles. Dense microgel packings should be used, so that the colloidal probe compresses a closed microgel layer. Then, a global E modulus (E_{glob}) can be obtained and adhesion forces F_{adh} can be determined.
It's important to note that keeping the type of cantilever and tip constant is essential when comparing data. Significant variations, especially in E moduli, can be observed when using different cantilevers or tips [161–163].

Measurement conditions and sample preparation

Force spectroscopy measurements were conducted during this thesis to study the mechanical properties of the adsorbed microgel particles in chapter 5 and their adhesive properties in chapter 6.
For both evaluations, the exact spring constant of the cantilever was determined with the Sader method [164, 165] through the analysis of its thermal resonance in air before starting the measurements. Subsequently, both the cantilever and the microgel sample were immersed in ultrapure water and the system was allowed to equilibrate for at least 30 min at temperatures of 20°C and 50°C. A force measurement on an empty spot of the hard silicon wafer was recorded to determine the invOLS. Force curves were done with an approach velocity of $800\,\mathrm{nm\,s^{-1}}$. The velocity does not change the results substantially [111]. For the determination of E moduli, variations in the approach velocity by two orders of magnitude resulted in variances of only about 10% for E. The fit region of the Hertz model (see eq. 3.21) was set to $0-40\%$ of the maximum indentation depth δ to exclude the impact of the underlying surface on the resulting moduli [74, 98, 107]. For PNIPAM microgels, we chose a Poisson ratio of $\nu = 0.4$ in accordance with literature [155].

In **chapter 5**, the **local E modulus E_{loc}** has been determined by *indenting a tip* into single adsorbed microgel particles. Microgel particles have been deposited on silicon wafers with a loose packing density, to measure a single particle without the influence of surrounding particles and resolve their structure laterally. Silicon wafers were cleaned in piranha solution (ratio 1:3 hydrogen peroxide H_2O_2 to sulfuric acid H_2SO_4) for 30 min. Afterwards, microgels were deposited on silicon wafers in a drying process combined with spin-coating: $75-200\,\mu\mathrm{l}$ of a $c = 0.5\,\mathrm{mg\,ml^{-1}}$ microgel dispersion were placed on the wafers for 30-90 s before spin coating was started with a rotational speed of 1000 rpm for 1 min.
Measurements were done with a Cypher AFM (Oxford Instruments, Abingdon, UK) equipped with a CoolerHeater Sample Stage to control the temperature of the samples. A 2x2 µm sized area with 30x30 pixel was measured with the force mapping tool. The size allowed a high resolution of the microgel particles while maintaining reasonable measurement times. Tips were selected as indenters to acquire both mechanical properties through the E modulus, and a lateral structure of the sample [61]. The resultant E moduli, obtained from specific positions across the microgel particles, can

be consequently regarded as local elastic moduli E_{loc}. The BL-AC40TS cantilever was chosen according to previous work of our group [74] (spring constant $k = 0.09\,\mathrm{N\,m^{-1}}$, resonance frequency $f_{res} = 110\,\mathrm{kHz}$) to enable the direct comparison of the data using the same cantilever type.
The measurement conditions were carefully checked, by varying the trigger point and checking the validity of the Hertz model for the pure reference PNIPAM microgel MG-$c_{B2,D0}$ (see table 3.2).

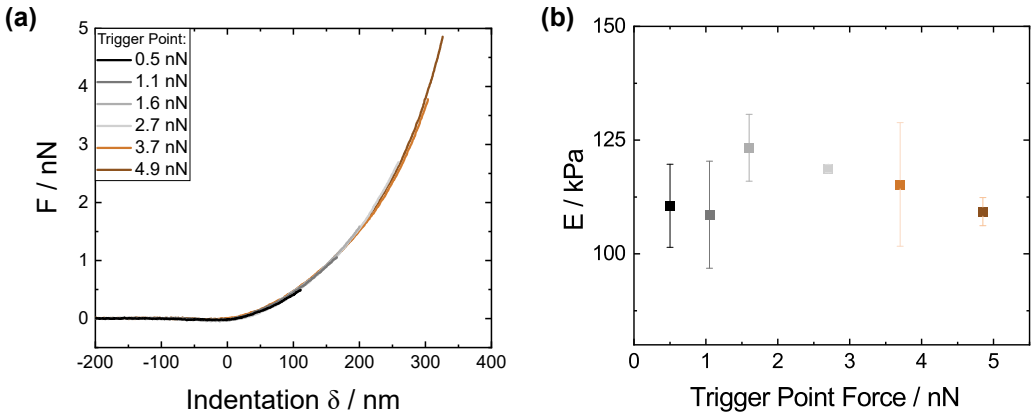

Figure 3.10: (a) Force curves received for the cantilever BL-AC40TS on a reference PNIPAM microgel MG-$c_{B2,D0}$ with different trigger points, defining the indentation depth of the cantilever. (b) The effect of the trigger point on the E modulus of a pure PNIPAM microgel MG-$c_{B2,D0}$. A trigger point of 2.7 nN was defined for further measurements.

In total six different trigger points from $0.5 - 4.9\,\mathrm{nN}$ were studied (see fig. 3.10). The trigger point must be in accordance to the sample's stiffness. Large trigger points, corresponding to large indentation depths, can damage the sample and/or the tip. On the other hand, excessively small trigger points may not fully resolve the microgel structure, i.e. by only indenting into the outer shell of the microgels, leading to inaccurate E moduli. In this work, nonetheless, no systematic change in E is observed for varied trigger points, as depicted in fig. 3.10 (b), indicating minimal influence within the range of $0.5 - 4.9\,\mathrm{nN}$. For the measurements, a medium trigger point of 2.7 nN was chosen.
The validity of the Hertz model was studied as well. The BL-AC40TS cantilever is much stiffer than the sample and the area of contact is assumed to be small [61, 166] to fulfil the requirements of the Hertz model. Three exemplary force curves, conducted

in the centre of three microgel particles of MG-$c_{B2,D0}$, are given in fig. 3.11 (a). The three exemplary force curves are plotted in log-log scale in fig. 3.11 (b). A linear fit to the logarithmic force curves provides slopes of 1.47 to 1.56 N m^{-1} up to indentation depths of 100 nm, confirming the Hertzian model (see eq. 3.21, slope $= \frac{3}{2}$).
After setting up the measurement conditions, at least 10 force curves were evaluated in the centre of 10 microgel particles at 20°C to obtain an average E modulus for the microgels with varying DMA content (see table 3.2). E moduli over the particle's cross-section of a pure PNIPAM MG-$c_{B2,D0}$ and a P(NIPAM-co-DMA) microgel MG-$c_{B2,D10}$ were analysed for 5 individual microgel particles at 20°C and 50°C.

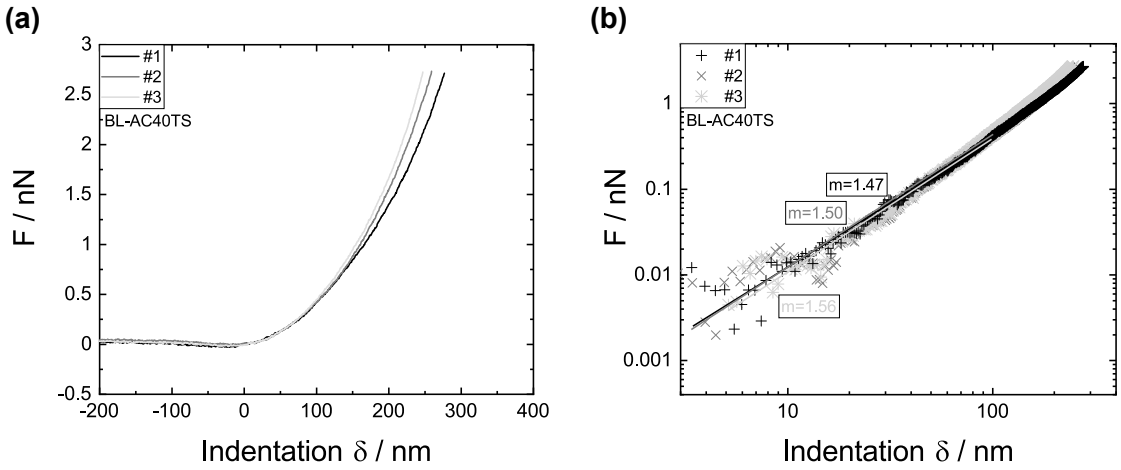

Figure 3.11: Exemplary force curves of MG-$c_{B2,D0}$, obtained by force spectroscopy measurements, indented by a BL-AC40TS cantilever and plotted in linear (a) and logarithmic (b) scale. (b) includes linear fits with a slope of 1.47-1.56 N m^{-1} confirming the validity of the Hertzian model in ultrapure water up to indentation depths of 100 nm.

In **chapter 6, adhesion forces F_{adh} and global E moduli E_{glob}** of the microgel samples were determined by *indenting a colloidal probe* into a microgel layer.
Therefore, microgel dispersions were deposited on silicon wafers from a water/ethanol interface by using the Langmuir-Blodgett technique. The Langmuir trough is made of a hydrophobic material such as teflon. It was thoroughly cleaned prior to each sample preparation with chloroform and ultrapure water. Subsequently, 130 ml of ultrapure water were added, serving as the sub phase. A microgel dispersion with a concentration of $c = 10$ mg ml^{-1} mixed with a volatile solvent such as ethanol is then added to the surface. The microgels were further purified through centrifugation

to enhance their purity and remove any residual impurities or contaminations prior to the deposition. After the evaporation of ethanol, the microgels adsorb on the water-air interface in a monolayer ("spreading"). The system was allowed to equilibrate for at least 20 min. The compression of the monolayer was started by moving the trough's barriers. The monolayer can then be transferred onto the silicon wafers, prior cleaned by sonification with ethanol for 10 min, via an installed dipping mechanism as follows: They were fully dipped into the water sub phase, before the spreading. When a defined surface pressure Π is reached during the movement of the trough's barriers, the system is allowed to equilibrate for 20 min again. Then, the dipping arm began to move the silicon wafers upwards with a defined velocity of $0.1\,\mathrm{mm\,s^{-1}}$. Depending on the surface pressure Π within the Langmuir trough, the distance of the microgel particles can be controlled with a high precision, resulting in highly ordered microgel samples. It's important to note that each sample comprises a monolayer of microgel particles, considered as a closed layer. The samples were prepared by Carina Schneider.

The colloidal probes used during these measurements were prepared with following procedure: a single silica microsphere (Bangs Laboratories Inc., Fishers, Indiana, USA) having an approximate radius of $R = 2.5\,\mu\mathrm{m}$ was glued to the end of a tipless CSC38/No Al cantilever (spring constant $k = 0.09\,\mathrm{N\,m^{-1}}$, resonance frequency $f_{\mathrm{res}} = 20\,\mathrm{kHz}$) from µmasch (Tallinn, Estonia). This attachment was achieved with the help of a micro-manipulator MP-225 (Sutter Instrument, Novato, California, USA) and a light microscope Axiovert 40 CFL (Carl Zeiss GmbH, Oberkochen, Deutschland). The spring constant of the cantilever was chosen to match that of the BL-AC40TS cantilevers used in chapter 5. The cantilevers were sintered at 1150°C for at least 3 h. Colloidal probes were analysed by scanning electron microscopy (SEM) after sintering, as explained in sec. 3.10. This allows to determine their radius $R_{\mathrm{P,SEM}}$ and identify any impurities. In addition, three colloidal probes were exemplarily characterised using a silicon test grating (TGT1 by ScanSens GmbH, Bremen, Germany). The grating features sharp spikes of a radius $R \leq 10\,\mathrm{nm}$ in a distance of $2.2 - 3.0\,\mu\mathrm{m}$ from each other. The spikes have an angle smaller than 50° and are designed for the visualisation of tips. Colloidal probes have been scanned over this test grating in contact mode at low scanning speeds of 0.5 Hz. By subtracting a sphere fit from the image, the surface topography of the colloidal probes was determined. SEM images in comparison with AFM scans can be found in fig. A2, appendix. The radii obtained by both methods are listed in table A1 (appendix). The radii of both methods were comparable, but $R_{\mathrm{P,AFM}}$

determined using the test grating exhibited slightly larger variations from sphere to sphere. For all three colloidal probes, the surface topography proves to be very smooth, making the contribution of the colloidal probe's surface roughness negligible [148]. Only SEM images were provided for the remaining colloidal probes used in this thesis, as they were deemed sufficient. The silicon wafer, used to conduct the calibration curves, and the colloidal probes were cleaned with a Diener Zepto plasma cleaner (Diener electronic GmbH + Co. KG, Ebhausen, Germany) by exposure to oxygen plasma before each measurement. Each colloidal probe was used exclusively for one single microgel sample to avoid cross-contaminations.
Measurements were conducted at 20°C using a MFP-3D AFM (Asylum Research, Santa Barbara, California, USA). A 10x10 µm sized area with 20x20 pixel was measured with the force mapping tool, resulting in 400 force curves for each force map. Thus, each curve was conducted with a distance of 500 nm from the adjacent one. Force maps were conducted for each sample at three different positions A,B and C on the wafer. This approach allows us to study changes in the results, referred to as "ageing effects". Specifically, one force map was conducted on position A. On position B, two successive force maps were conducted. Subsequently, one force map was conducted at position C. While the positional change helps to examine the effects related to the colloidal probe's fatigue and potential contaminations adhering to the probe upon measurement, using two consecutive force maps at position B provides insights into the material's fatigue within the microgel layer. A trigger point of 15 nN was chosen according to [97, 167], resulting in indentation depths between 100 and 200 nm (see table A4 and table A5, appendix).
The measurements were conducted for the microgels with varying DMA content (see table 3.2). The adhesion force F_{adh} was determined by averaging the results from 400 force curves within each force map as follows: Given that each force curve yields a different adhesion force F_{adh}, a distribution of F_{adh} is obtained. A Gaussian fit is applied to the data. The average adhesion force then corresponds to the maximum of the fit, which is illustrated in fig. 3.12 for the reference microgel MG-$c_{B2,D0}$. It's important to note that the colloidal probe does not always indent into the centre of microgel particles, as depicted in the scheme in fig. 3.9; instead, it may indent into the spaces between two particles within the microgel layer. This variation occurs because each force curve is conducted at a distance of 500 nm from the subsequent force curve, while the particles at the surface exhibit varying widths depending on the radius of each type of microgel particle. This variation accounts for the significantly lower

adhesive forces observed in the distribution.

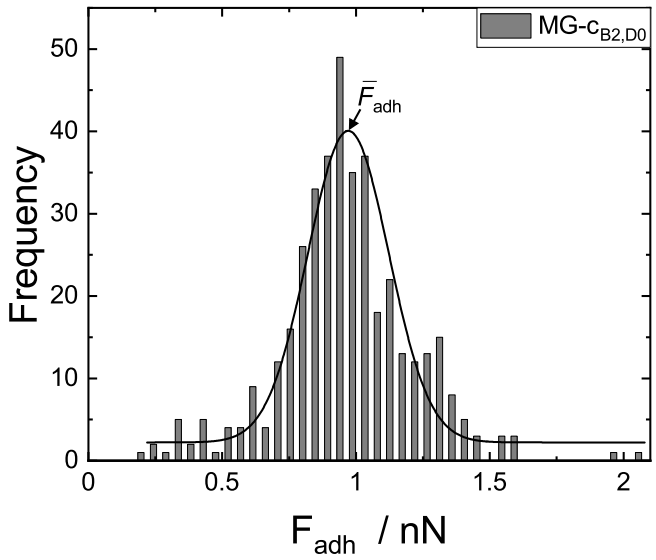

Figure 3.12: Distribution of F_{adh} exemplarily shown for the pure PNIPAM microgel MG-c$_{B2,D0}$. Each force curve yields an adhesion force value F_{adh}, contributing to the depicted distribution. The maximum of a Gaussian function, applied to the distribution, corresponds to the average adhesion force.

Since stiffer samples lead to smaller indentation depths δ for same trigger points, the adhesion force was normalised by the contact area A for each sample. Indentation depths δ were calculated as an average from 10 force curves. The contact radius a can be derived from the indentation depth δ and the indenter radius R_P by:

$$a^2 = \delta R_P. \tag{3.22}$$

The contact area A can be calculated over a ball segment as:

$$A = \pi\delta(4R_P - \delta). \tag{3.23}$$

Additionally, a global elastic modulus E_{glob} can be derived from the measurements, by analysing 10 force curves per sample. Equivalently to chapter 5, the Hertz model (eq. 3.21) was fitted to the approach curves. The application of the Hertz model was verified identically as described before for the reference PNIPAM microgel MG-c$_{B2,D0}$ up to indentation depths of 100 nm (see fig. A3, appendix).

3.7 Nuclear magnetic resonance (NMR) spectroscopy

Theory and instrument

Nuclear magnetic resonance (NMR) spectroscopy is a technique used to investigate the molecular structure, dynamics or reaction states of molecules. For a more detailed description, refer to [168].

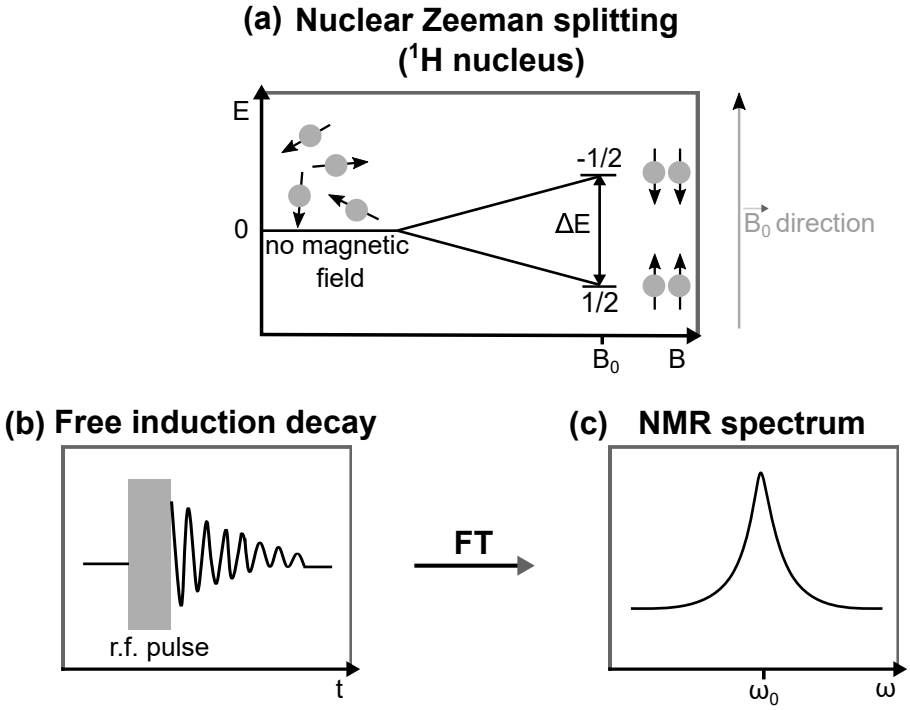

Figure 3.13: Basics of NMR spectroscopy: (a) Nuclear Zeeman splitting of ^{1}H nucleus in an applied outer magnetic field $\vec{B}_0$. (b) After a radio-frequency pulse is applied in a 90° angle to the $\vec{B}_0$ field, spins relax into equilibrium, generating the time-dependent NMR signal called free induction decay (FID). (c) By Fourier transformation (FT) the time-dependent NMR signal is transferred into a frequency-dependent NMR signal, which is the well-known NMR spectrum.

NMR spectroscopy uses the physical properties of an atomic nucleus, which possess a weak magnetism and an angular momentum called spin, described by the quantum number I. The magnetic moment $\vec{\mu}$ of a nucleus is linked to its spin via the gyromag-

netic ratio γ in the relationship:

$$\vec{\mu} = \gamma \vec{I}. \tag{3.24}$$

When nuclei are exposed to an outer magnetic field $\vec{B}_0$, nuclei with the quantum number I split into $(2I + 1)$ spin states, each possessing different energies, known as **nuclear Zeeman splitting** - the basis of NMR spectroscopy. This phenomenon is illustrated in fig. 3.13 (a) for a ^{1}H nucleus. Nuclei with zero spin, such as ^{12}C and ^{16}O, do not exhibit nuclear Zeeman splitting, and are termed "NMR silent". Nuclear Zeeman splitting increases with the strength of the external magnetic field $\vec{B}_0$ (see fig. 3.13 (a)). Therefore, large magnetic fields from 4 to 20 T are required in NMR spectroscopy.
In the absence of an external magnetic field, nuclear spin vectors can be aligned in any direction, as depicted in fig. 3.13 (a). Upon the application of an external magnetic field $\vec{B}_0$, these spin vectors precess around $\vec{B}_0$ in a cone-like motion, referred to as spin precession. The frequency of the spin precession is called **nuclear Larmor frequency** ω_0 and is given by:

$$\omega_0 = -\gamma B_0. \tag{3.25}$$

Thus, each nucleus has its specific Larmor frequency. This leads to various types of NMR spectroscopy, with ^{1}H and ^{13}C being among the most prominent ones.
The basic working principle of an **NMR spectrometer** can be summarised as follows: (1) Nuclear spins align along the applied magnetic field $\vec{B}_0$ (equilibrium state). (2) A radio-frequency (r.f.) pulse is applied in a 90° angle to $\vec{B}_0$, creating a transverse net magnetisation of the spins. (3) Subsequently, the magnetisation of the spins recovers, called "relaxation", until equilibrium is restored. The net magnetisation of the spins induces an electric current at the receiver coil, generating the time-dependent NMR signal, **free induction decay (FID)**, as depicted in fig. 3.13 (b). The time-dependent FID can be transferred into a frequency-dependent signal by Fourier transformation (FT). This transformation leads to the well-known NMR spectrum, as illustrated in fig. 3.13 (c).
Different compounds of a sample can be distinguished in the NMR spectrum due to the **chemical shift** δ. Nuclei are surrounded by electrons, being magnetic themselves and consequently changing the Larmor frequency of the nuclei spins. Each nucleus is therefore dependent on its chemical environment. The chemical shift is defined as:

$$\delta = \frac{\omega_0 - \omega_{\text{ref}}}{\omega_{\text{ref}}}, \tag{3.26}$$

where ω_{ref} is the Larmor frequency of a reference substance. Chemical shifts δ are typically expressed in parts per million (ppm). Some important chemical shifts in ^{1}H NMR spectroscopy are summarised in table 3.3.

Table 3.3: Chemical shifts of some functional groups in ^{1}H NMR spectroscopy (tetramethylsilane used as reference compound). Values obtained from [168].

Functional group	δ / ppm
-CH_3	≈ 1
-CH_2	$\approx 2 - 2.5$
-CH-	$\approx 4 - 5$
Aromatics	$\approx 6 - 8.5$

Nuclear spin-spin coupling of nuclei with a non-zero spin, is an additional factor that affects the NMR spectrum. The Larmor frequency of one nucleus is influenced by the magnetic nuclear spins of its neighbours, leading to the splitting of peaks into multiplets. Hence, this phenomenon provides valuable informations about the chemical environment of the nucleus.
Lastly, the peak intensity in ^{1}H NMR spectra offers insights about the number of nuclei contributing to each peak. Thereby, the integral of the peaks provides more details about the chemical structure of the measured sample. Nevertheless, integrating peaks arising from protons bonded to oxygen or nitrogen, such as OH and NH groups, is a challenge due to the exchangeability of their protons with other protons.

Measurement conditions

^{1}H and ^{13}C NMR spectra of DMA in DMSO-d_6 were recorded using a 300 MHz NMR Avance II spectrometer (Bruker BioSpin GmbH, Rheinstetten, Germany). ^{1}H NMR spectra of P(NIPAM-co-DMA) microgels were recorded in two different solvents, DMSO-d_6 and methanol-d_4, to ensure that no relevant signals are hidden by the solvent peaks. Either the 300 MHz Avance II or a 500 MHz DRX Avance 500 (Bruker BioSpin GmbH, Rheinstetten, Germany) spectrometer were used. Measurements were carried out with a high number of scans (NS $=$ 506 or 1024) and with a recycle delay of D1 $=$ 5 s to improve resolution. Measurements were provided by the NMR team of the Chemistry Department (TU Darmstadt).

Determination of incorporated amount of DMA $c_{\mathbf{DMA,incorporated}}$: NMR spectroscopy was used as one of two methods to determine the amount of incorporated DMA $c_{\mathrm{DMA,incorporated}}$ in P(NIPAM-co-DMA) microgels based on literature [13, 16, 169]. Exemplary spectra of MG-$t_{10,270}$ in DMSO-d_6 are shown in fig. 3.14 (a), while (b) highlights the higher chemical shift region, which was used for the calculation. The spectra of microgels in methanol-d_4 cannot be used for the calculation, as methanol-d_4 is a protic solvent, and thus, protons can exchange with the NH and OH groups of P(NIPAM-co-DMA), leading to an incorrect integration of the peaks. The amount of incorporated DMA $c_{\mathrm{DMA,incorporated}}$ was calculated by using the corresponding peaks of the catechol group of DMA (denoted as "h") and the CH-group of NIPAM (denoted as "f") by following equation:

$$c_{\mathrm{DMA,NMR}} = \frac{\frac{\int \mathrm{DMA("h")}}{3\mathrm{H}}}{\frac{\int \mathrm{DMA("h")}}{3\mathrm{H}} + \frac{\int \mathrm{NIPAM("f")}}{1\mathrm{H}}}. \tag{3.27}$$

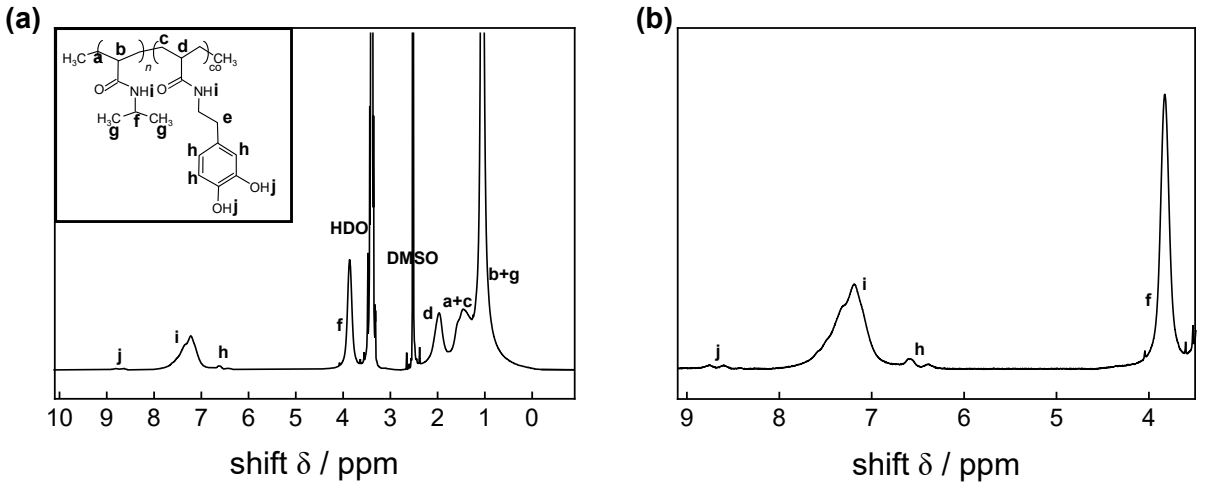

Figure 3.14: (a) Exemplary ^{1}H NMR spectra of MG-$t_{10,270}$ in DMSO-d_6. (b) Highlights the regions at higher chemical shifts, where the relevant peaks of the catechol group of DMA (denoted as "h") and the CH-group of NIPAM (denoted as "f") are present, used for the calculation of incorporated amount of DMA $c_{\mathrm{DMA,incorporated}}$.

The influence of BIS cannot be derived from the spectra. However, since only $0.2 - 0.4\,\mathrm{mmol}$ of BIS was used in comparison to the total amount of reactants ($20 - 24\,\mathrm{mmol}$), its impact is assumed to be negligible. The deconvolution tool of mestrenova analysis software, which fits a Gaussian function to the peaks of the spectra, was used to minimise the influence of the overlapping NH peaks of NIPAM and

DMA (denoted as "i") with the peaks arising from the catechol groups of DMA (denoted as "h") (see fig. 3.14). Results can be found in table 3.2.

3.8 UV-vis spectroscopy

Theory

UV-vis spectroscopy measures the absorbance of electromagnetic radiation within the ultraviolet (UV) wavelength range ($220 - 380\,\text{nm}$ [170]) and the visible (vis) wavelength range ($380 - 800\,\text{nm}$ [170]) as it interacts with a sample. For a more detailed description, see [170, 171].
Light can be regarded as either an electromagnetic wave or a particle known as photon. The energy of a photon is given by:

$$E = h\nu. \tag{3.28}$$

Here, $h = 6.626 \cdot 10^{-34}\,\text{J s}$ represents the Planck constant and ν denotes the frequency of light measured in s^{-1}. The frequency ν of the wave is related to the wavelength λ through:

$$\nu = \frac{c}{\lambda}, \tag{3.29}$$

where $c = 2.99 \cdot 10^{8}\,\text{m s}^{-1}$ is the speed of light in vacuum.
UV-vis spectroscopy now uses the interaction between light and molecules of the sample. The sample adsorbs the light, causing a transition of electrons from their energetic ground state to a specific excited state. These transitions are highly dependent on the energy of light and the characteristics of the material itself.
The amount of light absorbed by the sample, expressed by the absorbance A, is related to the transmittance T of light passing through the sample. T is further connected to the incident I_0 and the transmitted I intensity of light as follows:

$$A = -\log T = \log \frac{I_0}{I}. \tag{3.30}$$

Utilising the Beer-Lambert law, one can put A in direct relationship with the optical path length l and the concentration c_S of the sample:

$$A = \log \frac{I_0}{I} = \epsilon c_S l, \tag{3.31}$$

where ϵ is the molar absorption or extinction coefficient.

Measurement conditions

UV-vis spectra were acquired using a Lambda 650 spectrometer from PerkinElmer (Waltham, Massachusetts, USA) at room temperature, offering spectral resolutions of $\leq 0.17\,\text{nm}$. For the measurements, 2 ml of the microgel dispersion with a concentration of $c = 0.5\,\text{mg}\,\text{ml}^{-1}$ were filled in quartz cuvettes with an optical path length of $l = 1\,\text{cm}$. The full spectra of the microgels were recorded over a wavelength range spanning from 180 to 800 nm. Additionally, UV-vis standard addition was used as a second method to determine the amount of incorporated DMA $c_{\text{DMA,incorporated}}$ in P(NIPAM-co-DMA) microgels. For this purpose, the wavelength range was set to 200 to 350 nm. Further details of these measurements are provided below.

Determination of incorporated amount of DMA $c_{\text{DMA,incorporated}}$: The incorporation of DMA leads to an additional peak in the UV-vis spectra of the microgels at $\lambda_{\text{max}} = 282\,\text{nm}$, as illustrated in fig. 3.15, distinguishing them from pure PNIPAM microgels. The peak is attributed to the unoxidised catechol groups of DMA [172].
The amount of incorporated DMA $c_{\text{DMA,incorporated}}$ in P(NIPAM-co-DMA) microgels was then determined by UV-Vis standard addition. After filling the UV-vis quartz cuvettes with the microgel dispersion, DMA (dissolved in ethanol) was added to the cuvettes in concentration ranges from $0 - 200\,\mu\text{g}\,\text{ml}^{-1}$. This addition results in a rise of the absorbance at λ_{max}, as depicted in fig. 3.15.
The signal arising from pure PNIPAM was subtracted as background from all measured UV-Vis spectra, as indicated by the red line in fig. 3.15. When dealing with low levels of incorporated DMA, it can be, however, challenging to differentiate the microgel background from the relatively small catechol peak. The absorbance at λ_{max} is plotted against the added DMA concentration, as shown in fig. 3.15 (b). DMA concentrations were volume corrected. For every microgel, at least two calibration curves were recorded. A linear fit was applied to the averaged calibration curve to determine the unknown DMA concentration $c_{\text{DMA,unkn}}$ in the microgel. The DMA content was then calculated using the following equations:

$$c_{\text{DMA,UV-Vis}} = \frac{c_{\text{DMA,unkn}} M_{\text{W,gel}}}{c_{\text{gel}} M_{\text{W,DMA}}}, \tag{3.32}$$

where

$$M_{\text{W,gel}} = 0.93 \cdot M_{\text{W,NIPAM}} + 0.02 \cdot M_{\text{W,BIS}} + 0.05 \cdot M_{\text{W,DMA}}. \tag{3.33}$$

In addition, errors for the slope and the y-intercept of the linear fit were used to calculate the error of the DMA content. Results can be found in table 3.2.

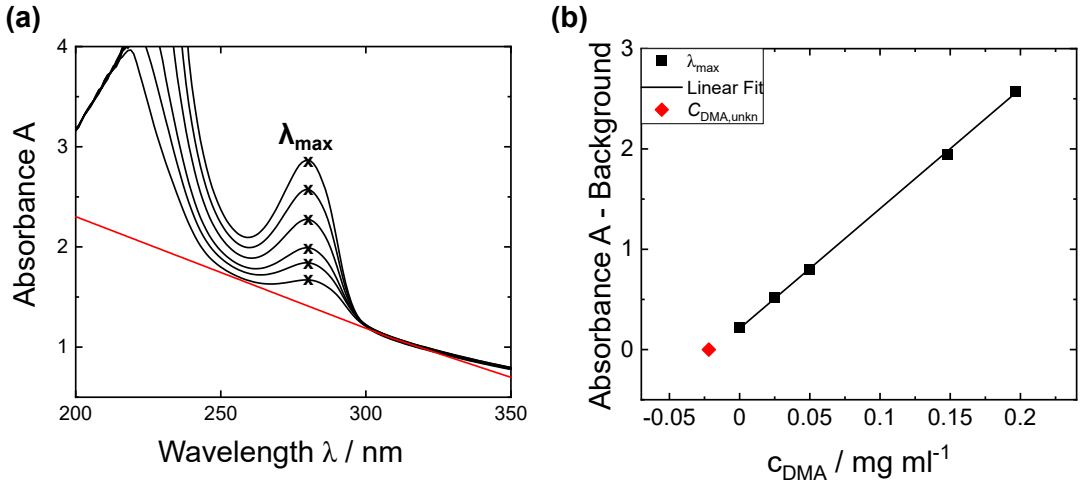

Figure 3.15: (a) Standard addition experiment of MG-$t_{10,270}$: The addition of DMA results in a rise of the absorbance at $\lambda_{max} = 282\,nm$, originating from the incorporated DMA. The red line represents the microgel background within the peak region. (b) corresponding calibration curve: The absorbance A at λ_{max} minus the microgel background is plotted as a function of the added DMA concentration. By a linear fit, the unknown DMA concentration $c_{DMA,unkn}$ in the microgel is determined.

3.9 Mass spectrometry (MS)

Theory and instrument

Mass spectrometry (MS) operates on the fundamental principle of generating ions from the sample to be measured using a suitable ionisation method. Subsequently, these ions are separated by their specific mass-to-charge ratio m/z. The resulting mass spectrum plots the abundance against the m/z ratio of the measured compound. For a more detailed description, see [173, 174].

The definition already implies the necessity for MS of having charged particles that can be ionised. Ions can be accelerated or decelerated within the instrument. Isotopes are distinctively separated in the spectrum due to their differences in mass, while neutral

particles cannot be measured directly by MS. Instead, their are represented by the distance $\Delta m/h$ between the resulting signals.

A mass spectrometer consists of mainly three components: (1) an ion source generating the ions, (2) a mass analyser separating the ions through the application of an electric and/or magnetic field and (3) a detector to measure the ions. During this thesis, electrospray ionisation (ESI) was used as the ion source and a quadrupole time-of-flight (quadrupole TOF) analyser was employed as a mass analyser. Additionally, a high-performance liquid chromatograph (HPLC) was utilised prior to the ion source. These components should be briefly discussed in the following.

A **high-performance liquid chromatograph (HPLC)** is installed before the ion source. A liquid chromatograph (LC) separates different components of a mixed solution. The mixture (mobile phase) travels through a column containing a material (stationary phase). Components are separated based on their different tendencies to interact with the stationary phase, resulting in different retention times t_R to travel through the column. For HPLC, a really small stationary phase is used, while high pressures sustain the flow of the mobile phase through the column.

During **electrospray ionisation (ESI)**, the sample solution, which contains ions, undergoes a transition into the gas phase. Therefore, the sample solution is transported through a capillary tube, where a voltage is applied to the tube walls. Charged droplets, emerging from the end of the tube, are produced. Afterwards, the solvent starts to evaporate, rising the surface charge density until the droplet size becomes sufficiently small to produce ions in a gaseous phase ("aerosol"). The ions can then be transferred into the mass analyser through an interface.

A **quadrupole time-of-flight (TOF) analyser** was employed as the mass analyser. During TOF, ions with a charge $q = ez$, where z represents the number of electrons with charge e, are separated based on their different travelling times t through a flight tube. Upon application of a voltage to accelerate the ions, they possess the energy $E_{el} = ezU_b$. Subsequently, ions are travelling through the tube with a kinetic energy E_{kin}, so it follows:

$$ezU_b = \frac{1}{2}mv^2. \tag{3.34}$$

This equation leads to:

$$v = \sqrt{\frac{2ezU_b}{m}}. \tag{3.35}$$

It implies that the ion velocity v, and consequently their travelling time $t = s/v$, depend on m/z - the fundamental basis of MS.

The TOF is coupled with a quadrupole analyser. A quadrupole analyser consists of four parallel rods, where a radio-frequency (RF) alternating voltage and a direct voltage (DC) are applied to each pair of oppositely lying rods. The ions are attracted toward the rods with charges opposite to their own. To prevent the ions from colliding with the rods, their polarity is periodically reversed in time. Ions then move with a stable trajectory through the mass analyser. At the end, only ions with a specific m/z ratio follow a stable trajectory, while ions of different ratio collide with the rods.

Measurement conditions

Time-samples, collected at different times during the synthesis process, were evaluated by high performance liquid chromatography electrospray ionisation mass spectrometry (HPLC-MS/ESI) on an Impact II mass spectrometer (Bruker Daltonik GmbH, Bremen, Germany) by the mass spectrometry core facility team of the Chemistry Department (TU Darmstadt). The instrument was provided by the German Research Foundation (DFG) through grant no INST 163/444-1 FUGG (QTOF MS).
During the microgel synthesis, time-samples were collected using 1 ml syringes, whose walls were previously wetted by the reaction stopper THQ. The time-samples were centrifuged in Amicon Ultra filters with a cut-off of 30 kDA at spinning speeds of 14500 rpm for 30 min to separate the unreacted monomers from oligo- and polymers that had already formed.
The solution containing the unreacted monomers (NIPAM, BIS and DMA) was then analysed using HPLC-MS/ESI. The decrease of the signal integral for each monomer corresponds to the decrease in its concentration over the course of the reaction, resulting in the monomer consumption c, as further elaborated in literature [16, 69]. To ease illustration, the relative monomer consumption cc_0^{-1} is plotted.
To describe the kinetics of the reaction, the reaction order can be determined. More details on the polymerisation kinetics in free radical precipitation polymerisation are given in chapter 2.1.1. For second-order reactions, the rate of reaction is proportional to the square of one of the monomers. The monomer consumption can then be described by a function of the form [175]:

$$c^{-1} = c_0^{-1} + kt. \tag{3.36}$$

Here, k represents the slope of the function and corresponds to the reaction rate. Error analysis of MS data was omitted due to numerous factors influencing the data, such

as concentration deviations, minor deviations in taking the time-samples, monomers retained in the centrifugation filters etc.

3.10 Scanning electron microscopy (SEM)

Theory

The principle of scanning electron microscopy (SEM) is creating images of a sample by scanning it by a focused electron beam in a defined pattern. For a more comprehensive understanding of this technique, refer to [176, 177].
In SEM, electrons are generated via an electron source, creating a focused electron beam. The electrons typically exhibit energies between $0.1 - 30\,\mathrm{keV}$ [176]. The electrons are accelerated, usually under high vacuum, and modified to reduce the beam diameter. Subsequently, the sample is systematically scanned in a raster pattern by the electron beam, yielding two types of electrons: (1) backscattered electrons and (2) secondary electrons. Backscattered electrons are those originating from the primary electron beam, which are scattered backwards when interacting with the sample. Conversely, secondary electrons are created by the electron beam: electrons from the beam transfer energy to the atom electrons of the sample, which are then emitted. These secondary electrons are then detected by one ore more detectors, and the resulting signals are employed to create the SEM image. SEM typically achieves resolutions ranging from $1 - 10\,\mathrm{nm}$ [177].

Measurement conditions

Colloidal probes were analysed using scanning electron microscopy (SEM) at the Electron Microscopy Center Darmstadt (EMC-DA) by Ulrike Kunz. Images were recorded with the Focused Ion-Beam Microscope JIB 4600F from JEOL Ltd. (Akishima, Japan), offering a resolution of 1.2 nm. These images served to confirm the low surface roughness of the colloidal probes and to ensure the absence of contaminations after their preparation.

4 Co-polymerisation kinetics of P(NIPAM-co-DMA) microgels

Similar content is published in "Copolymerization Kinetics of Dopamine Methacrylamide during PNIPAM Microgel Synthesis for Increased Adhesive Properties" Sandra Forg, Alexandra Karbacher, Zhishuang Ye, Xuhong Guo, and Regine von Klitzing, *Langmuir*, 2022, 38, 17, 5275-5285. [16] doi: https://doi.org/10.1021/acs.langmuir.1c02749.

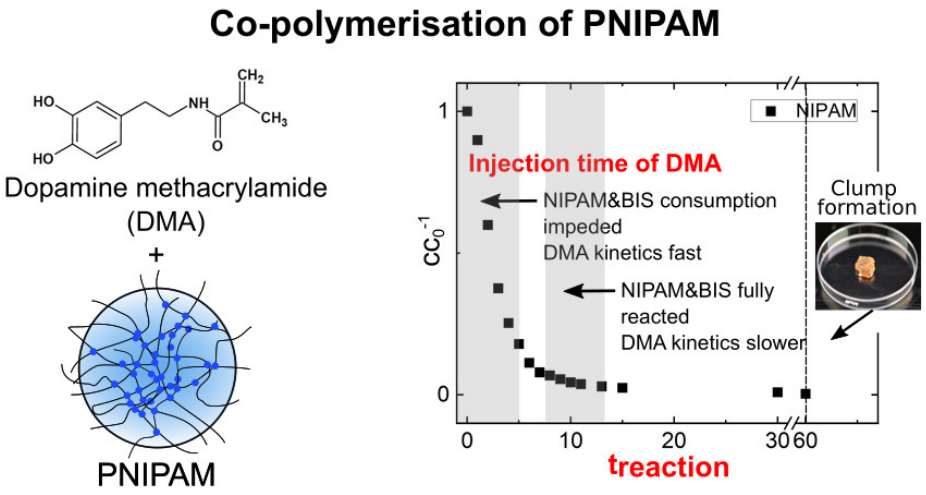

Abstract

Combining the stimuli-responsive properties of gels with the robust mechanical properties and exceptional adhesion capabilities inspired by mussels holds significant promise for a large field of applications. This chapter focuses on the co-polymerisation of poly(*N*-isopropylacrylamide) (PNIPAM) microgels with dopamine methacrylamide

(DMA). A detailed understanding of reaction kinetics is crucial to establish an optimised synthesis protocol. The present chapter addresses the influence of relevant synthesis parameters as the injection time of DMA during the microgel synthesis and the overall reaction time. The kinetics of the polymerisation are explored by analysing time-samples taken during the microgel synthesis by mass spectrometry (MS). This allows to determine the consumption of NIPAM, the cross-linker *N,N'*-methylene-bis(acrylamide) (BIS) and the DMA monomer. DMA exhibits a second-order reaction kinetic. The amount of DMA incorporated in the resultant microgel is successfully ascertained via a combination of UV-vis and NMR spectroscopy. Surprisingly, comparable DMA contents are incorporated for all microgel samples, whereas differences in their reaction kinetics are found. While an early injection of DMA impedes the PNIPAM polymerisation due to scavenging of radicals, it greatly enhances the DMA's reaction rate. Contrary, a delayed DMA injection results in a complete NIPAM and BIS consumption. An overall reaction time of 60 min ensures the DMA incorporation, with longer reaction times leading to the formation of larger gel clumps. The microgel syntheses are reproducible and insensitive to UV light. Microgels exclusively cross-linked by DMA exhibit similar reaction kinetics compared to their BIS cross-linked counterparts, but display changes in the microgels' morphology.

4.1 Introduction

Poly(*N*-isopropylacrylamide) (PNIPAM) microgels can be easily synthesised with a narrow size distribution [47] by free radical precipitation polymerisation [48] as reviewed in chapter 2.1. *N,N'*-methylene-bis-acrylamide (BIS) is typically employed as cross-linker in the microgel formation and is known to have a faster reaction kinetic than NIPAM. Consequently, BIS accumulates faster within the core of the microgel, leading to the characteristic core-shell structure [50, 51]. NIPAM can be also co-polymerised readily [52–55] with monomers holding specific properties, thereby enabling the creation of architectures tailored to precise requirements.
The combination of the stimuli-responsive PNIPAM with the adhesive capabilities and mechanical toughness found in marine organisms like mussels, holds immense potential for various applications. These include biomedicine [8], bioelectronics [125], adhesive coatings [57, 58] and self-healing materials [13, 29, 30]. Primarily responsible for the mussel adhesion is the catechol group found in dopamine-based amino acids

within the mussel's byssus [2], as detailed in chapter 2.2. Catechol chemistry is highly versatile; for example, they have the ability to cross-link structures [4–6] and enhance mechanical properties of materials [112, 178] owing to cohesive interactions. Additionally, they are known as radical scavengers [20], which implies the need to study the reaction kinetics of such compounds.

The catechol-based monomer dopamine methacrylamide (DMA) has been successfully employed as a mussel-inspired co-monomer for PNIPAM microgels [4, 13–15] as highlighted in chapter 2.2. For example, Xue *et al.* [4] synthesised P(NIPAM-co-DMA) microgels by using DMA as the sole cross-linker. The radical scavenging of catechols can impede or even stop gel growth. Therefore, the challenge lies in optimising the DMA incorporation without disturbing the microgel polymerisation. While the study [4] verified that the injection time of DMA has to be delayed, the comprehensive role of the DMA's injection time was not clarified. Until now, the kinetics of DMA co-polymerisation are unknown.
Hence, the present chapter compares different strategies of the co-polymerisation of PNIPAM microgels with DMA. Reaction kinetics are evaluated by collecting time-samples during the microgel synthesis. These time-samples are analysed with mass spectrometry (MS) to determine the monomer consumption of NIPAM, BIS and DMA separately. Through this examination, we systematically study the impact of key synthesis parameters, including the injection time of DMA t_{DMA} and the overall reaction time t_{reac} with regard to DMA's scavenging ability. The analysis aims to enable the precise control over the synthesis process and fully characterise the co-polymerisation. While the primary focus of this thesis is the development of P(NIPAM-co-DMA) microgels cross-linked with BIS, the study is complemented by comparing the results with microgels synthesised using DMA as the sole cross-linker. The incorporated amount of DMA is investigated with a combination of UV-vis and NMR spectroscopy. Dynamic light scattering (DLS) measurements are conducted to acquire insights into the temperature-responsive behaviour of the microgels, while atomic force microscopy (AFM) imaging is employed to investigate their size distribution. Electrophoretic mobility measurements of the microgels are performed to gain information about their surface charge.

4.2 Results

Microgels are denoted as "MG-$t_{t_{DMA},t_{reac}}$" in the following, where t_{DMA} represents the respective dopamine methacrylamide (DMA) injection time after polymerisation start and t_{reac} the overall reaction time. In the case that no DMA was injected, t_{DMA} is replaced by "ref". In cases where microgels were synthesised without the additional cross-linker *N,N'*-methylene-bis-acrylamide (BIS), they are labelled with the additional suffix "-noBIS". "t" denotes variations in the time parameters of the microgel synthesis. It allows a clear differentiation between microgels of chapter 4 and chapter 5 and 6, where the composition was altered.

4.2.1 Reaction kinetics

Reference microgel without DMA (MG-$t_{ref,270}$)

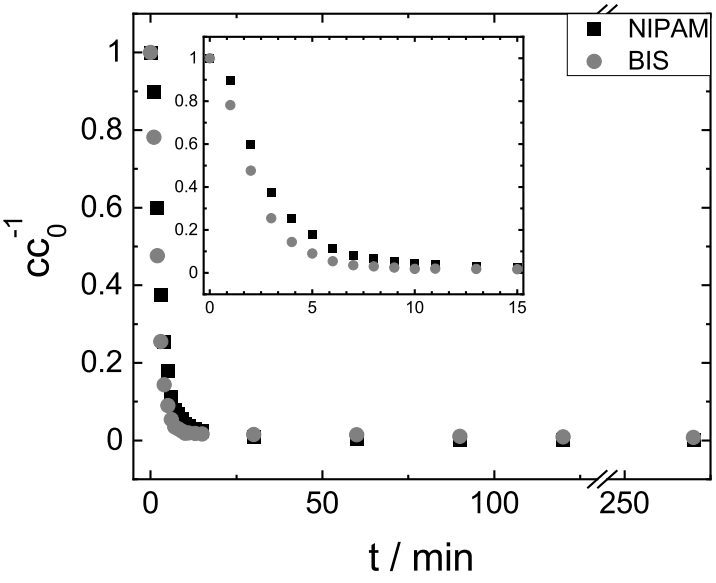

Figure 4.1: The relative monomer consumption cc_0^{-1} of the reference microgel MG-$t_{ref,270}$ as a function of the reaction time t. Results were obtained by MS for monomer NIPAM and cross-linker BIS separately. The inset highlights the decay of cc_0^{-1} at short times.

A reference pure poly(*N*-isopropylacrylamide) (PNIPAM) microgel MG-$t_{ref,270}$ was synthesised without DMA according to table 3.2. Fig. 4.1 displays the relative consumption cc_0^{-1} of the monomer *N*-isopropylacrylamide (NIPAM) and the cross-linker BIS as a function of the reaction time t. Results were obtained by mass spectrometry (MS) as specified in chapter 3.9.
The relative monomer consumption cc_0^{-1} declines sharply in the initial $4-5$ min of the reaction. 93.2 % of the monomer NIPAM and 97 % of the cross-linker BIS are consumed within the first 8 min of polymerisation, consistent with previous studies [179, 180]. The consumption reaches a plateau at approximately $10-15$ min, implying a slowdown of the reaction. After 60 min, 99.7 % of NIPAM and 98.5 % of BIS are consumed, only changing marginally until the end of the reaction. Overall, BIS reacts faster than NIPAM.
Furthermore, the hydrodynamic radii R_H and the electrophoretic mobility μ_e of MG-$t_{ref,270}$ at 20°C and 50°C are provided in table A2 in the appendix. The measurements were conducted using dynamic light scattering (DLS) as described in chapter 3.4, and by electrophoretic dynamic light scattering (EDLS) as detailed in chapter 3.5. The hydrodynamic radius R_H decreases from 20°C to 50°C, due to the temperature-dependent collapse of the microgels. μ_e is positive, corresponding to a positive surface charge, which originates from the positively charged initiator 2,2'-azobis-2-methyl-propanimidamide dihydrochloride (AAPH). An atomic force microscopy (AFM) image of MG-$t_{ref,270}$ (for details see chapter 3.6.1) confirms the monomodal size distribution of the microgel. The image can be found in fig. 4.2 (a).

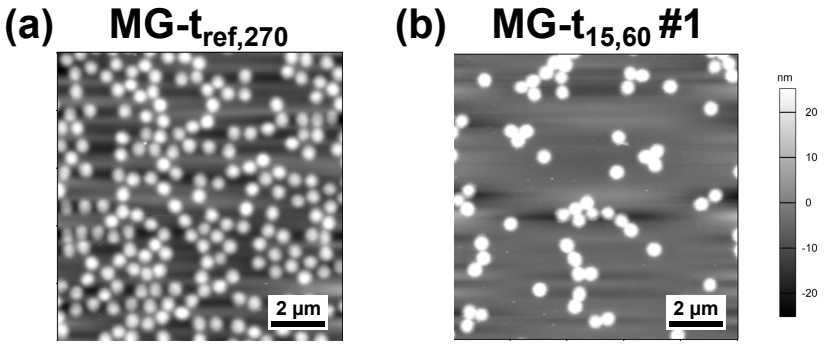

Figure 4.2: Exemplary AFM images of MG-$t_{ref,270}$ and MG-$t_{15,60}$ #1, conducted at ambient conditions, confirming a monomodal size distribution.

Microgels with DMA

All microgels were synthesised with an identical composition, according to table 3.2: 93 mol% NIPAM, 2 mol% BIS and 5 mol% DMA respectively. An exemplary AFM image comparing MG-$t_{15,60}$ #1 to the reference microgel MG-$t_{ref,270}$ under ambient condition (as described in chapter 3.6.1) is displayed in fig. 4.2. The AFM image confirms a monomodal size distribution of the P(NIPAM-co-DMA) microgel, consistent with findings for the pure PNIPAM microgel. Hydrodynamic radii R_H in both swollen and shrunken state, along with the electrophoretic mobility μ_e, are provided in table A2 in the appendix. The microgels exhibit a temperature-dependent collapse, similar to the reference pure PNIPAM microgel, when the temperature is increased from 20°C to 50°C. While the hydrodynamic radius $R_H(20°C)$ of the swollen microgels ranges from 310 to 500 nm, the hydrodynamic radius $R_H(50°C)$ of the collapsed microgels at 50°C varies between 110 and 175 nm. At both temperatures, μ_e is positive, indicating a positive surface charge for all microgels. Only MG-$t_{0,60}$ holds a slight negative surface charge at 20°C. However, the value falls within the device's range of error variations. In-depth investigations of the temperature-dependent swelling behaviour and surface charge of P(NIPAM-co-DMA) microgels are presented in chapter 5 and are therefore not further discussed in this chapter.

Our primary focus lies on the development of PNIPAM microgel particles cross-linked with BIS and co-polymerised with DMA. However, DMA is also established for its cross-linking ability [4, 6] as stated in the beginning of the chapter - a topic that will be further explored in the subsequent chapter 5. Thus, PNIPAM microgel particles can be synthesised by exclusively cross-linking with DMA. In cases where DMA is introduced later during the reaction, the microgel formation process until its injection primarily relies on the self-cross-linking properties of NIPAM [71–73], briefly discussed in chapter 2.1. To complete our study, P(NIPAM-co-DMA) microgel particles were synthesised solely cross-linked by DMA with the same composition (93 mol% NIPAM and 5 mol% DMA) according to table 3.2. The DMA injection times t_{DMA} were varied. Their temperature-dependent swelling curves, determined through dynamic light scattering (DLS) as described in chapter 3.4, are presented in fig. A20 (appendix). A more detailed discussion of their swelling behaviour is also provided in the appendix. All microgels exhibit the characteristic temperature-responsive swelling-deswelling behaviour: the microgels collapse upon heating.

Atomic force microscopy (AFM) images of the microgels, conducted at ambient conditions as detailed in chapter 3.6.1, are displayed in fig. 4.3. The microgel MG-$t_{0,60}$-noBIS with a DMA injection time of $t_{\mathrm{DMA}} = 0\,\mathrm{min}$, exhibits a morphology akin to that of the microgels cross-linked additionally with BIS. The microgels, where DMA was added at later stages during the reaction, remarkably display a raspberry-like structure.

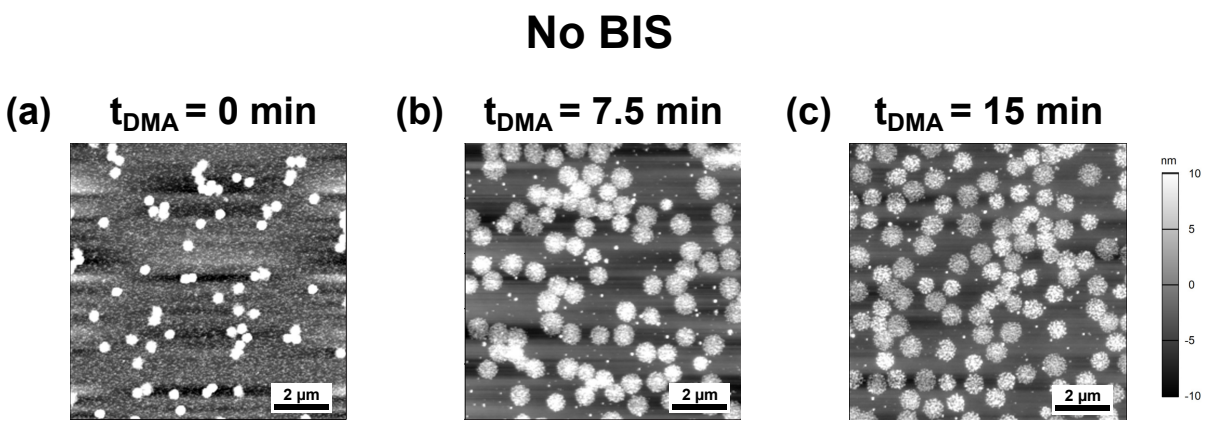

Figure 4.3: AFM scans, taken in ambient conditions, of microgels synthesised without the additional cross-linker BIS with different DMA injection times (a) $t_{\mathrm{DMA}} = 0\,\mathrm{min}$, (b) $t_{\mathrm{DMA}} = 7.5\,\mathrm{min}$ and (c) $t_{\mathrm{DMA}} = 15\,\mathrm{min}$. Microgels in (b) and (c) display a raspberry-like structure.

Reaction time t_{reac} As demonstrated by MG-$t_{\mathrm{ref},270}$, the reaction kinetics of NIPAM and BIS change from fast to slow after approximately $4-5\,\mathrm{min}$, significantly slowing down after $10-15\,\mathrm{min}$. In order to achieve almost complete NIPAM and BIS consumption, while avoiding the scavenging effect of DMA, the DMA injection was therefore delayed to $t_{\mathrm{DMA}} = 10\,\mathrm{min}$. First, a reaction time of $t_{\mathrm{reac}} = 270\,\mathrm{min}$ was selected based on literature [4] to ensure the DMA incorporation. Fig. 4.4 (a) displays the relative monomer consumption cc_0^{-1} of this microgel MG-$t_{10,270}$ as a function of the reaction time t, calculated from MS results (see chapter 3.9). The reaction of the microgel resulted in the formation of a large gel clump, as shown in the inset of fig. 4.4 (a).

The NIPAM and BIS consumption reaches nearly a plateau at around 10 min, similar to MG-$t_{\mathrm{ref},270}$. By that point, NIPAM and BIS have almost entirely reacted ($> 95\,\%$).
Comparing the reaction of DMA to those of NIPAM and BIS, notable differences in their kinetics can be observed. The reaction of DMA is significantly slower than that

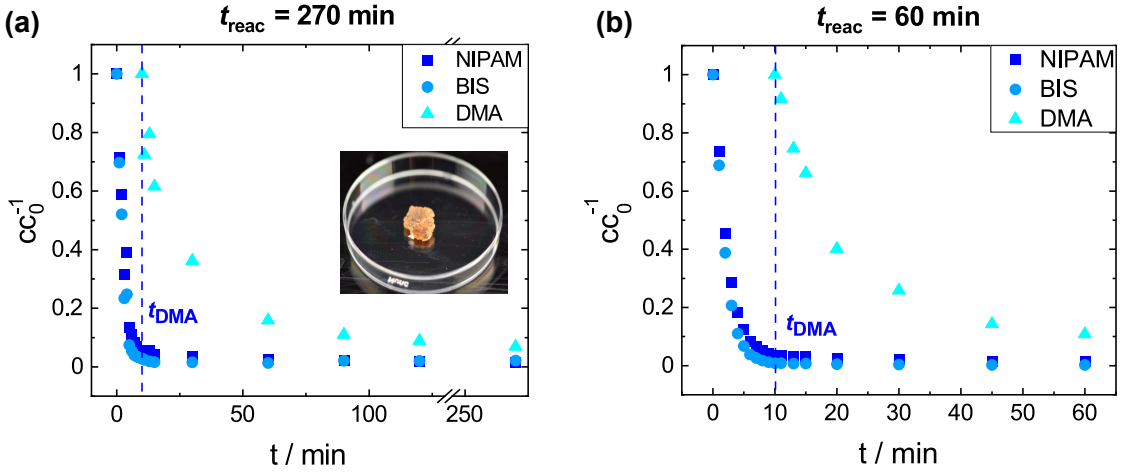

Figure 4.4: The relative monomer consumption cc_0^{-1} of NIPAM, BIS and DMA as a function of the reaction time t for two different overall reaction times: (a) $t_{reac} = 270\,min$ and (b) $t_{reac} = 60\,min$, with DMA injected at $t_{DMA} = 10\,min$ for both microgels. The inset of (a) shows the formation of a gel clump at the end of the reaction.

of NIPAM and BIS. At 30 min, 98.4 % of BIS and 96.4 % of NIPAM are consumed, while only 63.8 % of DMA is consumed. While nearly 97.4 % and 98.6 % of monomer NIPAM and cross-linker BIS react within the first 60 min, only 85 % of DMA reacts within this time. Over the whole synthesis, DMA reaches a conversion of 93.1 %.

Due to the gel clump formation, the overall reaction time t_{reac} was reduced to $t_{reac} = 60\,min$, while the injection time of DMA was kept constant at $t_{DMA} = 10\,min$. Results are shown in fig. 4.4 (b) for MG-$t_{10,60}$. No clumps formed during this microgel polymerisation. The reaction of NIPAM and BIS is comparable to the former microgel MG-$t_{10,270}$ with a longer reaction time of $t_{reac} = 270\,min$. 74.2 % of DMA is consumed in the first 30 min and 89.2 % is consumed until the end of the reaction. This level of conversion is still highly favourable and similar to that achieved with a longer reaction time. Shorter reaction times should not be chosen to achieve at least a 90 % conversion of DMA.

Both freeze-dried microgels exhibit a light orange to pinkish colour (see fig. A4, appendix).

Injection time of DMA t_{DMA} After fixing the overall reaction time to $t_{reac} = 60\,min$ to prevent clump formation, the influence of the injection time t_{DMA} was studied while considering the reaction kinetics of MG-$t_{ref,270}$. (Note: NIPAM and BIS react rapidly

until $4 - 5$ min, followed by a reduction in the reaction speed, significantly slowing down after 10 min). No gel clump formation was observed for any of the microgels. Fig. 4.5 displays the relative monomer consumption cc_0^{-1} of the different microgels for varying injection times of DMA t_{DMA}, calculated from MS results for (a) NIPAM, (b) BIS and (c) DMA. In the case of DMA, the results are plotted over the effective reaction time $t - t_{\mathrm{DMA}}$. (d) illustrates the inverse monomer consumption c^{-1} of DMA.

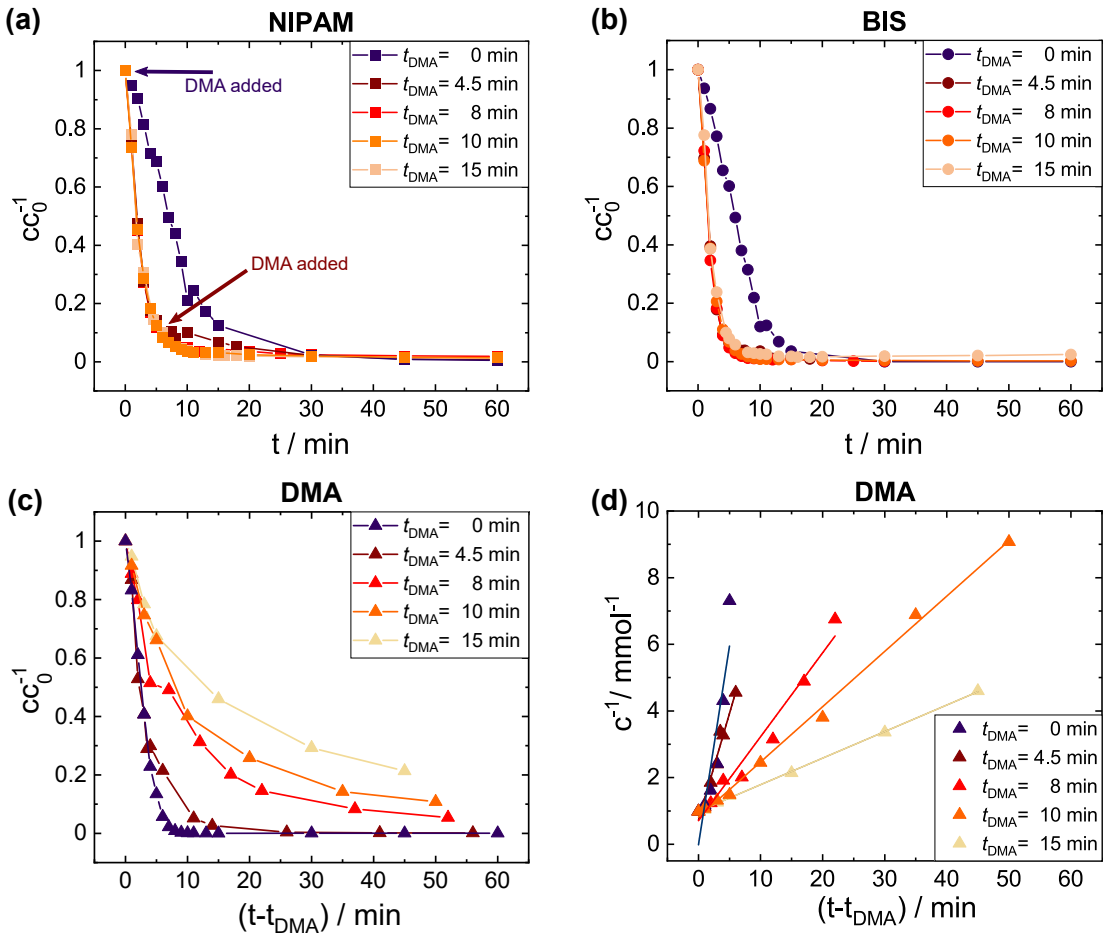

Figure 4.5: The relative monomer consumption cc_0^{-1} of NIPAM (a) and BIS (b) as function of the reaction time t. (c) The relative monomer consumption cc_0^{-1} of DMA as function of the effective reaction time $t - t_{\mathrm{DMA}}$. (d) the absolute inverse consumption c^{-1} of DMA. Microgels were synthesised with different DMA injection times t_{DMA}, but a constant reaction time of $t_{\mathrm{reac}} = 60$ min.

First, the consumption of NIPAM and BIS is examined: For the injection times $t_{\mathrm{DMA}} = 8 - 15$ min, the change in cc_0^{-1}(NIPAM) is similar for all microgels. The same holds

true for the relative consumption cc_0^{-1}(BIS) of the cross-linker BIS. In contrast, for an injection time $t_{\mathrm{DMA}} = 0\,\mathrm{min}$ (MG-$t_{0,60}$), the consumptions of NIPAM and BIS are notably impeded. For $t_{\mathrm{DMA}} = 4.5\,\mathrm{min}$ (MG-$t_{4.5,60}$), the relative consumption of NIPAM is also inhibited. In all cases, the consumptions of NIPAM and BIS approach complete conversion towards the end of the reaction.
Regarding DMA, the relative monomer consumption cc_0^{-1} exhibits different reaction rates for different injection times t_{DMA}. For an injection time of $t_{\mathrm{DMA}} = 0\,\mathrm{min}$ (MG-$t_{0,60}$), 58.6% of DMA reacts within the first 3 min and 99.1% within the first 8 min. In contrast, for an injection time of $t_{\mathrm{DMA}} = 15\,\mathrm{min}$ (MG-$t_{15,60}$), 21.6% of DMA reacts within the first 3 min and around 26% within the first 8 min. Thus, the reaction kinetics of DMA are significantly faster for earlier injection times.
In fig. 4.5 (d) the absolute inverse consumption c^{-1} of DMA is plotted against the effective reaction time $t - t_{\mathrm{DMA}}$ of DMA. A linear fit according to eq. 3.36 describes the data well up to around 85 % conversion of DMA, corresponding to a second-order reaction. All freeze-dried microgels show a colour ranging from light orange to pink (see fig. A4, appendix).

Reproducibility and influence of UV light To test the reproducibility of the reaction kinetics, three microgels were synthesised with an injection time of $t_{\mathrm{DMA}} = 15\,\mathrm{min}$ and an overall reaction time $t_{\mathrm{reac}} = 60\,\mathrm{min}$. Fig. 4.6 (a) displays the relative monomer consumption cc_0^{-1} as a function of the effective reaction time $t - t_{\mathrm{DMA}}$ of DMA alone, calculated from MS results. The consumptions of NIPAM and BIS are similar to those of MG-$t_{\mathrm{ref},270}$ and the microgels with DMA injection times of $t_{\mathrm{DMA}} > 8\,\mathrm{min}$. Thus, they are not included in fig. 4.6 (a) to ease illustration. They are given in fig. A5, appendix.
While the microgel synthesis #1 (MG-$t_{15,60}$ #1) was carried out as before, the microgel syntheses #2 and #3 (MG-$t_{15,60}$ #2 and MG-$t_{15,60}$ #3) were conducted identically, but with the exclusion of UV light by covering the reactor and fume hood with aluminium foil.
UV light plays an important role during dopamine reactions and its derivatives, as it can accelerate or even enable dopamine polymerisations in the presence of oxidation agents [133]. Moreover, it is known to break the double bond of the initiator 2,2'-azobis-2-methyl-propanimidamide dihydrochloride (AAPH), which might change the reaction behaviour of the polymerisation. Additionally, auto-oxidation of catechol groups in the presence of oxidation agents [181] could influence the reaction kinetics of DMA.

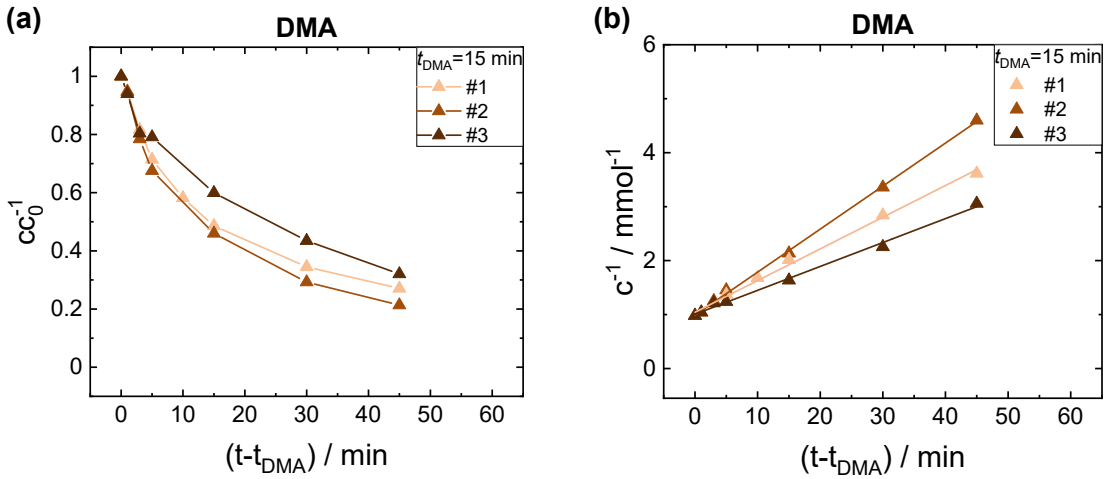

Figure 4.6: (a) The relative monomer consumption cc_0^{-1} of DMA as function of the effective reaction time $t - t_{\mathrm{DMA}}$. (b) the absolute inverse consumption c^{-1} of DMA. Microgels were synthesised with identical reaction parameters ($t_{\mathrm{reac}} = 60\,\mathrm{min}$, $t_{\mathrm{DMA}} = 15\,\mathrm{min}$) to test the reproducibility of the reaction. #2 and #3 were synthesised with UV light protection.

Contrary to the synthesis #1 (MG-$t_{15,60}$ #1), the reaction mixture of #2 and #3 (MG-$t_{15,60}$ #2 and MG-$t_{15,60}$ #3), where UV light was excluded, exhibited no colour change upon the injection of DMA. However, freeze-dried microgels show a light orange to pinkish colour again (see fig. A4, appendix).
Regarding the reaction rate of DMA, synthesis #2 exhibits the fastest DMA reaction, followed by #1, and then #3, as depicted in fig. 4.6 b. Taking into account the uncertainties in the MS results, as described in chapter 3.9, the reaction appears to be unaffected by UV light. If DMA would auto-oxidate, its reaction kinetics should be linked to the age of its batch. The age of DMA follows the order #1 $>$ #2 $=$ #3. Hence, it is apparent that auto-oxidation does not affect the reaction kinetics of DMA during the microgel syntheses.
Fig. 4.6 (b) depicts the absolute inverse consumption c^{-1} of DMA against its effective reaction time $t - t_{\mathrm{DMA}}$ for all microgels. As before, a linear fit was applied corresponding to a second-order reaction using equation 3.36, and it describes the data well.

Influence of cross-linker BIS Three microgel were synthesised with the same composition (93 mol% NIPAM and 5 mol% DMA), but with varying DMA injection times t_{DMA}. The choice of t_{DMA} was made to be comparable to their BIS-cross-linked

counterparts MG-$t_{0,60}$, MG-$t_{8,60}$ and MG-$t_{15,60}$ #1. The microgels were only cross-linked by DMA to assess the impact of the absence of the cross-linker BIS.

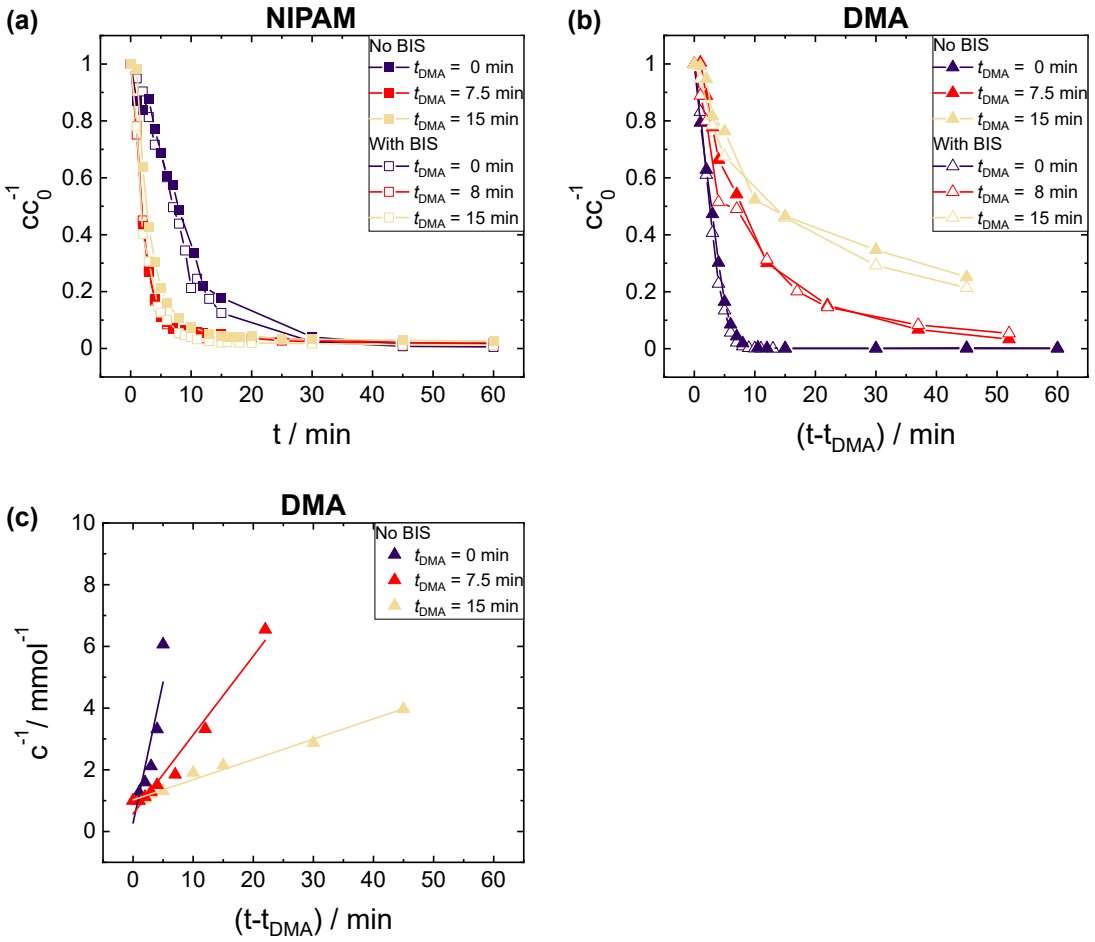

Figure 4.7: Relative monomer consumptions cc_0^{-1} of reactants NIPAM (a) as a function of the reaction time t, and DMA (b) as function of the effective reaction time $t - t_{\mathrm{DMA}}$, presented for microgels synthesised without the cross-linker BIS. Results are displayed alongside their BIS-cross-linked counterparts. (c) shows the inverse monomer consumption c^{-1} of DMA as function of the effective reaction time $t - t_{\mathrm{DMA}}$. A linear fit can be applied, which confirms that DMA possesses a second-order reaction kinetics.

Fig. 4.7 displays the relative consumption cc_0^{-1} of NIPAM in (a) as a function of the reaction time t and of DMA in (b) as function of the effective reaction time $t - t_{\mathrm{DMA}}$. The reaction kinetics of their BIS-cross-linked counterparts with similar DMA injection times, which were discussed previously in this chapter, are also provided in (a)

and (b) to facilitate comparative analysis. Fig. 4.7 (c) displays the inverse monomer consumption c^{-1} of DMA as function of the effective reaction time $t - t_{\mathrm{DMA}}$. Results were obtained by mass spectrometry (MS) as specified in chapter 3.9.

The early introduction of DMA during the reaction impedes the NIPAM conversion (fig. 4.7 (a)). Moreover, DMA reacts faster when injected earlier (fig. 4.7 (b)). Additionally, the inverse absolute consumption c^{-1} of DMA was successfully fitted with a linear function for a DMA consumption up to 85 % (fig. 4.7 (c)). This corresponds to a second-order reaction kinetics. Remarkably, the results are nearly identical to those obtained from microgels synthesised with the additional cross-linker BIS (2 mol%) and equivalent injection times (MG-$t_{0,60}$, MG-$t_{8,60}$ and MG-$t_{15,60}$ #1).

4.2.2 Incorporated DMA

UV-vis

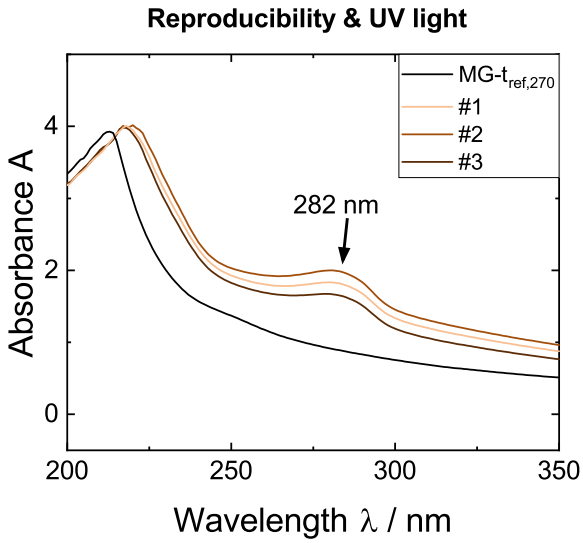

Figure 4.8: Exemplary UV-vis spectra for P(NIPAM-co-DMA) microgels synthesised with an injection time of $t_{\mathrm{DMA}} = 15\,\mathrm{min}$ and an overall reaction time $t_{\mathrm{reac}} = 60\,\mathrm{min}$ (MG-$t_{15,60}$ #1, MG-$t_{15,60}$ #2 and MG-$t_{15,60}$ #3) in comparison to the reference PNIPAM microgel MG-$t_{\mathrm{ref},270}$.

The successful incorporation of DMA is confirmed by UV-vis spectroscopy as explained in chapter 3.8. The exemplary UV-vis spectra in fig. 4.8 reveal an additional peak at $\lambda_{max} = 282\,nm$ for the P(NIPAM-co-DMA) microgels MG-$t_{15,60}$ #1, MG-$t_{15,60}$ #2 and MG-$t_{15,60}$ #3 in contrast to the reference microgel MG-$t_{ref,270}$. This peak is attributed to the unoxidised catechol group of DMA [172]. The pure DMA spectrum is given in fig. A6 (appendix). Spectra of all remaining P(NIPAM-co-DMA) microgels are provided in fig. A7 (appendix), and they exhibit the same distinctive peak.

UV-Vis standard addition

The amount of incorporated DMA $c_{DMA,incorporated}$ was ascertained for all microgels following the methodology outlined in chapter 3.8. The corresponding calibration curves are given in fig. A8, fig. A9, fig. A10 and fig. A11 (appendix). The results are listed in table 4.1.
Remarkably, $c_{DMA,incorporated}$ is similar for all of the microgels, suggesting that the DMA content in the microgel structure is independent of the injection time of DMA t_{DMA} and the overall reaction time t_{reac}. The DMA amount varies between 2.0 and 4.4 mol%. The microgel synthesised with a DMA injection time of $t_{DMA} = 4.5\,min$ (MG-$t_{4.5,60}$), displays the highest levels of incorporated DMA (around 4.4 mol%). The microgels synthesised with nearly identical reaction parameters (MG-$t_{15,60}$ #1, MG-$t_{15,60}$ #2 and MG-$t_{15,60}$ #3; #2 and #3 were synthesised with UV light protection), yield comparable results. This further indicates that the absence of UV light has no influence on the results and underscores the reproducibility of the synthesis process. Moreover, microgels synthesised in the absence of the cross-linker BIS, depending solely on the cross-linking mechanism of DMA, exhibit comparable amounts of incorporated DMA when compared to their BIS cross-linked counterparts with comparable DMA injection times.

NMR

The amount of incorporated DMA $c_{DMA,incorporated}$ in all P(NIPAM-co-DMA) microgels was additionally determined by nuclear magnetic resonance (NMR) spectroscopy as specified in chapter 3.7. The results are summarised in table 4.1. The corresponding NMR spectra are available in the appendix (fig. A12, fig. A13, fig. A14, fig. A15, fig. A16, fig. A17, fig. A18 and fig. A19).

Table 4.1: Incorporated amount of DMA $c_{\mathrm{DMA,incorporated}}$ in P(NIPAM-co-DMA) microgels determined by UV-vis standard addition and NMR spectroscopy.

Microgel	Incorporated amount of DMA $c_{\mathrm{DMA,incorporated}}$	
	$c_{\mathrm{DMA,UV\text{-}vis}}$ / mol%	$c_{\mathrm{DMA,NMR}}$ / mol%
Influence of overall reaction time t_{reac}		
MG-$t_{10,270}$	2.4 ± 0.1	0.9
MG-$t_{10,60}$	2.7 ± 0.1	3.5
Influence of DMA injection time t_{DMA}		
MG-$t_{0,60}$	2.8 ± 0.2	4.1
MG-$t_{4.5,60}$	4.4 ± 0.4	0.9
MG-$t_{8,60}$	2.0 ± 0.0	0.9
MG-$t_{10,60}$	2.7 ± 0.1	3.5
MG-$t_{15,60}$ #1	2.2 ± 0.4	1.7
Reproducibility and influence of UV light		
MG-$t_{15,60}$ #1	2.2 ± 0.4	1.7
MG-$t_{15,60}$ #2	2.9 ± 0.0	2.5
MG-$t_{15,60}$ #3	2.1 ± 0.0	1.1
Influence of cross-linker BIS		
MG-$t_{0,60}$-noBIS	3.9 ± 0	1.8
MG-$t_{7.5,60}$-noBIS	3.4 ± 0	4.4
MG-$t_{15,60}$-noBIS	2.5 ± 0	2.9

The DMA content varies from 0.9 to 4.4 mol%, illustrating a broader variance as obtained through UV-vis standard addition. The microgel with an injection time of DMA $t_{\mathrm{DMA}} = 7.5$ min only cross-linked by DMA (MG-$t_{7.5,60}$-noBIS) contains the highest amount of DMA with 4.4 mol%. For the three microgels synthesised to test the reproducibility of the reaction (MG-$t_{15,60}$ #1, MG-$t_{15,60}$ #2 and MG-$t_{15,60}$ #3), the NMR results are similar. Generally, NMR results may exhibit larger uncertainties due to the signal overlap between the catechol groups of DMA and the NH groups (see

chapter 3.7). Since we used the deconvolution tool of the analysis software, the exact error value is challenging to quantify.

Generally, NMR and UV-vis results are akin to each other for most microgels, possessing a difference of approximately 1 mol %. Nonetheless, larger discrepancies are observed in the case of the microgel with a DMA injection time of $t_{\mathrm{DMA}} = 4.5\,\mathrm{min}$ (MG-$t_{4.5,60}$).

4.3 Discussion

Poly(*N*-isopropylacrylamide) (PNIPAM) microgels were successfully co-polymerised with the catechol-based monomer dopamine methacrylamide (DMA), using the cross-linker *N,N'*-methylene-bis(acrylamide) (BIS). Additionally, microgels were successfully synthesised without BIS using only DMA for cross-linking. Pure PNIPAM and P(NIPAM-co-DMA) microgels exhibit a temperature-dependent collapse and a monomodal size distribution, confirming the successful synthesis via free radical precipitation polymerisation.

Reaction kinetics

The reference pure PNIPAM microgel MG-$t_{\mathrm{ref},270}$ supports existing literature findings: BIS reacts faster than the monomer NIPAM as explained in chapter 2.1. Consequently, BIS tends to accumulate in the microgel's core leading to a core-shell structure of the microgel with a denser core [50].
The consumption of NIPAM and BIS exhibits an abrupt decrease until about $4 - 5\,\mathrm{min}$, which then slows down at around $10 - 15\,\mathrm{min}$. After 30 min, both monomer NIPAM and cross-linker BIS reach a consumption of around 99%. Three for us relevant reaction steps occur during precipitation polymerisation, as reviewed in chapter 2.1.1: (1) initiation, (2) propagation and (3) termination [182]. In the initiation step, the amount of free radicals increases. During the propagation step, the amount of free radicals stays constant. Here, initiation and termination of radicals are in an equilibrium-state, considering the half-life time of the initiator. Monomers are consumed rapidly during this phase. Precursor particles are formed at the beginning of the synthesis [68, 81], which aggregate or grow by reacting with further monomers or oligomers, until

stable "primary particles" are obtained. Subsequently, the number of particles remains constant, but the particles grow in size. In the final termination step, the amount of free radicals diminishes due to termination processes, either by recombination or disproportionation of radicals. This decelerates the monomer consumptions [183]. That aligns with the ascertained consumption of NIPAM and BIS. The initiation step cannot be examined due to its fast reaction kinetics. Nevertheless, the decrease until about $4-5\,\mathrm{min}$ can be clearly linked to the propagation step of the reaction. The deceleration in the NIPAM and BIS reactions between $10-15\,\mathrm{min}$ is attributed to their significant consumption at this stage of the reaction. AAPH possesses a half-life of 175 h at 37°C [184] and approximately 30 min at 80°C [185]. Therefore, the concentration of free radicals remains constant until at least 30 min into the reaction. After 30 min, the amount of free radicals might begin to decline; However, this cannot be confirmed with the available MS data, as NIPAM and BIS monomers were already completely consumed.

While an overall reaction time of $t_{\mathrm{reac}} = 270\,\mathrm{min}$ proves suitable for the pure PNIPAM reference microgel MG-$t_{\mathrm{ref,270}}$, the same reaction time leads to the formation of gel clumps in the case of the P(NIPAM-co-DMA) microgel MG-$t_{10,270}$ (see fig. 4.4). As a consequence, the reaction time was shortened to $t_{\mathrm{reac}} = 60\,\mathrm{min}$ (MG-$t_{10,60}$), which effectively prevented gel clump formation not only in this particular synthesis but also in all subsequent microgel syntheses. Furthermore, even when the DMA injection is delayed to $t_{\mathrm{DMA}} = 10\,\mathrm{min}$, a reaction time of $t_{\mathrm{reac}} = 60\,\mathrm{min}$ still results in the consumption of about 90 % of DMA until the end of the reaction. Further shortening of the reaction time is not recommended (or needed) to ensure the DMA incorporation.

The injection time of DMA t_{DMA} significantly affects the NIPAM and BIS reaction kinetics, due to DMA's scavenging ability [20]. For microgels with early DMA injection times of $t_{\mathrm{DMA}} \leq 4.5$,min (MG-$t_{0,60}$ and MG-$t_{4.5,60}$), the NIPAM monomer and BIS cross-linker consumption is largely impeded. Contrary, the NIPAM and BIS consumption remain unaffected when DMA is injected at later times of $t_{\mathrm{DMA}} \geq 8\,\mathrm{min}$. As observed in the case of MG-$t_{\mathrm{ref,270}}$ and confirmed for the P(NIPAM-co-DMA) microgels, NIPAM and BIS are almost entirely consumed by $t_{\mathrm{DMA}} = 10-15\,\mathrm{min}$.
The reaction of DMA is remarkably faster for microgels with earlier injection times. Therefore, the DMA reaction speed is significantly influenced by its injection time t_{DMA}, as related to its scavenging ability and the incomplete conversion of NIPAM

and BIS.
While the rapid reaction of DMA when injected early is advantageous for a high conversion, it must be balanced against the drawback of inhibited PNIPAM polymerisation. For an injection time of DMA greater than 10 min, the PNIPAM polymerisation can be ensured. This aligns with our requirement that DMA is only needed in the outer shell of the microgel particles to obtain adhesive properties. Introducing DMA at a later state of the reaction, when only particle growth but no nucleation occurs, is therefore a reasonable strategy in our case. The DMA injection time was fixed to $t_{\mathrm{DMA}} = 15\,\mathrm{min}$.
The inverse absolute consumption c^{-1} of DMA was successfully fitted with a linear function for a DMA consumption up to 85 %, suggesting a second-order reaction behaviour.

The consumptions of NIPAM, BIS and DMA are comparable for the three microgels synthesised with identical reaction parameters ($t_{\mathrm{DMA}} = 15\,\mathrm{min}$ and $t_{\mathrm{reac}} = 60\,\mathrm{min}$; see fig. 4.6), confirming the reproducibility of the polymerisation kinetics. DMA follows a second-order reaction kinetics. The DMA reaction shows to be insensitive to UV light. In comparison to the microgel without UV protection, but identical reaction parameters, the reaction mixture of the microgels with UV exclusion showed no colour change upon the injection of DMA - a direct consequence of the absence of UV light [132].
Additionally, auto-oxidation of DMA does not influence the reaction kinetics: Even when DMA was exposed to oxygen for preparation purposes, the DMA reaction speed does not decrease with increasing DMA age.

The reaction kinetics of microgel synthesised without the additional cross-linker BIS, exclusively relying on DMA for cross-linking, are nearly identical to those of their BIS-cross-linked counterparts with similar injection times ($t_{\mathrm{DMA}} = 0$, 7.5 & 15 min, $t_{\mathrm{reac}} = 60\,\mathrm{min}$). As discussed in chapter 2.1.1, the primary determinants of reaction kinetics are the concentrations of radicals and unreacted monomers during the synthesis. BIS does not contribute significantly to the monomer concentration, with only 0.4 mmol used in a total of 20 mmol of reactants; therefore, its impact appears to be negligible. This explains why the results are so similar.

Incorporation of DMA

The incorporation of DMA was confirmed for all P(NIPAM-co-DMA) microgels through UV-vis and nuclear magnetic resonance (NMR) spectroscopy. The presence of an additional peak in the UV-vis spectrum at $\lambda_{max} = 282\,nm$ (see fig. 4.8) confirms not only the successful DMA incorporation, but also provides insights into its oxidation state. Covalently coupled catechols would result in a maximal absorbance at $\lambda_{max} = 274\,nm$, while catechols in the oxidised quinone state exhibit a maximum at λ_{max} around 400 nm [172]. The observed maximum at $\lambda_{max} = 282\,nm$ implies the presence of unoxidised catechol groups of DMA, known to greatly enhance the adhesion ability of such systems [186, 187].
During the microgel syntheses, the transition from a white to orange-pink colour upon the injection of DMA is also directly linked to the oxidation state of the catechol group: pink corresponds to the radical, yellow to a quinone and orange to a semiquinone formation [132]. The colouration remains after freeze-drying, additionally confirming the incorporation of DMA.

The amount of incorporated DMA $c_{DMA,incorporated}$, as quantified by UV-vis and NMR spectra, is unexpectedly similar for all of the microgels (see table 4.1). It is found to be unaffected by UV light exposure and the presence of an additional cross-linker like BIS. For microgels with identical injection times of DMA of $t_{DMA} = 10\,min$ but different reaction durations ($t_{reac} = 60\,min$ for MG-$t_{10,6}$ and $t_{reac} = 270\,min$ for MG-$t_{10,270}$), a higher DMA incorporation would have been expected for the longer reaction time. For MG-$t_{10,270}$ microgel, around 4 % more DMA is consumed during the reaction. A large amount of this DMA might be contained as side-product in the gel clump occurring at the end of the reaction. Additionally, the 4 % difference in DMA consumption corresponds to a minor 0.2 mol% difference in the final microgel structure when taking into account the initially injected amount of DMA (5 mol%).
For the microgels with different injection times of DMA, a higher incorporated amount would have been expected for earlier injections due to the following reasons: DMA has more time to include into the structure and exhibits a faster reaction kinetic. Moreover, the NIPAM and BIS consumptions are hindered. Nevertheless, the overall reaction time of the polymerisation $t_{reac} = 60\,min$ appears to level off the differences in the final microgel composition, as a minimum of 80 % DMA conversion is achieved for all microgels. It's important to note that differences might lie in the internal

microgel structure, making it an intriguing outlook for future investigations using techniques such as small-angle neutron scattering, X-ray scattering or super-resolution fluorescence microscopy.

The evaluating methods for the amount of incorporated DMA, however, exhibit limitations. Values calculated by UV-vis standard addition differ from results obtained by NMR spectroscopy for some of the microgels. This discrepancy arises due to the spectral overlap between the catechol group of DMA and the NH groups (from DMA and NIPAM) in the NMR spectra, as described in chapter 3.7. Moreover, quantifying low amounts of incorporated DMA during UV-vis standard addition experiments can be challenging due to potential difficulties in distinguishing the microgel background signal from the small catechol peak (for details see chapter 3.8). Both limitations contribute to the differences observed between NMR and UV-vis results. Viewed together, both methods compensate their drawbacks and provide a robust qualifying system for assessing the amount of DMA incorporation. This is why combining the both methods is recommended for future investigations.

4.3.1 Morphology of microgels synthesised without BIS

For microgels synthesised without the additional cross-linker BIS, the injection time of DMA not only affects the DMA reaction rate but also dictates the resulting particle morphology. A raspberry-like structure was observed for the microgels with later DMA injection times (MG-$t_{7.5,60}$-noBIS and MG-$t_{15,60}$-noBIS), which could be explained as follows: During the early stages of the reaction, microgel particles begin to form owing to the self-cross-linking ability of NIPAM, serving as central "core" particles [188]. When solely relying on the self-cross-linking of NIPAM, microgel particles with ultra-low cross-linking are typically obtained [189]. Within our approach, two scenarios can now be envisioned: (1) The "core" particles undergo further cross-linking upon the introduction of DMA, which we refer to as "post cross-linking". As a result, some "core" particles become inter-connected, directly forming the raspberry-like structure. (2) The "core" particle primarily consists of self-cross-linked PNIPAM. When DMA is introduced, the remaining NIPAM and DMA monomers form smaller nanoparticles. These can be subsequently linked to the "core" particle, either by physical adsorption or chemical cross-linking. The second scenario employs the conventional approach to form raspberry-like structures [188, 190].

This structural phenomenon aligns with the findings of Xue *et al.* [4], who obtained similar structures for P(NIPAM-co-DMA) microgel particles when using low NIPAM to DMA ratios of 1/20. Notably, Xue *et al.* did not further explain this observation in their work. It is interesting to note that such morphologies were not observed for larger DMA contents. This reinforces the idea that the structure primarily arises from the self-cross-linking ability of NIPAM.
Raspberry-like particles hold great potential for the development of novel materials. They offer advantages such as an increased surface area, which is valuable for various applications. Especially raspberry-like particles with a PNIPAM core have been barely developed [188]. Therefore, further investigations in this direction promise exciting prospects. It is, however, crucial to investigate their mechanical stability in the future since the linkages between the "core" particles and nanoparticles are known to exhibit low strength [188, 190]. In the context of this thesis, the formation of raspberry-like structures is not desired as the goal is to create microgels with both high mechanical strength and adhesive properties. Throughout the subsequent work, BIS is therefore included as an additional cross-linker.

We extended the findings from existing literature [4], which already confirmed the importance of delaying the injection of DMA during the reaction due to its role as a scavenger. In this chapter, the impact of the different synthesis parameters on the reaction kinetics of the compounds and on the incorporated amount of DMA was systematically explored. Additionally, the impact of the cross-linker BIS on both was investigated. As a result, the co-polymerisation of PNIPAM with DMA can now be precisely controlled.
The findings from this chapter enable the design of microgels to meet specific requirements in future applications. The combination of the adhesive abilities and mechanical robustness of mussels, coupled with the stimuli-responsiveness of PNIPAM holds immense potential for a wide range of applications.

4.4 Conclusion

We successfully co-polymerised poly(*N*-isopropylacrylamide) (PNIPAM) microgels with the catechol-based monomer dopamine methacrylamide (DMA). These P(NIPAM-co-DMA) microgels exhibit a temperature-responsive behaviour and have

a monomodal size distribution, as confirmed by dynamic light scattering (DLS) and atomic force microscopy (AFM) measurements. The incorporation of DMA was confirmed using UV-vis and nuclear magnetic resonance (NMR) spectroscopy. Both methods possess advantages and disadvantages, but together counterbalance their drawbacks and thus build a good qualifying system. Reaction kinetics of NIPAM, *N*,*N*'-methylene-bis-acrylamide (BIS) and DMA were analysed by mass spectrometry (MS), varying the injection time t_{DMA} of DMA and overall reaction time t_{reac} of the synthesis to find an optimised synthesis protocol. While an early injection of DMA accelerates its reaction, it impedes the NIPAM and BIS reactions due to the scavenging ability of DMA. A delayed injection of DMA ($10 - 15$ min) slows down its reaction, but ensures a full conversion of NIPAM and BIS before the DMA introduction. This is preferred to guarantee a complete PNIPAM polymerisation. The cross-linker BIS does not influence the reaction kinetics, as shown by microgels solely cross-linked by DMA. Surprisingly, the amount of incorporated DMA is similar across all microgels, regardless of the injection and reaction times. Taking into account the slower reaction kinetics for later injection times of DMA, a total reaction time of 60 min ensures the DMA incorporation. Prolonging the reaction time beyond 60 min leads to gel clump formation without significantly increasing DMA incorporation. Based on the results, an optimised synthesis protocol is established for the upcoming chapters: DMA is introduced after 15 min and a total reaction time of 60 min is chosen. The reaction kinetics of DMA can be described as a second-order reaction. The synthesis was shown to be reproducible and insensitive to UV light. For microgels exclusively cross-linked by DMA and with delayed DMA injection times, the reaction leads to the formation of raspberry-like microgels. This is driven by the necessity of NIPAM to self-cross-link within the first minutes of the reaction.

5 Swelling behaviour and mechanical properties of P(NIPAM-co-DMA) microgels

Similar content is contained in "Influence of Dopamine Methacrylamide on swelling behaviour and nanomechanical properties of PNIPAM microgels" Sandra Forg, Xuhong Guo, and Regine von Klitzing, *submitted*.

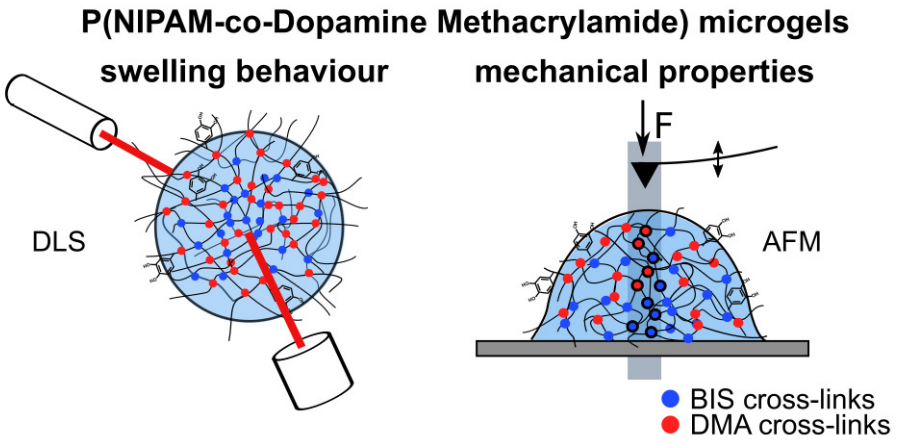

Abstract

The combination of the catechol-containing co-monomer dopamine methacrylamide (DMA) with stimuli-responsive microgels such as poly(*N*-isopropylacrylamide) (PNIPAM) bears a huge potential in research and for applications due to the versatile properties of catechols. This chapter gives first detailed insights into the influence of DMA on the swelling of PNIPAM microgels and the correlation with their nanomechanical

properties. Dynamic light scattering (DLS) is used to analyse the swelling behaviour of microgels in bulk solution. The incorporation of DMA decreases the volume phase transition temperature (VPTT) and completion temperature (VPT CT) due to its higher hydrophobicity when compared to NIPAM, while sharpening the transition. The cross-linking ability of DMA decreases swelling ratios and mesh sizes of the microgels. Microgels adsorbed at the solid surface are characterised by atomic force microscopy (AFM): Scanning provides information about the microgel's shape at the surface and force spectroscopy measurements determine their nanomechanical properties in form of a localised E modulus. As the DMA content increases, microgels protrude more from the surface, correlating with an increase in E modulus and a stiffening of the microgels - confirming the cross-linking ability of DMA. Force spectroscopy measurements below and above the VPTT display a stiffening of the microgels with the incorporation of DMA and upon heating across its entire cross-section. The affine network factor β, derived from the Flory-Rehner theory describing the elasticity and swelling of the microgel network, is linearly correlated with the E moduli of the microgels for both - pure PNIPAM and P(NIPAM-co-DMA) microgels. However, for large amounts of DMA, DMA appears to hinder the microgel shrinking, while still ensuring mechanical stiffness, possibly due to catechol interactions within the microgel network.

5.1 Introduction

Hydrogels can absorb large amounts of water [31], similar to human body tissues, making them widely applicable especially in the biomedical field [13, 21–30] as detailed in chapter 2.1. Their micro-network, characterised by the mesh size, facilitates the diffusion and transport of oxygen, nutrients and drugs. They are manufacturable with good biocompatibility and a variety of properties. Nevertheless, hydrogels possess some weaknesses, i.e. a low stiffness, restricting their use for applications demanding mechanical robustness [22]. To overcome this limitation, stiffness can be incorporated and adjusted by chemically cross-linking the polymer network.
The introduction of stimuli-responsiveness through the use of polymers like poly(*N*-isopropylacrylamide) (PNIPAM) further promotes the use of such hydrogels [25, 27, 28, 191, 191, 192, 192], as deepened in chapter 2.1. The incorporation of hydrophobic or hydrophilic co-monomers allows their volume phase transition temperature (VPTT), normally at around 32°C, to be tuned to lower or higher temperatures regarding their

particular needs. Tuning the sharpness of the transition allows, e.g. drugs incorporated in the hydrogel network to be released faster or slower [56].
The use of catechol chemistry, inspired by mussels as explained in chapter 2.2, introduces further advantages in the biomedical field [7–9]. The exceptional under-water performance of mussels is attributed to a balance of mussel adhesion and cohesion, where latter one provides the strength of the mussel byssus. Dopamine methacrylamide (DMA) can be used as a synthetic replacement to mimic the mussel's properties (see chapter 2.2.1).
DMA acts as a cross-linker [4, 6, 16] and was already included in hydrogels as the sole cross-linker, as documented in literature [4] and explored in chapter 4. Theoretically, this approach should increase the stiffness of the microgels. The reaction kinetics of DMA during the polymerisation of P(NIPAM-co-DMA) microgels were studied in-depth in chapter 4. This analysis was essential to optimise the synthesis parameters and achieve a precise control over the polymerisation, especially regarding the scavenging effect of DMA [20]. But so far, there is only limited research [4, 13–16] on P(NIPAM-co-DMA) materials. A comprehensive understanding of the influence of DMA onto the swelling behaviour and mechanical properties of PNIPAM microgels is still missing, especially in terms of its cohesive performance. Furthermore, DMA's increased hydrophobicity in comparison to NIPAM, suggests a decrease of the VPTT [13–15, 193, 194].
Therefore, we synthesise P(NIPAM-co-DMA) microgels with increasing DMA amount and varying cross-linker *N,N'*-methylene-bis(acrylamide) (BIS) concentration (see table 3.2, chapter 3.3). For a full evaluation of their properties, we conduct a multi-faceted characterisation:
- **Swelling behaviour:** Microgels in bulk solution are characterised by dynamic light scattering (DLS). The investigation involves the determination of the VPT, as well as swelling ratios and mesh sizes of the microgels. Additionally, electrophoretic mobility measurements in the swollen and shrunken state of the microgels are carried out to gain information about their surface charge.
- **Nanomechanical properties:** Microgels adsorbed at the solid surface are examined by atomic force spectroscopy (AFM). The scanning of the microgels allows the investigation of the microgel's shape under ambient conditions. Force spectroscopy measurements provide information about the local elastic modulus E_{loc} of the microgels.
- **Correlation:** The correlation between the affine network factor β (eq. 2.11), derived from the Flory-Rehner theory [90, 91] describing the elasticity and swelling of the mi-

crogels (for details see chapter 2.1.2), with the E_{loc} modulus of the microgels is investigated. This examination aims to test the validity of the theory for the microgels and detect differences between pure PNIPAM microgels and their P(NIPAM-co-DMA) counterparts.

5.2 Results

Microgels were synthesised with an increasing amount of dopamine methacrylamide (DMA), as detailed in table 3.2, chapter 3.3. In this chapter, "c" denotes the alteration of microgel composition. The notation "B" followed by a number represents the molar percentage of cross-linker *N,N'*-methylene-bis(acrylamide) (BIS) with respect to the total reactants. Similarly, "D" followed by a number represents the injected amount of DMA, denoted as $c_{\mathrm{DMA,injected}}$ in molar percentage relative to the total reactants.
As evaluated in detail in chapter 4, the incorporated amount of DMA $c_{\mathrm{DMA,incorporated}}$ can be determined reliably through a combination of UV-vis standard addition (chapter 3.8) and nuclear magnetic resonance (NMR) spectroscopy (chapter 3.7). The results are given in table 3.2 and the corresponding calibration curves and NMR spectra can be found in the appendix, fig. A22, fig. A23 and fig. A24.
Mass spectrometry (MS) data were gathered following the procedure as explained in chapter 3.9 to proof the reliability of the reaction, as discussed in chapter 4. These MS data are available in fig. A21 (appendix) for reference.

5.2.1 Swelling behaviour of microgels in bulk solutions

Microgels in bulk solutions were characterised with dynamic light scattering (DLS) to study their swelling behaviour as described in chapter 3.4. Their swelling curves, namely their hydrodynamic radii R_{H} in dependence of temperature T, are shown in fig. 5.1 (a).
The hydrodynamic radius $R_{\mathrm{H}}(20^{\circ}\mathrm{C})$ of the swollen microgels is similar for the microgels with 1 mol% and 2 mol% of cross-linker BIS (MG-$c_{B1,D0}$ compared to MG-$c_{B2,D0}$ and MG-$c_{B1,D5}$ compared to MG-$c_{B2,D5}$). It decreases continuously from 419.1 ± 19.8 nm (MG-$c_{B2,D0}$) to 188.9 ± 5.6 nm (MG-$c_{B2,D20}$) for an increasing amount of DMA.
The hydrodynamic radius $R_{\mathrm{H}}(50^{\circ}\mathrm{C})$ of the shrunken microgel increases around 38 nm

from the reference microgels MG-$c_{B1,D0}$ to MG-$c_{B2,D0}$, while $R_H(50°C)$ is similar for MG-$c_{B1,D5}$ and MG-$c_{B2,D5}$ containing 5 mol% DMA. $R_H(50°C)$ stays constant at around 138 nm for an increasing amount of DMA (from MG-$c_{B2,D0}$ to MG-$c_{B2,D15}$). For MG-$c_{B2,D20}$, swelling curves could only be conducted for temperatures up to 40°C, as the dispersion flocculated at higher temperatures.
Temperature-dependent swelling curves were fitted with a sigmoidal function (see fig. A25, appendix). The derivatives of the function dR_H/dT are plotted in fig. 5.1 (b). The volume phase transition (VPT) completion temperature (CT), according to [14, 16, 138] and as explained in chapter 3.4, is illustrated by vertical lines and is given in table 5.1. The minimum of the derivative dR_H/dT corresponds to the volume phase transition temperature (VPTT).
The VPT CT significantly decreases for an increasing amount of cross-linker (MG-$c_{B1,D0}$ compared to MG-$c_{B2,D0}$ and MG-$c_{B1,D5}$ compared to MG-$c_{B2,D5}$), leading to sharper transitions. The VPTT is similar for an increasing amount of cross-linker from MG-$c_{B1,D0}$ to MG-$c_{B2,D0}$ and decreases from MG-$c_{B1,D5}$ to MG-$c_{B2,D5}$. For MG-$c_{B1,D5}$, data fluctuate largely around the VPT. For an increasing amount of incorporated DMA, the VPT CT decreases from 40°C to 27°C from MG-$c_{B2,D0}$ to MG-$c_{B2,D15}$, therefore exhibiting sharper transitions. The incorporation of DMA reduces the VPTT. For MG-$c_{B2,D20}$, the sigmoidal function cannot describe the VPT completion adequately, since values at higher temperatures are not available due to the flocculation of the sample. Therefore, no VPT CT was determined.

From the swelling curves, the swelling ratio α and the mesh size ξ were evaluated by eq. 2.9 and eq. 3.10 (see table 5.1 and fig. A26, appendix). The swelling ratio α is the highest for the reference microgel MG-$c_{B1,D0}$ with 1 mol% cross-linker BIS due to the smallest $R_H(50°C)$. In comparison, the swelling ratio α of the reference microgel MG-$c_{B2,D0}$ (2 mol% cross-linker BIS) is only 1/3 of the swelling ratio of MG-$c_{B1,D0}$. However, α was calculated from the two hydrodynamic radii at 20°C and 50°C, which can be prone to error. The swelling ratio decreases from the lower cross-linked MG-$c_{B1,D5}$ to the higher cross-linked MG-$c_{B2,D5}$. With increasing amount of DMA (from MG-$c_{B2,D0}$ to MG-$c_{B2,D15}$), the swelling ratio decreases from 27.9 $\pm$ 4.1 to 4.4 $\pm$ 0.3. The swelling ratio of MG-$c_{B2,D20}$ was calculated with the hydrodynamic radius of the shrunken microgel at 40°C $R_H(40°C)$ due to the flocculation of the sample at higher temperatures. Therefore, the swelling ratio is prone to smaller errors and is slightly higher than the swelling ratio of MG-$c_{B2,D15}$.
Mesh sizes decrease for an increasing amount of cross-linker BIS (MG-$c_{B1,D0}$ compared

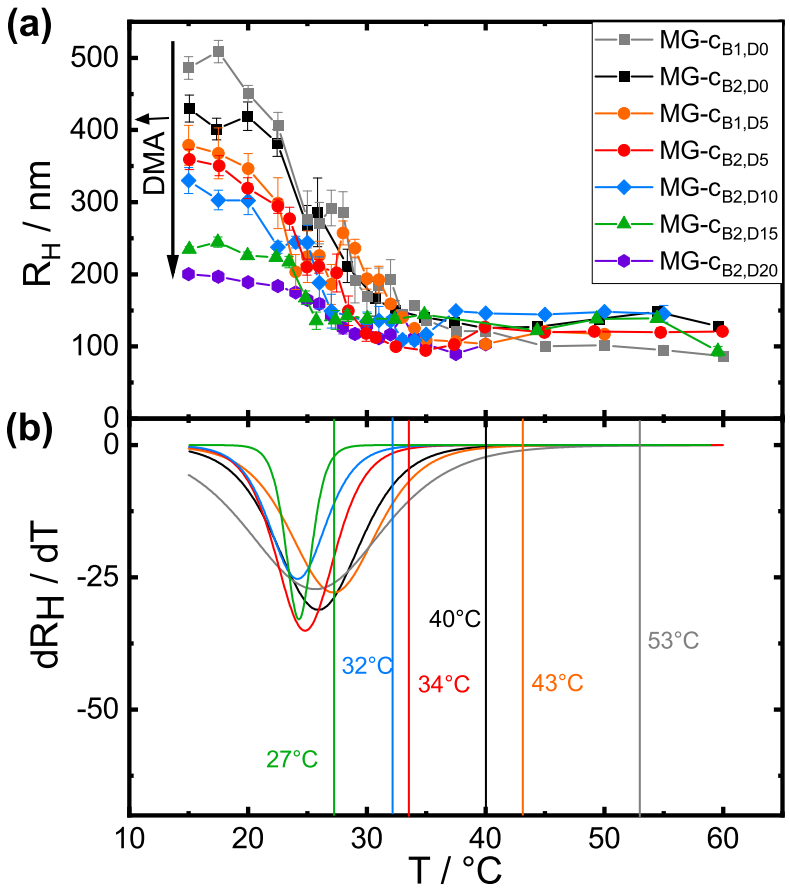

Figure 5.1: (a) R_H in dependence of temperature T for the different microgels. (b) Derivative dR_H/dT of corresponding sigmoidal functions. Vertical lines show the VPT CT for the different microgels. For MG-$c_{B2,D20}$, no VPT CT can be defined, because the sigmoidal function cannot describe the VPT (flocculation of sample at higher temperatures).

to MG-$c_{B2,D0}$ and MG-$c_{B1,D5}$ compared to MG-$c_{B2,D5}$). They further decrease for an increasing amount of DMA (from MG-$c_{B2,D0}$ to MG-$c_{B2,D15}$), from 12.2 nm to 6.5 nm. Again, MG-$c_{B2,D20}$ possesses a slightly higher value than MG-$c_{B2,D15}$, since it had to be calculated with the value at 40°C.

The electrophoretic mobility μ_e was measured as described in chapter 3.5 at 20°C and 50°C to gain information about the charge of the microgels. Values are given in table 5.1. μ_e is positive and in the same order for every microgel, corresponding to a positive surface charge of the microgels. It increases with increasing temperature.

Table 5.1: Characterisation of microgels in bulk solution: Swelling ratio α and mesh size ξ of microgels calculated from results obtained by DLS by eq. 2.9 and eq. 3.10. VPT CT determined according to [14, 16, 138] and as described in chapter 3.4. Electrophoretic mobility μ_e measured as described in chapter 3.5.

Microgel	α	ξ / nm	VPT CP / °C	μ_e(20°C) / µm cm V^{-1} s^{-1}	μ_e(50°C) / µm cm V^{-1} s^{-1}
MG-$c_{B1,D0}$	87.5±9.0	24.2	53	0.55±0.02	3.66±0.22
MG-$c_{B2,D0}$	27.9±4.1	12.2	40	1.01±0.02	5.57±0.14
MG-$c_{B1,D5}$	26.0±4.8	16.4	43	0.49±0.03	4.71±0.13
MG-$c_{B2,D5}$	18.4±2.9	10.3	34	0.28±0.02	5.45±0.06
MG-$c_{B2,D10}$	8.5±1.7	7.9	32	0.12±0.03	4.30±0.07
MG-$c_{B2,D15}$	4.4±0.3	6.5	27	0.65±0.02	4.30±0.10
MG-$c_{B2,D20}$	6.6±1.1[a]	7.3 [a]	- [b]	1.44±0.02	4.84±0.04

[a] α and ξ were calculated with the hydrodynamic radius of the shrunken microgel at 40°C (R_H(40°C)) due to the flocculation of the sample at higher temperatures. [b] not available due to flocculation of the sample.

5.2.2 Mechanical properties of microgels at the solid surface

Height profiles of adsorbed microgel particles

In fig. 5.2 the height profiles of all the microgels adsorbed on silicon wafers are shown, determined by AFM scanning in ambient condition as explained in chapter 3.6.1. The corresponding AFM scans can be found in fig. A27, appendix. The value of the height-to-width ratio $h_{amb,AFM}/w_{amb,AFM}$ is given in table 5.2, which is calculated from the height $h_{amb,AFM}$ and width $w_{amb,AFM}$ of 5 different microgels per sample (values are given in table A3, appendix).
The $h_{amb,AFM}/w_{amb,AFM}$ ratio of the microgels increases with an increasing amount of cross-linker (MG-$c_{B1,D0}$ compared to MG-$c_{B2,D0}$ and MG-$c_{B1,D5}$ compared to MG-$c_{B2,D5}$) and with an increasing amount of DMA from MG-$c_{B2,D0}$ to MG-$c_{B2,D20}$ at 20°C.

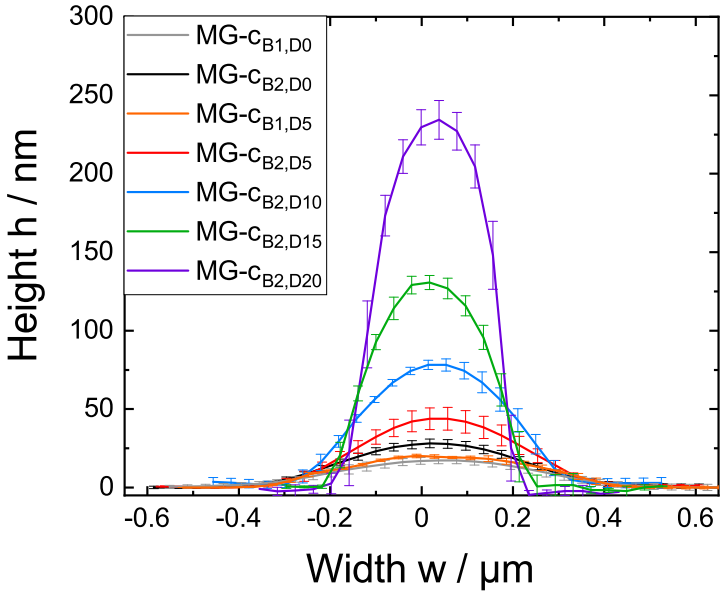

Figure 5.2: Height profiles of microgels scanned by AFM in ambient conditions. Profiles are an average of 5 different microgel particles per sample.

Table 5.2: Characterisation of microgels at the surface by AFM scanning in ambient conditions: height-to-width ratio ($h_{amb,AFM}/w_{amb,AFM}$) calculated from the height $h_{amb,AFM}$ and width $w_{amb,AFM}$ of 5 different microgel particles per sample (values are given in fig. A3, appendix).

Microgel	$h_{amb,AFM}/w_{amb,AFM}$ ratio
MG-c$_{B1,D0}$	0.014 ± 0.002
MG-c$_{B2,D0}$	0.026 ± 0.004
MG-c$_{B1,D5}$	0.020 ± 0.002
MG-c$_{B2,D5}$	0.049 ± 0.009
MG-c$_{B2,D10}$	0.110 ± 0.011
MG-c$_{B2,D15}$	0.278 ± 0.029
MG-c$_{B2,D20}$	0.540 ± 0.060

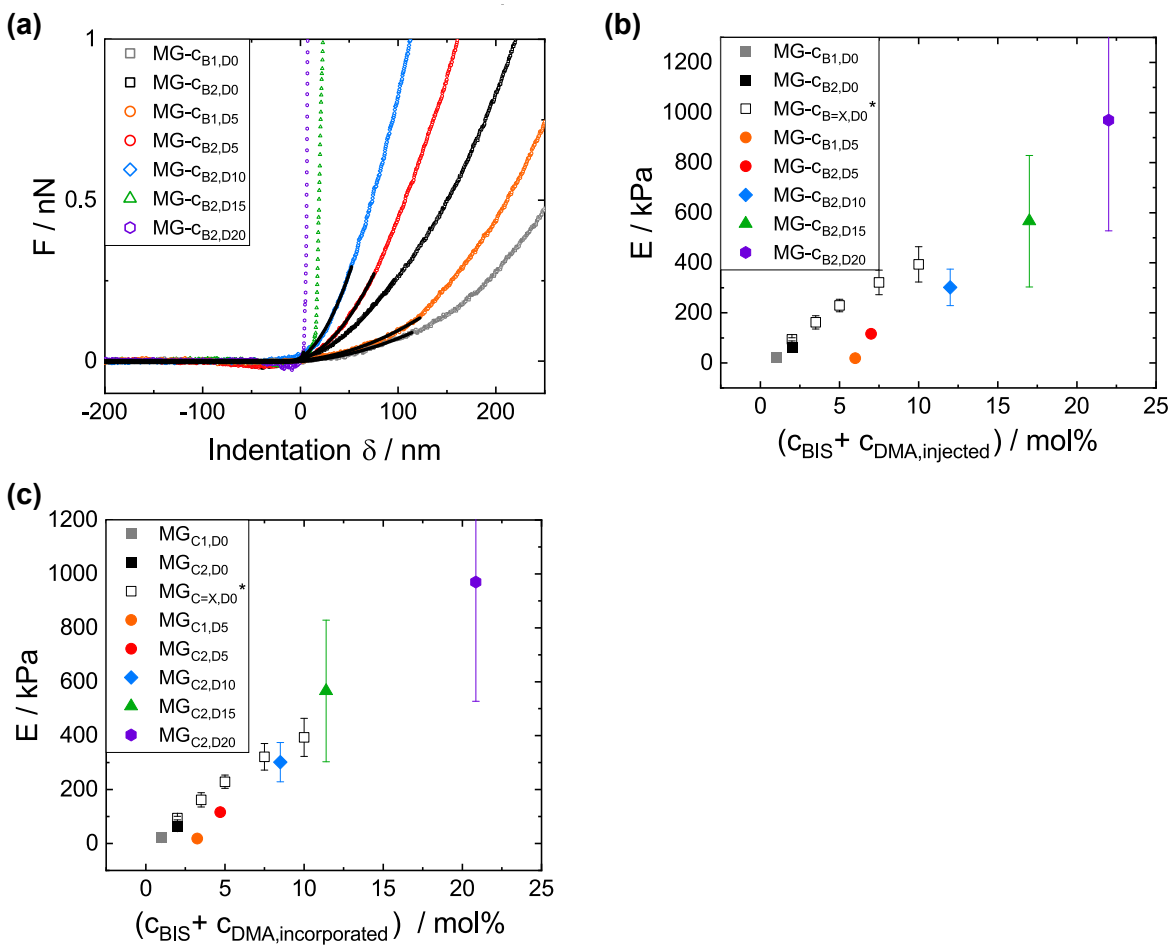

Figure 5.3: (a) Exemplary force curves for each type of microgel (open symbols) conducted at the centre of one particle together with the corresponding Hertzian fit (solid black line). (b) Averaged E moduli from force curves conducted in the centre of 10 microgel particles of each type of microgel plotted over the sum of concentration of the cross-linker BIS c_{BIS} and injected co-monomer DMA $c_{\mathrm{DMA,injected}}$. (c) Averaged E moduli plotted over the sum of c_{BIS} and incorporated amount of DMA $c_{\mathrm{DMA,incorporated}}$ determined by UV-vis and NMR spectroscopy [16]. *Open symbols in (b) and (c) correspond to results obtained by Kühnhammer *et al.* [74] for pure PNIPAM microgels without DMA with varying (x) amount of cross-linker BIS.

Mechanical properties of adsorbed microgel particles

Mechanical properties of the adsorbed microgels swollen in water were studied with AFM force spectroscopy as explained in chapter 3.6.2. In this context, a tip is indented

into individual adsorbed microgel particles in order to gain structural details alongside a position-dependent E modulus. This modulus can be regarded as a local modulus E_{loc}. For the sake of simplification, it will be referred to as E modulus in the following chapter. Fig. 5.3 (a) shows an exemplary force curve of each type of microgel measured at its centre, along with the corresponding Hertzian fit. All force curves used for the analysis of E can be found in fig. A28, appendix.

The slope of the force curves increases with an increasing amount of cross-linker BIS and an increasing amount of co-monomer DMA. At high indentations ($> 300\,nm$), the force curves of microgels cross-linked by 1 mol% BIS (MG-$c_{B1,D0}$ and MG-$c_{B1,D5}$) exhibit a vertical increase of force over indentation, indicating a complete penetration of the cantilever through the microgel down to the substrate (see fig. A28 (a), appendix). For some force curves, negative forces are observed before reaching the actual contact point (see fig. A28 (b), appendix). They are caused by attractive interactions between cantilever and tip just before the cantilever indents into the sample. The effect was most prominent for the microgel with the highest amount of DMA MG-$c_{B2,D20}$ (see fig. A28 (b), appendix).

The resulting E moduli, from force curves conducted in the centre of 10 microgel particles of each type of microgel, over the sum of the concentrations of cross-linker BIS c_{BIS} and injected co-monomer DMA $c_{DMA,injected}$ are plotted in fig. 5.3 (b). Resulting E moduli are also shown in dependence of the sum of the concentrations of cross-linker BIS c_{BIS} and incorporated co-monomer DMA $c_{DMA,incorporated}$ in fig. 5.3 (c). The results are shown together with results obtained by Kühnhammer *et al.* [74] and show an increase of E with an increase in cross-linker BIS amount for pure PNIPAM microgels. These PNIPAM microgels were synthesised with different cross-linker BIS amount in our group with a similar recipe. The excellent agreement between our data and the data from literature underlines that the E modulus determination is valid.

The E modulus also increases for an increasing amount of DMA equivalently to an increasing amount of cross-linker BIS. When E is plotted over the sum of the concentration of BIS c_{BIS} and the injected amount of DMA $c_{DMA,injected}$ in fig. 5.3 (b), the increase in E moduli is shifted to lower E moduli in comparison to the E moduli of pure PNIPAM microgels. When E is plotted over the sum of the concentration of BIS c_{BIS} and the incorporated amount of DMA $c_{DMA,incorporated}$ in fig. 5.3 (c), the values of E are shifted towards the values obtained for the pure PNIPAM microgels, but are still lower.

The error bars of E enlarge for an increasing amount of BIS and DMA, which is a well-

known effect. Microgels of the same sample have been found to show some variation in heterogeneity in the centre of the particle, getting more distinct for microgels with higher cross-linker contents [51, 54]. Moreover, the trigger point is set at a constant force. So for steeper force curves the number of data points is lower in a smaller indentation range [104] as seen in fig.5.3 (a). For the microgels, with the two highest concentrations of DMA (MG-$c_{B2,D15}$ and MG-$c_{B2,D20}$), E moduli exhibit the largest errors. Therefore, a different approach is tried to fit the force curves of MG-$c_{B2,D15}$ and MG-$c_{B2,D20}$ based on the study from Aufderhorst-Roberts *et al.* [104] for force curves with steeper increases. The force curves were fitted with a constant force range instead of a constant indentation range (constant y-range instead of x-range). However, the maximum fit range, which can describe the force curve sufficiently, is 100 pN. 100 pN is well above the noise of the force curves, but doesn't include significantly more data points than fitting with a constant indentation range of $0-40\%$ for MG-$c_{B2,D15}$ and MG-$c_{B2,D20}$. Setting a larger fit range of 150 or 200 pN results in deviances from fit to the force curve, especially in the lower part of the force curve. An exemplary force curve of MG-$c_{B2,D20}$ with different fitting procedures is given in fig. A29, appendix. The resulting E moduli are shown in fig. A30 (b) (appendix), but did not lead to a significant improvement of the data. For MG-$c_{B2,D15}$, both results are comparable, but the second approach results in slightly smaller errors. E moduli for MG-$c_{B2,D20}$ deviate significantly for both methods. Fitting with a constant force range leads to even larger errors. The trend that E moduli increase for an increasing amount of DMA remains for both methods.

The E modulus profile for two exemplary microgels MG-$c_{B2,D0}$ and MG-$c_{B2,D10}$ is shown in fig. 5.4 at (a) 20°C and (b) 50°C. The errors of MG-$c_{B2,D10}$ can be explained as before. Comparing the pure PNIPAM microgel MG-$c_{B2,D0}$ and the P(NIPAM-co-DMA) microgel MG-$c_{B2,D10}$, both show the highest E modulus in the centre, decreasing towards the outer periphery. Overall, the P(NIPAM-co-DMA) microgel exhibits higher E moduli than the pure PNIPAM microgel with the same BIS amount. When heating from 20°C to 50°C above the VPT(T), E moduli increase significantly for both types of microgels. While MG-$c_{B2,D0}$ possesses a stiffening factor $E(50°C)/E(20°C)$ of around 20 in the centre of the microgel particle upon heating, MG-$c_{B2,D10}$ stiffens by more than 2 orders of magnitude. E decreases again from the centre towards the outer regions of the microgels. The particle cross-section width decreases from 20°C to 50°C for both microgels in the same order, similarly to the results obtained for the microgels when scanned in ambient condition.

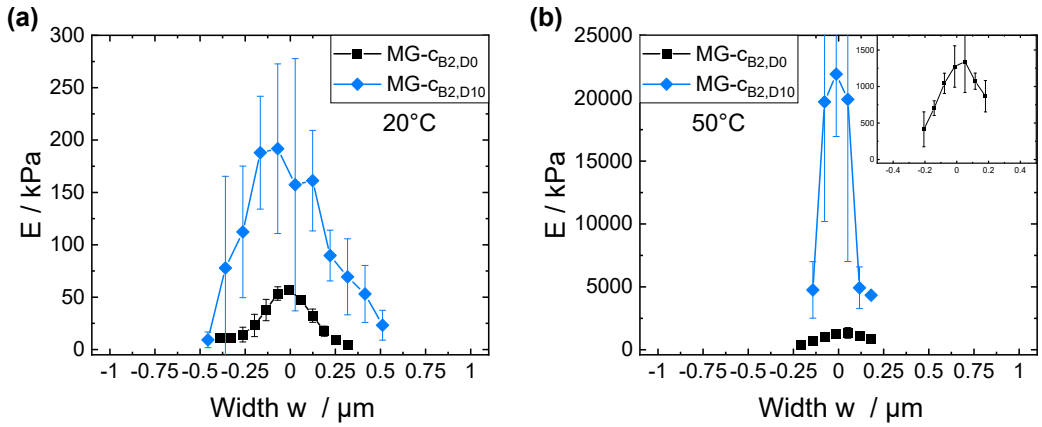

Figure 5.4: *E* modulus distribution over particle cross-section width for the two microgels MG-$c_{B2,D0}$ and MG-$c_{B2,D10}$ calculated from 5 different microgel particles at (a) 20°C and (b) 50°C. The inset of (b) displays the enlarged cross-section of MG-$c_{B2,D0}$.

Fig. 5.5 depicts the topography and lift-off map obtained from the force mapping tool (for more details see chapter 3.6.2) for the two microgels MG-$c_{B2,D0}$ and MG-$c_{B2,D10}$ at (a) 20°C and (b) 50°C.
At 20°C interestingly, the pure PNIPAM microgel particle (MG-$c_{B2,D0}$) is barely visible in the topography map while clearly identifiable in the corresponding lift-off map. In contrast to that, the P(NIPAM-co-DMA) microgel particle (MG-$c_{B2,D10}$) is visible in both maps, although exhibiting slightly larger radii in the lift-off map.
At 50°C both microgels are visible in the topography map and lift-off map. Both microgels possess slightly larger radii in the lift-off map compared to the topography map, while the difference is larger for the pure PNIPAM microgel MG-$c_{B2,D0}$.

5.3 Discussion

Swelling behaviour of microgels in bulk solutions

The swelling behaviour of microgels can be described by the Flory-Rehner theory, as specified in chapter 2.1.2. The theory offers insights into how the presence of a cross-linker in the microgel network influences their swelling behaviour - resulting in an increased elasticity of the microgel network.
Moreover, the hydrodynamic radius $R_H(20°C)$ of the swollen microgel is known to

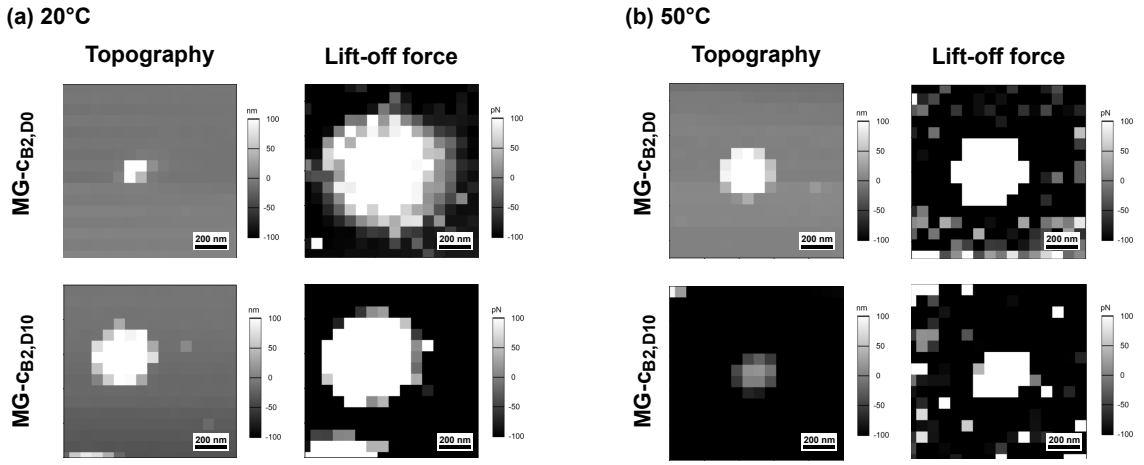

Figure 5.5: Exemplary force maps providing information about the topography (a) and lift-off force at (a) 20°C and (b) 50°C of MG-$c_{B2,D0}$ (top) and MG-$c_{B2,D10}$ (bottom).

decrease for an increase in cross-linker *N,N'*-methylene-bis(acrylamide) (BIS) amount [76, 195–198], since a higher cross-linked microgel structure is less capable of swelling (reflected by smaller mesh sizes and smaller swelling ratios). For the hydrodynamic radius $R_H(50°C)$ of the shrunken microgel, an increase in size (larger rigid core) is expected for an increasing BIS content [88, 196] - BIS has a higher reaction kinetic than *N*-isopropylacrylamide (NIPAM), therefore mainly accumulating in the microgel's centre [16, 50, 69] as explained in chapter 2.1. Nevertheless, in a lot of studies, no (systematic) effect was observed [195, 198]. For the lower cross-linked pure PNIPAM microgel MG-$c_{B1,D0}$ a lower shrunken hydrodynamic $R_H(50°C)$ is obtained than for the higher cross-linked MG-$c_{B2,D0}$ (around 38 nm difference), indicating the expected smaller core and leading to significantly larger mesh sizes. However, there was no difference found for the differently cross-linked P(NIPAM-co-DMA) microgels. The values from literature [70, 198, 199] for an increase from 1 to 2 mol% cross-linker amount are in agreement with our results of hydrodynamic radii, swelling ratios and mesh sizes.

Dopamine methacrylamide (DMA) is known to cross-link structures as well [4, 6, 16], promoting the cohesive strength of catechol-based materials as clarified in chapter 2.2.1. This results in a decrease of the hydrodynamic radius $R_H(20°C)$ of the swollen microgel in our study (see fig. 5.1), same as for an increasing cross-linker amount [76, 195–198]. This systematic effect, to the best of our knowledge, has not been observed for DMA cross-linked microgels so far. $R_H(50°C)$ of the shrunken

microgel stays constant for different amounts of DMA, indicating that the core size is unaffected by the addition of DMA. Consequently, microgels with increasing DMA are less capable to swell, underlined by the decreasing mesh size ξ and swelling ratio α. This is in good agreement with the results from the group of Xue *et al.* [4].
It should be noted that the given values of mesh sizes ξ in table 5.1 for P(NIPAM-co-DMA) microgels are estimated values. We assume that only BIS acts as cross-linker (see eq. 3.10). Since DMA acts (at least partially) as an additional cross-linker, mesh sizes are likely smaller. However, it is unclear how much of DMA serves as a cross-linker due to the assumption of free catechol moieties within the microgel network. In contrast, the calculation of ξ is based on the swelling ratio α of the microgels rather than using the degree of swelling Q, calculated from the completely dehydrated microgel state. This method underestimates ξ. Nonetheless, we are only interested in the trend of mesh sizes, which remains distinct. Therefore, eq. 3.10 was not adjusted.
The microgel's volume phase transition (VPT), as explained by the Flory-Rehner theory (refer to chapter 2.1.2), is characterised by a sudden change in the swelling of the microgels. Introducing co-monomers with varying hydrophilicities compared to NIPAM can modify this VPT. For example, BIS being more hydrophilic than NIPAM increases the overall hydrophilicity of the microgel, theoretically increasing the VPT temperature (VPTT). When heating a microgel above its VPTT, hydrophobic interactions become dominant, which are now compensated by hydrophilic interactions caused by the cross-linker BIS. In literature, none or only slight effects are observed [76, 195, 198] and the VPTT remains constant at about 32°C irrespective of the BIS content. This is in agreement with our data, where the VPTT is similar for the pure PNIPAM microgels with 1 mol% and 2 mol% cross-linker BIS (MG-$c_{B1,D0}$ compared to MG-$c_{B2,D0}$; see fig. 5.1). However, from MG-$c_{B1,D5}$ to MG-$c_{B2,D5}$ the VPTT decreases, which is in contrast to the expectation. This could be a result of the fluctuating hydrodynamic radii of MG-$c_{B1,D5}$ around the VPTT. Conformational changes in the microgel particles around the VPTT can lead to fluctuations in their radii. That supports that the VPT CT is more reliable in our case.
In contrast to BIS, DMA is more hydrophobic than NIPAM, and hydrophobic groups are known to decrease the VPTT [13–15, 193, 194] due to an enhancement of hydrophobic interactions. DMA has the tendency to press water out of the microgel network. Especially the VPT onset was shown to decrease significantly [14]. The present study shows that the incorporation of DMA leads to a slight decrease of the VPTT (point of deflection; see fig. 5.1), which is in good agreement with literature

[13–15]. A significant decrease of the VPT CT is observed, which refers to a sharpening of the transition in contrast to literature [13, 14]. In these studies, a broadening of the transition is described, explained by the statistical distribution of the hydrophobic groups generating local hydrophobic inhomogeneities. We assume that the observed sharp VPT in our study is a consequence of our synthesis protocol, differing from other literature procedures [13, 14]. In this thesis, DMA is introduced into the reaction at a later time [16], following the optimised synthesis protocol outlined in chapter 4. DMA is added when BIS is already fully consumed. This might lead to a different distribution of the more hydrophobic DMA within the microgel network. The sharp VPT is favourable for biomedical applications [56], because it results in a faster and more controlled release of i.e. incorporated drugs.
All microgels, both at 20° and 50°C, possess a positive electrophoretic mobility and therefore a positive surface charge since they were synthesised with the positively charged initiator 2,2'-azobis-2-methyl-propanimidamide dihydrochloride (AAPH). Assuming a constant number of charges, the collapsed microgels at 50°C with a smaller particle surface have a higher surface charge density than the swollen microgels [99], which is confirmed by our data (table 5.1). Values are similar for all the microgels, so DMA has no effect on the surface charge. This leads to the conclusion, that the flocculation of the microgel dispersion of MG-$c_{B2,D20}$ with the highest DMA amount is not caused by a lack of electrostatic stabilisation at temperatures above the VPT [76, 102], but probably caused by the increased hydrophobicity due to the incorporation of DMA itself.

To *summarise*, P(NIPAM-co-DMA) microgels exhibit reduced sizes in the swollen state when compared to pure PNIPAM microgels. The size difference arises from DMA's role as an additional cross-linker, reducing the swelling capacity of P(NIPAM-co-DMA) microgels, as illustrated in fig. 5.6. The smaller mesh sizes and swelling ratios for P(NIPAM-co-DMA) further underline this behaviour. Both types of microgels collapse to similar sizes above the VPTT, which can be attributed to similar core sizes. Due to the incorporation of DMA with an increased hydrophobicity in comparison to NIPAM, the VPT(T) of P(NIPAM-co-DMA) microgels is shifted to lower temperatures and results in sharper phase transitions.

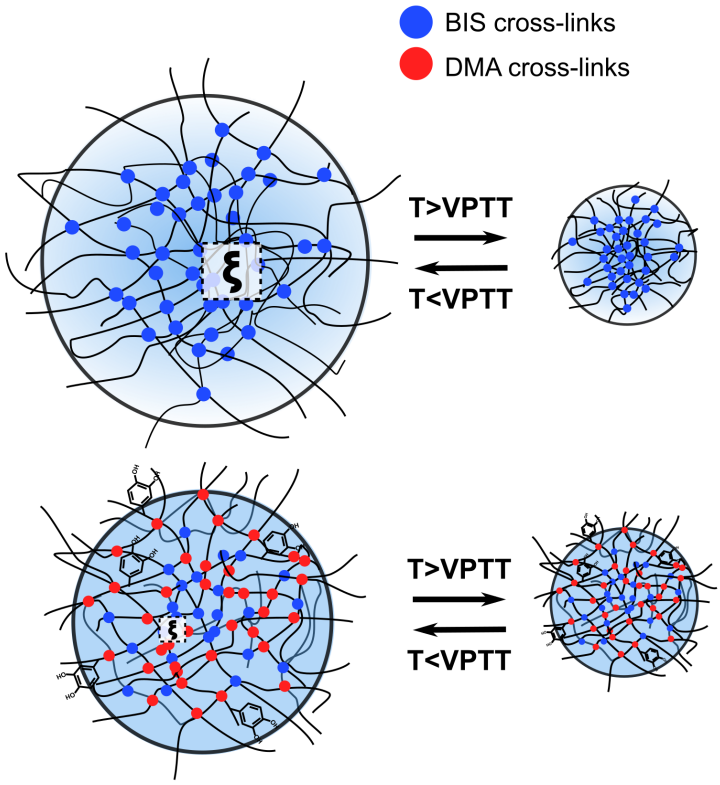

Figure 5.6: Summarising scheme of swelling behaviour of pure PNIPAM and P(NIPAM-co-DMA) microgels in bulk solution. For a more detailed description, see text.

Mechanical properties of microgels adsorbed at the solid surface

Microgels adsorb to silicon wafers due to two reasons: the positively charged microgels are electrostatically attracted by the negatively charged silicon wafers. However, the adhesive properties of DMA might also contribute to the adsorption of P(NIPAM-co-DMA) microgels, which should be kept in mind.

Microgel particles adsorbed at interfaces, such as a silicon wafer, deform owing to their soft nature as explained extensively in chapter 2.1.3. This can highly alter their physical properties. Our data underline the significant influence of the cross-linking density as explained in this chapter: The $h_{\mathrm{amb,AFM}}/w_{\mathrm{amb,AFM}}$ ratio increases with increasing amount of both, cross-linker BIS and co-monomer DMA. This arises from an augmentation in the microgel's height $h_{\mathrm{amb,AFM}}$ coupled with a reduction in its

width $w_{\text{amb,AFM}}$ (see fig. 5.2), consistent with findings in literature [51, 74, 104] and as explained in chapter 2.1.3. As the microgels become stiffer, due to a higher cross-linker content induced by both BIS and DMA, their decreased flexibility results in a reduced deformability when adsorbed at the silicon wafer - they protrude more from the surface. Additionally, differences in the water uptake of the microgel particles after spin coating might further enhance this effect. Here, the higher hydrophobicity of DMA might lower the water content in the microgel network structure.

The sole force curves obtained from force spectroscopy measurements of the different microgels already show an increase in stiffness as the amount of cross-linker BIS and co-monomer DMA increases. For some force curves, attractive forces prior to the contact point are observed, which become more pronounced for higher cross-linker amounts [74, 104]. These attractions are likely a result of the increased polymer concentration at the surface, which occurs with higher cross-linker densities, leading to stronger surface forces. This effect is most pronounced in the case of MG-$c_{\text{B2,D20}}$, which has the highest DMA content and, consequently, the greatest stiffness. Nevertheless, not only its high polymer density, but also the adhesive abilities of DMA itself might contribute to this phenomenon.
The obtained values for the E modulus are consistent with literature. Studies have reported E moduli ranging from 17 to 600 kPa for PNIPAM microgels [51, 74, 97, 98, 104–106]. These values increase with increasing amounts of the cross-linker BIS from 1 to 10 mol%, as detailed in chapter 2.1.3. In the case of P(NIPAM-co-DMA) microgels, the E modulus increases with an increasing DMA content, indicating DMA's role as cross-linker similar to BIS. This is in good agreement with the work of Yang *et al.* [6], who found an increase in stiffening for DMA cross-linked polymers.
Plotting the E moduli of P(NIPAM-co-DMA) microgels against the sum of concentration of BIS c_{BIS} and *incorporated* DMA $c_{\text{DMA,incorporated}}$, (calculated by UV-vis standard addition and nuclear magnetic resonance (NMR) spectroscopy; see fig. 5.3 (c)), E moduli are shifted towards the E moduli of pure PNIPAM microgels. Nevertheless, the E moduli of microgels with DMA remain lower than these of the pure ones. This suggests that some free dopamine moieties are still present in the microgel network structure, not serving as cross-linker, as supported by literature. The group of Xue *et al.* [4] found out that the catechol group of DMA forms interchains with another polymer chain - either a C-O or a C-C bond - but some free catechol moieties are still present. These free dopamine moieties can potentially support the adhesiveness of

these materials in the future, which will be explored in the next chapter 6.
As for pure PNIPAM microgels, the E modulus decreases from the centre to the outer periphery of the microgel particles exemplary shown for the P(NIPAM-co-DMA) microgel MG-$c_{B2,D10}$ (see fig. 5.4), confirming a heterogeneous microgel structure with a stiffer core and a more loosely cross-linked shell with dangling ends. E moduli increase significantly when heating upon the VPTT, consistent with prior research [51, 75, 97, 107, 108] and as stated in chapter 2.1.3. Additionally, the cross-section of the particles undergoes changes, with a decrease in width and an increase in height upon heating [51, 54, 97], equivalently as for an increase of cross-linker amount. The stiffening factor $E(50°C)/E(20°C)$ of 20 in the centre of the pure PNIPAM microgel and of 2 orders of magnitude in the centre of the P(NIPAM-co-DMA) microgel is in the same order as found in literature [75, 107], where values of $42 - 110$ have been reported, increasing from low to high cross-linked PNIPAM. The stiffening is attributed to the higher cross-linker density [75] and a decrease in elasticity of the polymer chains in between two cross-links upon collapsing [108]. This highlights the likeness of P(NIPAM-co-DMA) microgels with microgels of high cross-linker content, but without DMA.
The studied topography and lift-off maps of MG-$c_{B2,D0}$ and MG-$c_{B2,D10}$ support the results received by AFM scanning of the microgels in ambient condition and the results of the E modulus distribution: MG-$c_{B2,D0}$ particles are barely detectable in the topography map at 20°C due to their strong deformation when adsorbed at silicon wafers. Specifically, adsorbed PNIPAM microgels are known to form the so-called "fried egg" structure [92, 104], where the dangling ends spread at the surface (details see chapter 2.1.3). They are not detectable in the topography map due to their small dimensions. MG-$c_{B2,D10}$ is however clearly detectable, since it protrudes more from the surface due to a decreased flexibility, and due to an overall stiffening of the microgel upon the incorporation of DMA (see E modulus distribution). Both types of particles can be clearly identified in the lift-off map. This is because the cantilever adheres to the particles, including their dangling ends, during the retraction, as specified in chapter 3.6.2. The microgel particles exhibit in both cases a larger diameter in the lift-off map than in the topography map, due to the heterogeneous nature of both microgel types. This is in accordance with the results obtained for the E modulus distribution.
Upon heating to 50°C, both particles increase in stiffness, therefore the pure PNIPAM microgel MG-$c_{B2,D0}$ is now visible in the topography map as well. Both microgels

possess slightly larger radii in the lift-off map compared to the topography map. The difference is larger for the pure PNIPAM microgel MG-$c_{B2,D0}$, which agrees well with the data of E moduli across the microgel's cross-section: Even if the pure PNIPAM microgel MG-$c_{B2,D0}$ stiffens from 20°C to 50°C, the P(NIPAM-co-DMA) microgel MG-$c_{B2,D10}$ stiffens much more.

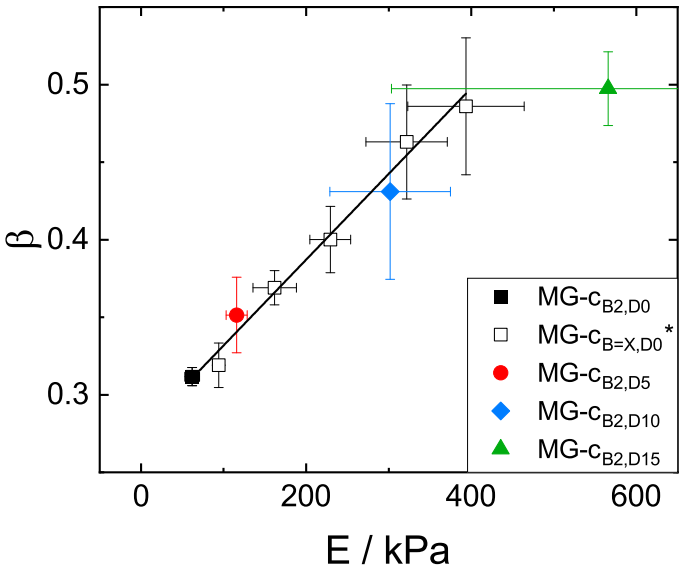

Figure 5.7: Affine network factor β (calculated as described in chapter 2.1.2 in eq. 2.11) and E moduli for an increasing amount of sole BIS cross-links and increasing amount of DMA cross-links (from MG-$c_{B2,D0}$ compared to MG-$c_{B2,D15}$). *Open symbols correspond to results obtained by Kühnhammer *et al.* [74] for pure PNIPAM microgels without DMA with varying (x) amount of cross-linker BIS. Pure PNIPAM microgels can be fitted by a linear function.

The affine network factor β, calculated as described in chapter 2.1.2 by eq. 2.11, is shown in dependency of the microgel's E moduli in fig. 5.7. According to the Flory-Rehner theory, the E modulus of the microgels is linearly correlated with β, which was experimentally proven [74].
For pure PNIPAM microgels a linear dependency is confirmed with increasing cross-linker BIS amount, including data obtained from Kühnhammer *et al.* [74] for pure PNIPAM microgels without DMA.* P(NIPAM-co-DMA) microgels with an

*Results of MG-$c_{B1,D0}$ with 1 mol% BIS where excluded due to its significantly larger swelling ratio.

increasing amount of DMA (from MG-$c_{B2,D0}$ to MG-$c_{B2,D10}$) show the same linear trend in agreement with data for pure PNIPAM microgels and fall on the same master curve. MG-$c_{B2,D15}$, though, deviates from the linear dependency. Despite the large error bars of the E modulus, which are a result of the smaller number of data points (i.e. small indentations), the deviation is distinct.[†] DMA surprisingly decreases the affine network factor β more than the cross-linker BIS, even when possessing a higher hydrophobicity than NIPAM. Catechols can interact with each other by a variety of mechanisms, such as hydrogen bonding, covalent cross-linking, metal coordination or $\pi - \pi$ stacking [3, 5, 113, 114], as explained in-depth in chapter 2.2. Due to the small mesh size of the microgel MG-$c_{B2,D15}$, catechol groups of DMA might interact with each other and consequently suppress the collapse of the microgels, while increasing the stiffness.

To *summarise:* P(NIPAM-co-DMA) microgels have a higher effective cross-linker density than pure PNIPAM microgels, due to the additional cross-linking of DMA, also in the shell of the microgel particles. Therefore, the cantilever tip compresses more cross-links while indenting as illustrated in fig. 5.8. As a consequence of the increased cross-linker density, the microgels protrude more from the surface and E moduli increase. This enables tuning the E modulus by incorporating DMA, making it more applicable for biomedical applications. The versatility of free catechol groups additionally enables more advantages by e.g. enhancing adhesive properties, as explored in the upcoming chapter. Above the VPTT, both types of microgels collapse in size (lateral and horizontal), which leads to a significant stiffening of the microgels. P(NIPAM-co-DMA) microgels with an increasing DMA amount show the same linear trend of the affine network factor β and E moduli than pure PNIPAM microgels for an increasing BIS amount, but only until a DMA percentage of 10 mol%. For a DMA amount of 15 mol%, DMA surprisingly hinders the shrinking of the microgel in a greater tendency as expected for a cross-linker like BIS, while still exhibiting a high stiffness, possibly attributed to catechol interactions within the microgel network.

[†]MG-$c_{B2,D20}$ was excluded due to the flocculation of the sample at higher temperatures.

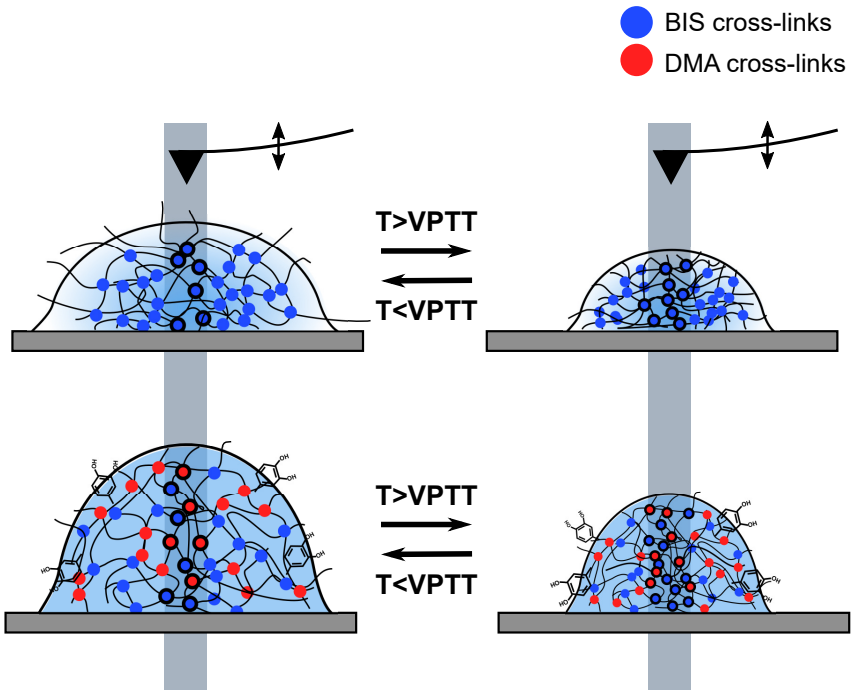

Figure 5.8: Summarising scheme of pure PNIPAM and P(NIPAM-co-DMA) microgels at the surface, measured by AFM force spectroscopy: the cantilever indents into the adsorbed microgel particle at a defined position and compresses the polymer including its cross-links (illustrated by grey area). Subsequently, it retracts. For a more detailed description, see text.

5.4 Conclusion

This present chapter addresses the influence of dopamine methacrylamide (DMA) as a co-monomer on the behaviour of poly(*N*-isopropylacrylamide) (PNIPAM) microgels, particularly focusing on their swelling behaviour in bulk solution and nanomechanical properties after adsorption at the solid surface. Temperature-dependent dynamic light scattering (DLS) measurements show a decrease in the swelling ability when incorporating DMA, since DMA acts as an additional cross-linker. The volume phase transition (temperature) (VPT(T)) is shifted to smaller temperatures as expected for the introduction of a co-monomer with a higher hydrophobicity than NIPAM like DMA, while showing a sharpening of the VPT. Atomic force microscopy (AFM) measurements performed on adsorbed P(NIPAM-co-DMA) microgels show an increasing E modulus, and therefore an increase in stiffness, as the DMA content rises. This is similar to what was shown for pure PNIPAM microgels with increasing BIS amount, con-

firming the role of DMA as a cross-linking agent. E moduli increase over the whole microgel's cross-section when comparing P(NIPAM-co-DMA) microgels to pure PNIPAM microgels without DMA. For both microgels, the smallest E moduli are found at the outer regions of the microgel particles, verifying the microgels' heterogeneous character. Nevertheless, the incorporation of DMA leads to a stiffening of the shell. Temperature-dependent AFM measurements below and above the VPTT show a significant stiffening of the microgels, attributed to a higher cross-linker and polymer density in the collapsed state. The affine network parameter β is proportional to the E modulus of the microgels and falls on the same master curve for both types of microgels. Nonetheless, a large DMA amount of 15 mol% suppresses the shrinkage of the microgel, while maintaining large E moduli, potentially owing to catechol interactions within the network. The results enable the possibility to design catechol-containing PNIPAM microgel systems customised for specific applications, especially by controlling their cohesive strength. Free catechol groups incorporated in the microgel network might further promote the applicability of these systems in the future by increasing the adhesion of these systems - which is the subject of the investigation in the upcoming chapter.

6 Adhesion of P(NIPAM-co-DMA) microgels

Similar content is contained in a draft of a manuscript, which will be submitted for publication in the near future. Sandra Forg, Carina Schneider, Bastian Füßer, Fiona Berner, Rüdiger Berger and Regine von Klitzing, *in preparation*.

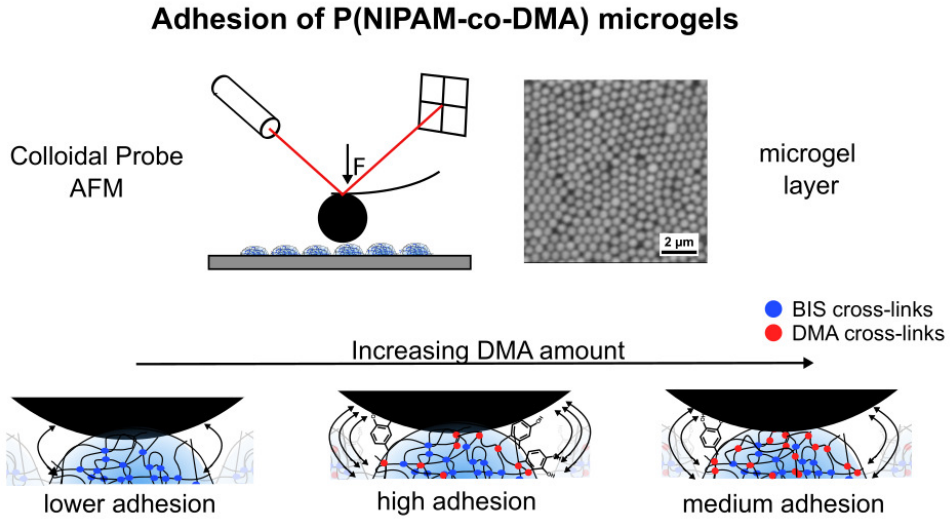

Abstract

Mussels can firmly adhere to a wide range of surfaces even in rough under-water environments, primarily achieved due to catechol groups contained in the mussel byssus. In this chapter, we investigate the adhesion of poly(*N*-isopropylacrylamide) (PNIPAM) microgels co-polymerised with varying concentrations of dopamine methacrylamide (DMA) using colloidal probe force spectroscopy. DMA, as a co-monomer, is able to

mimic the mussel's properties. The measurements are conducted on closed microgel layers prepared on silicon wafers. The interfacial arrangement of the microgel particles is precisely controlled by the Langmuir-Blodgett technique. By varying the surface pressure during the deposition, different packing densities are explored.
At low and medium packing densities, P(NIPAM-co-DMA) microgels exhibit superior adhesion compared to pure PNIPAM microgels. We have identified a DMA content of 10 mol% for optimal adhesive properties. However, increasing the DMA amount to 15 mol% results in reduced adhesion. This behaviour is associated with the increasing stiffness of the microgels, as confirmed by colloidal probe measurements and consistent with the findings of chapter 5, which, in turn, reduce their adhesive properties. With a further increase to 20 mol% DMA, dense microgel packing are no longer achievable due to the increased stiffness. Both results underline the challenging balance between adhesive and cohesive properties in the development of mussel-inspired materials. Interestingly, when employing high surface pressures during the Langmuir-Blodgett transfer, pure PNIPAM microgels possess higher adhesive properties than P(NIPAM-co-DMA) microgels. This phenomenon can be attributed to enhanced interactions between the microgel cores at such dense packings. Under these conditions, catechols within the microgels might interact with catechols of neighbouring particles, then being unavailable for interactions with the colloidal probe. These findings provide a full picture of the properties of P(NIPAM-co-DMA) microgels and open up possibilities for further applications.

6.1 Introduction

Catechols, as found in the mussel's byssus, enable strong adhesion to substrates through various interaction mechanisms like hydrogen bonding or metal coordination as explained in chapter 2.2. Additionally, they contribute to the cohesive strength of the mussel byssus, enhancing their mechanical resilience. The balance of both mechanisms is responsible for the exceptional under-water performance observed in marine systems such as mussels. Consequently, this balance is of great significance in the development of novel materials with analogous capabilities.
Putnam *et al.* [59] studied this interplay by investigating a terpolymer composed of three different types of monomers. While dopamine methacrylamide (DMA) was used as the adhesive co-monomer, methyl methacrylate provided the polymer stiffness and

poly(ethylene glycol) methyl ether methacrylate imparted flexibility. Lab shear adhesion tests were conducted on high surface energy (aluminium) and low surface energy (teflon) substrates. The tests reveal that the highest adhesive properties are achieved with a DMA content of 10 mol% for the former substrate, while 41 mol% are required for the latter. A further increase in catechol amount results in an increasing stiffness of the material at the expense of adhesion. The work highlights the significance of both, adhesive and cohesive properties, within a polymeric system - and their balance varies depending on the type of surface to which the polymer is applied.

The combination of hydrogels with catechol chemistry holds promise for future applications, especially in the biomedical field [8, 124, 127, 128], where both adhesion and stiffness are required. Wang *et al.* [30], for instance, synthesised negatively charged poly(acrylic-acid) (PAA) polymers containing 30 mol% of catechol moieties. By cross-linking the material with the metal chelator Zn^{2+}, they developed a switchable material: By increasing the pH value, the material switches from an adhesive coacervate to a cohesive, self-healing hydrogel with reduced adhesive properties.

We combined poly(*N*-isopropylacrylamide) (PNIPAM) microgels with the mussel-inspired co-monomer dopamine methacrylamide (DMA) during this thesis. In this chapter, the adhesive properties of these P(NIPAM-co-DMA) microgels are studied using colloidal probe force spectroscopy. While we examined the mechanical properties and swelling behaviour of the microgels in chapter 5, their adhesive properties remain an open question. Force maps conducted in chapter 5 already confirm the adhesive nature of both types of microgels, PNIPAM and P(NIPAM-co-DMA); the tip adheres to the microgels during the retraction, which is visualised in the lift-off maps. Nevertheless, it is essential to qualitatively determine the adhesion and investigate differences between the microgels. This chapter places particular emphasis on investigating the interplay between adhesive and cohesive properties and to the critical balance of them to achieve optimal microgel adhesion.

The colloidal probe technique is best suitable to determine adhesive forces via force spectroscopy since colloidal probes provide a well-defined contact area between probe and sample (details see chapter 3.6.2). To conduct these measurements, silica spheres are attached to cantilevers and then indented into a layer of densely packed microgel particles. The adhesion force, denoted as F_{adh}, is derived by analysing the retract curves obtained from force spectroscopy measurements as specified in chapter 3.6.2. F_{adh} is normalised to the contact area A between probe and sample to consider the different particle stiffnesses. The microgel layers are prepared on silicon wafers with

the Langmuir-Blodgett technique. At first, the influence of different microgel packing densities is studied for two representative microgel samples: a pure reference PNIPAM microgel and a P(NIPAM-co-DMA) microgel with 10 mol% of incorporated DMA. Subsequently, the impact of an increasing DMA content on the adhesive properties of the microgels is investigated. In the end, the global mechanical properties of the sample are ascertained (global E modulus E_{glob}) and compared to the nanomechanical properties (local E modulus E_{loc}) as assessed in chapter 5 with a tip as indenter. This chapter aims to provide a complementary understanding of the microgels developed in this thesis.

6.2 Results

6.2.1 Effect of packing density on adhesion forcse

Three samples of each microgel, the pure reference poly(*N*-isopropylacrylamide) (PNIPAM) microgel MG-$c_{B2,D0}$ and the P(NIPAM-co-DMA) microgel MG-$c_{B2,D10}$ with 10 mol% of dopamine methacrylamide (DMA), were prepared by deposition on silicon wafers using the Langmuir-Blodgett technique (details see chapter 3.6.2). Comprehensive information regarding the synthesised microgels can be found in table 3.2, chapter 3.3.
The microgels were transferred onto silicon wafers with an installed dipping mechanism in the Langmuir trough. Three distinct surface pressures Π were used for the deposition, resulting in the formation of microgel layers with varying packing densities: $5\,mN\,m^{-1}$ for low packing (lp), $21\,mN\,m^{-1}$ for medium packing (mp) and $24\,mN\,m^{-1}$ for dense packing (dp). It's noteworthy that each layer consists of a single monolayer of microgel particles. The microgel layers were scanned by atomic force microscopy (AFM) in ambient conditions (see chapter 3.6.1). The AFM scans are depicted in fig. 6.1 (a) for the pure PNIPAM microgel MG-$c_{B2,D0}$ and (b) for the P(NIPAM-co-DMA) microgel MG-$c_{B2,D10}$ and clearly illustrate the different packing densities of the microgel layers: with an increasing surface pressure, the distance between the microgel particles decreases.

The packing density was quantified by analysing the nearest neighbour distance (NND) of the microgels in the AFM scans with the image analysis software ImageJ

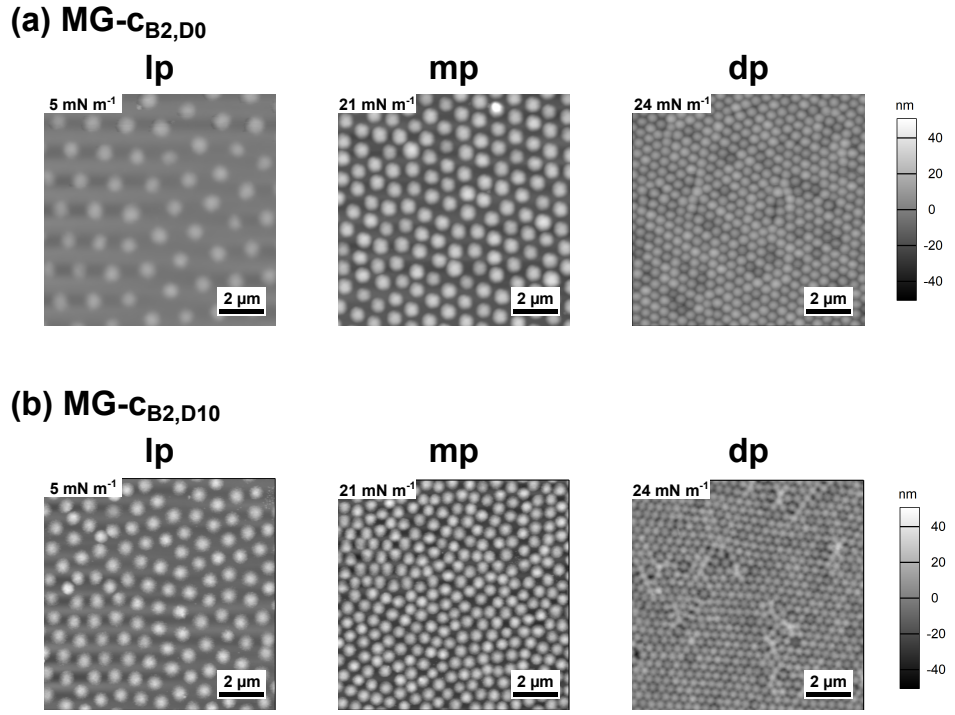

Figure 6.1: AFM scans of microgel layers prepared by the Langmuir-Blodgett technique at varying surface pressures Π. The surface pressures Π (5 mN m^{-1}, 21 mN m^{-1} and 24 mN m^{-1}) result in different packing densities: low packing (lp), medium packing (mp) and dense packing (dp). (a) illustrates the prepared microgel layers of the pure PNIPAM microgel MG-c$_{B2,D0}$ and (b) shows the microgel layers of the P(NIPAM-co-DMA) microgel MG-c$_{B2,D10}$.

(for details see 3.6.1). The NND, in dependence of the surface pressure Π applied in the Langmuir trough, is illustrated in fig. 6.2. The dashed horizontal lines represent the hydrodynamic diameters D_H of the microgels at 20°C, which is comparable to the room temperature in the lab.

For both types of microgels, the NND decreases with an increasing surface pressure Π, indicative of a higher packing density. This decrease is less pronounced for the mussel-inspired microgel P(NIPAM-co-DMA) microgel MG-c$_{B2,D10}$ due to relatively large NND errors. Nevertheless, the trend is clearly evident in the AFM scans. MG-c$_{B2,D10}$ consistently exhibits smaller NNDs than the pure PNIPAM microgel MG-c$_{B2,D0}$, which is distinct at low surface pressures. However, both approach similar values at larger compressions. At a surface pressure of $\Pi = 24\,\mathrm{mN\,m^{-1}}$, the NNDs of both are comparable.

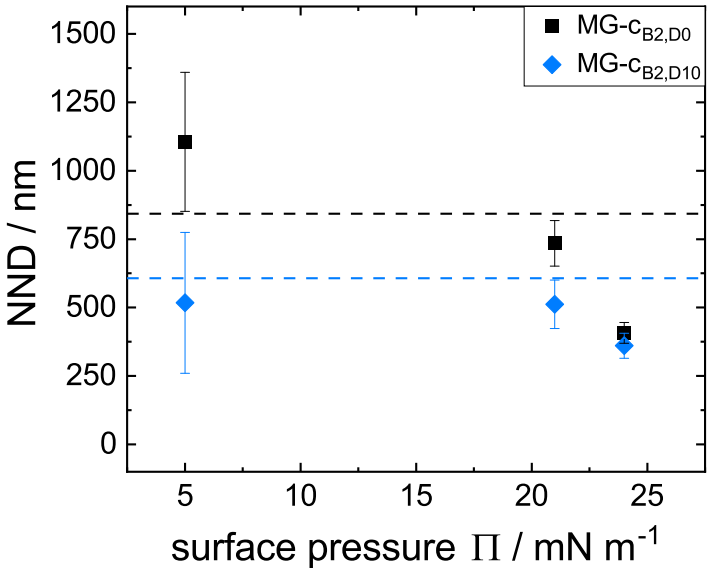

Figure 6.2: Mean nearest neighbour distance (NND) of the pure PNIPAM microgel MG-c$_{B2,D0}$ and the P(NIPAM-co-DMA) microgel MG-c$_{B2,D10}$ in dependence of the surface pressure Π. The NND was analysed from the AFM scans with ImageJ [152]. The dashed horizontal lines correspond to the hydrodynamic diameters D_H of the microgels at 20°C, chosen to be similar to the temperature in the lab.

When comparing the NND to the microgels' hydrodynamic diameter D_H, D_H is consistently larger than the NND. The only exception to this trend is observed in the case of the pure PNIPAM microgel MG-c$_{B2,D0}$, which was prepared at a low surface pressure of 5 mN m^{-1}. Though, it is important to note that the NND values exhibit significant errors at this specific, low surface pressure.

Colloidal probe force spectroscopy measurements were performed to determine the adhesion force F_{adh} for both types of microgels: the pure PNIPAM microgel MG-c$_{B2,D0}$ and the P(NIPAM-co-DMA) microgel MG-c$_{B2,D10}$. The technique is outlined in chapter 3.6.2 and the results are related to the packing density of the microgel particles. To assess potential ageing effects during the measurements caused by e.g. material ageing or contaminations, four force maps were captured at different positions with a trigger point of 15 nN: one at position A, two at position B and one

at C (for more details see chapter 3.6.2). Exemplary force curves of the measurements are shown in fig. A31 (appendix). Each force curve of the force maps was conducted with a 500 nm distance from the adjacent curve, resulting in a distribution of F_{adh}. The maximum of a Gaussian fit to this distribution was taken as the average adhesion force, as specified in chapter 3.6.2. It's worth noting that the colloidal probe might indent into the spaces between two particles when indenting the microgel layer, which explains the notably lower adhesive force values observed in the distribution. The medium indentation depth δ was determined from an average of 10 force curves (table A4, appendix).
The colloidal probes were analysed using scanning electron microscopy (SEM), as outlined in chapter 3.10. The corresponding SEM images are displayed in fig. A32 and were used to calculate the average probe radii R_P (values see table A4, appendix).
The adhesion force F_{adh} was normalised to the contact area A, which is calculated with eq. 3.23 (table A4, appendix). The normalisation considers the variations in contact area A between probe and sample, resulting from differences in microgel stiffness. For stiffer microgels, the colloidal probe indents less into the microgel layer than for softer ones due to the constant trigger point force.

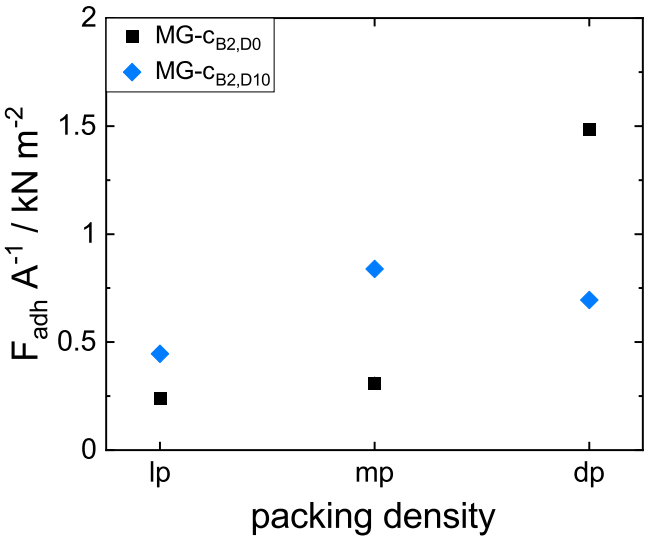

Figure 6.3: Average normalised adhesion forces $F_{adh}\,A^{-1}$ of the pure PNIPAM microgel MG-c$_{B2,D0}$ in comparison to the P(NIPAM-co-DMA) microgel MG-c$_{B2,D10}$ in dependence of their packing density.

Fig. 6.3 depicts the normalised adhesion force $F_{adh}\,A^{-1}$ (average from four force maps) in dependence of the packing density for the two microgels MG-$c_{B2,D0}$ and MG-$c_{B2,D10}$. The error of $F_{adh}\,A^{-1}$ values, calculated by Gaussian error propagation, is smaller than $0.01\,kN\,m^{-2}$; thus, these errors are not represented in fig. 6.3.
For an increasing packing density from lp to mp, the average normalised adhesion force $F_{adh}\,A^{-1}$ increases. The increase is larger for the mussel-inspired P(NIPAM-co-DMA) microgel than for the pure PNIPAM microgel MG-$c_{B2,D0}$. The P(NIPAM-co-DMA) microgel MG-$c_{B2,D10}$ demonstrates a higher $F_{adh}\,A^{-1}$ than MG-$c_{B2,D0}$ for both packing densities. However, as the packing density increases further from a mp to a dp, $F_{adh}\,A^{-1}$ only increases further for the pure PNIPAM microgel MG-$c_{B2,D0}$, but surprisingly decreases for the P(NIPAM-co-DMA) microgel MG-$c_{B2,D10}$. The increase of $F_{adh}\,A^{-1}$ for the pure PNIPAM microgel is significant (around $1.2\,kN\,m^{-2}$). Moreover, the pure PNIPAM microgel exhibits superior adhesion compared to the P(NIPAM-co-DMA) microgel for this high packing density. The decrease in the adhesion force for microgels with DMA at dp is found to be reproducible with a new sample and a new colloidal probe (details can be found in chapter A6.1, appendix).
For the pure PNIPAM microgel MG-$c_{B2,D0}$ with a dp, $F_{adh}\,A^{-1}$ decreases during successive measurements on different spots at the wafer. This ageing effect is reproduced with a new, freshly cleaned colloidal probe at a different spot on the silicon wafer (for additional information see chapter A6.1, appendix). It seems to result from colloidal probe contaminations, particularly in measurements involving dense microgel packings with high adhesion forces. To exclude the influence of this phenomenon from further analysis, the adhesion force $F_{adh}\,A^{-1}$ of this sample is only derived from the force map conducted at position A. For the remaining microgel samples, including those in the following section, no ageing effects were observed (see fig. A33, appendix).

6.2.2 Effect of DMA amount on adhesion forces

The adhesive properties of the pure PNIPAM microgel MG-$c_{B2,D0}$ compared to the mussel-inspired P(NIPAM-co-DMA) microgels with an increasing DMA content (MG-$c_{B2,D5}$, MG-$c_{B2,D10}$, MG-$c_{B2,D15}$ and MG-$c_{B2,D20}$) were investigated. Informations about the synthesised microgels can be found in table 3.2. Microgels were transferred onto silicon wafers using the Langmuir-Blodgett technique conducted at similar surface pressures (see chapter 3.6.2), resulting in a mp density of microgel particles. Mp

densities were chosen based on the results of the previous section, where samples prepared with a dp show ageing effects (pure PNIPAM microgel MG-$c_{B2,D0}$ with high adhesion forces $F_{adh}\,A^{-1}$) and an unexpected decrease in $F_{adh}\,A^{-1}$ (P(NIPAM-co-DMA) microgel MG-$c_{B2,D10}$ at high packing densities). These effects need to be eliminated from further considerations. AFM scans of the samples are provided in fig. 6.4.
For the microgel with the highest DMA amount MG-$c_{B2,D20}$, it was not possible to achieve a closed microgel layer (see fig. 6.4 (e)). Instead, microgel particles arrange in clusters at the silicon wafers. Since homogeneous microgel layers are required to reasonably conduct the colloidal probe measurements, the sample is unsuitable for the measurement conditions and was thus excluded.

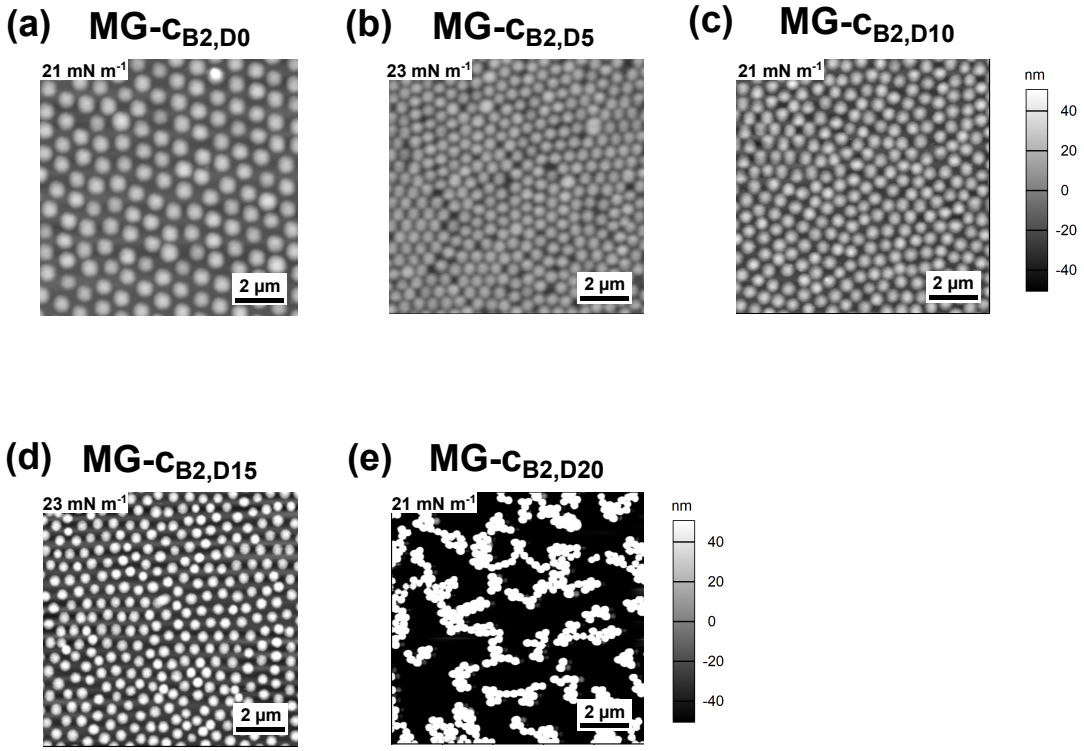

Figure 6.4: AFM scans of samples prepared by the Langmuir-Blodgett technique with a mp: (a) pure PNIPAM microgel MG-$c_{B2,D0}$ and P(NIPAM-co-DMA) microgels with increasing DMA content (b) MG-$c_{B2,D5}$, (c) MG-$c_{B2,D10}$, (d) MG-$c_{B2,D15}$ and (e) MG-$c_{B2,D20}$. For MG-$c_{B2,D20}$, no closed microgel layer could be obtained - instead particles arrange in clusters.

Equivalently to the previous section, the NND was calculated from the AFM scans using ImageJ. In fig. 6.5, the NND values (represented by closed symbols) are plotted

against the sum of the concentration of the cross-linker *N*,*N*′-methylene-bisacrylamide (BIS) c_{BIS} and the injected amount of DMA $c_{DMA,injected}$. Additionally, the hydrodynamic diameters D_H of the microgels at 20°C, selected to match the lab's room temperature, are illustrated in the same figure (open symbols).
The P(NIPAM-co-DMA) microgels have comparable NND values (around 500 nm), whereas the PNIPAM microgel exhibits a larger NND of about 735 nm. It's crucial to note though that the calculated NNDs possess large errors.
When comparing the NNDs to the hydrodynamic diameters D_H, it becomes evident that, in most cases, D_H slightly exceeds the NND. An exception to this is the microgel MG-$c_{B2,D15}$, where the NND is slightly larger than D_H.

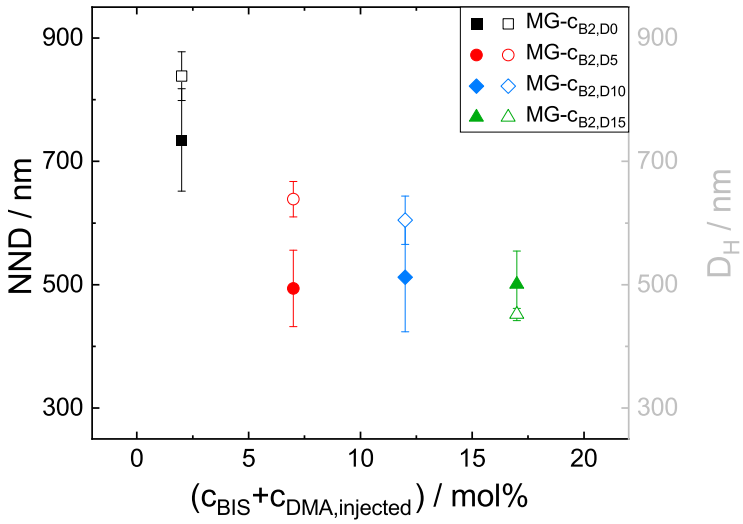

Figure 6.5: Mean NND of the pure PNIPAM microgel MG-$c_{B2,D0}$ and the P(NIPAM-co-DMA) microgels with increasing DMA amount in dependence of the sum of the concentration of the cross-linker BIS c_{BIS} and the injected amount of DMA $c_{DMA,injected}$ (closed symbols). The NND was analysed from the AFM scans with ImageJ [152]. Additionally, the hydrodynamic diameter D_H of the microgels at 20°C, selected to match the lab's room temperature, is illustrated (open symbols).

Colloidal probe force spectroscopy, as specified in chapter 3.6.2, was conducted to study the effect of an increasing DMA amount on the normalised adhesion force $F_{adh}\,A^{-1}$. An average indentation depth δ and contact area A were calculated

as detailed previously and their values are provided in table A5 (appendix). The indentation depth δ decreases from $193.3 \pm 15.2\,\text{nm}$ to $84.1 \pm 8.7\,\text{nm}$ with an increasing DMA amount from the pure, softer PNIPAM microgel MG-$c_{B2,D0}$ to the stiffer P(NIPAM-co-DMA) microgel MG-$c_{B2,D15}$. This highlights that, for the same trigger point force, the colloidal probe indents less into the microgel layer for stiffer microgels. As a consequence, the contact area A also decreases from $6.03 \pm 0.4\,\mu\text{m}^2$ to $2.21 \pm 0.23\,\mu\text{m}^2$. The mean colloidal probe radii R_P, derived from the SEM images (see fig. A36, appendix), are given in the same table A5.

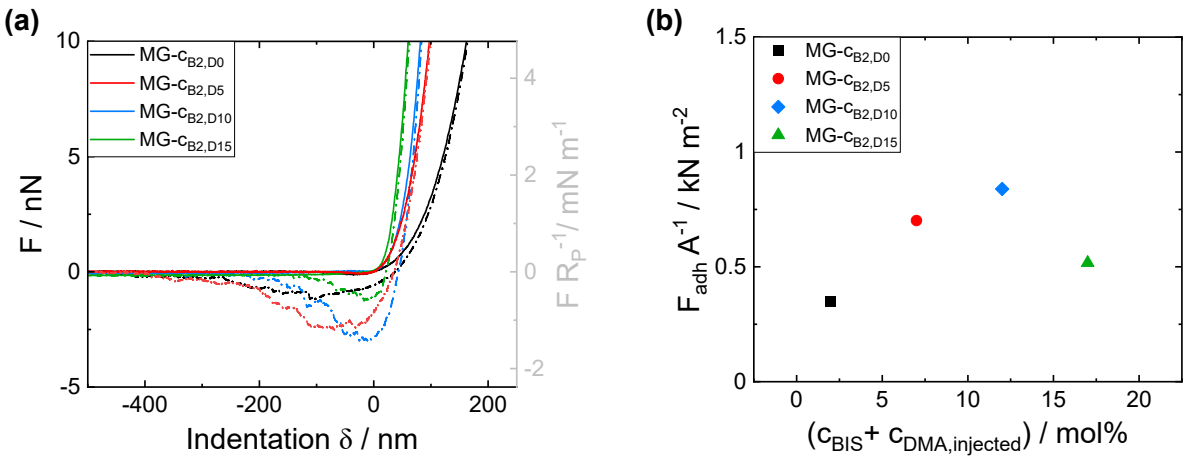

Figure 6.6: (a) Exemplary force curves of the investigated microgels: pure PNIPAM microgel MG-$c_{B2,D0}$ and P(NIPAM-co-DMA) microgels with increasing DMA amount. The continuous line represents the approach curve, while the dashed line represents the retract curve. The right y-axis is displayed in FR_P / $\text{mN}\,\text{m}^{-1}$ to facilitate a comparison with existing literature. (b) The average normalised adhesion $F_{adh}\,A^{-1}$ of the different microgels in dependence of the sum of cross-linker BIS concentration c_{BIS} and injected DMA amount $c_{DMA,injected}$.

Exemplary force curves of the pure PNIPAM microgel MG-$c_{B2,D0}$ and the P(NIPAM-co-DMA) microgels with increasing DMA content (from MG-$c_{B2,D5}$ to MG-$c_{B2,D15}$) are shown in fig. 6.6 (a). The approach curve is illustrated as a continuous line, while the retract curve is illustrated as a dashed line. To facilitate the comparison with force spectroscopy data of chapter 5, the left y-axis is given in F / nN. However, for colloidal probe measurements the force F is typically normalised by the probe radius R_P. For consistency with literature, the right y-axis is presented in FR_P / $\text{mN}\,\text{m}^{-1}$. The average

normalised adhesion $F_{adh}\,A^{-1}$ is plotted against the sum of the cross-linker BIS concentration c_{BIS} and the injected DMA amount $c_{DMA,injected}$ in fig. 6.6 (b). The $F_{adh}\,A^{-1}$ values exhibit errors smaller than $0.01\,kN\,m^{-2}$ again. Hence, they are excluded from fig. 6.6 (b).
The measurements show that the incorporation of DMA enhances the adhesion force of the mussel-inspired P(NIPAM-co-DMA) microgels when compared to the reference PNIPAM microgel MG-$c_{B2,D0}$. The highest adhesion is achieved with the microgel MG-$c_{B2,D10}$ containing 10 mol% DMA, reaching $F_{adh}\,A^{-1}$=$0.84\,kN\,m^{-2}$. Further increasing the DMA content to 15 mol% results in decreased adhesion forces of $F_{adh}\,A^{-1} = 0.52\,kN\,m^{-2}$. Yet, they still surpass the adhesion forces of the pure PNIPAM microgel.

6.2.3 Global vs. local *E* modulus

In addition to characterising the adhesive properties of the samples, comprehensive insights into the mechanical properties of the entire microgel layer (global mechanical properties) can be extracted from the colloidal probe force spectroscopy measurements [61]. These results are complementary to the nanomechanical properties of the microgel particles discussed in chapter 5, where a local E modulus (E_{loc}) was determined in the centre of 10 individually adsorbed microgel particles. Equivalently to chapter 5, the Hertz model (eq. 3.21) was applied to the approach curves to determine a global E modulus (E_{glob}) of the samples. The validity of the Hertz model was confirmed up to indentation depths of 100 nm (see fig. A3, appendix). For each sample, 10 force curves were evaluated and all analysed force curves are presented in fig. A37, provided in the appendix. One exemplary force curve for each microgel, along with the applied Hertzian fit, is depicted in fig. 6.7 (a). Notably, the slope of the force curves increases with an increasing amount of DMA from the reference pure PNIPAM microgel MG-$c_{B2,D0}$ (black curve) to the P(NIPAM-co-DMA) microgel MG-$c_{B2,D15}$ (green curve). The resulting E_{glob} moduli are plotted against the sum of the concentration of BIS c_{BIS} and the concentration of injected DMA $c_{DMA,injected}$ in fig. 6.7 (b). E_{glob} shows a slow gradual increase from $E_{glob} = 42.2 \pm 12.2\,kPa$ for the reference PNIPAM microgel MG-$c_{B2,D0}$ to $E_{glob} = 82.5 \pm 24.8\,kPa$ for the P(NIPAM-co-DMA) microgel MG-$c_{B2,D15}$. Errors of E_{glob} closely align with errors of local E moduli E_{loc} having comparable values, as determined in chapter 5.

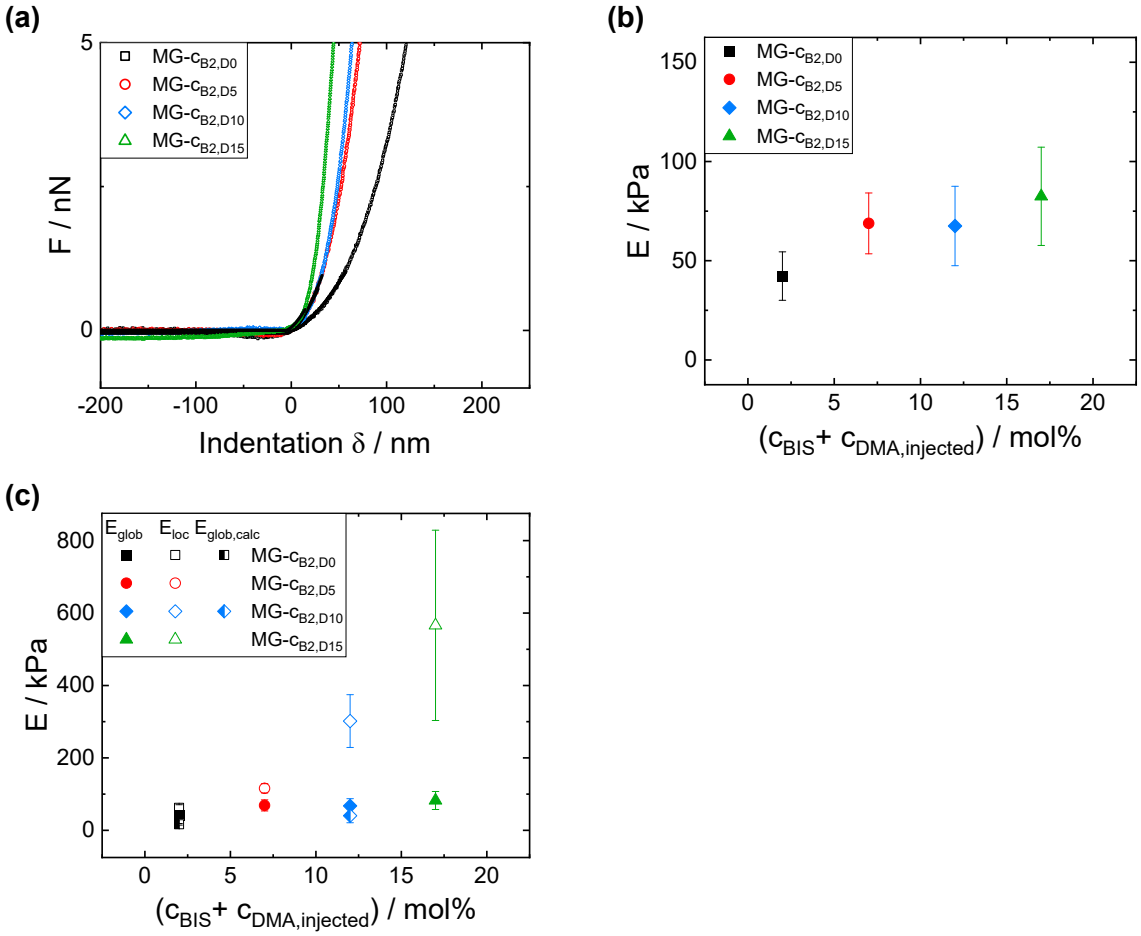

Figure 6.7: (a) Exemplary approach curves (open symbols) together with the corresponding Hertzian fit, presented for each microgel sample: the pure PNIPAM microgel MG-$c_{B2,D0}$ and the P(NIPAM-co-DMA) microgels MG-$c_{B2,D5}$, MG-$c_{B2,D10}$ and MG-$c_{B2,D15}$. (b) Resulting global modulus E_{glob} derived from an average of 10 force curves, plotted against the sum of the concentration of BIS c_{BIS} and the concentration of injected DMA $c_{DMA,injected}$. (c) Comparison between the measured global modulus E_{glob} (closed symbols), the calculated global modulus $E_{glob,\,calc}$ (half-closed symbols) and local modulus E_{loc} (open symbols) of the different microgels.

A comparison between the global modulus E_{glob} (closed symbols) to the local E modulus E_{loc} (open symbols) is presented in fig. 6.7 (c). The local modulus E_{loc} always exceeds the global E_{glob}. For the reference PNIPAM microgel MG-$c_{B2,D0}$, E_{loc} possesses a value of $E_{loc} = 62.0 \pm 8.8\,\text{kPa}$, while $E_{glob} = 42.2 \pm 12.2\,\text{kPa}$. For the mussel-inspired P(NIPAM-co-DMA) microgel MG-$c_{B2,D10}$, the disparity between these values

is even more pronounced. Here, the local modulus is notably higher with a value of $E_{loc} = 301.7 \pm 72.9\,kPa$, while the global one is $E_{glob} = 67.5 \pm 20.0\,kPa$. Thus, the impact of DMA on the global modulus E_{glob} is less significant compared to its effect on the local modulus E_{loc}.
Additionally, a global modulus $E_{glob,calc}$ can be calculated from the distribution of the local modulus E_{loc} across the particle cross-section, as determined in the previous chapter (see chapter 5, fig. 5.4). The distribution was determined for MG-$c_{B2,D0}$ and MG-$c_{B2,D10}$ as an average of 5 particles.
To obtain $E_{glob,calc}$, each local modulus E_{loc} is attributed to a specific annulus - a region between two circles of different radius - within the whole particle area when it is adsorbed at the surface. This association is determined through the calculation of the weighting factor w_i by:

$$w_i = \frac{\pi(R_a - R_i)^2}{\pi R_p^2}. \tag{6.1}$$

Here, R_a is the radius of the outer circle and R_i the radius of the inner circle (distance from centre of the particle to the annulus). R_p is the overall particle radius when adsorbed at the surface.
The global modulus $E_{glob,calc}$ is then determined by summing up the products of the weighting factors w_i and their respective local moduli E_i in this specific area, using the equation:

$$E_{glob,calc} = \sum_i w_i E_i. \tag{6.2}$$

The results are illustrated in fig. 6.7 (c) as half-closed symbols for MG-$c_{B2,D0}$ and MG-$c_{B2,D10}$. The values of $E_{glob,calc}$ are in the same order of magnitude as the measured modulus E_{glob}, but are slightly smaller.

6.3 Discussion

6.3.1 Interparticle interactions within deposited microgel particles

The pure poly(*N*-isopropylacrylamide) (PNIPAM) microgel MG-$c_{B2,D0}$ and the mussel-inspired P(NIPAM-co-DMA) microgel with 10 mol% dopamine methacrylamide (DMA) MG-$c_{B2,D10}$ were deposited onto silicon wafers with varying packing densities using the Langmuir-Blodgett technique. This deposition method was successfully used in literature [200–204] to achieve precisely ordered microgel structures

and control the particle distance. The particle distance, more precisely the nearest neighbour distance (NND), was found to decrease as the surface pressure Π during the deposition increases [200, 201, 203].

This aligns with our observations, where the NND decreases for an increasing surface pressure Π for both the reference PNIPAM microgel MG-$c_{B2,D0}$ and the mussel-inspired P(NIPAM-co-DMA) microgel MG-$c_{B2,D10}$ (see fig. 6.2). At low surface pressures, the NND of the reference microgel is significantly larger than that of the P(NIPAM-co-DMA) microgel. At high surface pressures (24 mN m^{-1}), the NND values converge for both types of microgels. These observations are akin to findings by Rauh *et al.* [203], who investigated particles with a rigid silica core surrounded by a soft PNIPAM shell of varying thickness. They reported that for a decreasing PNIPAM shell thickness, the NND decreases. At high surface pressures, the NNDs of all particles become similar. This behaviour is attributed to the preparation technique: a transition between shell-shell interactions at low compressions to particle core-core interactions at high compressions occurs [201]. During the Langmuir-Blodgett technique at low surface pressures, the NND is therefore dependent on the overall size of the particles, including their shells. In our case, the P(NIPAM-co-DMA) microgel MG-$c_{B2,D10}$ exhibits a smaller hydrodynamic diameter D_H in the swollen state than the pure PNIPAM microgel, as highlighted in fig. 6.2 (see additionally evaluation in chapter 5). At high surface pressures in contrast, core-core contacts are favoured, so only the core size matters. Both types of microgels, pure PNIPAM microgels and P(NIPAM-co-DMA) microgels, possess similar diameters in the collapsed state - attributed to similar core sizes. Considering these insights and further literature [200–202, 204], we assume that for the samples with the highest microgel packing density (dense packing, dp), the cores of the microgel particles are in direct contact with each other. This explains the similarities of our results to those obtained by Rauh *et al.* [203].

The NND is consistently smaller than the hydrodynamic diameter D_H at 20°C, indicating that the microgels experience more compression at the surface than in the bulk. An exception to this trend was shown for the soft PNIPAM microgel at a low surface pressure of 5 mN m^{-1}. As discussed in chapter 2.1.3, microgels undergo deformation when adsorbed at surfaces. Microgels with low cross-linker amounts expand parallel to the surface while compressing perpendicular, resulting in a fried egg structure. This behaviour vanishes as the cross-linker content is increased to $1-3$ mol% [92]. At these higher cross-linking degrees, the microgel diameter at the interface closely aligns with

the hydrodynamic diameter D_H of the microgels in bulk solution. In the case of the softer PNIPAM microgel prepared at a surface pressure of $5\,mN\,m^{-1}$, the microgel particles exhibit more substantial lateral stretching when adsorbed at the surface compared to the stiffer P(NIPAM-co-DMA) microgel. This behaviour is apparent from the larger NND compared to D_H in this case. The P(NIPAM-co-DMA) microgel is already too stiff (see chapter 5), causing it to experience greater compression at the surface than in bulk at this surface pressure. Consequently, its NND is smaller than its D_H. Nonetheless, it's important to note that at this low surface pressure, the NND values possess substantial errors, making it difficult to draw clear conclusions.

The average normalised adhesion force $F_{adh}\,A^{-1}$, as determined by colloidal probe AFM, of the pure PNIPAM microgel MG-$c_{B2,D0}$ increases for an increasing packing density. This trend is consistent with the expectation that a higher packing density leads to a larger number of microgel particles per area. The AFM scans (fig. 6.1) visually confirm this behaviour. Due to the augmented microgel and consequently, higher polymer density at the surface, the colloidal probe interacts with a larger amount of material. As a result, it is anticipated that higher packing densities will result in increased adhesion forces, a trend that is indeed confirmed by our data for the pure PNIPAM microgel.
For the mussel-inspired P(NIPAM-co-DMA) microgel, the increase of $F_{adh}\,A^{-1}$ is only observed when increasing from a low packing (lp) to a medium packing (mp) density. However, upon further increasing the packing density to a dp, a reproducible decrease in $F_{adh}\,A^{-1}$ is observed. The catechols of DMA incorporated in the microgel network can interact via various interaction mechanisms, such as hydrogen bonding, metal coordination or covalent cross-linking (for details see chapter 2.2). As the NND decreases due to the dense packing of microgels, interparticle interactions between the particles increase. The free catechol moieties [4] of neighbouring particles can then start to interact with each other. Additionally, the compressed shells of the microgel particles may lead to an overall shielding of the catechol groups. In both cases, some catechol moieties are excluded from adhesive interactions with the colloidal probe during the measurements. Thus, the measured adhesive forces decrease and become even lower than for the reference PNIPAM microgel. Nevertheless, for both lp and mp, the mussel-inspired P(NIPAM-co-DMA) microgel proves to be more adhesive than the pure PNIPAM microgel.

Additionally, studies were conducted on the remaining P(NIPAM-co-DMA) microgels with increasing DMA amounts and a mp.
The P(NIPAM-co-DMA) microgels exhibit similar NND values, as calculated by image analysis of the AFM scans as described before. In contrast, the pure PNIPAM microgel MG-$c_{B2,D0}$ possesses a larger NND. Similar studies have not been carried out for P(NIPAM-co-DMA) microgels yet, but insights can be drawn from studies involving PNIPAM-based particles [200–204]: From medium to high surface pressures, the microgel shells undergo further compression - compressed shell-shell contacts are slowly transitioned into core-core contacts. Consequently, the influence of the core sizes of the microgels becomes more dominant. Despite the P(NIPAM-co-DMA) microgels having smaller swollen sizes than the pure PNIPAM microgel due to their higher cross-linking density (detailed in chapter 5), the collapsed microgels have similar core sizes. Hence, one would have expected equal NNDs for all microgels, as the shells become fully compressed and only the core sizes matter. The results are consequently surprising and remain unexplained at this point.
Nevertheless, it's worth mentioning that the NND of the microgels possesses substantial errors, stemming from the re-arrangement of particles at the interface during the transition from shell-shell to core-core contacts, which is in accordance to literature [200, 201, 203]: As particles begin to move, some may be already closer to each other than others. Moreover, the arrangement of the particles is depending on the shell architecture [202, 205], which should differ between the pure PNIPAM microgel and the P(NIPAM-co-DMA) microgels due to the incorporation of the additional cross-links by DMA (see chapter 5) as stated before.
The NND is always smaller than the hydrodynamic diameter D_H of the particles, except for the microgel with the highest DMA amount MG-$c_{B2,D15}$. The explanation is similar to what was mentioned earlier: the microgel particles experience more compression on the surface compared to the bulk. In the case of the microgel MG-$c_{B2,D15}$, both values are comparable, taking into account the large error values associated with the NND. As previously mentioned, Mourran *et al.* [92] discovered that the microgel diameter at the interface closely matches the hydrodynamic diameter D_H of microgels in bulk solution at higher cross-linking degrees. This finding provides an explanation for the observed behaviour of this particular microgel.
For the microgel with the highest DMA content (MG-$c_{B2,D20}$), a closed microgel layer at medium surface pressures couldn't be achieved - instead the microgels form clusters. This is in line with the findings by Rauh *et al.* [203] as well. Their core-shell particles

(silica core, PNIPAM shell) form already clusters at medium compressions during the Langmuir-Blodgett deposition. This clustering is even amplified at higher surface pressures. The primary cause of this behaviour is attributed to the rigid nature of the core, which constrains the re-arrangement of its surrounding shell. In our case, the P(NIPAM-co-DMA) microgel with the highest DMA content (MG-$c_{B2,D20}$) possesses the highest E modulus when compared to the remaining microgels (see chapter 5). The increase in stiffness is predominant in the centre of MG-$c_{B2,D20}$, implying a more rigid core. Even if core sizes are similar for all microgels, the stiff nature of their core could provide an explanation for the formation of clusters, in accordance with literature studies [203]. The clustering is less likely to be caused by adhesive interactions between the particles, as one might expect for high DMA contents. This is because the microgel MG-$c_{B2,D20}$, with the highest DMA content, does not exhibit the strongest adhesion, as discussed in the subsequent section. Instead, MG-$c_{B2,D10}$ is the most adhesive microgel. MG-$c_{B2,D20}$ was excluded from the colloidal probe measurements due to its inability to produce a closed microgel layer.

6.3.2 Influence of DMA on adhesion

Due to the use of DMA as a mussel-inspired co-monomer, the focus of this study lies on determining the adhesive properties of P(NIPAM-co-DMA) microgels with varying DMA amounts through colloidal probe force spectroscopy. The average normalised adhesion forces $F_{adh}\,A^{-1}$ of microgels with varying DMA contents was evaluated. A mp density was chosen, which aims to create microgel layers as dense as possible while reducing interparticle interactions of free catechol moieties within the mussel-inspired microgel networks.

In the course of this investigation, an increase in $F_{adh}\,A^{-1}$ was observed from the pure PNIPAM microgel MG-$c_{B2,D0}$ to the P(NIPAM-co-DMA) microgel MG-$c_{B2,D10}$. As the DMA content is further increased to 15 mol%, $F_{adh}\,A^{-1}$ decreases (see fig. 6.6). Nonetheless, the microgel still remains more adhesive than the pure PNIPAM microgel. While this trend may appear surprising at first sight, it aligns perfectly with a well-known effect: there exists a specific threshold of catechol content in the mussel byssus and in mussel-inspired materials for which maximum adhesive properties are obtained. Increasing the catechol amount beyond this threshold results in greater cohesive instead of adhesive forces (for details see chapter 2.2).

For marine mussels, the optimal L-3,4-dihydroxyphenylalanine (DOPA) amount for

adhesion typically falls within the range of $3 - 30\,\mathrm{mol\%}$ [3], with an average of $10\,\mathrm{mol\%}$. Studies by Putnam *et al.* [59], focusing on polymers co-polymerised with DMA, reveal optimal catechol contents of $10\,\mathrm{mol\%}$ for the adhesion of the polymers to high surface energy substrates like aluminium and $41\,\mathrm{mol\%}$ for low surface energy substrates such as teflon. For higher catechol contents, only the stiffness of the polymer increases until reaching a critical point where the material becomes brittle. As the stiffness of the P(NIPAM-co-DMA) microgels increases with increasing DMA amount (see chapter 5), at one point the elevated mechanical stiffness compensates the increased adhesiveness of the microgels. Both properties need to be carefully balanced regarding future applications.

The values of $F_{\mathrm{adh}}\,A^{-1}$ obtained from our measurements range from 0.35 to $0.84\,\mathrm{kN\,m^{-2}}$ (fig. 6.6). The adhesion force F_{adh} can be also normalised to the probe radius R_{P}, which eases the comparison with literature results. This is essential for a comprehensive evaluation. (For reference, $F_{\mathrm{adh}}R_{\mathrm{P}}^{-1}$ is plotted in dependency of the sum of the cross-linker *N,N'*-methylene-bisacrylamide (BIS) concentration c_{BIS} and injected DMA amount $c_{\mathrm{DMA,injected}}$ in fig. A38 in the appendix.) However, direct comparisons are challenging since the results highly depend on the used materials and measurement techniques. To the best of our knowledge, the adhesive abilities of mussel-inspired DMA-co-polymerised microgels have not yet been studied by colloidal probe force spectroscopy. Nevertheless, some comparison can be drawn.

Lu *et al.* [206] examined the adhesive abilities of different mussel foot proteins (mfps), including mfp-3 and mfp-5, to silica surfaces. These are the key adhesive mfps contained in the mussel byssus, as specified in chapter 2.2. They conducted the experiments using a surface force apparatus (SFA), which is designed similarly to the AFM but specialised for measuring interaction forces between larger bodies. For short contact times lasting for 2 min, values of $F_{\mathrm{adh}}R_{\mathrm{P}}^{-1} = 1.2\,\mathrm{mN\,m^{-1}}$ (mfp-3) and $0.5\,\mathrm{mN\,m^{-1}}$ (mfp-5) are obtained. The forces increase by one order of magnitude when the contact time is increased to 60 min. The values are comparable to our results on P(NIPAM-co-DMA) microgels, where $F_{\mathrm{adh}}R_{\mathrm{P}}^{-1}$ values from $0.5\,\mathrm{mN\,m^{-1}}$ to $1.1\,\mathrm{mN\,m^{-1}}$ are achieved. However, it's important to note that the adhesiveness of P(NIPAM-co-DMA) microgels is influenced not only by DMA but also by NIPAM itself. This is demonstrated through the examination of the reference PNIPAM microgel MG-$c_{\mathrm{B2,D0}}$, which displays adhesive forces of $F_{\mathrm{adh}}\,A^{-1} = 0.35\,\mathrm{kN\,m^{-2}}$. Thus, it becomes evident that both DMA and NIPAM contribute to the adhesion. Additional factors such as contact time, measurement technique and variations in the material's stiffness can further impact the data.

This makes a precise value comparison impossible. Nevertheless, data from literature [206] provide confidence in the reliability of our measurement technique and results.

6.3.3 Global vs. local mechanical properties

Additionally to characterising the adhesion forces, global mechanical information of the closed microgel layer can be derived from the colloidal probe measurements as specified in chapter 3.6.2, yielding a global modulus E_{glob}.
Consistent with the findings of chapter 5, where a local modulus E_{loc} was determined, E_{glob} increases with an increasing amount of DMA. This can be ascribed to the increasing cross-linking density within the microgels upon the DMA incorporation, as discussed in detail in the previous chapter.
E_{loc} consistently exceeds E_{glob} due to the nature of the experiments: E_{loc}, determined at the centre of the microgel particles, reflects the stiffness of the core. In contrast, the structural heterogeneities within the core-shell microgels are averaged out during the colloidal probe measurements, as the entire microgel layer is compressed. Given that the core is significantly stiffer, the resultant average global modulus E_{glob} - which combines the core and soft shell - tends to be lower than E_{loc}. This disparity also explains why the increase in E_{glob} is notably smaller compared to the rise in E_{loc} upon the DMA incorporation. The higher polymer density in the centre of the microgel particle results in a more pronounced effect of DMA on E_{loc} than on the global modulus E_{glob} of the microgel layer.
A global modulus $E_{glob,calc}$ was additionally calculated from the local moduli E_{loc} across the particle cross-section of MG-$c_{B2,D0}$ ad MG-$c_{B2,D10}$ (see fig. 5.4). The calculated $E_{glob,calc}$ and measured E_{glob} are of the same order, validating the comparability between the two measurement types of chapter 5 and chapter 6. Nevertheless, differences in the measurement technique contribute to the observed slightly lower values of $E_{glob,calc}$ when compared to E_{glob}: (1) While the colloidal probe indents into the whole microgel layer, capturing the influence of neighbouring particles, for $E_{glob,calc}$ a tip was indented into single adsorbed microgel particles, unaffected by neighbouring particles. The neighbouring particles increase the value of E_{glob}. (2) For $E_{glob,calc}$, the E modulus was averaged over the microgel particle including its shell. However, these loosely cross-linked shells are compressed during the preparation of microgel layers with the Langmuir-Blodgett technique. Therefore, they might not contribute as significantly to E_{glob} than to $E_{glob,calc}$, thereby increasing the value.

A direct comparison of exact E modulus values is, nonetheless, difficult when using different cantilevers and/or tips as emphasised in chapter 3.6.2. However, the overall trend in the data remains and can be stated with pure conscience. The errors obtained from both methods additionally align with each other, further validating the results. The combination of both measurements offers a complete picture of the microgels regarding their mechanical properties. E_{loc} provides structural information about the microgels, including details about their core-shell architecture. Conversely, the global modulus E_{glob} gains predominance, particularly when regarding further applications of these microgels as coatings. Here, the mechanical behaviour of the whole microgel layer is of primary importance.

6.4 Conclusion

This chapter focuses on analysing the adhesive properties of mussel-inspired poly(*N*-isopropylacrylamide-co-dopamine methacrylamide) (PNIPAM-co-DMA) microgels in comparison to pure PNIPAM microgels using colloidal probe force spectroscopy. The microgels were transferred to silicon wafers using the Langmuir-Blodgett technique, providing the ability to adjust interparticle distances by varying the surface pressure during deposition. This directly influences the adhesive properties of the samples. In the case of low and medium packing densities, the P(NIPAM-co-DMA) microgel exhibits larger adhesion than the pure PNIPAM microgel. However, the opposite trend was observed for high packing densities. Due to increased interparticle interactions in this case, free catechol moieties of neighbouring particles might start to interact with each other, rendering them unavailable to contribute to the adhesive forces. At medium packing densities, P(NIPAM-co-DMA) microgels with 10 mol% DMA display the highest adhesion values. For larger DMA amounts of 15 mol%, the adhesion decreases, but the microgel still exhibits larger adhesion than the pure PNIPAM microgel. This behaviour is attributed to the counterbalance between adhesive properties and cohesive coupling in mussel-inspired catechol-containing materials - higher DMA contents confer increased stiffness but come at the cost of reduced adhesion. The stiffness of the microgel layers was confirmed through colloidal probe measurements as well and aligns with the findings of chapter 5, where the nanomechanical properties of single microgel particles were assessed. Both methods show an increase in stiffness for an increasing DMA amount. Together, they provide a comprehensive understanding

of the microgels' mechanical properties. P(NIPAM-co-DMA) microgel particles with 20 mol% DMA exhibit such a high stiffness, especially in their core, that they are unable to form a close layer. Instead they form into clusters.

7 Conclusion and outlook

7.1 Conclusions

This thesis presents the development of a mussel-inspired microgel based on poly(*N*-isopropylacrylamide) (PNIPAM), aiming to improve their mechanical and adhesive properties. Therefore, dopamine methacrylamide (DMA) was embedded as the mussel-inspired co-monomer.

Reaction kinetics

The introduction of a radical scavenger like DMA requires to be controlled. The precise control of the synthesis was achieved. For this purpose, time-samples were collected throughout the co-polymerisation of PNIPAM with a fixed amount of DMA. The samples were analysed via mass spectrometry (MS) to ascertain the individual consumption rates of NIPAM, cross-linker *N*,*N'*-methylene-bis(acrylamide) (BIS) and DMA. The incorporation of DMA was confirmed and quantified by UV-vis and nuclear magnetic resonance (NMR) spectroscopy. The influence of relevant synthesis parameters was addressed. A critical total reaction time threshold of 60 min is found, beyond which the introduction of DMA results in gel clump formation without increasing the DMA incorporation. The timing of the DMA injection is verified as key factor due to its scavenging ability. Early DMA injections impede the NIPAM and BIS conversion while accelerating the DMA reaction speed. Contrarily, a later injection of DMA (between $10 - 15$ min) yields a full NIPAM and BIS conversion, while decelerating its own reaction. In this case, the DMA incorporation can be ensured with a total reaction time of 60 min. Our study unveils that DMA follows a second-order reaction kinetics - which, to the best of our knowledge, is reported for the first time. The reaction is proven to be reproducible and insensitive to UV light. While microgels cross-linked

solely by DMA without the additional cross-linker BIS possess similar reaction kinetics when compared to P(NIPAM-co-DMA) microgels cross-linked by BIS, they exhibit a raspberry-like microgel morphology when DMA injection times are delayed.

Swelling behaviour and nanomechanical properties

The temperature-dependent swelling behaviour of P(NIPAM-co-DMA) microgels with different DMA contents was investigated by dynamic light scattering (DLS). The copolymerisation with DMA results in a volume phase transition (VPT) occurring at lower temperatures in comparison to pure PNIPAM microgels, primarily because of DMA's higher hydrophobicity in contrast to NIPAM. Moreover, DMA accelerates this transition, which could offer advantages in applications where a rapid release of encapsulated particles, such as drugs, within the microgel network is desired. DMA's cross-linking ability is confirmed as P(NIPAM-co-DMA) microgels exhibit reduced swelling ratios and smaller mesh sizes compared to PNIPAM microgels. This cross-linking ability was further elucidated by atomic force microscopy (AFM), where a tip was indented into individual adsorbed microgel particles. A significant increase in their nanomechanical stiffness is observed throughout the entire cross-section of the microgel - DMA cross-links the microgel over the whole structure. P(NIPAM-co-DMA) microgels exhibit a more substantial increase in stiffness upon heating above the VPT temperature (VPTT) when compared to pure PNIPAM. A linear correlation between the elasticity and swelling of the microgel network was validated by calculating the affine network factor, derived from the Flory-Rehner theory. For DMA contents exceeding 15 mol%, however, DMA is observed to impede the shrinking of the microgels. This phenomenon could potentially be attributed to interactions involving catechol groups within the microgel network, which suppress the collapse of the microgels while enhancing their mechanical stability.

Adhesive properties

A balance between adhesive and cohesive properties in mussel-inspired materials is crucial, since an excessive mechanical stiffness can potentially compromise the material's adhesive attributes, similar to what is observed in mussels. Therefore, we conclude this work by investigating the adhesive properties of P(NIPAM-co-DMA)

microgels with varying DMA contents by colloidal probe AFM: a large colloidal probe was indented into a closed microgel layer adsorbed on silicon wafers. These layers were prepared using the Langmuir-Blodgett technique to enable a precise control over their interfacial arrangement. Our findings identify superior adhesion of DMA-co-polymerised PNIPAM microgels for low and medium packing densities when compared to pure PNIPAM microgels. Interestingly, densely packed P(NIPAM-co-DMA) microgels exhibit reduced adhesion compared to pure PNIPAM microgels. This phenomenon is potentially arising from core-core interactions induced by the deposition at high surface pressures. In this case, free catechol moieties within the microgel network might interact with those of neighbouring particles. Additionally, the compressed shell of the microgel particles at this high surface pressures potentially leads to a shielding of the catechol groups. In both cases, they cannot contribute to the adhesive force measured by colloidal probe AFM.
At medium packing densities, P(NIPAM-co-DMA) microgels with a DMA content of 10 mol% display the highest adhesive properties. Elevated DMA concentrations (15 mol%) decrease the adhesion of the microgel due to its high stiffness - highlighting the critical balance required between adhesive and cohesive properties within mussel-inspired materials. The stiffness of the microgel layer was determined additionally from the measurements. The results are complementary to the nanomechanical stiffness determined for single microgel particles in chapter 5. Both together confirm the increasing stiffness of the microgels with an increasing DMA amount. Microgels containing 20 mol% DMA exhibit such high stiffness, particularly in their core, that the formation of a closed layer of microgel particles is not possible. Instead, they form clusters.

We successfully developed mussel-inspired P(NIPAM-co-DMA) microgels and conducted a comprehensive investigation of their various properties. The study encompasses reaction kinetics, swelling behaviour, mechanical properties, and adhesive properties, providing valuable insights into these novel microgels and establishing a robust foundation for potential future applications and research.

7.2 Open questions and future perspectives

While this thesis provides a comprehensive understanding of the newly developed mussel-inspired P(NIPAM-co-DMA) microgels, certain aspects need further clarification.

An unresolved aspect of our study concerns the internal network structure of the microgel particles. Based on the optimised P(NIPAM-co-DMA) synthesis, DMA was added later during the reaction, when NIPAM and BIS are already entirely consumed, and microgel particles have already formed. Consequently, it is conceivable that DMA is mainly located in the outer shell of the microgel particles. In the context of swelling as discussed in chapter 5, DMA shows to sharpen the VPT contrariwise to findings in literature [13, 14]. The discrepancies between our observed sharpened VPT to the broadening observed in literature is attributed to differences in the internal microgel network structures, stemming from variations in our synthesis protocol in comparison to those described in the literature. Obtaining a more profound understanding of the microgel structure is therefore of high importance, and techniques such as small-angle neutron scattering, X-ray scattering or super-resolution fluorescence microscopy could provide valuable insights.
This thesis underlines the significance of balancing adhesive and cohesive properties in mussel-inspired P(NIPAM-co-DMA) microgels. A yet unexplored factor in this context is the pH dependency of the two properties, similar to the pH dependent interactions of catechol groups in the mussel byssus (as discussed in chapter 2.2). Acidic conditions tend to enhance adhesive properties since catechols are primarily present in a reduced state. Conversely, basic conditions promote the cross-linking of catechols, as they are primarily present in their oxidised form. Thus, further investigations in this area are necessary.
In this context and regarding future applications, the chelation capability of catechol-containing polymers is highly promising (see chapter 2.2). Wang *et al.* [30] presented a promising catechol-containing polymer that switches from a highly adhesive coacervate at low pH to a self-healing hydrogel at high pH, when introducing the metal chelator Zn^{2+}. Hence, considering the incorporation of metal chelators becomes relevant when contemplating future applications.
DMA's ability to provide both adhesion and mechanical stiffness is highly versatile, as demonstrated by the previous example. However, other applications may explicitly

demand elevated adhesiveness and explore alternative cross-linking strategies. For these specific cases, the protection of DMA prior to the microgel synthesis might be advantageous, aiming to suppress the cross-linking ability of DMA and further enhance the adhesion of the materials. DMA can be protected, for instance, by using acetonide [207] or borax [208].
Lastly, the adhesion measurements can be further refined. Our investigation of adhesive forces between P(NIPAM-co-DMA) microgels and colloidal probes made out of silica (as detailed in chapter 6) unveil a reduction in adhesion for densely packed microgel particles. We attribute this phenomenon to core-core interactions, which enable interactions between catechol groups among neighbouring microgel particles. To deepen the understanding of these interactions, colloidal probes coated with microgel particles could be indented into microgel layers. A novel technique even enables the conduction of force spectroscopy measurements using colloidal particles, such as microgel particles, that are directly affixed to a cantilever through aspiration [209]. Both approaches allow a direct study of particle-particle interactions.
Additionally, the choice of different colloidal probe materials is of special interest. As demonstrated by Putnam *et al.* [59], the ideal DMA amount incorporated within the polymer structure for maximum adhesion varies depending on the substrate material. The optimal DMA content for adhesion to aluminum (characterised by a high surface energy) differs significantly from the content required for adhesion to teflon (characterised by a low surface energy). Thus, depending on the materials needed for future applications, adjustments in the DMA content may be necessary and should be further examined.

In summary, the successful development and initial comprehensive investigations of mussel-inspired P(NIPAM-co-DMA) microgels in this thesis paves the way for further research and applications, holding considerable future potential.

Bibliography

[1] U.S. Geological Survey (USGS) How Much Water is There on Earth? https://www.usgs.gov/special-topics/water-science-school/science/how-much-water-there-earth/, Online; accessed 28-august-2023.

[2] Waite, J. H.; Tanzer, M. L. Polyphenolic Substance of Mytilus edulis: Novel Adhesive Containing L-Dopa and Hydroxyproline. *Science* **1981**, *212*, 1038–40.

[3] Saiz-Poseu, J.; Mancebo-Aracil, J.; Nador, F.; Busqué, F.; Ruiz-Molina, D. The Chemistry behind Catechol-Based Adhesion. *Angewandte Chemie International Edition* **2019**, *58*, 696–714.

[4] Xue, J.; Zhang, Z.; Nie, J.; Du, B. Formation of Microgels by Utilizing the Reactivity of Catechols with Radicals. *Macromolecules* **2017**, *50*, 5285–5292.

[5] Yang, J.; Cohen Stuart, M. A.; Kamperman, M. Jack of all trades: versatile catechol crosslinking mechanisms. *Chem. Soc. Rev.* **2014**, *43*, 8271–8298.

[6] Yang, J.; Keijsers, J.; van Heek, M.; Stuiver, A.; Cohen Stuart, M. A.; Kamperman, M. The effect of molecular composition and crosslinking on adhesion of a bio-inspired adhesive. *Polym. Chem.* **2015**, *6*, 3121–3130.

[7] Kaushik, N. K.; Kaushik, N.; Pardeshi, S.; Sharma, J. G.; Lee, S. H.; Choi, E. H. Biomedical and Clinical Importance of Mussel-Inspired Polymers and Materials. *Marine Drugs* **2015**, *13*, 6792–6817.

[8] Balkenende, D. W.; Winkler, S. M.; Messersmith, P. B. Marine-inspired polymers in medical adhesion. *European Polymer Journal* **2019**, *116*, 134–143.

[9] Zhang, K.; Zhang, F.; Song, Y.; Fan, J.-B.; Wang, S. Recent Progress of Mussel-Inspired Underwater Adhesives. *Chinese Journal of Chemistry* **2017**, *35*, 811–820.

[10] Cha, H. J.; Hwang, D. S.; Lim, S. Development of bioadhesives from marine mussels. *Biotechnology Journal* **2008**, *3*, 631–638.

[11] Morgan, D. Two firms race to derive profits from mussels glue: despite gaps in their knowledge of how the mollusk produces the adhesive, scientists hope to recreate it. *Scientist* **1990**, *4*.

[12] Castillo, J. J.; Shanbhag, B. K.; He, L. In *Food Bioactives: Extraction and Biotechnology Applications*; Puri, M., Ed.; Springer International Publishing: Cham, 2017; pp 111–135.

[13] Vatankhah-Varnoosfaderani, M.; Hashmi, S.; GhavamiNejad, A.; Stadler, F. J. Rapid self-healing and triple stimuli responsiveness of a supramolecular polymer gel based on boron–catechol interactions in a novel water-soluble mussel-inspired copolymer. *Polym. Chem.* **2014**, *5*, 512–523.

[14] García-Peñas, A.; Biswas, C. S.; Liang, W.; Wang, Y.; Yang, P.; Stadler, F. J. Effect of Hydrophobic Interactions on Lower Critical Solution Temperature for Poly(N-isopropylacrylamide-co-dopamine Methacrylamide) Copolymers. *Polymers* **2019**, *11*.

[15] Marcisz, K.; Romanski, J.; Stojek, Z.; Karbarz, M. Environmentally sensitive hydrogel functionalized with electroactive and complexing-iron(III) catechol groups. *Journal of Polymer Science Part A: Polymer Chemistry* **2017**, *55*, 3236–3242.

[16] Forg, S.; Karbacher, A.; Ye, Z.; Guo, X.; von Klitzing, R. Copolymerization Kinetics of Dopamine Methacrylamide during PNIPAM Microgel Synthesis for Increased Adhesive Properties. *Langmuir* **2022**, *38*, 5275–5285.

[17] Glass, P.; Chung, H.; Washburn, N. R.; Sitti, M. Enhanced Reversible Adhesion of Dopamine Methacrylamide-Coated Elastomer Microfibrillar Structures under Wet Conditions. *Langmuir* **2009**, *25*, 6607–6612.

[18] Tiu, B. D. B.; Delparastan, P.; Ney, M. R.; Gerst, M.; Messersmith, P. B. Enhanced Adhesion and Cohesion of Bioinspired Dry/Wet Pressure-Sensitive Adhesives. *ACS Applied Materials & Interfaces* **2019**, *11*, 28296–28306.

[19] Xiong, X.; Liu, Y.; Shi, F.; Zhang, G.; Weng, J.; Qu, S. Enhanced Adhesion of Mussel-inspired Adhesive through Manipulating Contents of Dopamine Methacrylamide and Molecular Weight of Polymer. *Journal of Bionic Engineering volume* **2018**, *15*, 461–470.

[20] Thavasi, V.; Bettens, R. P. A.; Leong, L. P. Temperature and Solvent Effects on Radical Scavenging Ability of Phenols. *The Journal of Physical Chemistry A* **2009**, *113*, 3068–3077.

[21] Liu, J.; Zheng, H.; Poh, P. S. P.; Machens, H.-G.; Schilling, A. F. Hydrogels for Engineering of Perfusable Vascular Networks. *International Journal of Molecular Sciences* **2015**, *16*, 15997–16016.

[22] Chai, Q.; Jiao, Y.; Yu, X. Hydrogels for Biomedical Applications: Their Characteristics and the Mechanisms behind Them. *Gels* **2017**, *3*, 2310–2861.

[23] Li, J.; Mooney, D. Designing hydrogels for controlled drug delivery. *Nat Rev Mater* **2016**, *1*.

[24] Lee, K. Y.; Mooney, D. J. Hydrogels for Tissue Engineering. *Chemical Reviews* **2001**, *101*, 1869–1880.

[25] Mi, L.; Xue, H.; Li, Y.; Jiang, S. A Thermoresponsive Antimicrobial Wound Dressing Hydrogel Based on a Cationic Betaine Ester. *Advanced Functional Materials* **2011**, *21*, 4028–4034.

[26] Zhao, Y.; Song, S.; Ren, X.; Zhang, J.; Lin, Q.; Zhao, Y. Supramolecular Adhesive Hydrogels for Tissue Engineering Applications. *Chemical Reviews* **2022**, *122*, 5604–5640.

[27] Gupta, M. K.; Martin, J. R.; Werfel, T. A.; Shen, T.; Page, J. M.; Duvall, C. L. Cell Protective, ABC Triblock Polymer-Based Thermoresponsive Hydrogels with ROS-Triggered Degradation and Drug Release. *Journal of the American Chemical Society* **2014**, *136*, 14896–14902.

[28] Satarkar, N. S.; Hilt, J. Z. Magnetic hydrogel nanocomposites for remote controlled pulsatile drug release. *Journal of Controlled Release* **2008**, *130*, 246–251.

[29] Krogsgaard, M.; Behrens, M. A.; Pedersen, J. S.; Birkedal, H. Self-Healing Mussel-Inspired Multi-pH-Responsive Hydrogels. *Biomacromolecules* **2013**, *14*, 297–301.

[30] Wang, W.; Xu, Y.; Li, A.; Li, T.; Liu, M.; von Klitzing, R.; Ober, C. K.; Kayitmazer, A. B.; Li, L.; Guo, X. Zinc induced polyelectrolyte coacervate bioadhesive and its transition to a self-healing hydrogel. *RSC Adv.* **2015**, *5*, 66871–66878.

[31] McNaught, A.; Wilkinson, A. *IUPAC. Compendium of Chemical Terminology, 2nd ed. (the Gold Book)*; Blackwell Scientific Publications, Oxford, 1997.

[32] Senff, H.; Richtering, W. Temperature sensitive microgel suspensions: Colloidal phase behavior and rheology of soft spheres. *The Journal of Chemical Physics* **1999**, *111*, 1705–1711.

[33] Karg, M.; Pastoriza-Santos, I.; Rodriguez-González, B.; von Klitzing, R.; Wellert, S.; Hellweg, T. Temperature, pH, and Ionic Strength Induced Changes of the Swelling Behavior of PNIPAM-Poly(allylacetic acid) Copolymer Microgels. *Langmuir* **2008**, *24*, 6300–6306, PMID: 18489184.

[34] Berndt, I.; Pedersen, J. S.; Richtering, W. Structure of Multiresponsive "Intelligent" Core-Shell Microgels. *Journal of the American Chemical Society* **2005**, *127*, 9372–9373, PMID: 15984856.

[35] Hoare, T.; Pelton, R. Highly pH and Temperature Responsive Microgels Functionalized with Vinylacetic Acid. *Macromolecules* **2004**, *37*, 2544–2550.

[36] Fernández-Nieves, A.; Fernández-Barbero, A.; Vincent, B.; de las Nieves, F. J. Charge Controlled Swelling of Microgel Particles. *Macromolecules* **2000**, *33*, 2114–2118.

[37] Shibayama, M.; Ikkai, F.; Inamoto, S.; Nomura, S.; Han, C. C. pH and salt concentration dependence of the microstructure of poly(N-isopropylacrylamide-co-acrylic acid) gels. *The Journal of Chemical Physics* **1996**, *105*, 4358–4366.

[38] Lehmann, M.; Tabaka, W.; Möller, T.; Oppermann, A.; Wöll, D.; Volodkin, D.; Wellert, S.; Klitzing, R. v. DLS Setup for in Situ Measurements of Photoinduced Size Changes of Microgel-Based Hybrid Particles. *Langmuir* **2018**, *34*, 3597–3603, PMID: 29502414.

[39] Lange, H.; Juárez, B. H.; Carl, A.; Richter, M.; Bastús, N. G.; Weller, H.; Thomsen, C.; von Klitzing, R.; Knorr, A. Tunable Plasmon Coupling in Distance-Controlled Gold Nanoparticles. *Langmuir* **2012**, *28*, 8862–8866, PMID: 22416809.

[40] Witt, M. U.; Landers, J.; Hinrichs, S.; Salamon, S.; Kopp, J.; Hankiewicz, B.; Wende, H.; von Klitzing, R. Magnetic response of CoFe2O4 nanoparticles confined in a PNIPAM microgel network. *Soft Matter* **2022**, *18*, 1089–1099.

[41] Wang, J.; Gan, D.; Lyon, L. A.; El-Sayed, M. A. Temperature-Jump Investigations of the Kinetics of Hydrogel Nanoparticle Volume Phase Transitions. *Journal of the American Chemical Society* **2001**, *123*, 11284–11289.

[42] Pelton, R.; Hoare, T. *Microgel Suspensions: Fundamentals and Applications*; John Wiley & Sons, Ltd, 2011; Chapter 1, pp 1–32.

[43] Daly, A. C.; Riley, L.; Segura, T.; Burdick, J. A. Hydrogel microparticles for biomedical applications. *Nature Reviews Materials* **2020**, *5*, 20–34.

[44] Alzanbaki, H.; Moretti, M.; Hauser, C. A. E. Engineered Microgels - Their Manufacturing and Biomedical Applications. *Micromachines* **2021**, *12*.

[45] Wellert, S.; Richter, M.; Hellweg, T.; von Klitzing, R.; Hertle, Y. Responsive Microgels at Surfaces and Interfaces. *Zeitschrift für Physikalische Chemie* **2015**, *229*, 1225–1250.

[46] Uhlig, K.; Wegener, T.; Hertle, Y.; Bookhold, J.; Jaeger, M.; Hellweg, T.; Fery, A.; Duschl, C. Thermoresponsive Microgel Coatings as Versatile Functional Compounds for Novel Cell Manipulation Tools. *Polymers* **2018**, *10*.

[47] Virtanen, O. L. J.; Brugnoni, M.; Kather, M.; Pich, A.; Richtering, W. The next step in precipitation polymerization of N-isopropylacrylamide: particle number density control by monochain globule surface charge modulation. *Polym. Chem.* **2016**, *7*, 5123–5131.

[48] Pelton, R. H.; Chibante, P. Preparation of aqueous latices with N-isopropylacrylamide. *Colloids and Surfaces* **1986**, *20*, 247–256.

[49] Heskins, M.; Guillet, J. E. Solution Properties of Poly(N-isopropylacrylamide). *Journal of Macromolecular Science: Part A - Chemistry* **1968**, *2*, 1441–1455.

[50] Wu, X.; Pelton, R. H.; Hamielec, A. E.; Woods, D. R.; McPhee, W. The kinetics of poly(N-isopropylacrylamide) microgel latex formation. *Colloid and Polymer Science* **1994**, *272*, 467–477.

[51] Burmistrova, A.; Richter, M.; Uzum, C.; von Klitzing, R. Effect of cross-linker density of P(NIPAM-co-AAc) microgels at solid surfaces on the swelling/shrinking behaviour and the Young's modulus. *Colloid and Polymer Science* **2011**, *289*, 613–624.

[52] Hertle, Y.; Hellweg, T. Thermoresponsive copolymer microgels. *J. Mater. Chem. B* **2013**, *1*, 5874–5885.

[53] Plamper, F. A.; Richtering, W. Functional Microgels and Microgel Systems. *Accounts of Chemical Research* **2017**, *50*, 131–140.

[54] Burmistrova, A.; Richter, M.; Eisele, M.; Üzüm, C.; Von Klitzing, R. The Effect of Co-Monomer Content on the Swelling/Shrinking and Mechanical Behaviour of Individually Adsorbed PNIPAM Microgel Particles. *Polymers* **2011**, *3*, 1575–1590.

[55] Zakrevskyy, Y.; Richter, M.; Zakrevska, S.; Lomadze, N.; von Klitzing, R.; Santer, S. Light-Controlled Reversible Manipulation of Microgel Particle Size Using Azobenzene-Containing Surfactant. *Advanced Functional Materials* **2012**, *22*, 5000–5009.

[56] Li, Z.; Liang, B. Modulation of phase transition of poly(N-isopropylacrylamide)-based microgels for pulsatile drug release. *Polymers for Advanced Technologies* **2022**, *33*, 710–722.

[57] Lee, H.; Dellatore, S. M.; Miller, W. M.; Messersmith, P. B. Mussel-Inspired Surface Chemistry for Multifunctional Coatings. *Science* **2007**, *318*, 426–430.

[58] Chung, H.; Glass, P.; Pothen, J. M.; Sitti, M.; Washburn, N. R. Enhanced Adhesion of Dopamine Methacrylamide Elastomers via Viscoelasticity Tuning. *Biomacromolecules* **2011**, *12*, 342–347.

[59] Putnam, A. A.; Wilker, J. J. Changing polymer catechol content to generate adhesives for high versus low energy surfaces. *Soft Matter* **2021**, *17*, 1999–2009.

[60] Peak, C. W.; Wilker, J. J.; Schmidt, G. A review on tough and sticky hydrogels. *Colloid and Polymer Science* **2013**, *291*, 2031–2047.

[61] Schulte, M. F.; Izak-Nau, E.; Braun, S.; Pich, A.; Richtering, W.; Göstl, R. Microgels react to force: mechanical properties, syntheses, and force-activated functions. *Chem. Soc. Rev.* **2022**, *51*, 2939–2956.

[62] Ducker, W. A.; Senden, T. J.; Pashley, R. M. Direct measurement of colloidal forces using an atomic force microscope. *Nature* **1991**, *353*, 239–241.

[63] Ducker, W. A.; Senden, T. J.; Pashley, R. M. Measurement of forces in liquids using a force microscope. *Langmuir* **1992**, *8*, 1831–1836.

[64] Butt, H.-J. Measuring electrostatic, van der Waals, and hydration forces in electrolyte solutions with an atomic force microscope. *Biophysical Journal* **1991**, *60*, 1438–1444.

[65] Murray, M.; Snowden, M. The preparation, characterisation and applications of colloidal microgels. *Advances in Colloid and Interface Science* **1995**, *54*, 73–91.

[66] Tanaka, T. Kinetics of phase transition in polymer gels. *Physica A: Statistical Mechanics and its Applications* **1986**, *140*, 261–268.

[67] Stieger, M.; Richtering, W.; Pedersen, J. S.; Lindner, P. Small-angle neutron scattering study of structural changes in temperature sensitive microgel colloids. *The Journal of Chemical Physics* **2004**, *120*, 6197–6206.

[68] Rudyak, V. Y.; Kozhunova, E. Y.; Chertovich, A. V. Towards the realistic computer model of precipitation polymerization microgels. *Scientific Reports* **2019**, *9*, 13052.

[69] Acciaro, R.; Gilányi, T.; Varga, I. Preparation of Monodisperse Poly(N-isopropylacrylamide) Microgel Particles with Homogenous Cross-Link Density Distribution. *Langmuir* **2011**, *27*, 7917–7925.

[70] Witt, M. U.; Hinrichs, S.; Möller, N.; Backes, S.; Fischer, B.; von Klitzing, R. Distribution of CoFe2O4 Nanoparticles Inside PNIPAM-Based Microgels of Different Cross-linker Distributions. *The Journal of Physical Chemistry B* **2019**, *123*, 2405–2413.

[71] Gao, J.; Frisken, B. J. Cross-Linker-Free N-Isopropylacrylamide Gel Nanospheres. *Langmuir* **2003**, *19*, 5212–5216.

[72] Wang, J.; Liu, Y.; Chen, R.; Zhang, Z.; Chen, G.; Chen, H. Ultralow Self-Cross-Linked Poly(N-isopropylacrylamide) Microgels Prepared by Solvent Exchange. *Langmuir* **2019**, *35*, 13991–13998, PMID: 31596589.

[73] Brugnoni, M.; Nickel, A. C.; Kröger, L. C.; Scotti, A.; Pich, A.; Leonhard, K.; Richtering, W. Synthesis and structure of deuterated ultra-low cross-linked poly(N-isopropylacrylamide) microgels. *Polymer Chemistry* **2019**, *10*, 2397–2405.

[74] Kühnhammer, M.; Gräff, K.; Loran, E.; Soltwedel, O.; Löhmann, O.; Frielinghaus, H.; von Klitzing, R. Structure formation of PNIPAM microgels in foams and foam films. *Soft Matter* **2022**, *18*, 9249–9262.

[75] Matzelle, T. R.; Geuskens, G.; Kruse, N. Elastic Properties of Poly(N-isopropylacrylamide) and Poly(acrylamide) Hydrogels Studied by Scanning Force Microscopy. *Macromolecules* **2003**, *36*, 2926–2931.

[76] Senff, H.; Richtering, W. Influence of cross-link density on rheological properties of temperature-sensitive microgel suspensions. *Colloid and Polymer Science* **2000**, *278*, 830–840.

[77] Daly, E.; Saunders, B. R. Temperature–dependent electrophoretic mobility and hydrodynamic radius measurements of poly(N-isopropylacrylamide) microgel particles: structural insights. *Phys. Chem. Chem. Phys.* **2000**, *2*, 3187–3193.

[78] Elaissari, A.; Mahdavian, A. R. *Microgel Suspensions: Fundamentals and Applications*; John Wiley & Sons, Ltd, 2011; Chapter 2, pp 33–51.

[79] Pelton, R. Temperature-sensitive aqueous microgels. *Advances in Colloid and Interface Science* **2000**, *85*, 1–33.

[80] Pich, A.; Richtering, W. In *Chemical Design of Responsive Microgels*; Pich, A., Richtering, W., Eds.; Springer Berlin Heidelberg: Berlin, Heidelberg, 2011; pp 1–37.

[81] Virtanen, O. L. J.; Kather, M.; Meyer-Kirschner, J.; Melle, A.; Radulescu, A.; Viell, J.; Mitsos, A.; Pich, A.; Richtering, W. Direct Monitoring of Microgel Formation during Precipitation Polymerization of N-Isopropylacrylamide Using in Situ SANS. *ACS Omega* **2019**, *4*, 3690–3699.

[82] Sierra-Martin, B.; Lietor-Santos, J. J.; Fernandez-Barbero, A.; Nguyen, T. T.; Fernandez-Nieves, A. *Microgel Suspensions: Fundamentals and Applications*; John Wiley & Sons, Ltd, 2011; Chapter 4, pp 71–116.

[83] Flory, P. J. Thermodynamics of High Polymer Solutions. *The Journal of Chemical Physics* **1942**, *10*, 51–61.

[84] Huggins, M. L. Some Properties of Solutions of Long-chain Compounds. *The Journal of Physical Chemistry* **1942**, *46*, 151–158.

[85] Friesen, S.; Hannappel, Y.; Kakorin, S.; Hellweg, T. Comparison of different approaches to describe the thermotropic volume phase transition of smart microgels. *Colloid and Polymer Science* **2022**, *300*, 1235–1245.

[86] Erman, B.; Flory, P. J. Critical phenomena and transitions in swollen polymer networks and in linear macromolecules. *Macromolecules* **1986**, *19*, 2342–2353.

[87] Leite, D. C.; Kakorin, S.; Hertle, Y.; Hellweg, T.; da Silveira, N. P. Smart Starch–Poly(N-isopropylacrylamide) Hybrid Microgels: Synthesis, Structure, and Swelling Behavior. *Langmuir* **2018**, *34*, 10943–10954, PMID: 30132672.

[88] Friesen, S.; Hannappel, Y.; Kakorin, S.; Hellweg, T. Accounting for Cooperativity in the Thermotropic Volume Phase Transition of Smart Microgels. *Gels* **2021**, *7*.

[89] Kuhn, W. Dependence of the average transversal on the longitudinal dimensions of statistical coils formed by chain molecules. *Journal of Polymer Science* **1946**, *1*, 380–388.

[90] Flory, P. J.; Rehner, J., John Statistical Mechanics of Cross-Linked Polymer Networks I. Rubberlike Elasticity. *The Journal of Chemical Physics* **1943**, *11*, 512–520.

[91] Flory, P. J. *Principles of Polymer Chemistry*; Ithaca N.Y: Cornell University Press, 1953.

[92] Mourran, A.; Wu, Y.; Gumerov, R. A.; Rudov, A. A.; Potemkin, I. I.; Pich, A.; Möller, M. When Colloidal Particles Become Polymer Coils. *Langmuir* **2016**, *32*, 723–730, PMID: 26717422.

[93] Carrillo, J.-M. Y.; Raphael, E.; Dobrynin, A. V. Adhesion of Nanoparticles. *Langmuir* **2010**, *26*, 12973–12979, PMID: 20602529.

[94] Richtering, W. Responsive Emulsions Stabilized by Stimuli-Sensitive Microgels: Emulsions with Special Non-Pickering Properties. *Langmuir* **2012**, *28*, 17218–17229, PMID: 23020623.

[95] Destribats, M.; Lapeyre, V.; Wolfs, M.; Sellier, E.; Leal-Calderon, F.; Ravaine, V.; Schmitt, V. Soft microgels as Pickering emulsion stabilisers: role of particle deformability. *Soft Matter* **2011**, *7*, 7689–7698.

[96] Rey, M.; Fernandez-Rodriguez, M. A.; Karg, M.; Isa, L.; Vogel, N. Poly-N-isopropylacrylamide Nanogels and Microgels at Fluid Interfaces. *Accounts of Chemical Research* **2020**, *53*, 414–424, PMID: 31940173.

[97] Schmidt, S.; Zeiser, M.; Hellweg, T.; Duschl, C.; Fery, A.; Möhwald, H. Adhesion and Mechanical Properties of PNIPAM Microgel Films and Their Potential Use as Switchable Cell Culture Substrates. *Advanced Functional Materials* **2010**, *20*, 3235–3243.

[98] Witte, J.; Kyrey, T.; Lutzki, J.; Dahl, A. M.; Kühnhammer, M.; Klitzing, R. v.; Holderer, O.; Wellert, S. Looking inside Poly(N-isopropylacrylamide) Microgels: Nanomechanics and Dynamics at Solid–Liquid Interfaces. *ACS Applied Polymer Materials* **2021**, *3*, 976–985.

[99] Burmistrova, A.; von Klitzing, R. Control of number density and swelling/shrinking behavior of P(NIPAM–AAc) particles at solid surfaces. *J. Mater. Chem.* **2010**, *20*, 3502–3507.

[100] Höfl, S.; Zitzler, L.; Hellweg, T.; Herminghaus, S.; Mugele, F. Volume phase transition of "smart" microgels in bulk solution and adsorbed at an interface: A combined AFM, dynamic light, and small angle neutron scattering study. *Polymer* **2007**, *48*, 245–254.

[101] Wellert, S.; Hertle, Y.; Richter, M.; Medebach, M.; Magerl, D.; Wang, W.; Demé, B.; Radulescu, A.; Müller-Buschbaum, P.; Hellweg, T.; von Klitzing, R. Inner Structure of Adsorbed Ionic Microgel Particles. *Langmuir* **2014**, *30*, 7168–7176, PMID: 24920223.

[102] Schmidt, S.; Motschmann, H.; Hellweg, T.; von Klitzing, R. Thermoresponsive surfaces by spin-coating of PNIPAM-co-PAA microgels: A combined AFM and ellipsometry study. *Polymer* **2008**, *49*, 749–756.

[103] Cheng, H.; Shen, L.; Wu, C. LLS and FTIR Studies on the Hysteresis in Association and Dissociation of Poly(N-isopropylacrylamide) Chains in Water. *Macromolecules* **2006**, *39*, 2325–2329.

[104] Aufderhorst-Roberts, A.; Baker, D.; Foster, R. J.; Cayre, O.; Mattsson, J.; Connell, S. D. Nanoscale mechanics of microgel particles. *Nanoscale* **2018**, *10*, 16050–16061.

[105] Backes, S.; Witt, M. U.; Roeben, E.; Kuhrts, L.; Aleed, S.; Schmidt, A. M.; von Klitzing, R. Loading of PNIPAM Based Microgels with CoFe2O4 Nanoparticles and Their Magnetic Response in Bulk and at Surfaces. *The Journal of Physical Chemistry B* **2015**, *119*, 12129–12137.

[106] Witte, J.; Kyrey, T.; Lutzki, J.; Dahl, A. M.; Houston, J.; Radulescu, A.; Pipich, V.; Stingaciu, L.; Kühnhammer, M.; Witt, M. U.; von Klitzing, R.; Holderer, O.; Wellert, S. A comparison of the network structure and inner dynamics of homogeneously and heterogeneously crosslinked PNIPAM microgels with high crosslinker content. *Soft Matter* **2019**, *15*, 1053–1064.

[107] Harmon, M. E.; Kuckling, D.; Frank, C. W. Photo-Cross-Linkable PNIPAAm Copolymers. 5. Mechanical Properties of Hydrogel Layers. *Langmuir* **2003**, *19*, 10660–10665.

[108] Junk, M. J. N.; Berger, R.; Jonas, U. Atomic Force Spectroscopy of Thermoresponsive Photo-Cross-Linked Hydrogel Films. *Langmuir* **2010**, *26*, 7262–7269.

[109] Wiedemair, J.; Serpe, M. J.; Kim, J.; Masson, J.-F.; Lyon, L. A.; Mizaikoff, B.; Kranz, C. In-Situ AFM Studies of the Phase-Transition Behavior of Single Thermoresponsive Hydrogel Particles. *Langmuir* **2007**, *23*, 130–137, PMID: 17190495.

[110] Tagit, O.; Tomczak, N.; Vancso, G. J. Probing the Morphology and Nanoscale Mechanics of Single Poly(N-isopropylacrylamide) Microgels Across the Lower-Critical-Solution Temperature by Atomic Force Microscopy. *Small* **2008**, *4*, 119–126.

[111] Hashmi, S. M.; Dufresne, E. R. Mechanical properties of individual microgel particles through the deswelling transition. *Soft Matter* **2009**, *5*, 3682–3688.

[112] Backes, S.; von Klitzing, R. Nanomechanics and Nanorheology of Microgels at Interfaces. *Polymers* **2018**, *10*, 978.

[113] Li, Y.; Cao, Y. The molecular mechanisms underlying mussel adhesion. *Nanoscale Adv.* **2019**, *1*, 4246–4257.

[114] Zhang, C.; Wu, B.; Zhou, Y.; Zhou, F.; Liu, W.; Wang, Z. Mussel-inspired hydrogels: from design principles to promising applications. *Chem. Soc. Rev.* **2020**, *49*, 3605–3637.

[115] Lin, Q.; Gourdon, D.; Sun, C.; Holten-Andersen, N.; Anderson, T. H.; Waite, J. H.; Israelachvili, J. N. Adhesion mechanisms of the mussel foot proteins mfp-1 and mfp-3. *Proceedings of the National Academy of Sciences* **2007**, *104*, 3782–3786.

[116] Yu, J.; Wei, W.; Danner, E.; Israelachvili, J. N.; Waite, J. H. Effects of Interfacial Redox in Mussel Adhesive Protein Films on Mica. *Advanced Materials* **2011**, *23*, 2362–2366.

[117] Danner, E. W.; Kan, Y.; Hammer, M. U.; Israelachvili, J. N.; Waite, J. H. Adhesion of Mussel Foot Protein Mefp-5 to Mica: An Underwater Superglue. *Biochemistry* **2012**, *51*, 6511–6518, PMID: 22873939.

[118] Papov, V. V.; Diamond, T. V.; Biemann, K.; Waite, J. H. Hydroxyarginine-containing Polyphenolic Proteins in the Adhesive Plaques of the Marine Mussel Mytilus edulis. *Journal of Biological Chemistry* **1995**, *270*, 20183–20192.

[119] Waite, J. H.; Qin, X. Polyphosphoprotein from the Adhesive Pads of Mytilus edulis. *Biochemistry* **2001**, *40*, 2887–2893, PMID: 11258900.

[120] Zhao, H.; Waite, J. H. Linking Adhesive and Structural Proteins in the Attachment Plaque of Mytilus californianus. *Journal of Biological Chemistry* **2006**, *281*, 26150–26158.

[121] Pinnataip, R.; Lee, B. P. Oxidation Chemistry of Catechol Utilized in Designing Stimuli-Responsive Adhesives and Antipathogenic Biomaterials. *ACS Omega* **2021**, *6*, 5113–5118, PMID: 33681552.

[122] Holten-Andersen, N.; Harrington, M. J.; Birkedal, H.; Lee, B. P.; Messersmith, P. B.; Lee, K. Y. C.; Waite, J. H. pH-induced metal-ligand cross-links inspired by mussel yield self-healing polymer networks with near-covalent elastic moduli. *Proceedings of the National Academy of Sciences* **2011**, *108*, 2651–2655.

[123] Yu, J.; Wei, W.; Danner, E.; Ashley, R. K.; Israelachvili, J. N.; Waite, J. H. Mussel protein adhesion depends on interprotein thiol-mediated redox modulation. *Nature Chemical Biology* **2011**, *7*, 588–590.

[124] Wang, L.; Zhao, Z.; Dong, J.; Li, D.; Dong, W.; Li, H.; Zhou, Y.; Liu, Q.; Deng, B. Mussel-Inspired Multifunctional Hydrogels with Adhesive, Self-Healing, Antioxidative, and Antibacterial Activity for Wound Healing. *ACS Applied Materials & Interfaces* **2023**, *15*, 16515–16525, PMID: 36951622.

[125] Yu, Q.; Zheng, Z.; Zhang, X.; Dong, X.; Cao, R.; Zhang, S.; Wu, X. Mussel-Inspired Hydrogels as Tough, Self-Adhesive and Conductive Bioelectronics: A Review. *Soft Matter* **2021**, *17*, 8786–8804.

[126] Han, L.; Lu, X.; Liu, K.; Wang, K.; Fang, L.; Weng, L.-T.; Zhang, H.; Tang, Y.; Ren, F.; Zhao, C.; Sun, G.; Liang, R.; Li, Z. Mussel-Inspired Adhesive and Tough Hydrogel Based on Nanoclay Confined Dopamine Polymerization. *ACS Nano* **2017**, *11*, 2561–2574, PMID: 28245107.

[127] Li, L.; Smitthipong, W.; Zeng, H. Mussel-inspired hydrogels for biomedical and environmental applications. *Polym. Chem.* **2015**, *6*, 353–358.

[128] Rahimnejad, M.; Zhong, W. Mussel-inspired hydrogel tissue adhesives for wound closure. *RSC Adv.* **2017**, *7*, 47380–47396.

[129] Wilkinson, E. Oral zinc for arterial and venous leg ulcers. *Cochrane Database of Systematic Reviews* **2014**,

[130] Lee, H.; Lee, B. P.; Messersmith, P. B. A reversible wet/dry adhesive inspired by mussels and geckos. *Nature* **2018**, *448*, 338–341.

[131] Charisiadis, P.; Kontogianni, V. G.; Tsiafoulis, C. G.; Tzakos, A. G.; Siskos, M.; Gerothanassis, I. P. 1H-NMR as a Structural and Analytical Tool of Intra- and Intermolecular Hydrogen Bonds of Phenol-Containing Natural Products and Model Compounds. *Molecules* **2014**, *19*, 13643–13682.

[132] Anderson, D. G. R. Oxidation and reactivity of 3,4-dihydroxyphenylacetaldehyde, a reactive intermediate of dopamine metabolism. Ph.D. Thesis, University of Iowa, Iowa, 2011.

[133] Du, X.; Li, L.; Li, J.; Yang, C.; Frenkel, N.; Welle, A.; Heissler, S.; Nefedov, A.; Grunze, M.; Levkin, P. A. L. UV-triggered dopamine polymerization: control of polymerization, surface coating, and photopatterning. *Advanced Materials* **2014**, *26*, 8029–33.

[134] Glatter, O., Ed. *Scattering Methods and their Application in Colloid and Interface Science*; Elsevier, 2018.

[135] Berne, B. J., Pecora, R., Eds. *Dynamic Light Scattering - With Applications to Chemistry, Biology, and Physics*; John Wiley & Sons, Inc., 1976.

[136] Stetefeld, J.; McKenna, S. A.; Patel, T. R. Dynamic light scattering: a practical guide and applications in biomedical sciences. *Biophysical reviews* **2016**, *8*, 409–427.

[137] Koppel, D. E. Analysis of Macromolecular Polydispersity in Intensity Correlation Spectroscopy: The Method of Cumulants. *The Journal of Chemical Physics* **2003**, *57*, 4814–4820.

[138] Pasparakis, G.; Tsitsilianis, C. LCST polymers: Thermoresponsive nanostructured assemblies towards bioapplications. *Polymer* **2020**, *211*, 123146.

[139] Canal, T.; Peppas, N. A. Correlation between mesh size and equilibrium degree of swelling of polymeric networks. *Journal of Biomedical Materials Research* **1989**, *23*, 1183–1193.

[140] Peppas, N. A.; Moynihan, H. J.; Lucht, L. M. The structure of highly crosslinked poly(2-hydroxyethyl methacrylate) hydrogels. *Journal of Biomedical Materials Research* **1985**, *19*, 397–411.

[141] Fänger, C.; Wack, H.; Ulbricht, M. Macroporous Poly(N-isopropylacrylamide) Hydrogels with Adjustable Size "Cut-off" for the Efficient and Reversible Immobilization of Biomacromolecules. *Macromolecular Bioscience* **2006**, *6*, 393–402.

[142] Bhattacharjee, S. DLS and zeta potential – What they are and what they are not? *Journal of Controlled Release* **2016**, *235*, 337–351.

[143] Debye, P.; Hückel, E. Zur Theorie der Elektrolyte. I. Gefrierpunktserniedrigung und verwandte Erscheinungen. *Physikalische Zeitschrift* **1923**, *24*, 305.

[144] Jüttner, F. Handbuch der Elektrizität und des Magnetismus. In fünf Bünden. Bearbeitet von F. Auerbach, Jena, K. Baedeker †, Jena, A. Becker, Heidelberg, E. Bräuer, Charlottenburg, P. Cermak, Gießen, H. Dießelhorst, Braunschweig, A. Eichenwald, Moskau, A. Gehlhoff, Berlin, E. Gehrcke, Charlottenburg, H. Geiger, Charlottenburg, G. von Hevesy, Kopenhagen, R. von Hirsch, München, W. Jaeger, Berlin, J. Koenigsberger, Freiburg i.B., K. F. W. Kohlrausch, Wien, O. Lummer, Breslau, E. Riecke †, Göttingen, W. H. Schmidt †, Gießen, E. Schrödinger, Wien, E. von Schweidler, Innsbruck, R. Seeliger, Greifswald, M. von Smoluchowski †, Lemberg, M. Trautz, Heidelberg, W. Voigt †, Göttingen. Herausgegeben von L.Graetz. Verlag von Joh. Ambr. Barth, Leipzig 1920. Bd. III, Lieferung 3, S. 351-724, mit 156 Abbildungen im Text. Preis geh. 64 Mk.; Bd. IV, Lieferung 3, S. 711 bis 1360, mit 319 Abbildungen im Text (Schlußheft des IV. Bandes). Preis geh. 84 Mk. *Zeitschrift für Elektrochemie und angewandte physikalische Chemie* **1921**, *27*, 582–583.

[145] Binnig, G.; Quate, C. F.; Gerber, C. Atomic Force Microscope. *Phys. Rev. Lett.* **1986**, *56*, 930–933.

[146] Sanders, W. C. *Atomic Force Microscopy: Fundamental Concepts and Laboratory Investigations (1st ed.)*; CRC Press, 2019.

[147] Meyer, E. Atomic force microscopy. *Progress in Surface Science* **1992**, *41*, 3–49.

[148] Butt, H.-J.; Cappella, B.; Kappl, M. Force measurements with the atomic force microscope: Technique, interpretation and applications. *Surface Science Reports* **2005**, *59*, 1–152.

[149] Hafner, J.; Cheung, C.-L.; Woolley, A.; Lieber, C. Structural and functional imaging with carbon nanotube AFM probes. *Progress in Biophysics and Molecular Biology* **2001**, *77*, 73–110.

[150] Schwarz, U. D.; Haefke, H.; Reimann, P.; Güntherodt, H.-J. Tip artefacts in scanning force microscopy. *Journal of Microscopy* **1994**, *173*, 183–197.

[151] Gołek, F.; Mazur, P.; Ryszka, Z.; Zuber, S. AFM image artifacts. *Applied Surface Science* **2014**, *304*, 11–19, Selected Papers from the 6th International Workshop on Surface Physics "Functional Materials".

[152] Yuxiong Mao Nearest Neighbor Distances Calculation with ImageJ. `https://icme.hpc.msstate.edu/mediawiki/index.php/Nearest_Neighbor_Distances_Calculation_with_ImageJ.html`, Online; accessed 16-august-2023.

[153] Kappl, M.; Butt, H.-J. The Colloidal Probe Technique and its Application to Adhesion Force Measurements. *Particle & Particle Systems Characterization* **2002**, *19*, 129–143.

[154] Hertz, H. Über die Berührung fester elastischer Körper. *Journal für die reine und angewandte Mathematik* **1881**, *92*, 156–171.

[155] Voudouris, P.; Florea, D.; van der Schoot, P.; Wyss, H. M. Micromechanics of temperature sensitive microgels: dip in the Poisson ratio near the LCST. *Soft Matter* **2013**, *9*, 7158–7166.

[156] Hirotsu, S. Softening of bulk modulus and negative Poisson's ratio near the volume phase transition of polymer gels. *The Journal of Chemical Physics* **1991**, *94*, 3949–3957.

[157] Boon, N.; Schurtenberger, P. Swelling of micro-hydrogels with a crosslinker gradient. *Phys. Chem. Chem. Phys.* **2017**, *19*, 23740–23746.

[158] Geissler, E.; Hecht, A. M. The Poisson Ratio in Polymer Gels. *Macromolecules* **1980**, *13*, 1276–1280.

[159] Derjaguin, B.; Muller, V.; Toporov, Y. Effect of contact deformations on the adhesion of particles. *Journal of Colloid and Interface Science* **1975**, *53*, 314–326.

[160] Johnson, K. L.; Kendall, K.; Roberts, A. D.; Tabor, D. Surface energy and the contact of elastic solids. *Proceedings of the Royal Society of London. A. Mathematical and Physical Sciences* **1971**, *324*, 301–313.

[161] Zemła, J.; Bobrowska, J.; Kubiak, A.; Zieliński, T.; Pabijan, J.; Pogoda, K.; Bobrowski, P.; Lekka, M. Indenting soft samples (hydrogels and cells) with cantilevers possessing various shapes of probing tip. *Eur Biophys J* **2020**, *49*, 485–495.

[162] Sokolov, I.; Dokukin, M. Mechanics of Biological Cells Studied with Atomic Force Microscopy. *Microscopy and Microanalysis* **2014**, *20*, 2076–2077.

[163] Alcaraz, J.; Otero, J.; Jorba, I.; Navajas, D. Bidirectional mechanobiology between cells and their local extracellular matrix probed by atomic force microscopy. *Seminars in Cell & Developmental Biology* **2018**, *73*, 71–81.

[164] Sader, J. E.; Chon, J. W. M.; Mulvaney, P. Calibration of rectangular atomic force microscope cantilevers. *Review of Scientific Instruments* **1999**, *70*, 3967–3969.

[165] Sader, J. E.; Sanelli, J. A.; Adamson, B. D.; Monty, J. P.; Wei, X.; Crawford, S. A.; Friend, J. R.; Marusic, I.; Mulvaney, P.; Bieske, E. J. Spring constant calibration of atomic force microscope cantilevers of arbitrary shape. *Review of Scientific Instruments* **2012**, *83*, 103705.

[166] Popov, V. L.; Heß, M.; Willert, E. *Handbook of Contact Mechanics*; Springer Berlin, Heidelberg, 2019.

[167] Hellwig, J. Nanomechanics & nanorheology of polymer networks: An AFM study. Ph.D. Thesis, Technische Universität Berlin, Berlin, 2020.

[168] Levitt, M. H. *Spin Dynamics: Basics of Nuclear Magnetic Resonance*, 2nd ed.; John Wiley & Sons, 2008.

[169] Peng, W.; Zhang, Z.; Rong, M.; Zhang, M. Core-Shell Structure Design of Hollow Mesoporous Silica Nanospheres Based on Thermo-Sensitive PNIPAM and pH-Responsive Catechol-Fe3+ Complex. *Polymers* **2019**, *11*.

[170] Hinderer, F. *UV/Vis-Absorptions- und Fluoreszenz-Spektroskopie: Einführung in die spektroskopische Analyse mit UV- und sichtbarer Strahlung*; Springer Fachmedien Wiesbaden, 2020.

[171] Hof, M.; Macháň, R. *Handbook of Spectroscopy*; John Wiley & Sons, Ltd, 2014; Chapter 3, pp 31–38.

[172] Burzio, L. A.; Waite, J. H. Cross-Linking in Adhesive Quinoproteins: Studies with Model Decapeptides. *Biochemistry* **2000**, *39*, 11147–11153.

[173] Ho, C. S.; Lam, C. W. K.; Chan, M. H. M.; Cheung, R. C. K.; Law, L. K.; Lit, L. C.-W.; Ng, K. F.; Suen, M. W. M.; Tai, H. L. Electrospray ionisation mass spectrometry: principles and clinical applications. *The Clinical biochemist. Reviews* **2003**, *24*, 3–12.

[174] Gross, J. *Massenspektrometrie: Spektroskopiekurs kompakt*; Springer Berlin Heidelberg, 2019.

[175] Atkins, P. W.; de Paula, J. *Physikalische Chemie, Wiley-VCH-Lehrbuchkollektion 1*, 5th ed.; John Wiley & Sons, 2012.

[176] Goldstein, J.; Newbury, D.; Michael, J.; Ritchie, N.; Scott, J.; Joy, D. *Scanning Electron Microscopy and X-Ray Microanalysis*; Springer New York, 2017.

[177] Egerton, R. *Physical Principles of Electron Microscopy: An Introduction to TEM, SEM, and AEM*; Springer New York, NY, 2005.

[178] Zhang, F.; Liu, S.; Zhang, Y.; Xu, J.; Chi, Z. A simplified approach to achieve gecko-mimic nano-structural adhesives by a simple polymer. *International Journal of Adhesion and Adhesives* **2011**, *31*, 583–586.

[179] Lehmann, M. Light-induced phase transition of gold-microgel hybrids. Ph.D. Thesis, Technische Universität Berlin, Berlin, 2020.

[180] Witt, M. U. Poly-N-isopropylacrylamide Based Microgels: A Study on Magnetic Microgels and Their Structure. Ph.D. Thesis, Technische Universität Darmstadt, Darmstadt, 2021.

[181] Branch, G. E.; Joslyn, M. The Kinetics of the Auto-oxidation of Catechol in the Presence of Several Foreign Substances. *Journal of the American Chemical Society* **1935**, *57*, 2388–2394.

[182] McGrath, J. E. Chain reaction polymerization. *Journal of Chemical Education* **1981**, *58*, 844.

[183] Koltzenburg, S.; Maskos, M.; Nuyken, O. *Polymer Chemistry*; Springer-Verlag Berlin Heidelberg, 2017.

[184] Niki, E. *Oxygen Radicals in Biological Systems Part B: Oxygen Radicals and Antioxidants*; Methods in Enzymology; Academic Press, 1990; Vol. 186; pp 100–108.

[185] FUJIFILM Wako Chemicals U.S.A. Corporation V-50 Azo Initiator. https://www.wakospecialtychemicals.com/brand/wako/product/v-50-azo-initiator/, Online; accessed 28-may-2021.

[186] Yu, M.; Hwang, J.; Deming, T. J. Role of l-3,4-Dihydroxyphenylalanine in Mussel Adhesive Proteins. *Journal of the American Chemical Society* **1999**, *121*, 5825–5826.

[187] Lee, B. P.; Chao, C.-Y.; Nunalee, F. N.; Motan, E.; Shull, K. R.; Messersmith, P. B. Rapid Gel Formation and Adhesion in Photocurable and Biodegradable Block Copolymers with High DOPA Content. *Macromolecules* **2006**, *39*, 1740–1748.

[188] Dechézelles, J.-F.; Malik, V.; Crassous, J. J.; Schurtenberger, P. Hybrid raspberry microgels with tunable thermoresponsive behavior. *Soft Matter* **2013**, *9*, 2798–2802.

[189] Schulte, M. F.; Bochenek, S.; Brugnoni, M.; Scotti, A.; Mourran, A.; Richtering, W. Stiffness Tomography of Ultra-Soft Nanogels by Atomic Force Microscopy. *Angewandte Chemie International Edition* **2021**, *60*, 2280–2287.

[190] Puretskiy, N.; Ionov, L. Synthesis of Robust Raspberry-like Particles Using Polymer Brushes. *Langmuir* **2011**, *27*, 3006–3011, PMID: 21314161.

[191] Metawea, O. R.; Abdelmoneem, M. A.; Haiba, N. S.; Khalil, H. H.; Teleb, M.; Elzoghby, A. O.; Khafaga, A. F.; Noreldin, A. E.; Albericio, F.; Khattab, S. N. A novel 'smart' PNIPAM-based copolymer for breast cancer targeted therapy: Synthesis, and characterization of dual pH/temperature-responsive lactoferrin-targeted PNIPAM-co-AA. *Colloids Surf B Biointerfaces* **2021**, *202*.

[192] Lima, L. H.; Morales, Y.; Cabral, T. Ocular Biocompatibility of Poly-N-Isopropylacrylamide (pNIPAM). *J Ophthalmol.* **2016**, *2016*.

[193] Yoshida, R.; Sakai, K.; Okano, T.; Sakurai, Y. Modulating the phase transition temperature and thermosensitivity in N-isopropylacrylamide copolymer gels. *Journal of Biomaterials Science, Polymer Edition* **1995**, *6*, 585–598.

[194] Feil, H.; Bae, Y. H.; Feijen, J.; Kim, S. W. Effect of comonomer hydrophilicity and ionization on the lower critical solution temperature of N-isopropylacrylamide copolymers. *Macromolecules* **1993**, *26*, 2496–2500.

[195] Karg, M.; Prévost, S.; Brandt, A.; Wallacher, D.; von Klitzing, R.; Hellweg, T. Poly-NIPAM Microgels with Different Cross-Linker Densities. Intelligent Hydrogels. Cham, 2013; pp 63–76.

[196] Schlattmann, D.; Schönhoff, M. Interplay of the Influence of Crosslinker Content and Model Drugs on the Phase Transition of Thermoresponsive PNiPAM-BIS Microgels. *Gels* **2022**, *8*.

[197] Kratz, K.; Hellweg, T.; Eimer, W. Effect of connectivity and charge density on the swelling and local structural and dynamic properties of colloidal PNIPAM microgels. *Berichte der Bunsengesellschaft für physikalische Chemie* **1998**, *102*, 1603–1608.

[198] Thiele, S.; Andersson, J.; Dahlin, A.; Hailes, R. L. N. Tuning the Thermoresponsive Behavior of Surface-Attached PNIPAM Networks: Varying the Crosslinker Content in SI-ATRP. *Langmuir* **2021**, *37*, 3391–3398.

[199] Lehmann, M.; Krause, P.; Miruchna, V.; von Klitzing, R. Tailoring PNIPAM hydrogels for large temperature-triggered changes in mechanical properties. *Colloid and Polymer Science* **2019**, *297*, 633–640.

[200] Geisel, K.; Richtering, W.; Isa, L. Highly ordered 2D microgel arrays: compression versus self-assembly. *Soft Matter* **2014**, *10*, 7968–7976.

[201] Rey, M.; Fernandez-Rodriguez, M. A.; Steinacher, M.; Scheidegger, L.; Geisel, K.; Richtering, W.; Squires, T. M.; Isa, L. Isostructural solid–solid phase transition in monolayers of soft core–shell particles at fluid interfaces: structure and mechanics. *Soft Matter* **2016**, *12*, 3545–3557.

[202] Feller, D.; Karg, M. Fluid interface-assisted assembly of soft microgels: recent developments for structures beyond hexagonal packing. *Soft Matter* **2022**, *18*, 6301–6312.

[203] Rauh, A.; Rey, M.; Barbera, L.; Zanini, M.; Karg, M.; Isa, L. Compression of hard core–soft shell nanoparticles at liquid–liquid interfaces: influence of the shell thickness. *Soft Matter* **2017**, *13*, 158–169.

[204] Schneider, C. Interaktion zwischen weichen und harten Nanopartikeln an der Wasser-Luft Grenzfläche bei steigendem Lateraldruck. Bachelor thesis, TU Darmstadt, Darmstadt, 27.07.2022.

[205] Menath, J.; Eatson, J.; Brilmayer, R.; Andrieu-Brunsen, A.; Buzza, D. M. A.; Vogel, N. Defined core–shell particles as the key to complex interfacial self-assembly. *Proceedings of the National Academy of Sciences* **2021**, *118*, e2113394118.

[206] Lu, Q.; Danner, E.; Waite, J. H.; Israelachvili, J. N.; Zeng, H.; Hwang, D. S. Adhesion of mussel foot proteins to different substrate surfaces. *Journal of The Royal Society Interface* **2013**, *10*, 20120759.

[207] Patil, N.; Falentin-Daudré, C.; Jérôme, C.; Detrembleur, C. Mussel-inspired protein-repelling ambivalent block copolymers: controlled synthesis and characterization. *Polym. Chem.* **2015**, *6*, 2919–2933.

[208] Yang, J.; Bos, I.; Pranger, W.; Stuiver, A.; Velders, A. H.; Cohen Stuart, M. A.; Kamperman, M. A clear coat from a water soluble precursor: a bioinspired paint concept. *J. Mater. Chem. A* **2016**, *4*, 6868–6877.

[209] Mark, A.; Helfricht, N.; Rauh, A.; Karg, M.; Papastavrou, G. The Next Generation of Colloidal Probes: A Universal Approach for Soft and Ultra-Small Particles. *Small* **2019**, *15*, 1902976.

Appendices

A3 Appendix for chapter 3

A3.1 DMA batch

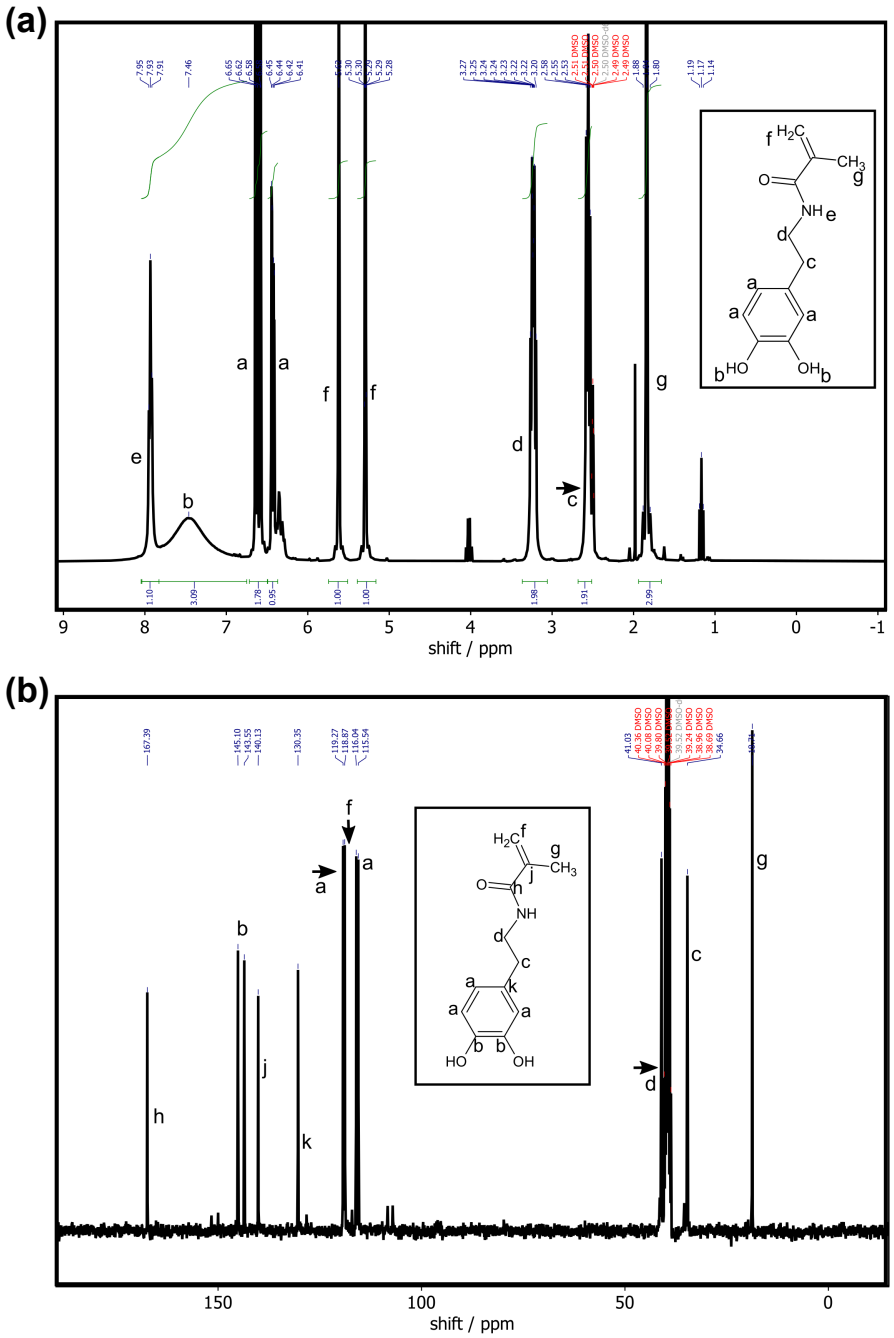

Figure A1: (a) ^{1}H NMR and (b) ^{13}C NMR spectra of exemplary DMA batch solved in DMSO-d$_6$.

A3.2 Colloidal probe characterisation

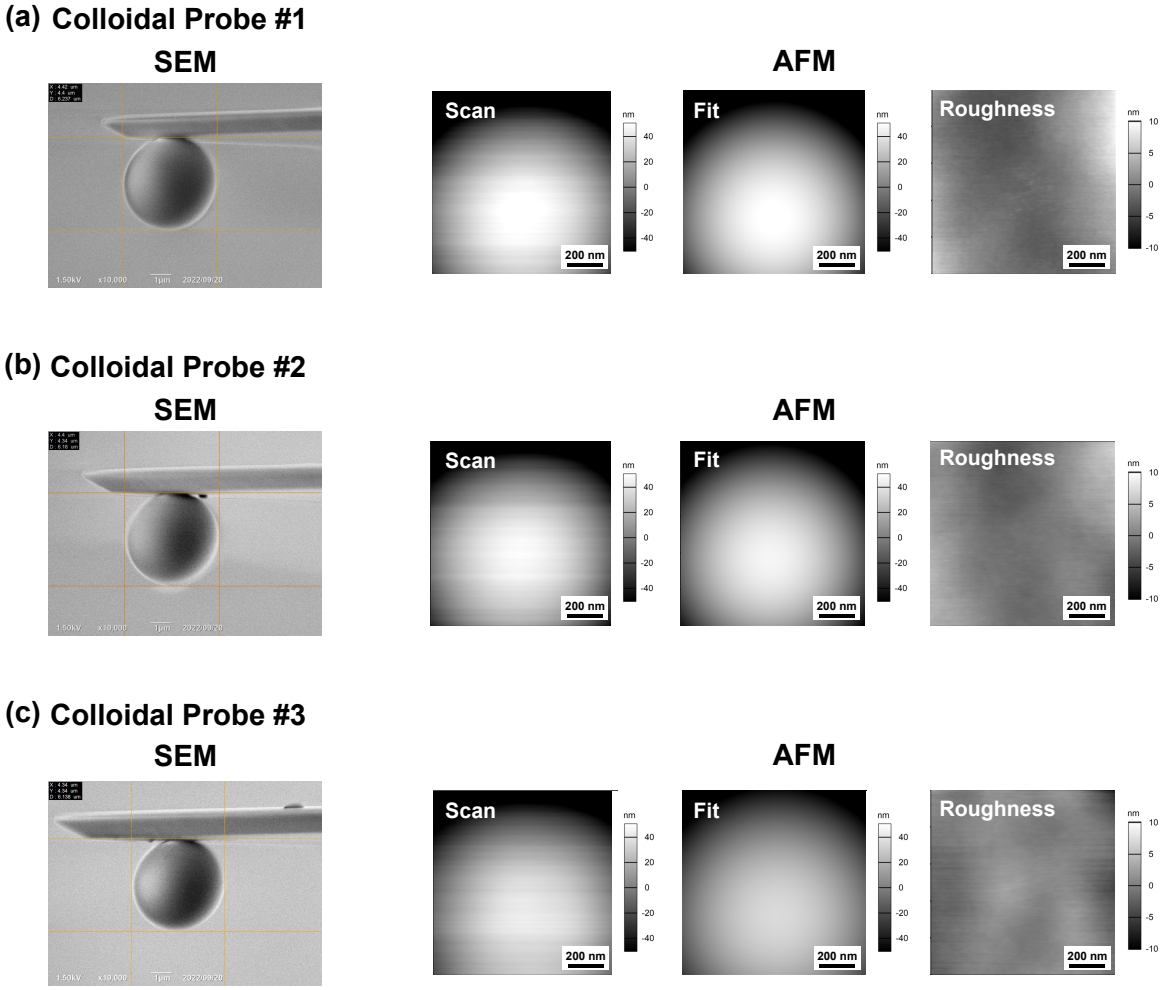

Figure A2: Three exemplary colloidal probes characterised using scanning electron microscopy (SEM), provided by Ulrike Kunz at the Electron Microscopy Center Darmstadt (EMC-DA), and atomic force microscopy (AFM). In the case of AFM, colloidal probes were scanned over a silicon test grating (TGT1) grating. Subsequently, a sphere fit was subtracted from the image to determine the roughness of the probes.

Table A1: The probe radius R_P was determined for three exemplary colloidal probes using SEM and AFM. By scanning the colloidal probe over the test grating TGT1 and subtracting a sphere fit from the image, the roughness of the colloidal probe was calculated as the root mean square (RMS).

Colloidal Probe	$R_{P,SEM}$ / µm	$R_{P,AFM}$ / µm	RMS / nm
#1	2.21	2.02	1.46
#2	2.20	2.05	1.38
#3	2.17	2.88	1.31
Average	2.19 ± 0.02	2.32 ± 0.40	1.38 ± 0.06

A3.3 Validation of Hertz model for colloidal probe force spectroscopy

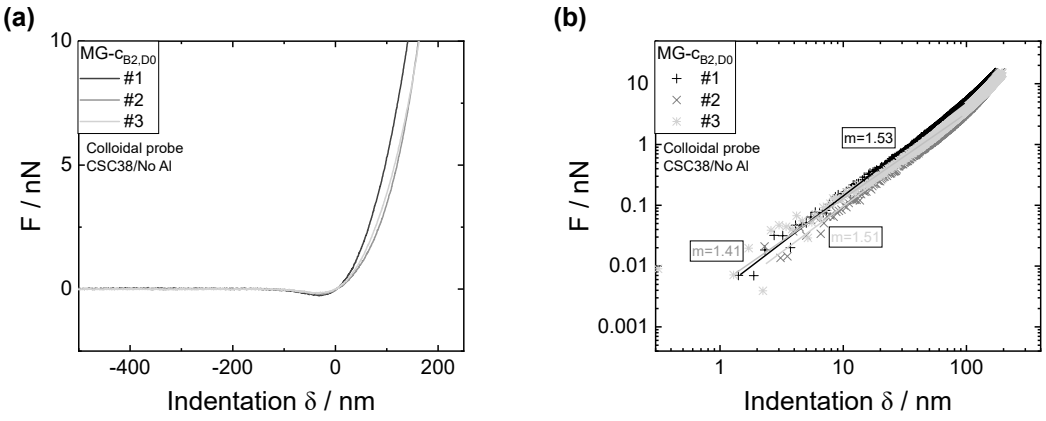

Figure A3: Exemplary force curves of MG-$c_{B2,D0}$, obtained by force spectroscopy measurements, indented by a colloidal probe and plotted in linear (a) and logarithmic (b) scale. (b) includes linear fits with a slope of $1.41 - 1.53\,\mathrm{N\,m^{-1}}$ confirming the validity of the Hertzian model in ultrapure water up to indentation depths of 100 nm.

A4 Appendix for chapter 4

A4.1 Freeze-dried microgels

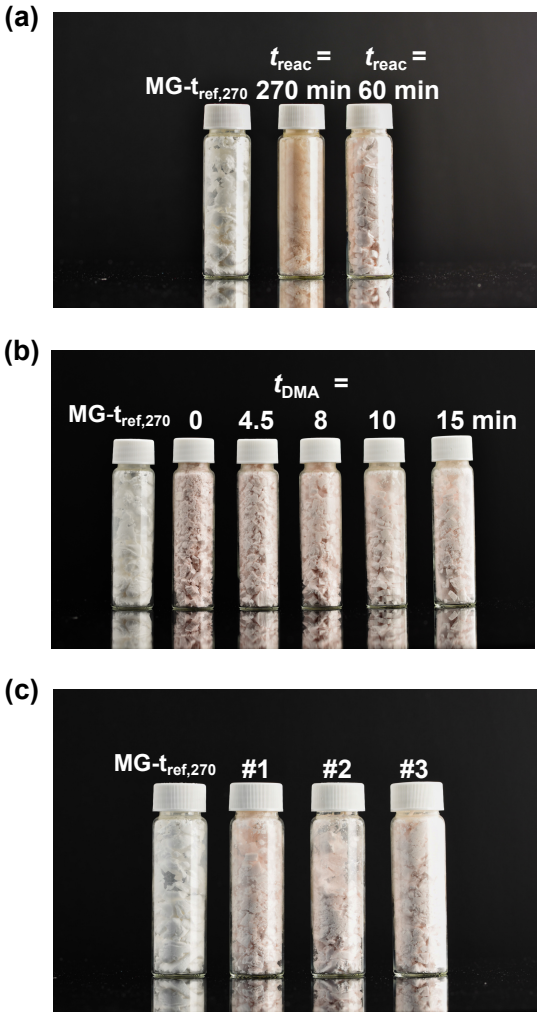

Figure A4: Freeze-dried microgels: (a) Reference microgel MG-$t_{ref,270}$ compared to microgels with different reaction times t_{reac}. (b) Reference microgel MG-$t_{ref,270}$ compared to microgels with different DMA injection times t_{DMA}. (c) Reference microgel MG-$t_{ref,270}$ compared to microgels synthesised with the same t_{reac} and t_{DMA} to test the reproducibility. Microgels #2 and #3 were synthesised with UV light protection. The reference PNIPAM microgel MG-$t_{ref,270}$ has a purely white colour, while P(NIPAM-co-DMA) microgels possess an orange to pinkish colour.

A4.2 DLS and EDLS measurements

Table A2: Hydrodynamic radii R_H of microgels conducted at 20°C and 50°C by dynamic light scattering (DLS) als explained in chapter 3.4. Electrophoretic mobility μ_e measured as described in chapter 3.5.

Microgel	R_H(20°C) / nm	R_H(50°C) / nm	μ_e(20°C) / µm cm V^{-1} s^{-1}	μ_e(50°C) / µm cm V^{-1} s^{-1}
Reference microgel				
MG-$t_{ref,270}$	499.5 ± 18.4	129.1 ± 18.0	0.50 ± 0.01	4.66 ± 0.07
Influence of overall reaction time t_{reac}				
MG-$t_{10,270}$	423.5 ± 68.7	151.7 ± 31.6	0.20 ± 0.01	3.97 ± 0.11
MG-$t_{10,60}$	341.2 ± 26.2	145.6 ± 4.0	1.21 ± 0.02	5.42 ± 0.24
Influence of DMA injection time t_{DMA}				
MG-$t_{0,60}$	335.8 ± 9.5	144.9 ± 4.1	-0.32 ± 0.01	1.58 ± 0.05
MG-$t_{4.5,60}$	380.1 ± 13.7	175.7 ± 10.9	0.09 ± 0.01	2.95 ± 0.17
MG-$t_{8,60}$	339.4 ± 18.3	135.0 ± 6.2	0.78 ± 0.03	3.71 ± 0.31
MG-$t_{10,60}$	341.2 ± 26.2	145.6 ± 4.0	1.21 ± 0.02	5.42 ± 0.24
MG-$t_{15,60}$ #1	310.2 ± 5.1	111.3 ± 7.9	0.55 ± 0.02	3.91 ± 0.05
Reproducibility and influence of UV light				
MG-$t_{15,60}$ #1	310.2 ± 5.1	111.3 ± 7.9	0.55 ± 0.02	3.91 ± 0.05
MG-$t_{15,60}$ #2	441.3 ± 34.4	136.9 ± 4.1	1.24 ± 0.04	5.45 ± 0.06
MG-$t_{15,60}$ #3	497.7 ± 24.8	145.2 ± 7.4	0.85 ± 0.02	4.63 ± 0.25
Influence of cross-linker BIS				
MG-$t_{0,60}$-noBIS	273.0 ± 12.2	99.7 ± 6.8	0.95 ± 0.06	4.53 ± 0.54
MG-$t_{7.5,60}$-noBIS	356.2 ± 14.1	113.9 ± 5.0	-	-
MG-$t_{15,60}$-noBIS	459.0 ± 38.8	117.7 ± 1.3	1.57 ± 0.07	6.50 ± 0.19

A4.3 Additional reaction kinetics

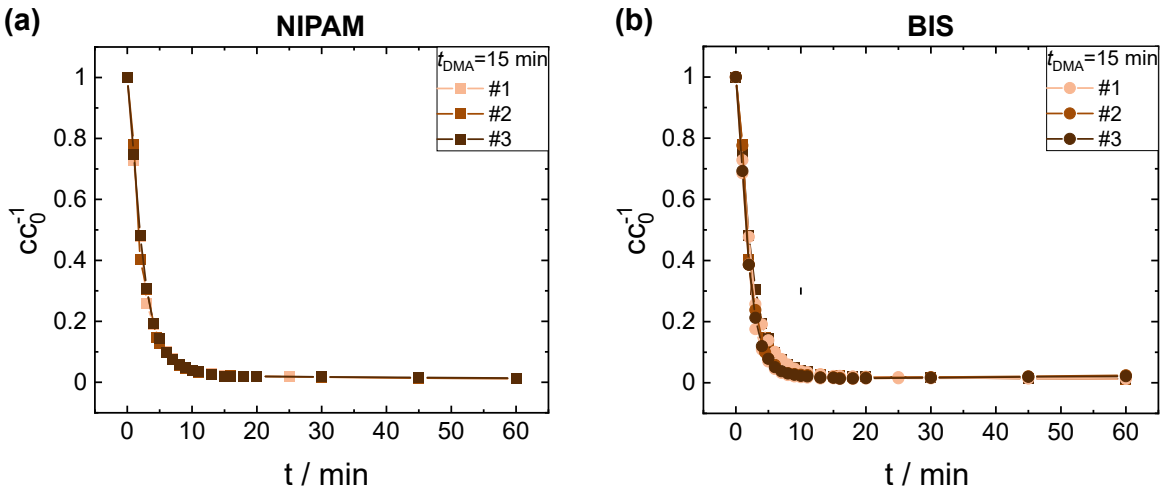

Figure A5: The relative monomer consumption cc_0^{-1} of (a) NIPAM and (b) BIS for microgels synthesised with identical reaction parameters ($t_{\text{reac}} = 60\,\text{min}$, $t_{\text{DMA}} = 15\,\text{min}$) to test the reproducibility of the reaction. #2 and #3 were synthesised with UV light protection.

A4.4 UV-vis spectra

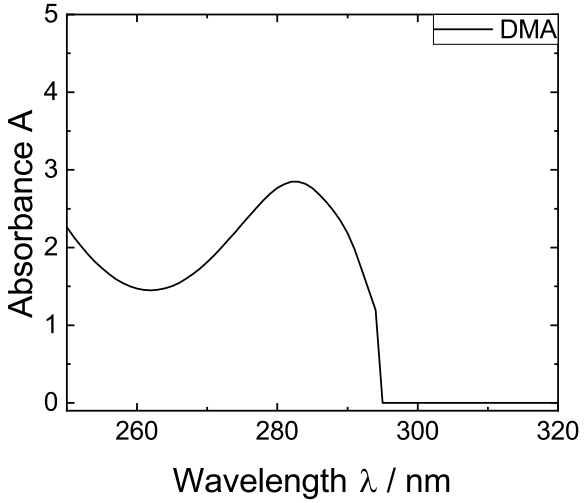

Figure A6: UV-vis spectrum of pure DMA solved in ethanol, showing the characteristic peak at 282 nm.

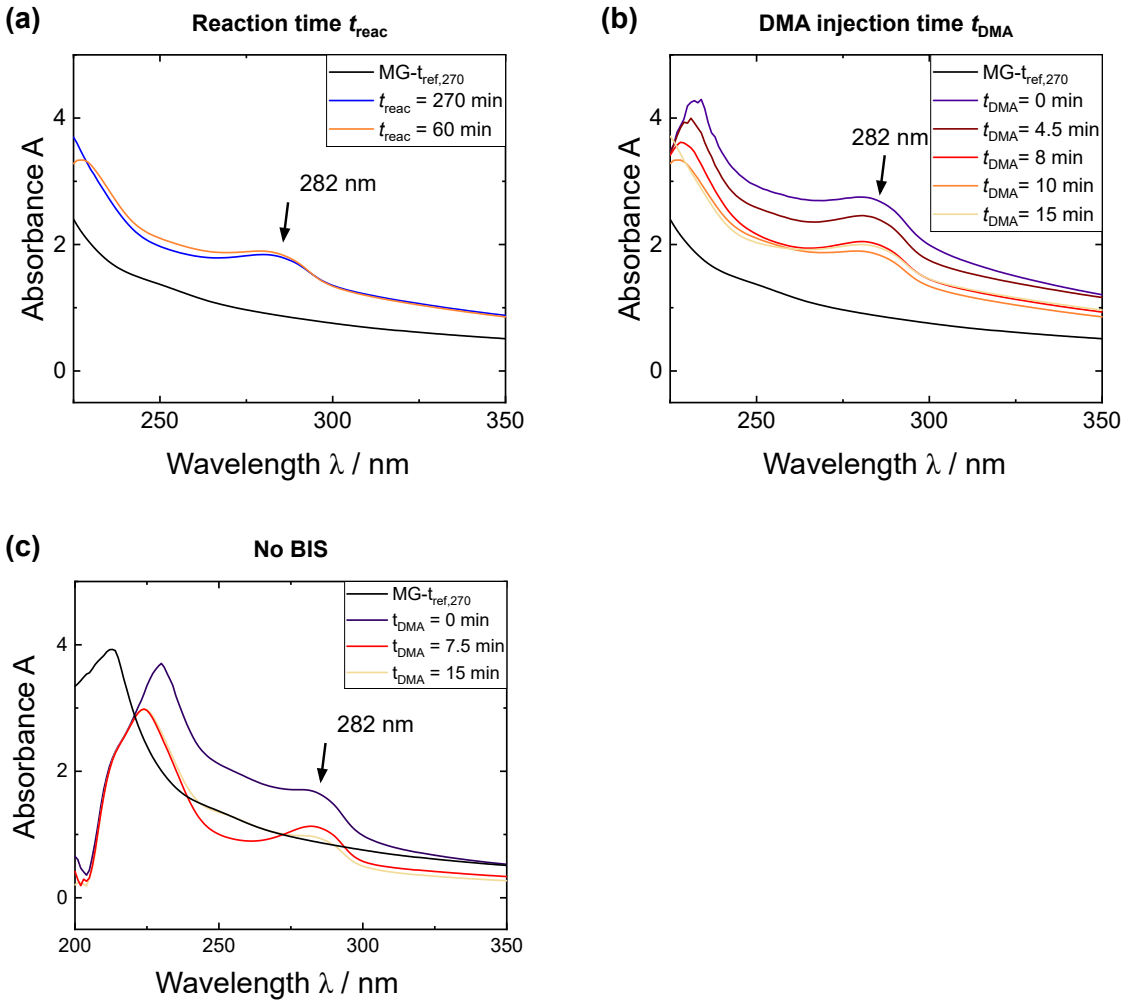

Figure A7: UV-vis spectra for P(NIPAM-co-DMA) microgels synthesised with different (a) overall reaction times t_{reac} and (b) & (c) DMA injection times t_{DMA} in comparison to the reference PNIPAM microgel MG-$t_{ref,270}$ (black). Microgels in (b) were cross-linked with BIS, while those in (c) were synthesised without BIS, solely relying on DMA's cross-linking ability.

A4.5 UV-vis standard addition calibration curves

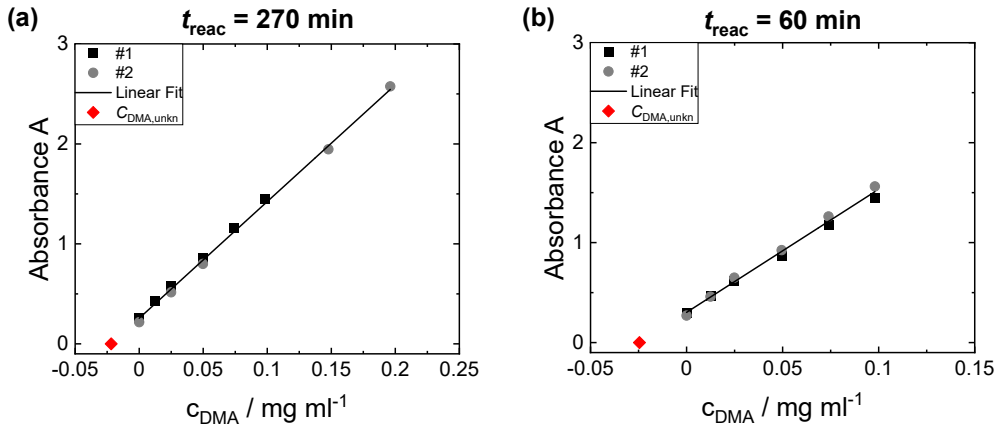

Figure A8: Calibration curves obtained by UV-vis standard addition for microgels with different overall reaction times (a) $t_{\mathrm{reac}} = 270\,\mathrm{min}$ and (b) $t_{\mathrm{reac}} = 60\,\mathrm{min}$: The absorbance at $\lambda_{\mathrm{max}} = 282\,\mathrm{nm}$, corresponding to the unoxidised catechol group of DMA, was plotted against the added DMA concentration for two calibration curves. A linear fit was applied to determine the unknown DMA concentration $c_{\mathrm{DMA,unkn}}$ in the microgel.

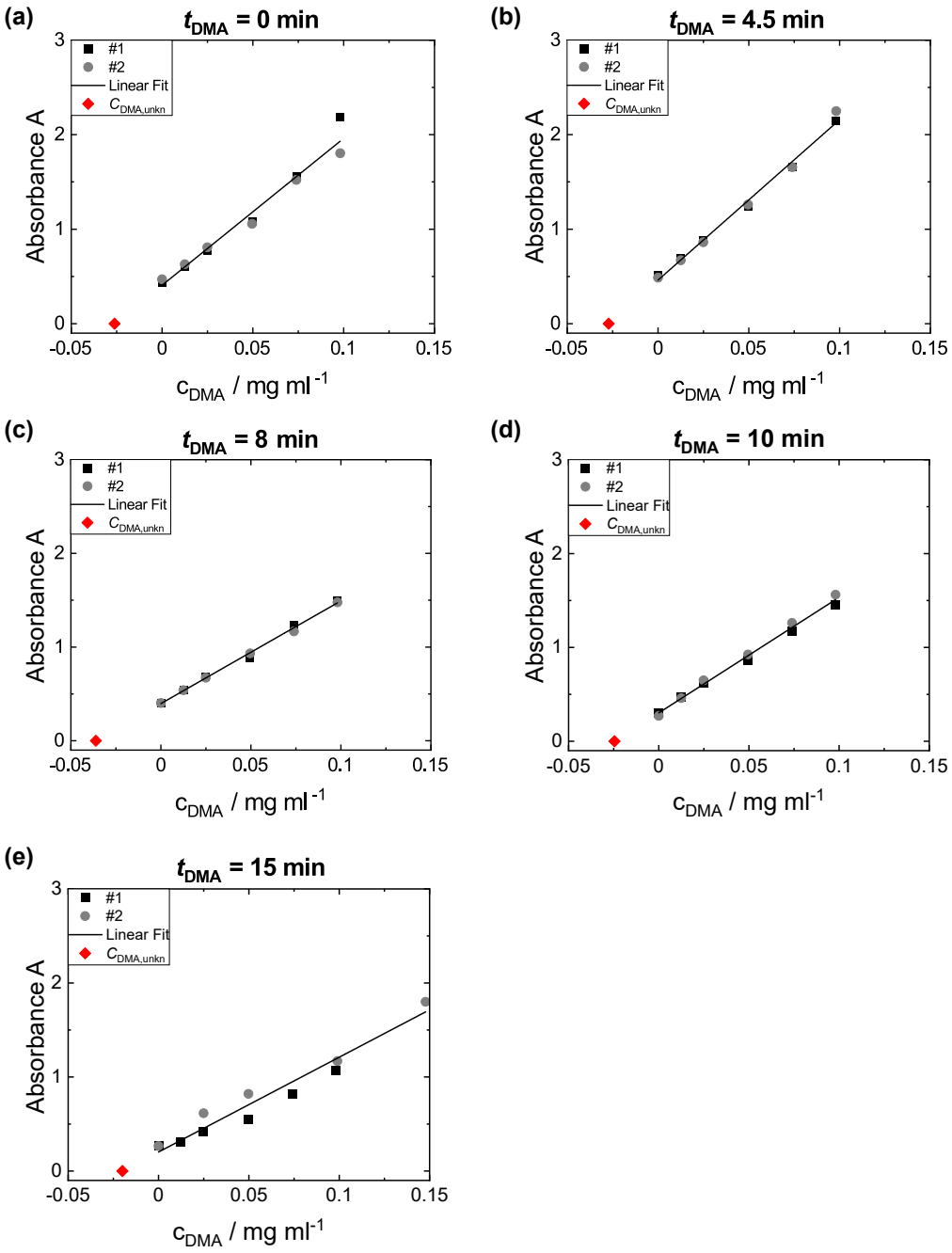

Figure A9: Calibration curves obtained by UV-vis standard addition for microgels with different DMA injection times (a) $t_{DMA} = 0\,min$, (b) $t_{DMA} = 4.5\,min$, (c) $t_{DMA} = 8\,min$, (d) $t_{DMA} = 10\,min$ and (e) $t_{DMA} = 15\,min$: The absorbance at $\lambda_{max} = 282\,nm$, corresponding to the unoxidised catechol group of DMA, was plotted against the added DMA concentration for two calibration curves. A linear fit was applied to determine the unknown DMA concentration $c_{DMA,unkn}$ in the microgel.

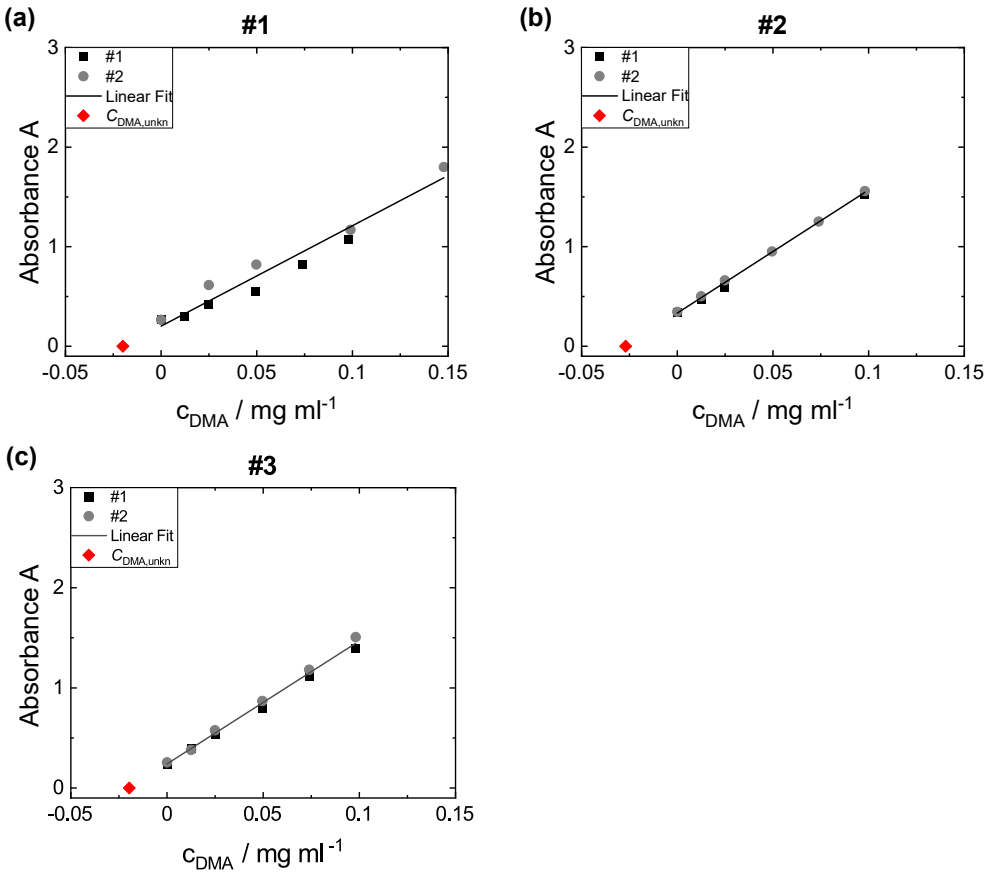

Figure A10: Calibration curves obtained by UV-vis standard addition for microgels synthesised with the same reaction parameters $t_{reac} = 60\,\text{min}$ and $t_{DMA} = 15\,\text{min}$ to test the reproducibility. Microgel #2 (b) and #3 (c) were synthesised with UV light protection. The absorbance at $\lambda_{max} = 282\,\text{nm}$, corresponding to the unoxidised catechol group of DMA, was plotted against the added DMA concentration for two calibration curves. A linear fit was applied to determine the unknown DMA concentration $c_{DMA,unkn}$ in the microgel.

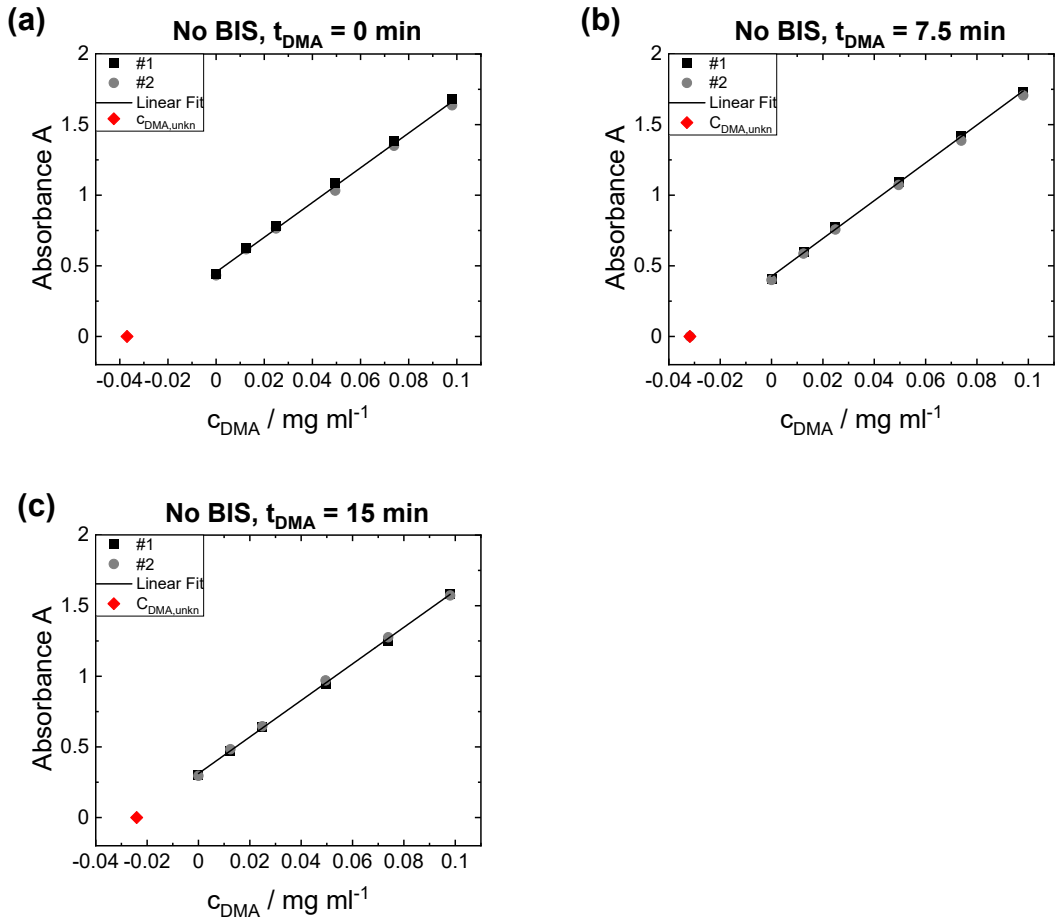

Figure A11: Calibration curves obtained by UV-vis standard addition for microgels synthesised without BIS (suffix "-noBIS") with different DMA injection times (a) $t_{\mathrm{DMA}} = 0\,\mathrm{min}$, (b) $t_{\mathrm{DMA}} = 7.5\,\mathrm{min}$ and $t_{\mathrm{DMA}} = 15\,\mathrm{min}$: The absorbance at $\lambda_{\mathrm{max}} = 282\,\mathrm{nm}$, corresponding to the unoxidised catechol group of DMA, was plotted against the added DMA concentration for two calibration curves. A linear fit was applied to determine the unknown DMA concentration $c_{\mathrm{DMA,unkn}}$ in the microgel.

A4.6 NMR spectra

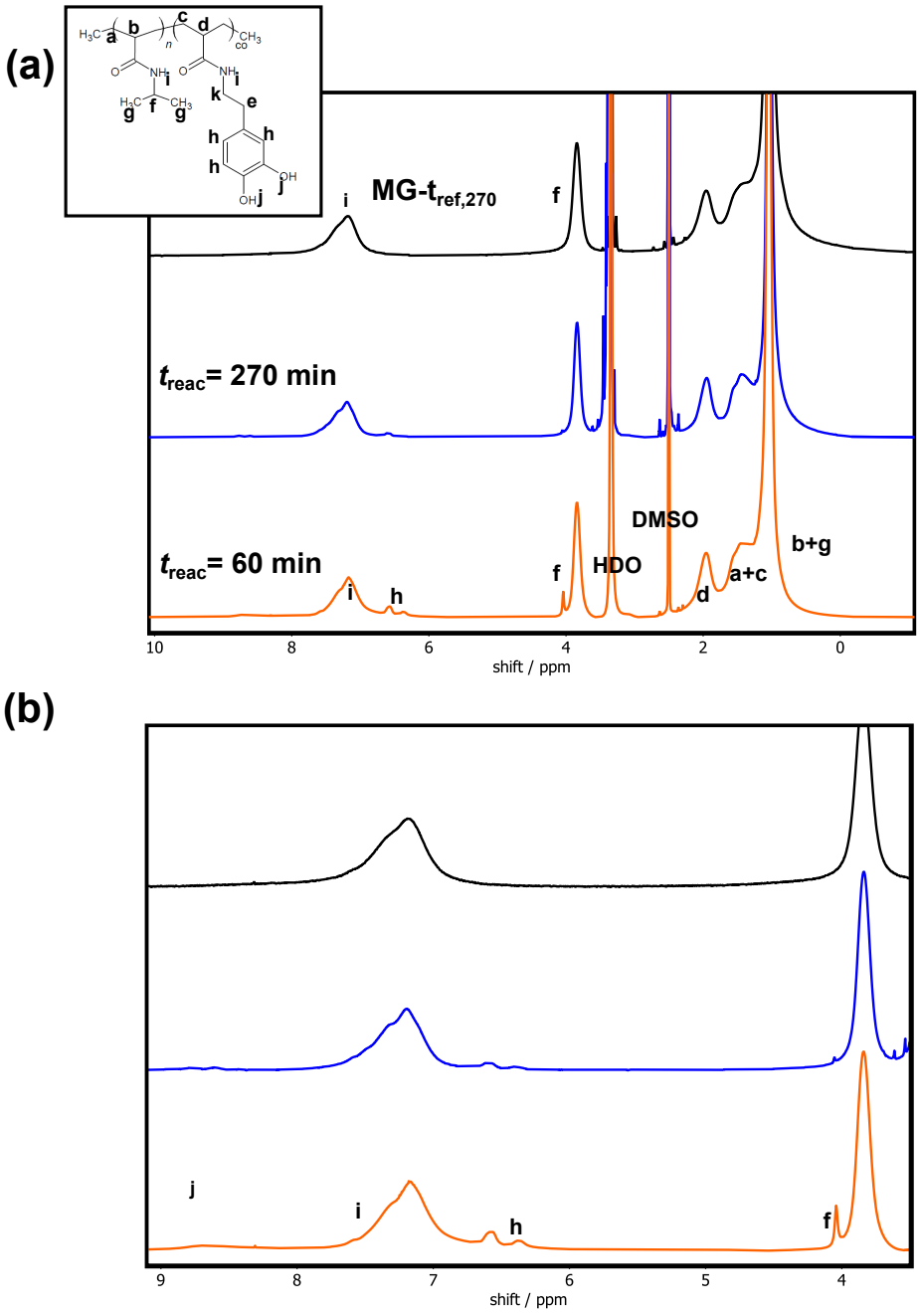

Figure A12: ^{1}H NMR spectra of MG-t$_{ref,270}$ compared to microgels with different reaction times t_{reac} in DMSO-d$_6$ with an enlargement of the higher shift region in (b).

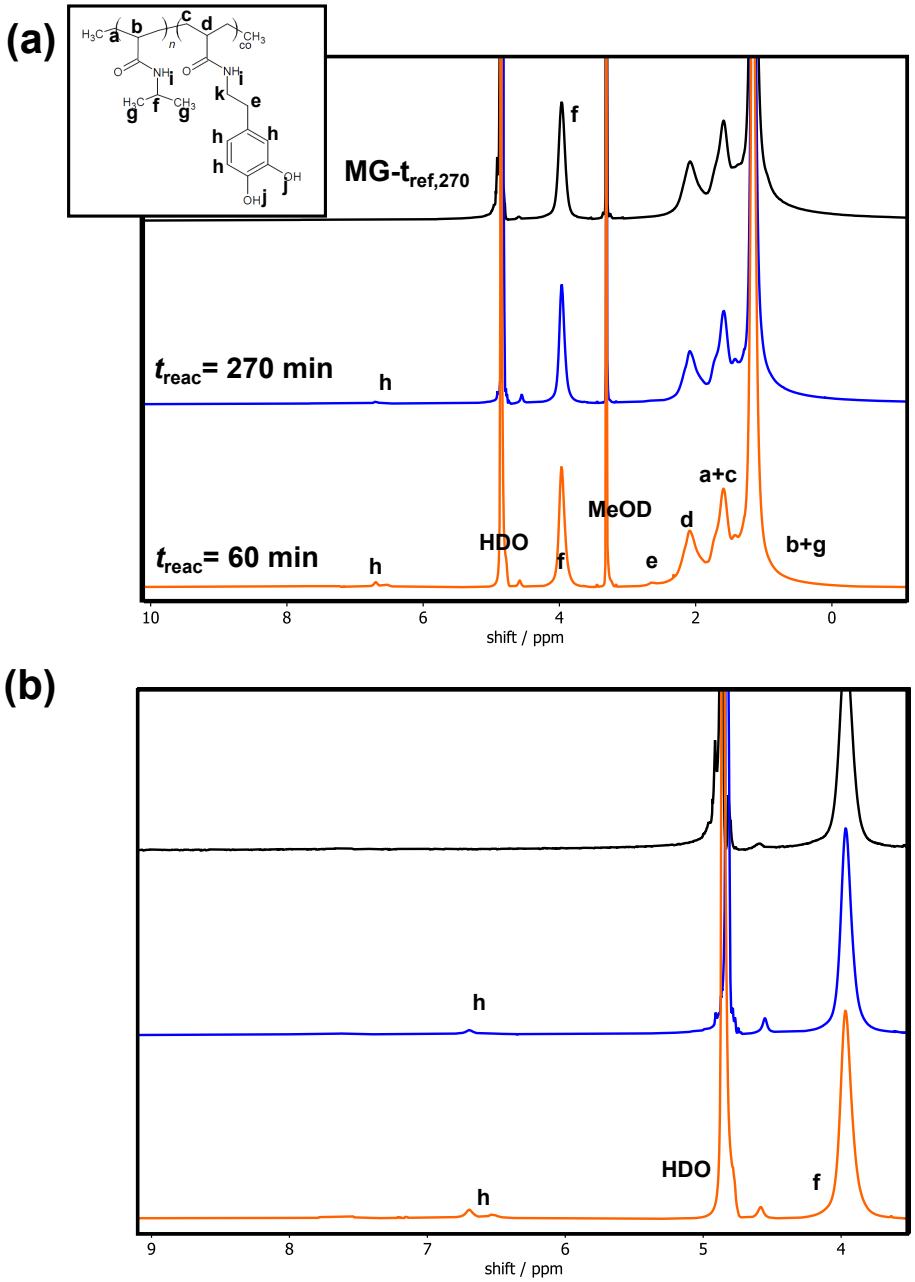

Figure A13: ^{1}H NMR spectra of MG-t$_{ref,270}$ compared to microgels with different reaction times t_{reac} in methanol-d$_4$ with an enlargement of the higher shift region in (b).

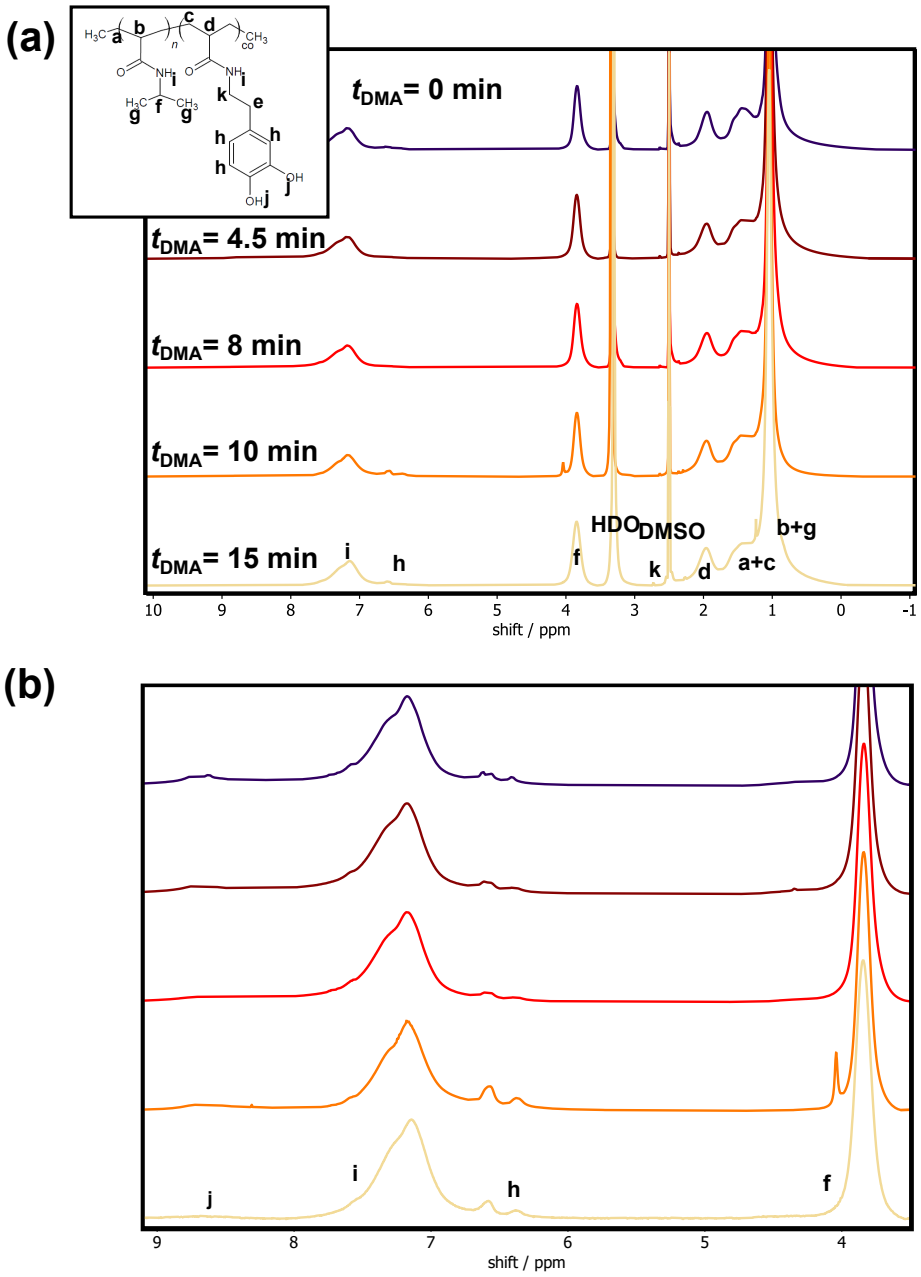

Figure A14: (a) ^{1}H NMR spectra of microgels with different DMA injection times t_{DMA} in DMSO-d_6 with an enlargement of the higher shift region in (b).

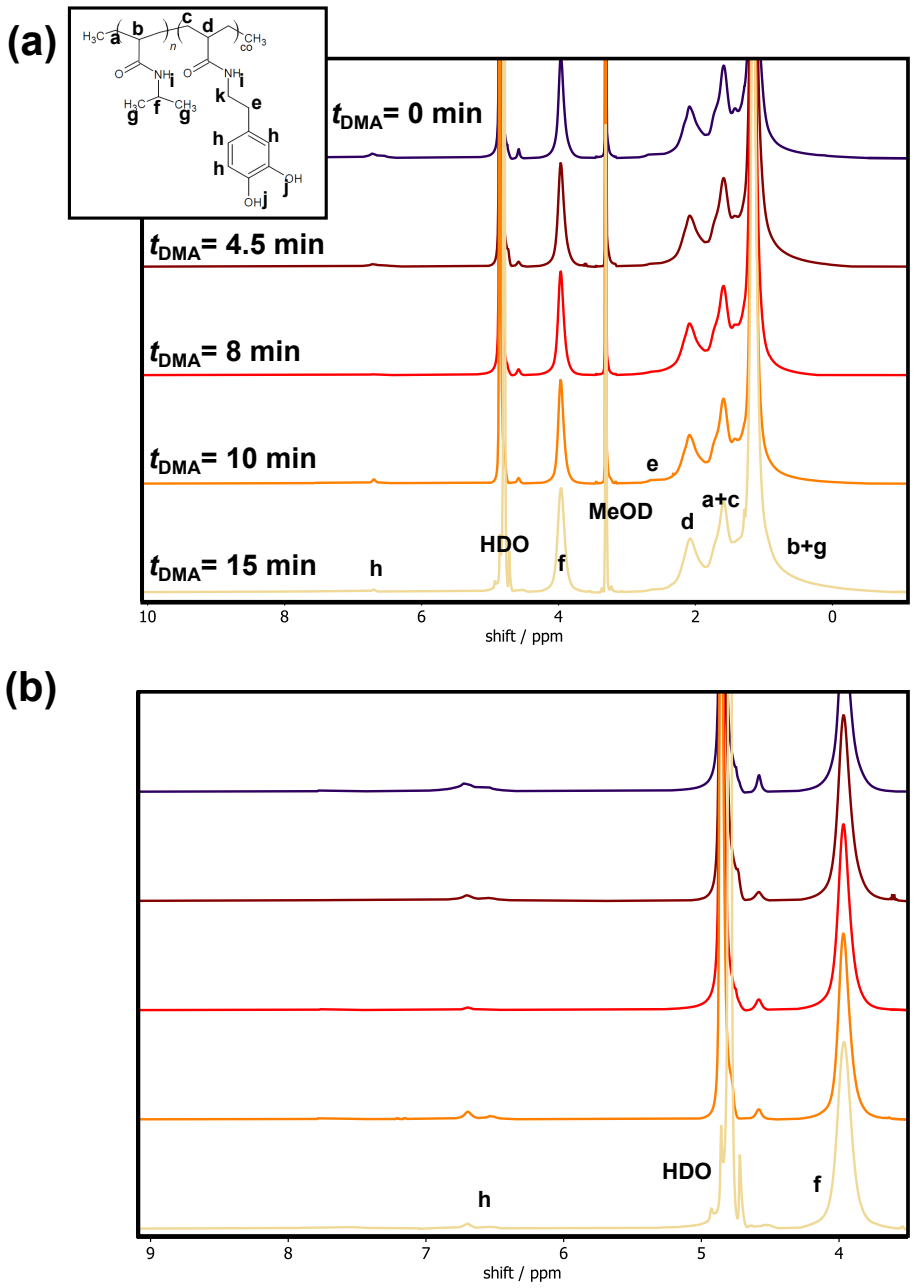

Figure A15: (a) ^{1}H NMR spectra of microgels with different DMA injection times t_{DMA} in methanol-d$_4$ with an enlargement of the higher shift region in (b).

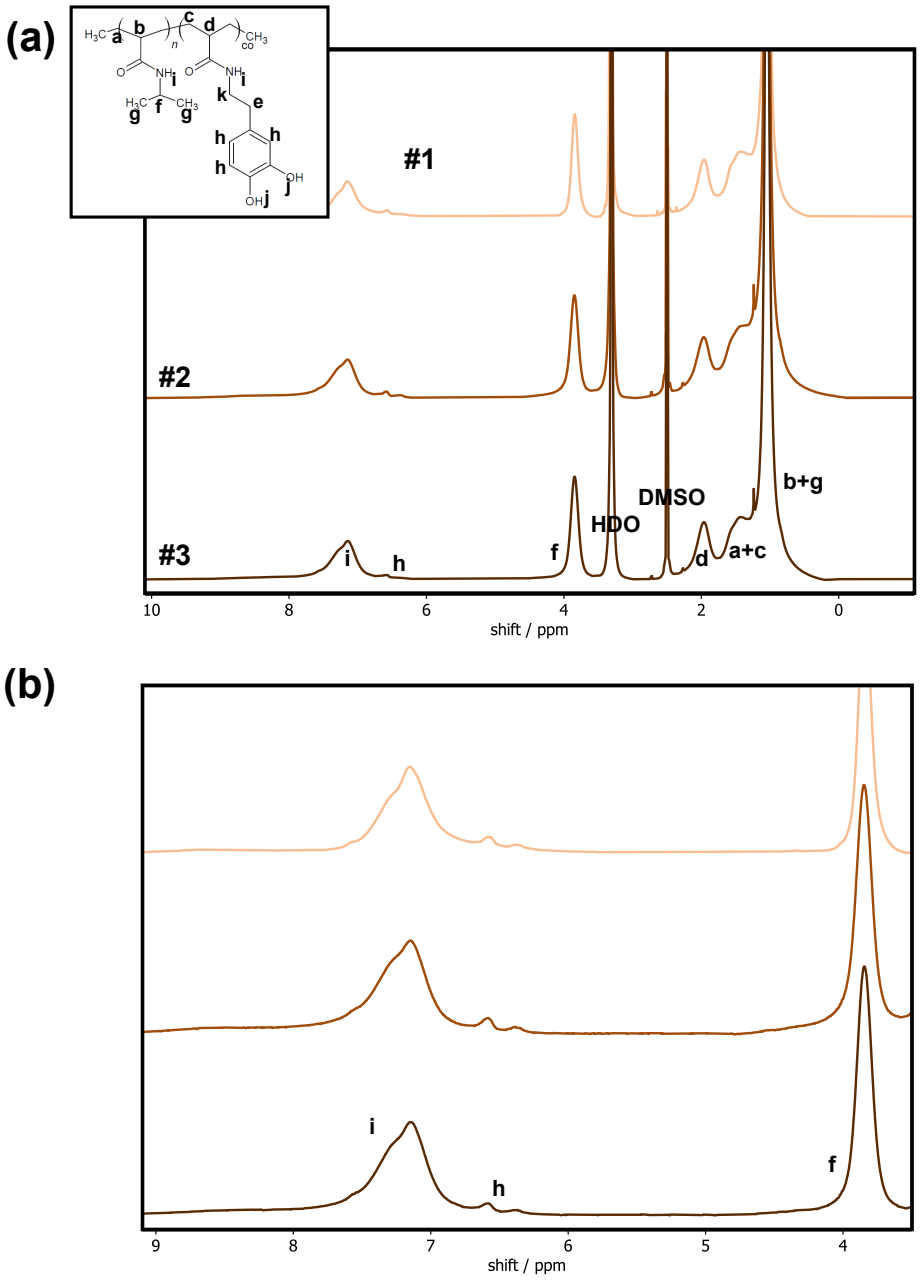

Figure A16: (a) ^{1}H NMR spectra of microgels synthesised with the same reaction parameters $t_{\mathrm{reac}} = 60\,\mathrm{min}$ and $t_{\mathrm{DMA}} = 15\,\mathrm{min}$ in DMSO-d_6, to test the reproducibility. #2 and #3 were synthesised with UV light protection. (b) shows an enlargement of the higher shift region.

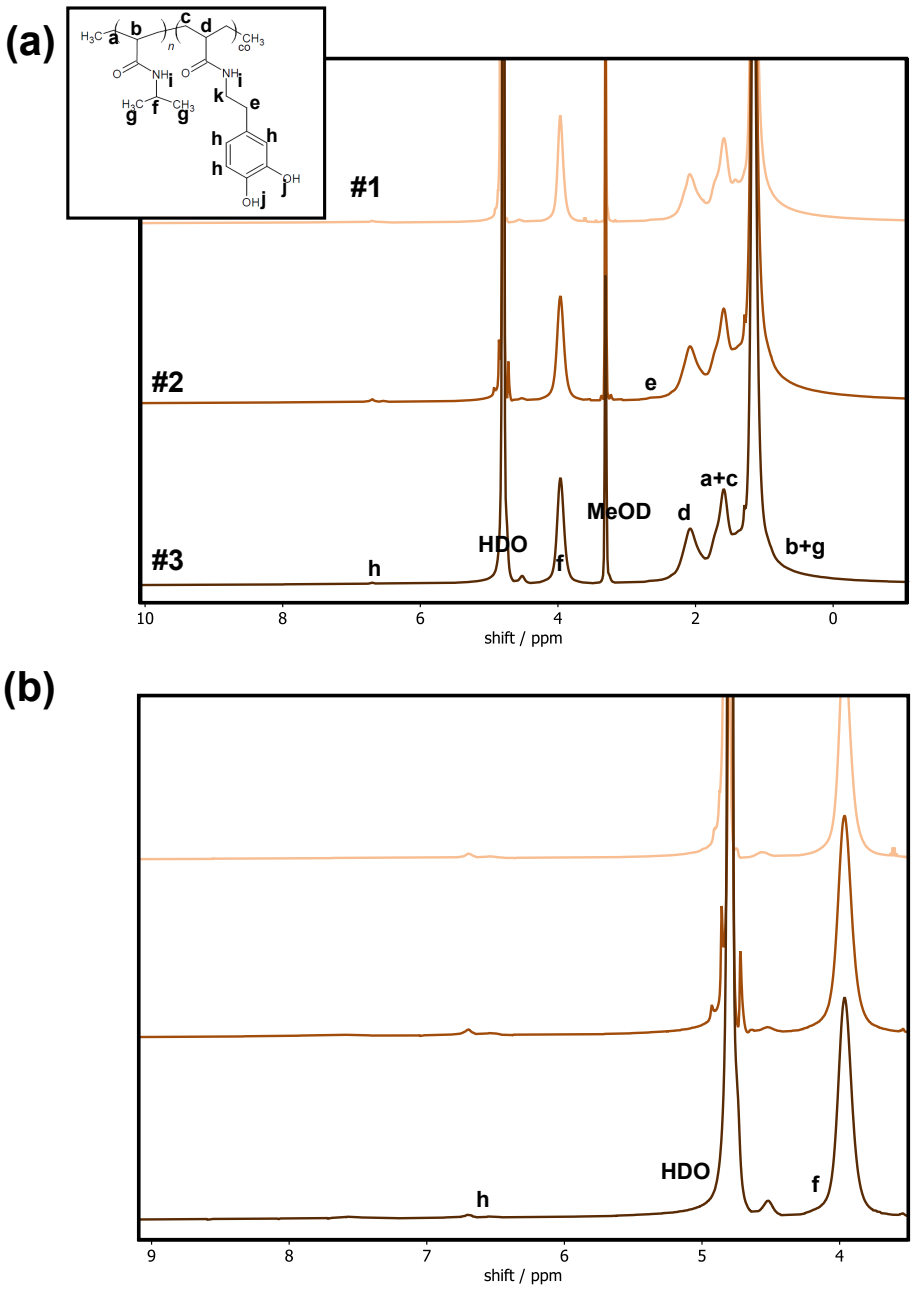

Figure A17: (a) ^{1}H NMR spectra of microgels synthesised with the same reaction parameters $t_{\mathrm{reac}} = 60\,\mathrm{min}$ and $t_{\mathrm{DMA}} = 15\,\mathrm{min}$ in methanol-d_4, to test the reproducibility. #2 and #3 were synthesised with UV light protection. (b) shows an enlargement of the higher shift region.

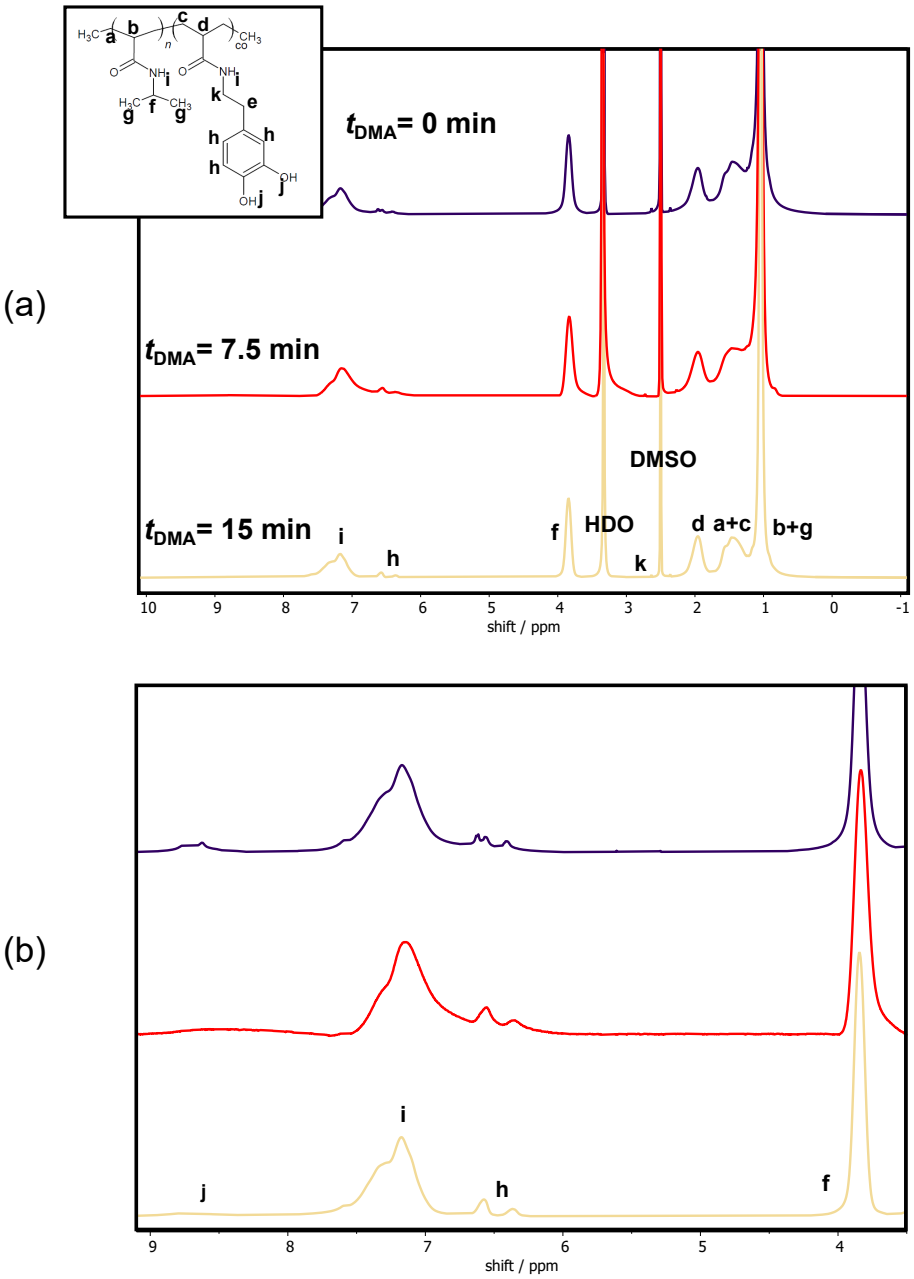

Figure A18: (a)^{1}H NMR spectra of microgels synthesised without BIS (suffix "-noBIS") with different DMA injection times $t_{DMA} = 0$ min, $t_{DMA} = 7.5$ min and $t_{DMA} = 15$ min in DMSO-d_6. An enlargement of the important shift region is shown in (b).

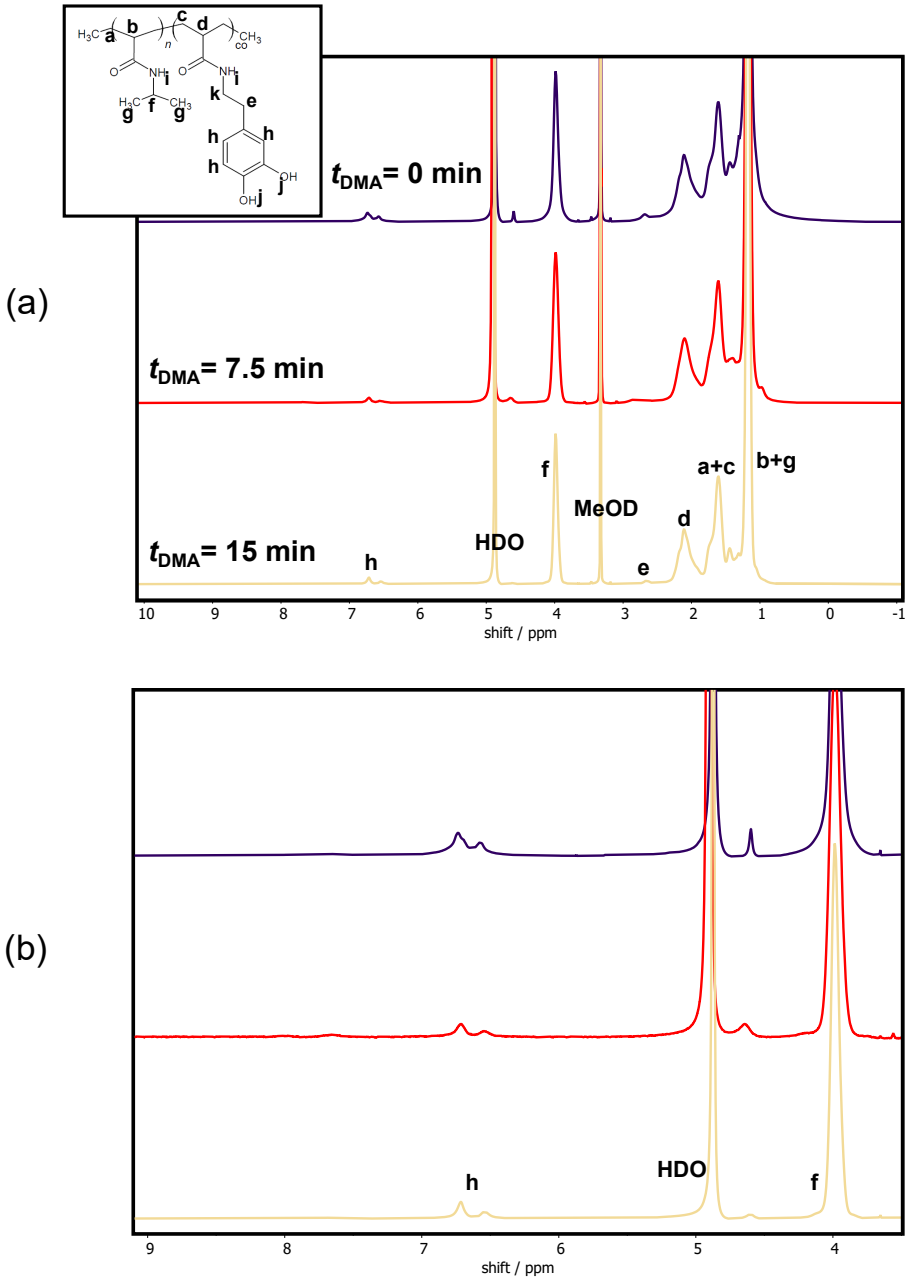

Figure A19: (a)^{1}H NMR spectra of microgels synthesised without BIS (suffix "-noBIS") with different DMA injection times $t_{\mathrm{DMA}} = 0\,\mathrm{min}$, (b) $t_{\mathrm{DMA}} = 7.5\,\mathrm{min}$ and $t_{\mathrm{DMA}} = 15\,\mathrm{min}$ in methanol-d_4. An enlargement of the important shift region is shown in (b).

A4.7 DLS measurements of microgels synthesised without BIS

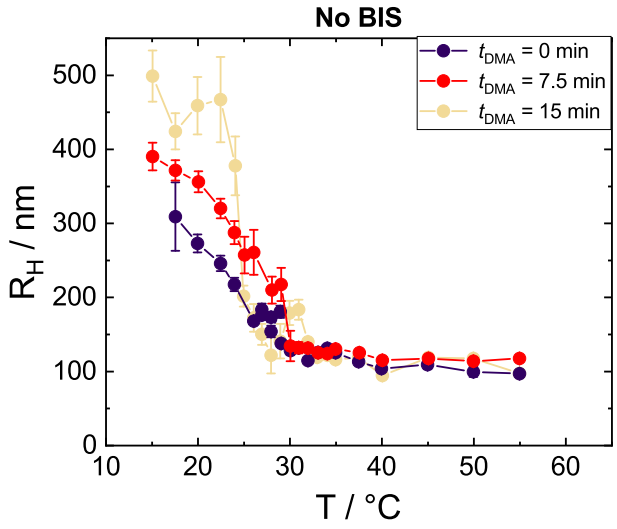

Figure A20: R_H in dependence of temperature T for the different microgels synthesised without the additional cross-linker BIS (suffix "-noBIS").

Fig. A20 shows the swelling curves of the microgels synthesised without BIS, solely relying on the cross-linking ability of DMA, as a function of temperature. The curves were determined using dynamic light scattering (DLS), as detailed in chapter 3.4. The results demonstrate the characteristic temperature-responsive behaviour of the microgels, where they undergo a collapse in size upon heating.

Notably, the microgel MG-$t_{15,60}$-noBIS with a DMA injection time of $t_{DMA} = 15\,\text{min}$ possesses the largest swollen hydrodynamic radius $R_H(20°C)$. $R_H(20°C)$ subsequently decreases for earlier injection times of DMA. The shrunken hydrodynamic radius $R_H(50°C)$ is comparable for the three microgels.

This phenomenon can be explained as follows: When DMA is introduced into the reaction at a later stage, it necessitates NIPAM's self-cross-linking ability [71–73] at the beginning of the synthesis. Typically, this leads to the formation of microgels with a low degree of cross-linking [189]. Structures with a lower cross-linking density, however, have a greater capacity to swell, as discussed in chapter 5. Conversely, when DMA is introduced at the beginning of the synthesis, the microgel structure is cross-linked by DMA. This should theoretically increase the overall cross-linking density of the microgel - the microgels are less prone to swelling, leading to smaller hydrodynamic radii.

A5 Appendix for chapter 5

A5.1 Reaction kinetics

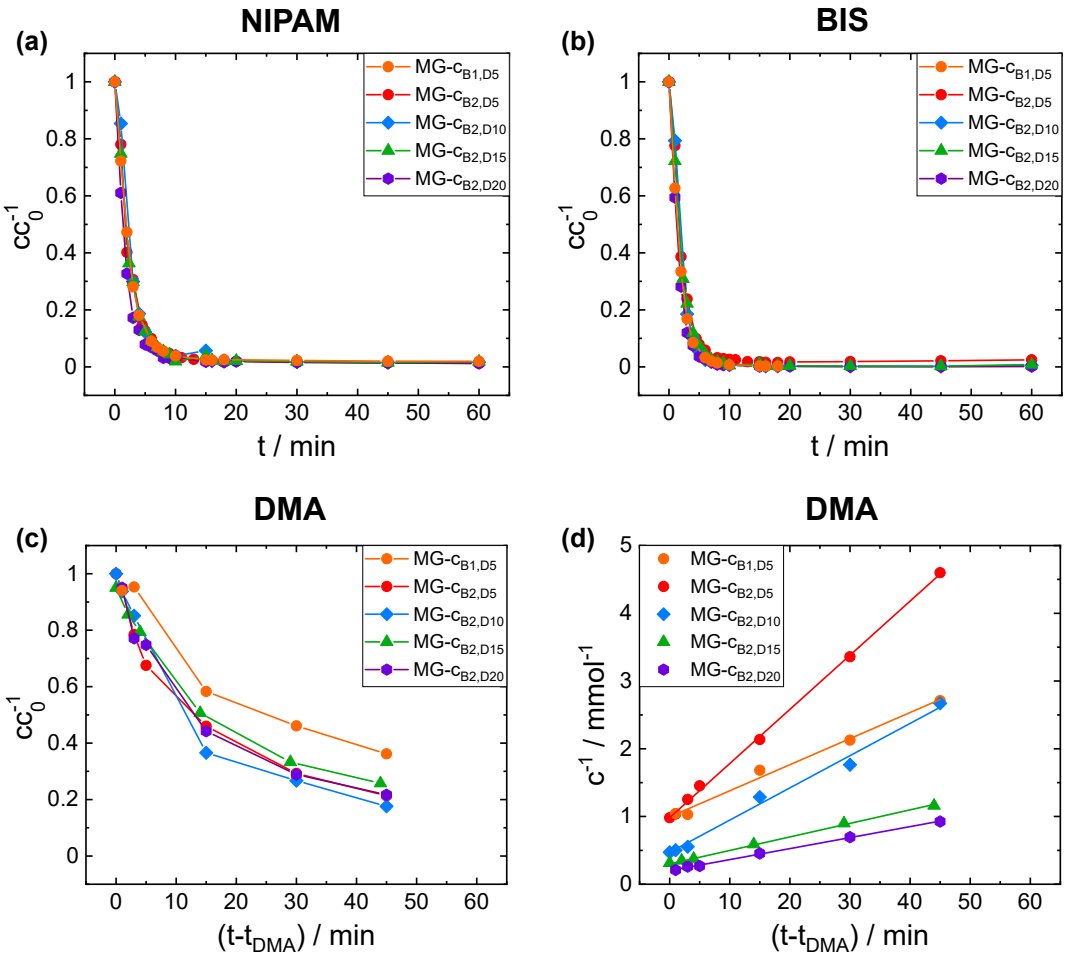

Figure A21: Relative monomer consumptions cc_0^{-1} of reactants NIPAM (a) and BIS (b) as a function of the reaction time t obtained by MS. (c) Relative monomer consumptions cc_0^{-1} of DMA as a function of the effective reaction time $t - t_{\mathrm{DMA}}$. (d) shows the inverse monomer consumption c^{-1} of DMA. A linear fit can be applied, which underlines that DMA possesses a second-order reaction kinetics.

A5.2 UV-vis standard addition

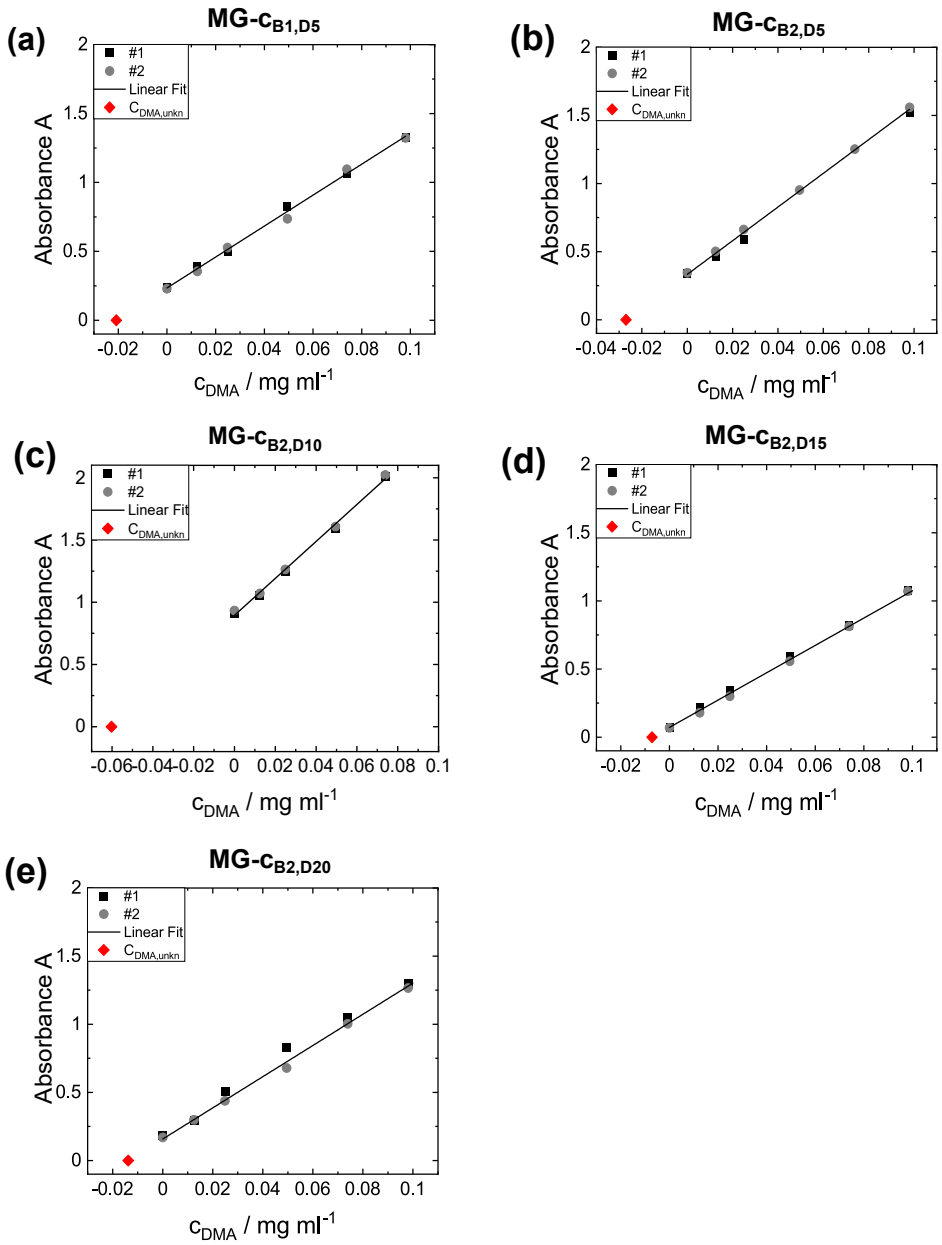

Figure A22: Calibration curves obtained by UV-Vis standard addition for (a) MG-$c_{B1,D5}$, (b) MG-$c_{B2,D5}$, (c) MG-$c_{B2,D10}$, (d) MG-$c_{B2,D15}$ and (e) MG-$c_{B2,D20}$. The microgel sample concentration was 0.05 wt% for (a)-(c) and 0.005 wt% for (d)-(e). The absorbance A at $\lambda_{max} = 282$ nm was plotted over the added concentration of DMA solution. Calibration curves were repeated 2 times. A linear function was fitted to the medium of the two curves to obtain the unknown DMA concentration $c_{DMA,unkn}$.

A5.3 NMR spectra

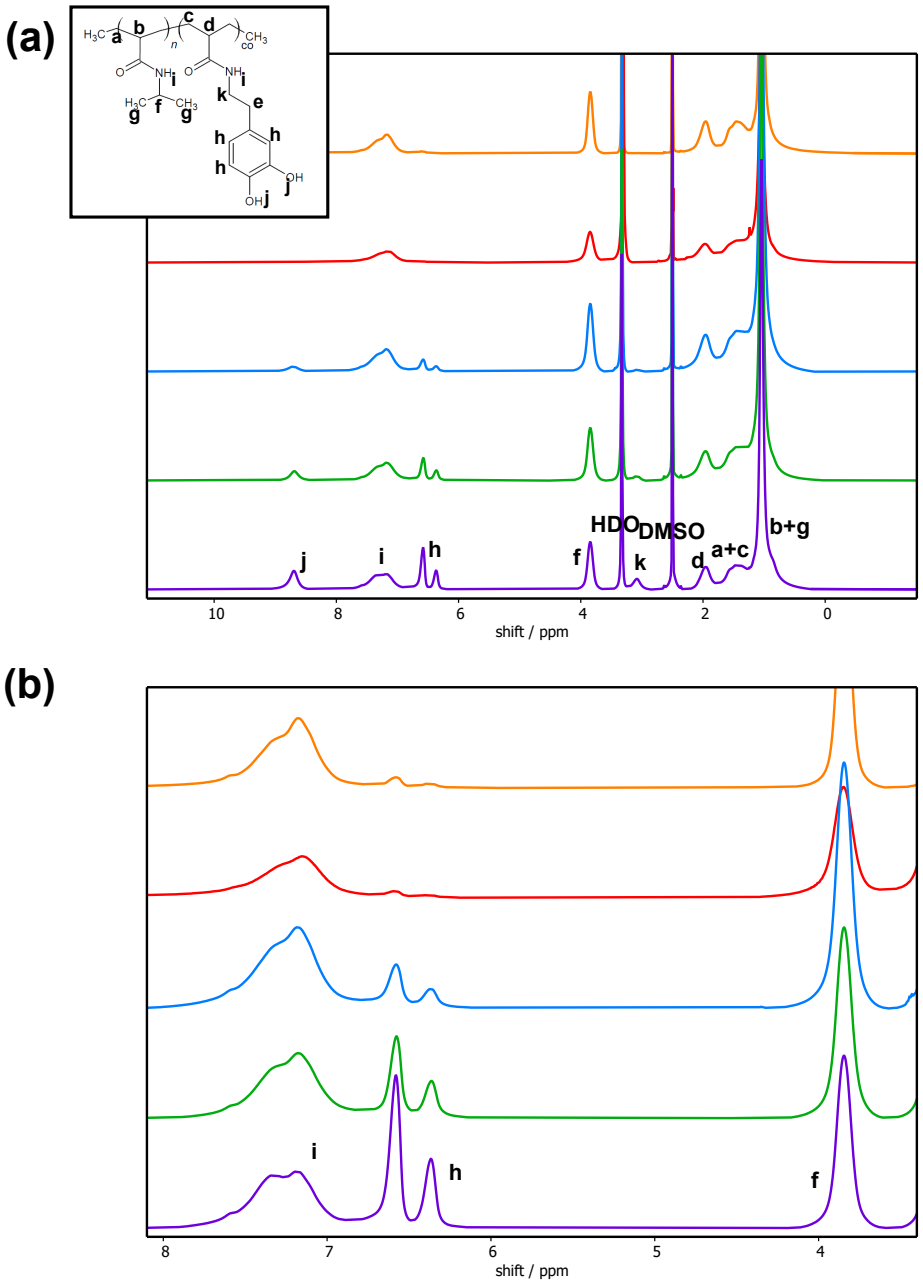

Figure A23: (a)^{1}H NMR spectra of different microgels MG-$c_{B1,D5}$ (orange), MG-$c_{B2,D5}$ (red), MG-$c_{B2,D10}$ (blue), MG-$c_{B2,D15}$ (green) and MG-$c_{B2,D20}$ (purple) in DMSO-d_6. An enlargement of the important shift region is shown in (b).

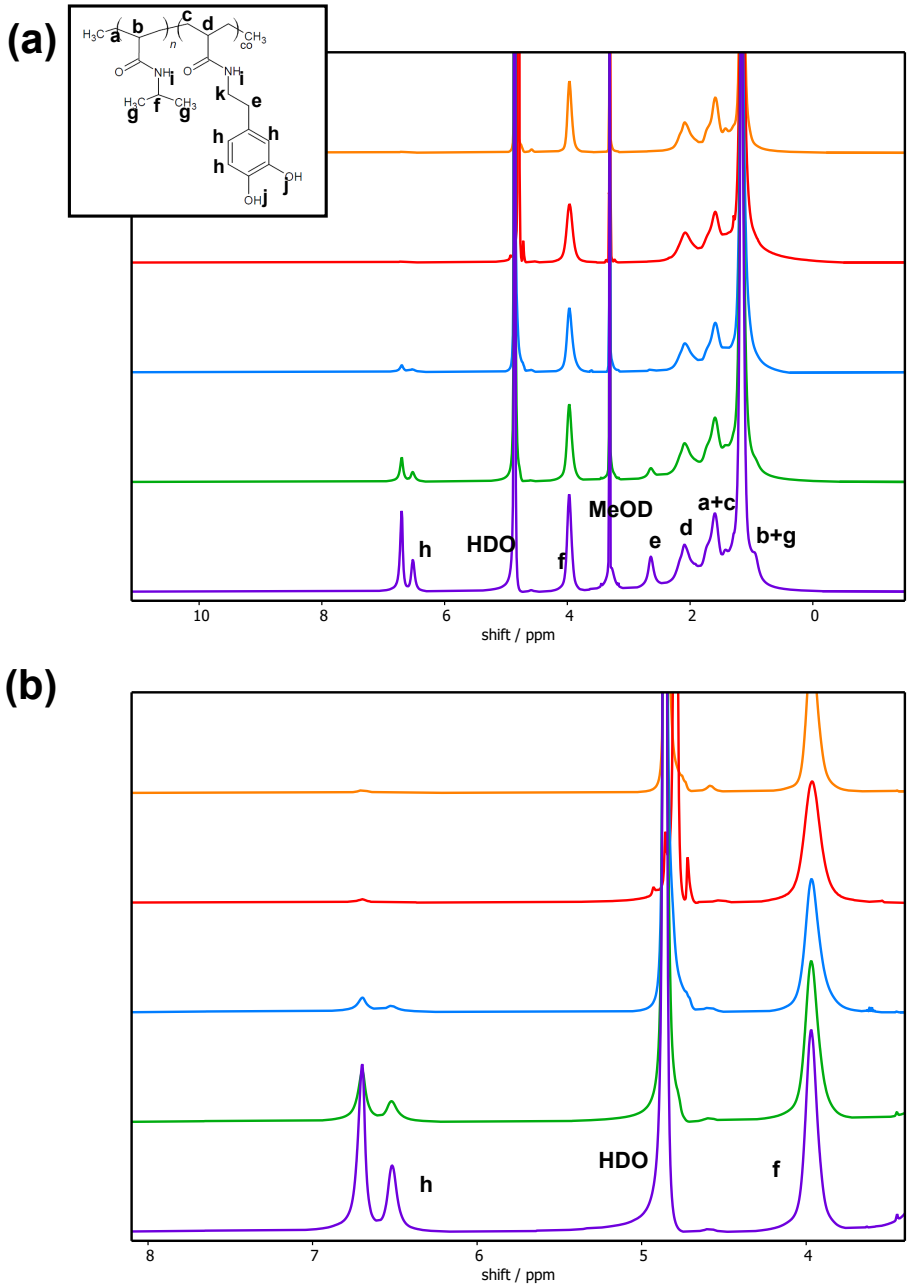

Figure A24: (a)^{1}H NMR spectra of different microgels MG-$c_{B1,D5}$ (orange), MG-$c_{B2,D5}$ (red), MG-$c_{B2,D10}$ (blue), MG-$c_{B2,D15}$ (green) and MG-$c_{B2,D20}$ (purple) in methanol-d_4. An enlargement of the important shift region is shown in (b).

A5.4 DLS measurements

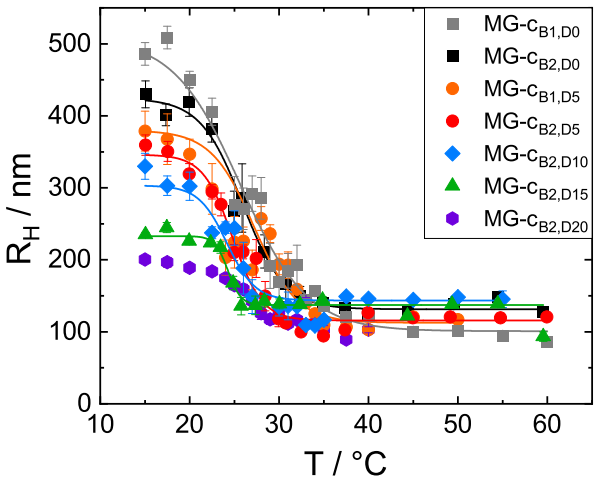

Figure A25: Swelling curves of microgels fitted by a sigmoidal function.

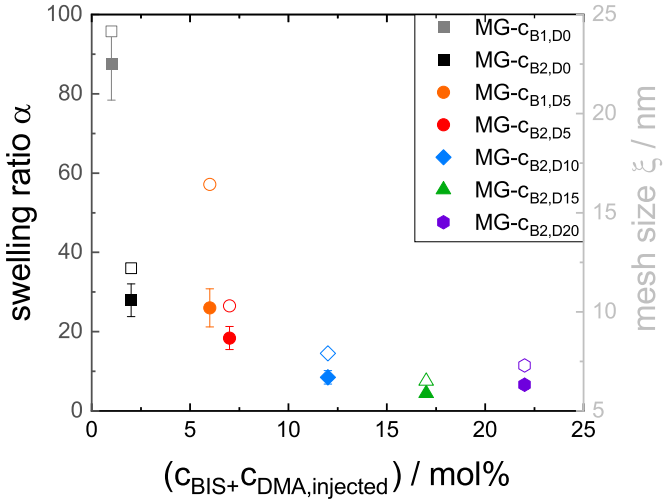

Figure A26: Calculated swelling ratios α (filled symbols) and mesh sizes ξ (open symbols) plotted against the concentration of BIS c_{BIS} and injected DMA $c_{DMA,injected}$.

A5.5 AFM

AFM imaging

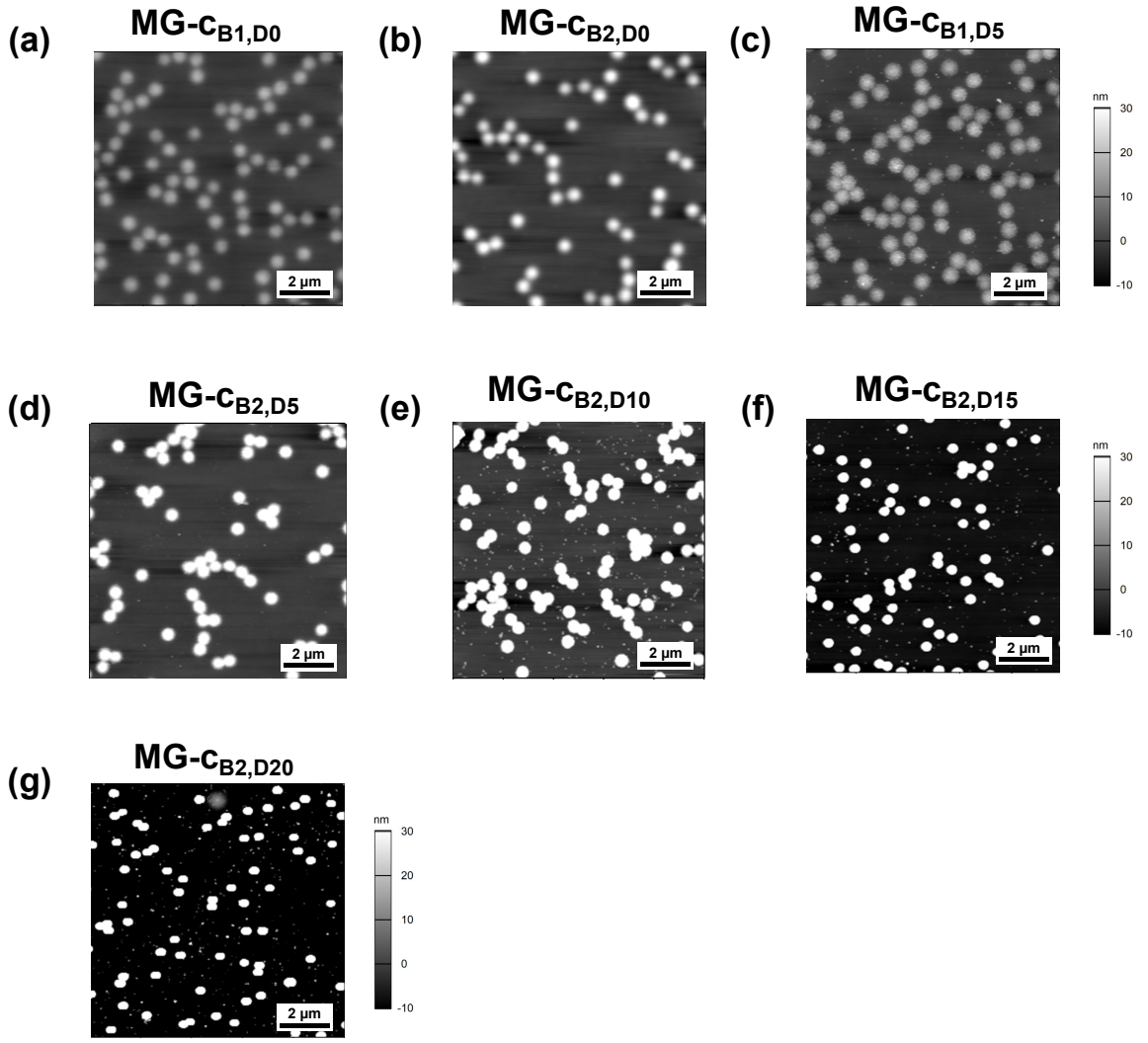

Figure A27: AFM scans taken in ambient conditions at a temperature of $T = 20°C$ for (a) MG-c$_{B1,D0}$, (b) MG-c$_{B2,D0}$, (c) MG-c$_{B1,D5}$, (d) MG-c$_{B2,D5}$, (e) MG-c$_{B2,D10}$, (f) MG-c$_{B2,D15}$ and (g) MG-c$_{B2,D20}$. They were used to calculate the height $h_{\text{amb,AFM}}$ and the width $w_{\text{amb,AFM}}$ of the microgels.

Table A3: Characterisation of microgels at the surface by AFM scanning in ambient conditions. Values are derived from an average of 5 different microgels per sample. While the error of the height $h_{amb,AFM}$ was obtained directly by standard deviation of the 5 particles, the error of the width $w_{amb,AFM}$ was assumed to be 10% as estimated by eye for the microgel with the highest width MG-$c_{B2,D0}$.

Microgel	$h_{amb,AFM}$ / nm	$w_{amb,AFM}$ / nm
MG-$c_{B1,D0}$	17 ± 2	1177 ± 118
MG-$c_{B2,D0}$	28 ± 3	1061 ± 106
MG-$c_{B1,D5}$	20 ± 1	984 ± 98
MG-$c_{B2,D5}$	44 ± 7	904 ± 90
MG-$c_{B2,D10}$	78 ± 3	706 ± 71
MG-$c_{B2,D15}$	131 ± 4	471 ± 47
MG-$c_{B2,D20}$	234 ± 12	433 ± 43

AFM force spectroscopy

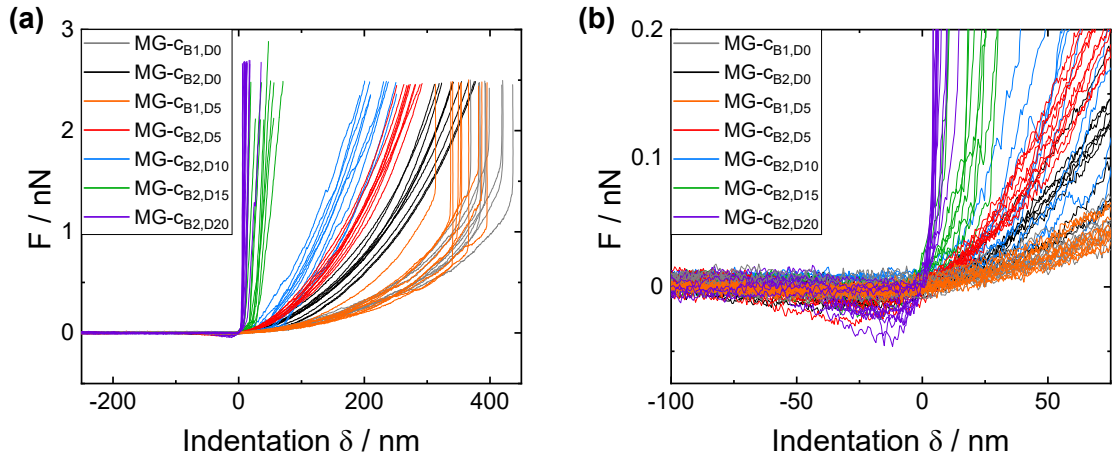

Figure A28: (a) Pure force curves received for the different microgels with a BL-AC40TS cantilever, used for the calculation of *E* moduli. (b) Inset of (a) highlighting the attraction before the actual indentation. For the microgels with lower cross-linker amount (MG-$c_{B1,D0}$ and MG-$c_{B1,D5}$), the microgel's height is so small that the cantilever already touches the substrate's surface before reaching the trigger point. This could damage the tip when forces get too high. However, the measurement of 10 different microgels with the same tip showed no large deviations in force curves and *E* moduli, so we conclude that the tip stays intact.

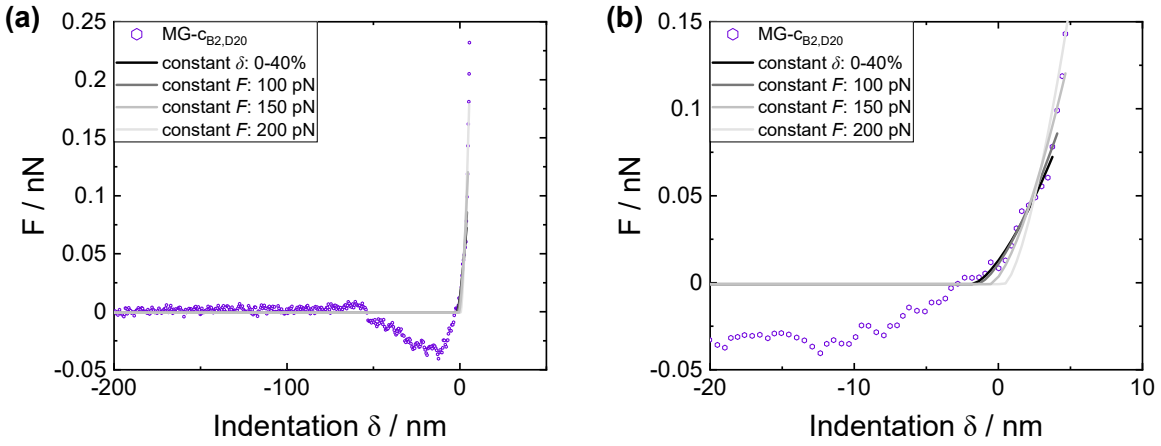

Figure A29: (a) Exemplary force curve of MG-c$_{B2,D20}$ microgel fitted by different methods: either a constant indentation range δ or a constant force range F was chosen. (b) Inset of (a) visualising the choice of fitting values. Constant forces above 100 pN cannot describe the force curve adequately.

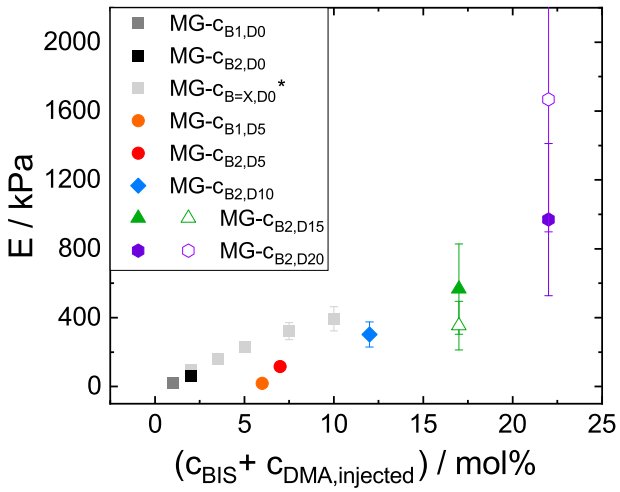

Figure A30: (a) E moduli obtained from 10 force curves of each microgel particle plotted over the concentration of BIS c_{BIS} and injected DMA $c_{DMA,injected}$, calculated by fitting the approach force curves with a constant indentation range of $0-40\%$. Light grey symbols correspond to results obtained by Kühnhammer *et al.*[50]. For MG-c$_{B2,D15}$ and MG-c$_{B2,D20}$, the approach force curves were fitted additionally with a constant force range of 100 pN (open symbols).

A6 Appendix for chapter 6

A6.1 Increasing packing density

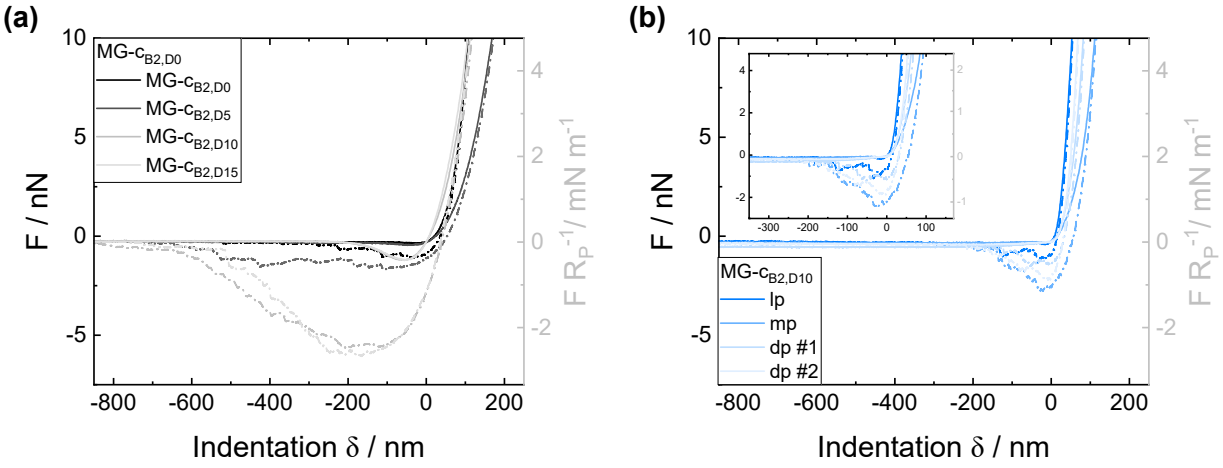

Figure A31: Exemplary force curves of the microgel samples prepared with an increasing packing density for (a) the pure PNIPAM microgel MG-$c_{B2,D0}$ and (b) the P(NIPAM-co-DMA) microgel MG-$c_{B2,D10}$. The approach curve is illustrated as continuous line, while the retract curve is illustrated as a dashed line.

Table A4: Relevant parameters of colloidal probe measurements on samples prepared in by the Langmuir-Blodgett technique with different surface pressures Π for (a) the pure PNIPAM microgel MG-$c_{B2,D0}$ and (b) the P(NIPAM-co-DMA) microgel MG-$c_{B2,D10}$: mean colloidal probe radius $\overline{R}_P$ (derived from SEM images), mean indentation depth $\overline{\delta}$, contact radius a (eq. 3.22) and contact area A (eq. 3.23) calculated from an average of 10 force curves.

Microgel	packing density	$\overline{R}_P$ / µm	$\overline{\delta}$ / nm	a / nm	A / µm^2
MG-$c_{B2,D0}$	lp	2.14 ± 0.03	114.6 ± 12.5	495.2 ± 27.2	3.04 ± 0.33
	mp	2.14 ± 0.03	193.0 ± 18.6	642.7 ± 31.3	5.07 ± 0.48
	dp #1	2.14 ± 0.03	131.1 ± 18.3	541.7 ± 37.2	3.63 ± 0.48
	dp #2	2.14 ± 0.03	143.6 ± 15.5	554.4 ± 30.17	3.80 ± 0.41
MG-$c_{B2,D10}$	lp	2.14 ± 0.03	97.6 ± 16.7	457.0 ± 39.2	2.59 ± 0.44
	mp	2.14 ± 0.03	100.8 ± 12.8	464.4 ± 29.7	2.68 ± 0.34
	dp #1	2.14 ± 0.03	82.8 ± 7.3	420.9 ± 18.8	2.21 ± 0.20
	dp #2	2.14 ± 0.03	81.1 ± 9.3	416.6 ± 24.1	2.16 ± 0.25

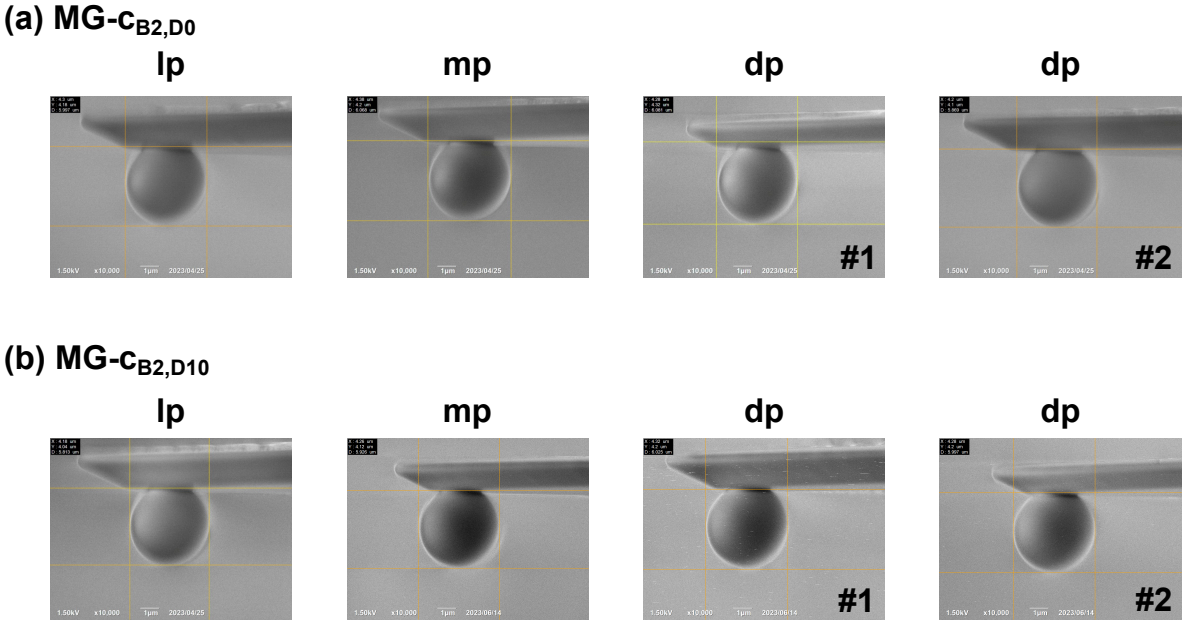

Figure A32: SEM images of colloidal probes used for force spectroscopy measurements on samples prepared by the Langmuir-Blodgett technique at different surface pressures Π: 5 mN m^{-1}, 21 mN m^{-1} and 24 mN m^{-1}, resulting in different packing densities - low packing (lp), medium packing (mp) and dense packing (dp). (a) shows images of colloidal probes used for the pure PNIPAM microgel MG-c$_{B2,D0}$ and (b) for the P(NIPAM-co-DMA) microgel MG-c$_{B2,D10}$.

Ageing effect of microgel layer and colloidal probe

As explained in chapter 3.6.2, force maps were conducted at different positions on the silicon wafers (A, B and C) to check for ageing effects arising from material fatigue or due to contaminations. The normalised adhesion force $F_{adh}\,A^{-1}$ of each independent spot is given in fig. A33 (a) for the pure PNIPAM microgel MG-c$_{B2,D0}$ and in (b) for the P(NIPAM-co-DMA) microgel MG-c$_{B2,D10}$. The microgels were deposited on silicon wafers using the Langmuir-Blodgett technique at different surface pressures (5 mN m^{-1}, 21 mN m^{-1} and 24 mN m^{-1}). This results in different packing densities: low packing (lp), medium packing (mp) and dense packing (dp).
For the pure PNIPAM microgel MG-c$_{B2,D0}$ with a dp (named dp #1 in the following), $F_{adh}\,A^{-1}$ clearly decreases with the ongoing measurement. Therefore, the measurement was repeated with a new, cleaned colloidal probe (see fig. A32) at a different position on the silicon wafer. The measurement is named dp #2. For the repeated

measurement, the normalised adhesion force $F_{adh}\,A^{-1}$ decreases as well, indicating an ageing effect. Values of both measurements are in good agreement with each other, demonstrating the reproducibility of the results. For the remaining samples, no ageing effects were observed.

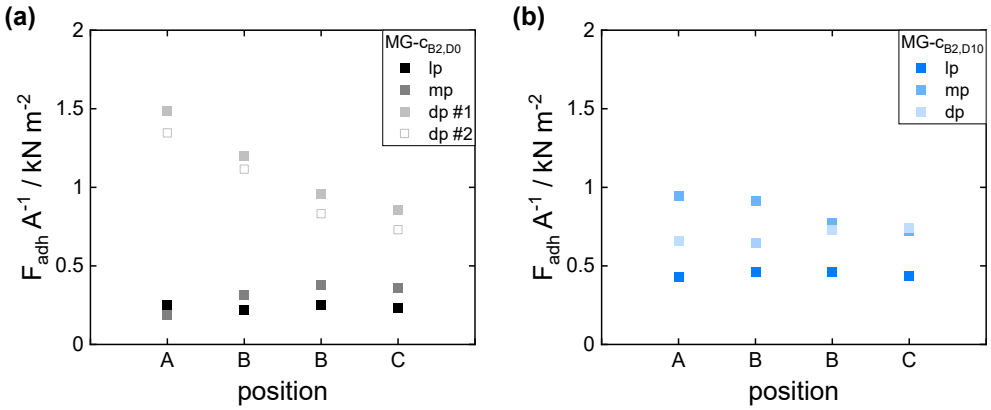

Figure A33: Normalised adhesion force $F_{adh}\,A^{-1}$ of (a) the pure PNIPAM microgel MG-$c_{B2,D0}$ and (b) the P(NIPAM-co-DMA) microgel MG-$c_{B2,D10}$, calculated from force maps conducted at different positions (A, B and C) at the silicon wafer with a trigger point of 15 nN. Due to ageing effects, measurements were repeated on the dp sample of the pure PNIPAM microgel MG-$c_{B2,D0}$ (dp #1 closed symbols and dp #2 open symbols).

Densely packed P(NIPAM-co-DMA) microgels

The pure PNIPAM microgel exhibits superior adhesion compared to the P(NIPAM-co-DMA) microgel for high packing densities. To conduct a more comprehensive assessment and validation of this phenomenon, a new P(NIPAM-co-DMA) microgel sample with a dp was prepared, referred to as dp #2. The AFM scan of this sample is illustrated in fig. A34 in comparison to the first sample prepared with a dp (dp #1). Force spectroscopy measurements on the sample dp #2 were conducted with a new colloidal probe. The SEM image of the colloidal probe is given in fig. A32. The average normalised adhesion force $F_{adh}\,A^{-1}$ aligns with the results obtained for the initial sample as illustrated in fig. A35.

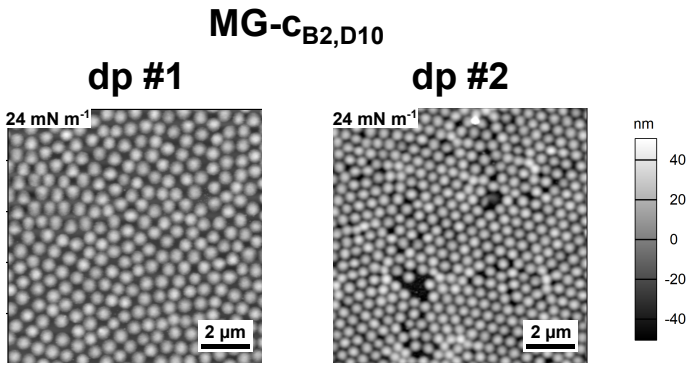

Figure A34: AFM scans of two different samples prepared by the Langmuir-Blodgett technique with a surface pressure Π of 24 mN m^{-1} resulting in a dense packing ("dp") for the P(NIPAM-co-DMA) (named dp #1 and dp #2). Colloidal probe measurements have been performed on both samples to test the reproducibility of the results.

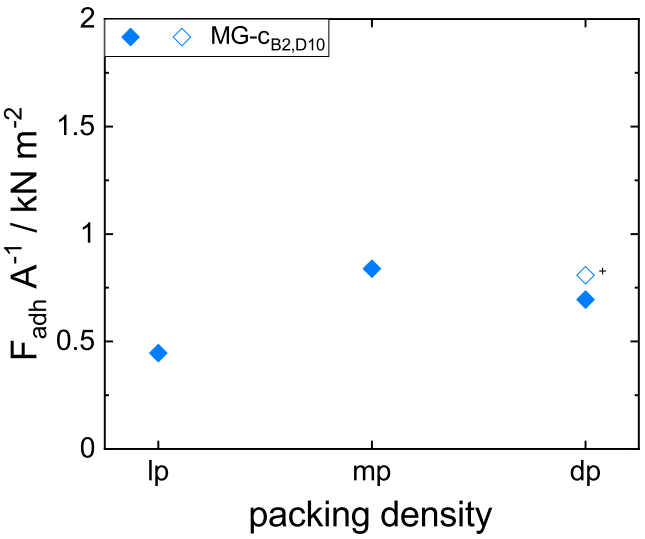

Figure A35: Averaged normalised adhesion force $F_{adh}\,A^{-1}$ of the P(NIPAM-co-DMA) microgel MG-$c_{B2,D10}$ in dependence of the packing density. The open rhomboid symbol illustrates the value obtained from the repeated measurement dp #2.

A6.2 Increasing DMA amount

Table A5: Relevant parameters of colloidal probe measurements on samples prepared by the Langmuir-Blodgett technique with a mp for the pure PNIPAM microgel MG-$c_{B2,D0}$ and the P(NIPAM-co-DMA) microgels with increasing DMA amount (MG-$c_{B2,D5}$, MG-$c_{B2,D10}$ and MG-$c_{B2,D15}$): mean colloidal probe radius $\overline{R}_P$ (derived from SEM images), mean indentation depth $\overline{\delta}$, contact radius a (eq. 3.22) and contact area A (eq. 3.23) calculated from an average of 10 force curves.

Microgel	$\overline{R}_P$ / µm	$\overline{\delta}$ / nm	a / nm	A / µm^2
MG-$c_{B2,D0}$	2.12 ± 0.04	193.3 ± 15.2	639.7 ± 25.9	5.03 ± 0.40
MG-$c_{B2,D5}$	2.12 ± 0.04	122.0 ± 7.3	508.6 ± 16.0	3.20 ± 0.20
MG-$c_{B2,D10}$	2.12 ± 0.04	102.8 ± 12.0	467.3 ± 27.6	2.71 ± 0.32
MG-$c_{B2,D15}$	2.12 ± 0.04	84.1 ± 8.7	422.0 ± 22.2	2.21 ± 0.23

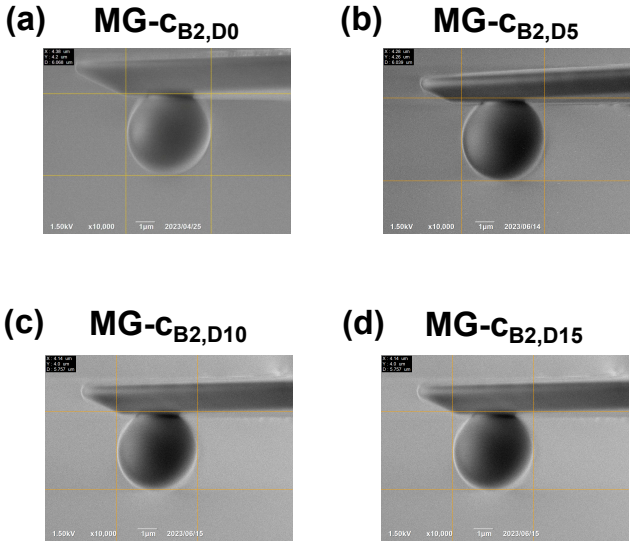

Figure A36: SEM images of colloidal probes used for force spectroscopy measurements on samples prepared with the Langmuir-Blodgett technique with a mp for (a) the pure PNIPAM microgel MG-$c_{B2,D0}$ and the P(NIPAM-co-DMA) microgels with increasing DMA amount ((b) MG-$c_{B2,D5}$, (c) MG-$c_{B2,D10}$ and (d) MG-$c_{B2,D15}$).

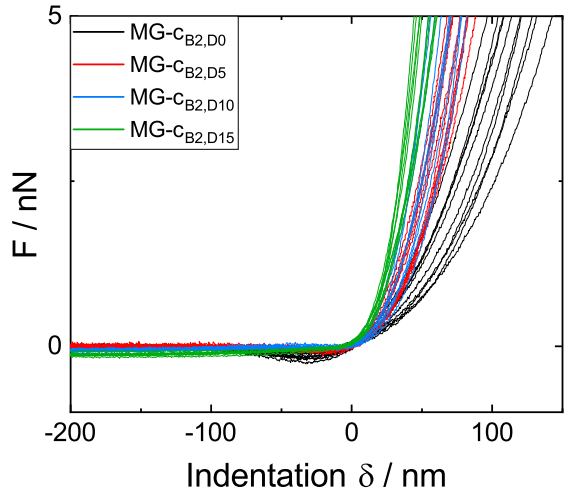

Figure A37: Pure force curves received for the different microgels indented by the colloidal probe, used for the calculation of the global modulus E_{glob}.

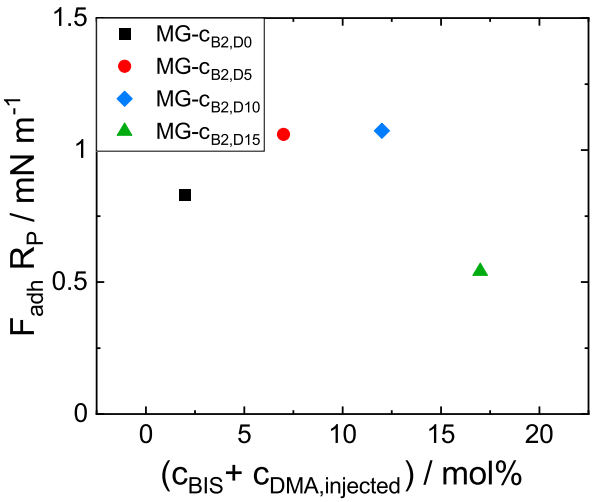

Figure A38: The average adhesion force normalised by the colloidal probe radius $F_{adh}\,R_P^{-1}$ of the different microgels in dependence of the sum of cross-linker BIS concentration c_{BIS} and injected DMA amount $c_{DMA,injected}$ for better comparison to literature values.

A7 AFM art

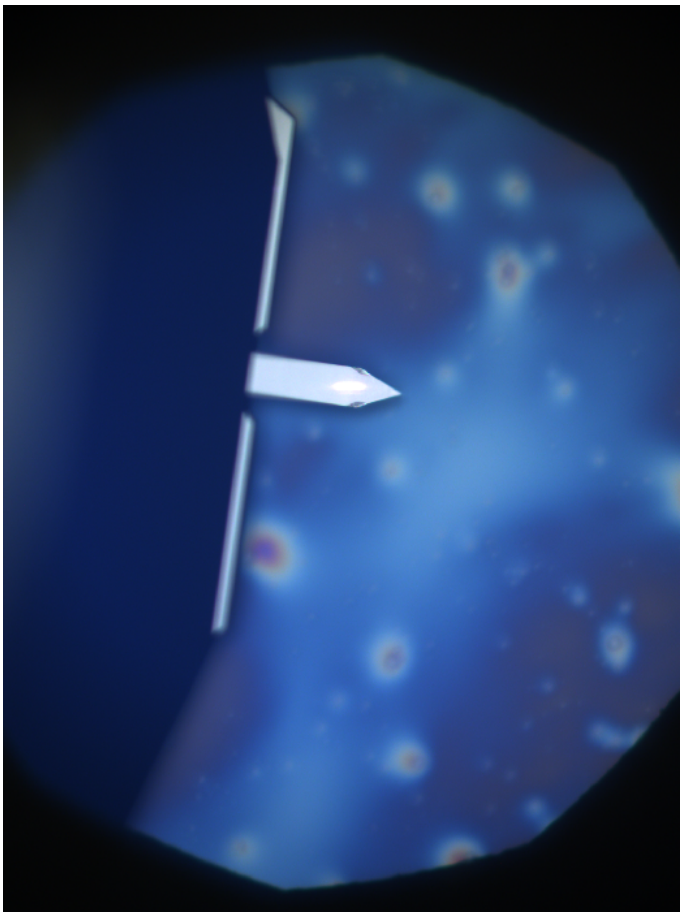

Figure A39: Top down view, provided by the Cypher AFM camera, on a cantilever and a random microgel sample. Due to large variances in height and roughness of the sample's surface, light is scattered differently in different regions of the sample. As a result, the sample visually resembles a night sky.

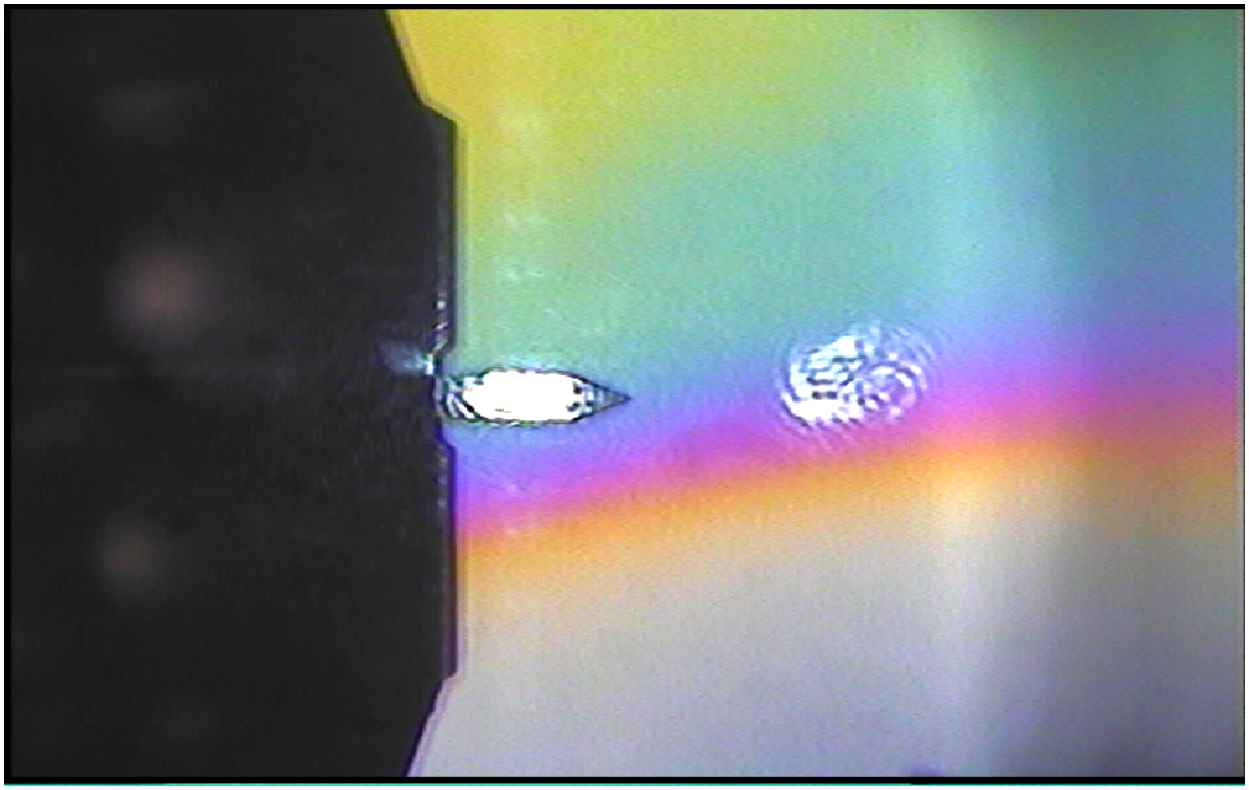

Figure A40: Top down view, provided by the MFP-3D AFM camera, on a cantilever and a random microgel sample. Due to the presence of a thin moisture film on the sample's surface, incident light is partially reflected at both the top and bottom surface of the film, leading to interference effects. This interference, involving both constructive and destructive interference, is influenced by the film's thickness and the angle of incident light. As a result, the surface of the sample displays vibrant colours, resembling a rainbow.

Danksagungen

[not available in online version]